The Dissertation Committee for Olaoluwa Opeoluwa Adepoju Certifies that this is the approved version of the following dissertation:

Scale-up of Dispersion for Simulation of Miscible Displacements

Committee:

Larry W. Lake, Supervisor

Russell T. Johns, Co-Supervisor

Kamy Sepehrnoori

Sanjay Srinivasan

Birol Dindoruk

Scale-up of Dispersion for Simulation of Miscible Displacements

by

Olaoluwa Opeoluwa Adepoju, B.Tech.; M.S

Dissertation

Presented to the Faculty of the Graduate School of

The University of Texas at Austin

in Partial Fulfillment

of the Requirements

for the Degree of

Doctor of Philosophy

The University of Texas at Austin

May 2013

Dedication

I dedicate this work to my family, especially my wife Omolola and children, Temilola and Kolawole, for their support through this journey.

Acknowledgements

I would like to acknowledge the support of my supervisors, Dr. Larry W. Lake and Dr. Russell T. Johns. They painstakingly and patiently worked me through the maze that this research poses and in turn developed my analytical and research skills.

I would like to appreciate all my committee members, Dr. Kamy Sepehrnoori, Dr. Sanjay Srinivasan and Dr. Birol Dindoruk for taking time to serve on my dissertation committee.

This work was made easier and more fun by the dedication of the administrative staff of this department, especially Dr. Roger Terzian, Frankie Hart, Cheryl Kruzie (retired), Joanna Castillo and Mary Pettengill.

I also extend my appreciation to my colleagues at the University of Texas at Austin, both past and present, for their intellectual and technical discussions that brought clarity to many subjects.

I acknowledge the funding from the Abu-Dhabi National Oil Company (ADNOC) and the member companies of the Gas Flooding Joint-Industry Project.

Finally I would like to thank my family for their support and my wife and children for standing by me through this program.

To God be the glory

Scale-up of Dispersion for Simulation of Miscible Displacements

Olaoluwa Opeoluwa Adepoju, Ph.D.

The University of Texas at Austin, 2013

Supervisor: Larry W. Lake and Russell T. Johns

Dispersion has been shown to degrade miscibility in miscible displacements by lowering the concentration of the injected solute at the displacement fronts. Dispersion can also improve oil recovery by increasing sweep efficiency. Either way, dispersion is an important factor in understanding miscible displacement performance.

Conventionally, dispersion is measured in the laboratory by fitting the solution of one-dimensional convection-dispersion equation (CDE) to the effluent concentration from a core flood. However dispersion is anisotropic and mixing occurs in both longitudinal and transverse directions.

This dissertation uses the analytical solution of the two-dimensional CDE to simultaneously determine longitudinal and transverse dispersion. The two-dimensional analytical solution for an instantaneous finite volume source is used to investigate anisotropic mixing in miscible displacements. We conclude that transverse mixing becomes significant with large a concentration gradient in the transverse direction and significant local variation in flow directions owing to heterogeneity.

We also utilized simulation models similar to Blackwell's (1962) experiments to determine transverse dispersion. This model coupled with the analytical solution for two-dimensional CDE for continuous injection source is used to determine longitudinal and

transverse dispersivity for the flow medium. The validated model is used to investigate the effect of heterogeneity and other first contact miscible (FCM) scaling groups on dispersion.

We derive the dimensionless scaling groups that affect FCM displacements and determine their impact on dispersion. Experimental design is used to determine the impact and interactions of significant scaling groups and generate a response surface function for dispersion based on the scaling groups. The level of heterogeneity is found to most significantly impact longitudinal dispersion, while transverse dispersion is most significantly impacted by the dispersion number.

Finally, a mathematical procedure is developed to use the estimated dispersivities to determine *a-priori* the maximum grid-block size to maintain an equivalent level of dispersion between fine-scale and upscaled coarse models. Non-uniform coarsening schemes is recommended and validated for reservoir models with sets of different permeability distributions. Comparable sweep and recovery are observed when the procedure was extended to multi-contact miscible (MCM) displacements.

Table of Contents

List of Tables

List of Figures

Chapter 1: Introduction

This chapter introduces dispersion and the significance of this research. The research objectives are highlighted and the outline of the dissertation is described.

1.1 Problem Description

Miscible displacement, such as high-pressure CO_2 flooding, recovers oil by achieving miscibility between the injected fluid and resident oil. The resulting miscibility increases the displacement efficiency and ultimately the oil recovery. Dispersion degrades miscibility in miscible displacements by lowering the concentration of the injected fluid at the displacement fronts, thereby reducing local displacement efficiency. Dispersion can also improve oil recovery by increasing sweep efficiency, as the injected fluid spreads to previously un-contacted areas of the reservoir. Therefore, dispersion is an important factor in understanding and predicting miscible displacement performance.

Dispersion is defined as the mixing that occurs during miscible displacements as a result of diffusion, velocity gradients along pore paths, heterogeneity, and mechanical mixing within pores (Bear 1972, Lake 1989). Dispersion results from molecular diffusion and mechanical mixing (Pickens and Grisak 1981). Molecular diffusion is the spreading of solute particles caused by concentration gradients while mechanical dispersion is mixing resulting from velocity variations along and across streamlines within the pore space.

Dispersivity is conventionally used as a quantitative measure of dispersion. In one-dimension, dispersivity is the proportionality constant between dispersion coefficient and average longitudinal velocity. Bear (1972) stated that dispersivity is a characteristic value of the permeable medium. However, it has been shown that dispersivity is not

constant but scale dependent (Pickens and Grisak 1981, Arya *et al.* 1988, Mahadevan *et al.* 2003, John *et al*. 2010, Jha *et al.* 2009, Garmeh and Johns 2010).

Dispersion is different from convective spreading. Convective spreading results as solute particles travel through different streamlines of varying velocity and arrive at a fixed location at different times. Macroscopically, convective spreading is caused by solute particles channeling through layers of different permeabilities. Detailed pore scale modeling has shown that convective spreading is reversible but actual mixing or dispersion is irreversible. Flow reversal has been shown to distinguish between convective spreading and local mixing (Jha *et al.* 2009). Dispersion estimated from the concentration profile at a particular point in a porous medium is a better indicator of mixing compared to the dispersion estimated from the effluent concentration at the outlet of the medium (Mahadevan *et al.* 2003). Mahadevan *et al.* (2003) showed that dispersion estimated from the effluent concentration at the outlet of the medium is usually greater because it is smeared by convective spreading and channeling of the solute along high permeability layers. This research focused on estimating dispersion using the local (grid-block) concentration profile.

Conventionally, dispersion is measured in the laboratory by fitting the solution of the one-dimensional convection-dispersion equation (CDE) to the effluent concentration from a core flood. The concentration is averaged over the cross section of the core. However, in more complicated flow, dispersion is anisotropic and mixing occurs in both longitudinal (the main direction of flow, here the x-direction) and transverse directions (perpendicular to the x-direction, here the y-direction). Transverse dispersion is thought to be much smaller than longitudinal dispersion in media such as core plugs, where concentration can quickly equilibrate across the cross section (Jha *et al.* 2009). In such cases estimated longitudinal dispersion from one-dimensional solution of the CDE is

accurate. However, where there is possibility of significant concentration gradients in the transverse direction, either because of cross flow or a change in the flow direction caused by heterogeneity, transverse dispersion may become significant. This dissertation focuses on using the analytical solution of the two-dimensional CDE to simultaneously determine longitudinal and transverse dispersion and investigate anisotropic mixing.

Compositional reservoir simulation is one of the tools used to design and evaluate miscible displacements. Reservoir simulations generally use finite-difference approximations to solve partial differential fluid flow equations. Finite difference approximations introduce truncation error that leads to numerical dispersion. The study of dispersion is thus challenging because of the presence of numerical dispersion in reservoir simulators. Numerical dispersion increases the apparent level of mixing in the reservoir model (Solano *et al.* 2001, Parakh and Johns 2004). Numerical dispersion, like local dispersion, has the effect of degrading miscibility by driving the composition route further into the two phase region (Haajizadeh *et al.* 2000). Numerical dispersion increases with increasing grid-block size and, depending on the grid-block size, can be much larger than physical dispersion (Haajizadeh *et al.* 1999, Lantz 1971, Fanchi 1983). However, the level of physical dispersion for highly complex flows is poorly known. This dissertation examines this question by determining total longitudinal and transverse dispersion for different permeability distributions.

Fine scale geological models contain detailed descriptions of reservoir properties such as porosity, permeability and fluid saturations. Simulations of these fine scale models are often too computationally demanding. Fine scale models must be coarsened to manageable sizes while maintaining the gross behavior of the fine scale model. Upscaling is the process of using an equivalent coarse grid block to replace a number of fine grid blocks. Upscaling homogenizes the medium by combining groups of fine scale cells into

a single cell thereby reducing local velocity variations in the upscaled coarse model. This reduction in velocity variations results in less mixing compared to the original fine scale model (Garmeh and Johns 2010). Conversely, the increased size of the upscaled grid block introduces more numerical dispersion compared to the smaller grid-block sizes in the fine scale model. Therefore, the net dispersion in the two scales (fine and coarse scales) may not be equivalent. We develop a procedure in this research that uses the estimated longitudinal and transverse dispersivity to determine the maximum grid-block sizes in both x- and z-directions that will maintain an equivalent level of dispersion between fine and coarse scale models.

1.2 RESEARCH OBJECTIVES

The objectives of this research are to:

1. Estimate longitudinal and transverse dispersivity in large-scale media.
2. Investigate the effect of permeability distribution on anisotropic mixing in miscible displacements.
3. Determine the effect and significance of dimensionless scaling groups for first contact miscible (FCM) displacements on longitudinal and transverse dispersivity and use experimental design to develop a response surface function for both longitudinal and transverse dispersivity based on these scaling groups.
4. Determine the maximum grid-block size in both x- and y-directions that will ensure equivalent mixing during upscaling for miscible floods.

5 Employ use of non-uniform coarsening schemes to account for different mixing levels in reservoir models with different sets of permeability distributions.

1.3 ORGANIZATION OF DISSERTATION

There are seven chapters in this dissertation. Chapter 2 conducts an extensive literature review on dispersion in porous media. The classical works of Taylor (1953) and others are discussed.

In chapter 3, we investigate anisotropic mixing in miscible displacements. In this chapter we present an instantaneous finite-volume source solution for the two-dimensional CDE and the procedure to estimate longitudinal and transverse dispersivity from local concentration profiles obtained with FCM simulations. We conclude that transverse dispersion is significant in the presence of concentration gradients in the transverse direction and when there are local changes in flow directions due to heterogeneity.

In chapter 4, we explore the determination of longitudinal and transverse dispersivity for large scale media using a continuous source solution for a two-dimensional CDE. We utilize a simulation model similar to the experiments of Blackwell (1962) to determine longitudinal and transverse dispersivities simultaneously. The procedure was validated and the effects of heterogeneity and permeability distribution on the estimated dispersivities are investigated.

In chapter 5, we present the mathematical formalism and approach to determine the maximum grid-block size that ensures equivalent mixing between fine and upscaled coarse models. We extend the method to a model with different sets of permeability distribution and propose the use of non-uniform coarsening schemes to properly upscale

the model. The upscaling method based on estimated dispersivities from FCM simulations is also extended to a multi-contact miscible displacement with good results.

In chapter 6, all scaling groups affecting FCM displacements are derived and their impacts on longitudinal and transverse dispersivity are determined. Experimental design is then utilized to develop an objective function for dispersivity based on the significant scaling groups.

Finally in chapter 7, a summary of the research contributions and conclusions are highlighted.

Chapter 2: Literature Review

There is extensive literature on the subject of dispersion. This review summarizes some classical and recent literature that is relevant to this dissertation.

2.1 THE CONCEPT OF CONTINUUM AND DISPERSION

Bear (1972) gave a classical explanation of the concept of continuum as it relates to fluid flow. The concept of continuum is an underlying assumption in the flow of fluid through porous media. The continuum assumption is invoked to aggregate a group of molecules in a control volume and treat them as particles. The fluid is now regarded as a flow of particles. This assumption is necessary, since it will be too cumbersome and computationally impossible to describe fluid flow at the molecular level. The size of the particle must be larger than the mean free path of the molecules but smaller than the fluid domain, such that meaningful average values such as density can be assigned to describe the fluid. The continuum assumption is also invoked to move from the microscopic (particle level) to macroscopic level, where porosity and its representative elementary volume (REV) are defined. The macroscopic medium properties such as porosity, permeability and dispersivity are introduced to describe fluid flow at the averaged macroscopic level. Therefore dispersion is an averaged property of the medium, introduced due to our inability to resolve fluid dynamics at the microscopic level (Bear 1972).

Dispersion is defined as a non-steady, irreversible mixing process, by which a miscible solute spreads due to velocity variations in a porous media (Bear 1972). Dispersion is mainly a microscopic phenomenon and we have to revert to the molecular level to describe and understand the dispersion phenomena (Bruggeman 1999).

Tracer particles in a fluid travel along different paths within irregular pore geometries. These particle paths have different local velocities resulting in different travel times as they travel through the porous medium. These complex flow paths cause tracer to spread gradually in the direction of flow resulting in longitudinal dispersion. Molecular diffusion, due to a concentration gradient, results in fluid particles moving from one streamline to the next and exchanging molecules with neighboring particles during fluid flow. The combination of diffusion and fluid flow through complex and irregular pore structure causes tracer molecules to spread considerably in the transverse direction. Transverse dispersion results in more spreading in the transverse direction than diffusion alone, though diffusion is required for dispersion. Bruggeman (1999) suggested that the spreading caused by transverse dispersion is of the order of the REV, while diffusion only results in spreading on the order of the particle size.

Longitudinal dispersion can be explained from a microscopic level, since it is mainly caused by flow through irregular pore geometry. Transverse dispersion has to be explained at a molecular level, since transverse spreading is initiated by diffusion and enhanced by flow through irregular pore systems (Bruggeman 1999).

Transverse dispersion is the dispersion in the direction perpendicular to the main flow direction. Transverse dispersion is usually considered to be smaller than longitudinal dispersion. The ratio of longitudinal to transverse dispersivity found in the literature ranges from about 5 to 100 (Blackwell 1959, Freeze and Cherry 1979, Lake and Hirasaki 1981, Dagan 1982, Gelhar and Axeness 1983, Anderson 1984). Lake and Hirasaki (1981) showed that the combination of transverse dispersion and longitudinal velocity result in Taylor's dispersion.

Transverse dispersion causes the solute concentration to equilibrate across the flow cross-section (Hassinger and Dale 1963, Jha *et al.* 2009). Heterogeneity can result

in spatial variations in velocity, which causes different parts of the solute plume to move at different velocities. Fluctuations in flow directions, due to local variations in velocities can result in increased dispersion, especially transverse dispersion (Goode and Konikow 1990). Goode and Konikow (1990) argued that this increase in transverse dispersion is because there are local changes in the main flow directions due to heterogeneity. Salandin and Fiorotto (2000) also explained that transverse dispersion is enhanced by complex flow geometry and pore scale anisotropy.

2.2 HYDRODYNAMIC DISPERSION

Hydrodynamic dispersion results as tracer particles travel through pores of irregular geometry. Hydrodynamic dispersion can be affected by the complex pore geometry, molecular diffusion, and variations in fluid properties, such as viscosity, adsorption and chemical reaction (Bear 1972). Mechanical dispersion and molecular diffusion are the two basic mechanisms for dispersion. Mechanical dispersion results from variations in local velocities due to heterogeneity. Mechanical dispersion dominates molecular diffusion. Molecular diffusion is only significant at low velocities.

Dispersion has been widely studied with different models. The two main ones use capillary tubes and statistical methods. Danel (1952), Taylor (1953), and Aris (1956) are some of the classical works that described dispersion using capillary tubes, while Saffman (1959), Scheidegger (1954) and De Jong (1958) used statistical method to describe dispersion.

Taylor (1953) in one of his classical works studied dispersion using capillary tubes. Taylor observed the spread of a solute through a single capillary tube of a small radius. He observed that the combination of transverse diffusion and longitudinal bulk

flow can result in longitudinal dispersion. He showed analytically that dispersion results in a concentration distribution that is centered about a point that moves with the mean speed of flow and is symmetrical in spite of the asymmetry of the flow. Taylor (1953) proposed that the longitudinal dispersion coefficient, which can be estimated from the solute concentration in the tube, is a measure for dispersion. Taylor described the longitudinal dispersion coefficient (D_L) to be proportional to the square root of the velocity and inversely proportional to the coefficient of molecular diffusion (D_o).

$$D_L = \frac{a^2 u_o^2}{192 D_o} \tag{2.1}$$

where a is the radius of the tube and u_o is the maximum velocity along the main flow axis.

Taylor (1953) also showed that the length of the mixing zone (L_2) where the concentration (C) changes from 90% of C to 10% of C is proportional to the square root of time (t) and inversely proportional to the square root of the coefficient of molecular diffusion (D_o).

$$L_2 = 3.62\left(D_L t\right)^{1/2} \tag{2.2}$$

Aris (1956) extended the work of Taylor to irregularly shaped capillary tubes. Aris (1956) concluded that dispersion results in a concentration distribution that is Gaussian (normal distribution) around a center of gravity, which is travelling at the mean velocity of the flow. Aris (1956) also extended Taylor's dispersion to include an additive diffusion term.

$$D_L = D_o + \frac{a^2 u_o^2}{192 D_o} \tag{2.3}$$

Aris and Amundson (1957) and Bear (1960) used a one-dimensional mixing cell to analyze dispersion. They also concluded that dispersion results in a concentration distribution that can be described by a normal distribution and showed that the

longitudinal dispersion coefficient is proportional to the velocity as opposed to the square of the velocity for capillary tubes.

The statistical approach has also been used to study dispersion. Such an approach breaks down the travel path of a particle into two components. The first component considers the motion of the particle due to the bulk flow along the streamline while the second component considers the random movement of a particle from one streamline to an adjacent streamline owing to diffusion. The statistical approach uses Darcy velocity to describe bulk flow and probability theory to describe random movement due to diffusion (Bear 1972). De Jong (1958, 1958a) used the statistical approach to show that longitudinal dispersion is greater than transverse dispersion. They also showed that the longitudinal dispersion coefficient is proportional to the average flow velocity and the proportionality constant is the characteristic length called dispersivity. Dispersivity is considered to be the order of the grain size and it depends on grain distribution.

Saffman (1959) also used the statistical approach to study dispersion and concluded that dispersion is proportional to the average velocity of the medium and showed that hydrodynamic dispersion is a combination of molecular diffusion and mechanical dispersion. Scheidegger (1961) using the statistical approach also concluded that the coefficient of mechanical dispersion is proportional to the average interstitial velocity and called the constant of proportionality the geometric dispersivity of the medium. They suggested that the geometric dispersivity depends on permeability heterogeneity, tortuosity and the length of the flow path.

2.2.1 Convection dispersion equation (CDE)

The CDE is a statement of conservation of mass. Assuming no chemical reaction and adsorption, the CDE is expressed as,

$$\frac{\partial C}{\partial t} + \nabla \cdot \left(\vec{v} C \right) - \nabla \cdot \left(\vec{\vec{D}} \nabla C \right) = 0 \tag{2.4}$$

where C is the solute concentration (mass/unit volume of solution), $\vec{v}$ is the interstitial velocity vector and $\vec{\vec{D}}$ is the dispersion tensor. The general form of the dispersion tensor for a single phase fluid is expressed as,

$$\vec{\vec{D}}_{mn} = \begin{bmatrix} D_{xx} & D_{xy} & D_{xz} \\ D_{yx} & D_{yy} & D_{yz} \\ D_{zx} & D_{zy} & D_{zz} \end{bmatrix} \tag{2.5}$$

where *m* and *n* are index for spatial directions. The components of the dispersion tensor are expressed as (Bear 1972, Lake 1989),

$$D_{xx} = \frac{D_o}{\tau} + \frac{\alpha_L v_x^2}{|v|} + \frac{\alpha_T \left(v_y^2 + v_z^2 \right)}{|v|} \tag{2.6a}$$

$$D_{yy} = \frac{D_o}{\tau} + \frac{\alpha_L v_y^2}{|v|} + \frac{\alpha_T \left(v_x^2 + v_z^2 \right)}{|v|} \tag{2.6b}$$

$$D_{zz} = \frac{D_o}{\tau} + \frac{\alpha_L v_z^2}{|v|} + \frac{\alpha_T \left(v_x^2 + v_y^2 \right)}{|v|} \tag{2.6c}$$

$$\left(D_{mn} \right)_{m \neq n} = \frac{\left(\alpha_L - \alpha_T \right) v_m v_n}{|v|} \tag{2.6d}$$

where α_L and α_T are the longitudinal and transverse dispersivity respectively, D_o is the molecular diffusion coefficient and $|v|$ is the magnitude of the interstitial velocity expressed as $|v| = \sqrt{v_x^2 + v_y^2 + v_z^2}$.

The parameters in the CDE equation are all macroscopic parameters which from continuum assumption are averaged properties (Anderson 1984, Bear 1972). The CDE equation assumes that dispersion is Fickian and can be represented analogous to the Fick's second law of diffusion. Fick's second law is expressed as,

$$\vec{J}_d = -\phi \vec{\vec{D}} \Delta C \tag{2.7}$$

where $\vec{J}_d$ is the mass flux vector due to dispersion (mass/area/time).

Taylor (1953) proposed that dispersion can be represented by a Fickian process. Matheron and DeMarsaily (1980), Gelhar and Axness (1981) and Dagan (1982) proposed that dispersion becomes Fickian after a substantial transport from the source, typically a distance of order 10 to 100 meters (m). They concluded that after dispersion becomes Fickian, the concentration-distance plot of a tracer from an instantaneous point source should approximate a Gaussian distribution. Mercado (1967) and Gelhar *et al.* (1979) suggested that dispersion may not approach the Fickian limit under certain conditions. They suggested that in flow parallel to bedding planes, where lateral dispersion is negligible, dispersion may never fully develop. Garmeh *et al.* (2009) used pore scale models and showed that the asymptotic limit of dispersion depends on the scale of heterogeneity in the medium.

2.2.2 Analytical solution of one-dimensional CDE

The CDE in one-dimension assuming incompressible fluid and rock, no reaction and adsorption, ideal mixing and single phase flow can be expressed in dimensionless form as (Lake 1989),

$$\frac{\partial C_D}{\partial t_D} + \frac{\partial C_D}{\partial x_D} - \frac{1}{N_{pe}} \frac{\partial^2 C_D}{\partial x_D^2} = 0 \tag{2.8}$$

where x_D is the dimensionless distance $\left(x/L\right)$ and t_D is the dimensionless time (pore volume injected) defined as,

$$t_D = \frac{qt}{A\phi L} = \frac{vt}{L} \tag{2.9}$$

where L is length of the medium in the x-direction, A is the cross-sectional area of the medium, q is the volumetric flow rate and v is the interstitial velocity. The Peclet number (N_{pe}) describes the ratio of convective to dispersive transport and it is expressed as,

$$N_{pe} = \frac{vL}{D_L} \tag{2.10}$$

where D_L is the longitudinal dispersion coefficient. The dimensionless concentration (C_D) is defined in terms of the initial concentration (C_i) and injected composition (C_j) as,

$$C_D = \frac{C(x,t) - C_i}{C_j - C_i} \tag{2.11}$$

Typical boundary and initial conditions imposed on the CDE equation can be expressed as,

$$C_D(x_D, 0) = 0 \tag{2.12a}$$

$$C_D(\infty, t_D) = 0 \tag{2.12b}$$

$$C_D(0, t_D) = 1 \quad . \tag{2.12c}$$

The analytical solution for the one-dimensional CDE subject to the above boundary and initial conditions is (Ogata and Banks 1961, Lake 1989),

$$C_D(x_D, t_D) = \frac{1}{2} erfc\left(\frac{x_D - t_D}{2\sqrt{\frac{t_D}{N_{pe}}}}\right) + \frac{e^{x_D N_{pe}}}{2} erfc\left(\frac{x_D + t_D}{2\sqrt{\frac{t_D}{N_{pe}}}}\right) \tag{2.13}$$

where erfc is the complementary error function. The second term approaches zero as x_D and N_{pe} increase. The dimensionless mixing length, which is the distance between C_D = 0.1 and C_D = 0.9, grows in proportion to the square root of time as shown by the expression,

$$\Delta x_D = 3.625\sqrt{\frac{t_D}{N_{pe}}} \tag{2.14}$$

Hassinger and Dale (1963) defined the Peclet number using the average particle size (D_p) as the characteristic length of the medium.

$$N_{pe} = \frac{vD_p}{D_L} \tag{2.15}$$

Perkins and Johnston (1963) conducted experiments that showed the relationship between the ratio of dispersion and diffusion coefficients with Peclet number. They showed that at low Peclet number (< 0.02), molecular diffusion dominates longitudinal dispersion (Figure 2.1). As the Peclet number exceeds a value of six, longitudinal dispersion dominates because velocity variations within the pores becomes significant.

A transition period (0.02 < Npe < 6) exists where both molecular diffusion and longitudinal dispersion are active. The authors defined an empirical relationship between Peclet number and the ratio of the dispersion coefficient (D_L) to molecular dispersion coefficient (D_o).

$$\frac{D_L}{D_o} = C_1 + C_2\left(\frac{vD_p}{D_o}\right)^{\beta} \tag{2.16}$$

C_1, C_2 and β are empirical constants. Peclet number is usually greater than 6 at normal reservoir velocities, which implies that longitudinal dispersion dominates diffusion and the ratio of dispersion to diffusion is proportional to Peclet number (i.e β=1). Lake (1989) indicates that if the interstitial velocity is greater than 3 cm per day, dispersion dominates and the longitudinal dispersion coefficient can be expressed as,

$$D_L = \frac{D_o}{C_1} + C_2\left(\frac{vD_p}{D_o}\right)^{\beta} \times D_o \approx \alpha_L v \tag{2.17}$$

where D_L is the longitudinal dispersion coefficient. This relationship does not preclude the presence of diffusion in normal reservoir conditions. Diffusion can still be important when there are dead end pores or adjacent non-flowing zones. The longitudinal dispersivity (α_L) is a characteristic mixing length of the medium.

2.2.3 Measurement of dispersion

Dispersivity is usually estimated by matching the effluent history of a conservative tracer to the solution of the one-dimensional CDE. Dispersivity from laboratory core-floods is usually on the order of 10^{-4} to 10^{-2} m compared to field range dispersivity of 10^{-1} to 10^{2} m (Anderson 1984). Dispersivity from laboratory core-floods result from microscopic heterogeneity owing to distribution of velocities within the pores, differences in pore-sizes and path lengths for individual solute particles, and converging and diverging flows (Freeze and Cherry 1979). However, field scale dispersivity results from variations in fluid velocity due to macroscopic heterogeneity in the porous medium, including the effect of cross-flow and layering (Freeze and Cherry 1979, Pickens and Grisak 1981a, Lake and Hirasaki 1981).

Gelhar *et al.* (1979) and Pickens and Grisak (1981a, b) noted that dispersivity is scale dependent, as estimated dispersivity increases with increasing distance of investigation. A collection of laboratory and field scale dispersivities shows that dispersivity increases as the volume of the sample increases (Arya *et al.* 1988, John *et al.* 2008) (Figure 2.2).

Mahadevan *et al.* (2003) analyzed and categorized dispersivity as echo, transmission and local dispersivity based on the method of measurement. Echo dispersivity is the dispersivity estimated from the tracer concentration profile at the point of injection after flow reversal. Transmission dispersivity is the dispersivity estimated from the effluent concentration profile at the outlet of the medium. Local dispersivity, which is considered as true mixing, is estimated from the concentration profile from a fixed point in the medium. The authors concluded that transmission dispersion is usually greater that echo dispersion because of the effect of spreading as solute channels through the medium owing to layering.

Kitanidis (1994) explained that spreading results in stretching and deformation of the solute plume, while mixing (dilution) results in solute occupying an increasing volume of the fluid. Experimental research of Hulin and Plona (1989) suggested that the reversible part of mixing is due to convection, while the irreversible part is due to mixing. Flow reversal in echo dispersion removes the effect of apparent mixing (spreading) (Jha *et al.* 2009, John *et al.* 2010).

Jha *et al.* (2009) used network modeling to show the difference between convective spreading and dispersion. John *et al.* (2010) used particle tracking simulation to demonstrate that flow reversal distinguishes between true mixing and convective spreading. Local measurements of dispersion also distinguish convective spreading from mixing (Garmeh *et al.* 2009). Cirpka and Kitanidis (2000) distinguished between convective spreading and mixing by using the temporal moments from breakthrough curves obtained at a single point in the medium. Locally estimated dispersivity also has the advantage of allowing the entire medium to be sampled, up to the outlet of the medium.

2.2.4 Effect of dispersion on miscible displacements

Miscible displacement, such as high pressure CO_2 flooding, recovers oil by achieving miscibility between the injected fluid and resident oil. The resulting miscibility increases the displacement efficiency and ultimately the oil recovery. Dispersion degrades miscibility in miscible floods by lowering the concentration of the injected solute at the displacement fronts (Johns *et al.* 2000). Dispersion can also degrade miscibility by driving the composition route deeper into the two-phase region (Haajizadeh *et al.* 2000, Solano *et al.* 2001).

Dispersion can also enhance recovery by causing the solute plume to dilute and occupy increasing volume of the fluid (Kitanidis 1994). Therefore, the relationship between recovery and dispersion is complex as dispersion affects the local displacement efficiency and the areal sweep efficiency (Haajizadeh *et al.* 2000). Thus, it is important to quantify the level of dispersion in miscible displacement and ensure that the level of dispersion is maintained during upscaling for accurate modeling of miscible displacements.

2.3 UPSCALING

Fine scale geological models can be very computationally demanding because of the order of the fine scale model, which can range from 10^7 to 10^8 grid-blocks (Chen *et al.* 2003). Upscaling is thus required to coarsen the fine scale model. The magnitude of coarsening varies in different directions due to spatial and directional distributions of properties. The fine scale model can be coarsened about 5-10 times to make the simulation models practical for routine reservoir simulation (Chen *et al.* 2003). The purpose of upscaling is to generate upscaled properties that will give comparable flow behavior to fine scale properties.

Fine scale models contain detailed descriptions of reservoir properties such as porosity, permeability and fluid saturations. Upscaled effective values of the porosity and fluid saturations are typically estimated using volume or pore-volume averaging (Durlofsky *et al.* 1996).

Begg *et al.* (1989) defines the effective permeability as the equivalent homogenous permeability that gives the same flux as the heterogeneous model subject to the same boundary condition. The effective permeability thus depends on the boundary

conditions and permeability distribution or heterogeneity. Effective permeability, unlike porosity, is not considered an intrinsic property of the medium (Begg *et al.* 1989). Durlofsky (1991) explained that the upscaled permeability can only be referred to as effective permeability if the region over which the permeability is averaged is larger relative to the scale of heterogeneity within the porous media. If the averaged permeability is computed over a region that is smaller than the scale of variation of permeability, the resulting averaged permeability is called an equivalent permeability (Durlofsky 1991). Equivalent permeability is not a constant property of the medium because under varying flow boundary conditions it may be expected to vary (Durlofsky 1991). Begg *et al.* (1989) concluded that effective permeability must be computed for a large volume of rock, such that it will be insensitive to boundary conditions.

Chen *et al.* (2003) categorized upscaling techniques based on the size of the region used in the computation of the coarse scale properties. They are local, extended local, global or quasi-global. In the local approach, only the grid blocks in the target coarse block region of the fine scale realization are used in the computation of upscaled permeability. In the extended local techniques, grid-blocks outside the target coarse block regions are included in the computation of the coarse scale properties. Global techniques utilize flow simulations over the entire fine scale to compute coarse scale parameters. Quasi-global techniques seek to reduce the computational expense of the global technique by using approximations of global information to replace global fine scale results.

There are various averaging techniques used in the scale-up of fine scale permeabilities, including power-law averaging, renormalization techniques, pressure-solver technique, tensor method and pseudo-function techniques (Qi and Hesketh, 2005). The local pressure-solver method is one of the most used methods for upscaling (Begg *et*

al. 1989, Qi and Hesketh 2005). The pressure-solver method uses a combination of the continuity equation and Darcy's law for a steady state flow of a single phase, incompressible fluid to obtain the pressure equation.

The steady-state continuity equation is given as

$$\vec{\nabla} \cdot \vec{u} = 0 \tag{2.18}$$

where $\vec{u}$ is the Darcy velocity vector. Darcy's law in vector form is expressed as,

$$\vec{u} = -\frac{\vec{\vec{k}}}{\mu} \vec{\nabla} P \tag{2.19}$$

where P is the pressure and $\vec{\vec{k}}$ is the permeability tensor. μ is the viscosity (usually considered as unity). The combination of these two equations gives the pressure equation that can be resolved to compute the pressure for each grid-block in the fine scale model. The pressure equation is given as,

$$\vec{\nabla} \cdot \left(\vec{\vec{k}} \cdot \vec{\nabla} P \right) = 0 . \tag{2.20}$$

The fine scale pressure equation is solved with finite-difference discretization. Chen *et al.* (2003) stated that a two-point flux calculation is appropriate for a diagonal permeability tensor where the flow from block (*i*,*j*) to block(*i*+1,*j*) depends only on the pressures in block (*i*,*j*) and (*i*+1,*j*). Therefore the discretized pressure equation is expressed as (Chen *et al.* 2003),

$$\begin{aligned} &\left(T_x\right)_{i-\frac{1}{2},j}\left(P_{i-1,j} - P_{i,j}\right) + \left(T_x\right)_{i+\frac{1}{2},j}\left(P_{i+1,j} - P_{i,j}\right) + \left(T_y\right)_{i,j-\frac{1}{2}}\left(P_{i,j-1} - P_{i,j}\right) \\ &+ \left(T_y\right)_{i,j+\frac{1}{2}}\left(P_{i,j+1} - P_{i,j}\right) = 0 \end{aligned} \tag{2.21}$$

where $\left(T_x\right)_{i\pm\frac{1}{2},j}$ and $\left(T_y\right)_{i,j\pm\frac{1}{2}}$ are the inter-block transmissibilites in the x- and y-directions, and $P_{i,j}$ are the pressures in each grid-block. Chen *et al.* (2003) defined the transmissibility in the x-direction as,

$$\left(T_x\right)_{i+\frac{1}{2},j} = \frac{2\left(k_x\right)_{i+\frac{1}{2},j} \Delta y_j h}{\Delta x_{i+1} + \Delta x_i} \tag{2.22}$$

where Δx and Δy are the grid block sizes and h is the model thickness. Harmonic averaging is used to compute the interface permeabilities as,

$$\left(k_x\right)_{i+\frac{1}{2},j} = \frac{\left(\Delta x_{i+1} + \Delta x_i\right)\left(k_x\right)_{i,j}\left(k_x\right)_{i+1,j}}{\Delta x_{i+1}\left(k_x\right)_{i,j} + \Delta x_i\left(k_x\right)_{i+1,j}}. \tag{2.23}$$

The boundary conditions imposed on the pressure equations are no flow at the lateral boundaries and constant pressures at the top and bottom edges (Begg and King, 1985). Other possible types of boundary conditions include periodicity and linear pressure (Chen *et al.* 2003). The boundary condition for the no-flow, constant pressure condition is specified as (Chen et al. 2003, Begg *et al.* 1989),

$$P\left(0, y\right) = 1 \tag{2.24a}$$

$$P\left(L_x, y\right) = 0 \tag{2.24b}$$

$$u_y\left(x, 0\right) = u_y\left(x, L_y\right) = 0. \tag{2.24c}$$

The pressure equation is solved both in the x and y-directions, with appropriate boundary conditions to obtain local flows that have strong x and y components, which allows for accurate computations of the upscaled properties. The upscaled effective permeability is determined by matching the flux through the fine model to the upscaled model. Pressure solver methods have been proven to be accurate for different levels of heterogeneity (Begg *et al.* 1989).

There is significant ongoing research on upscaling. Durlofsky *et al.* (1996) developed a method for upscaling using non-uniform coarsening scheme. This coarsening scheme has a finer resolution in the region of potentially high flow rate. However, in all upscaling procedures, the model is homogenized by replacing a group of grid-blocks in the fine scale model by fewer grid-blocks. This reduces the local velocity variations and hence the local mixing in the model. Conventional upscaling procedure does not consider

dispersion, though pseudo-relative permeabilities are sometimes added to account for heterogeneities at different scales (Durlofsky *et al.* 1996).

Garmeh and Johns (2010) used the estimated dispersivity from the one-dimensional CDE equation to iteratively determine the appropriate level of coarsening required for miscible displacement. This research will build on that approach.

2.4 NUMERICAL DISPERSION

Numerical dispersion, which is the truncation error from finite-difference approximations, smears saturation fronts similar to physical dispersion and increases the apparent level of mixing in the reservoir (Fanchi 1983, Solano *et al.* 2001, Parakh and Johns 2004). Johns et al. (1994) and Haajizadeh *et al.* (2000) showed that numerical dispersion degrades miscibility similar to physical dispersion, by driving the composition route further into the two phase region.

Numerical dispersion increases with increasing grid-block size and can dominate physical dispersion (Haajizadeh *et al.* 1999). Lantz (1971) developed a quantitative expression for the numerical dispersion. Fanchi (1983) derived expressions to estimate numerical dispersion in finite-difference approximations using truncation analysis on the three-dimensional CDE. The expression for numerical dispersion, when the finite difference scheme uses a backward spatial difference and implicit in time is expressed as

$$\vec{\vec{D}}_{num} = \frac{1}{2}\begin{bmatrix} v_x\left(\Delta x + v_x \Delta t\right) & v_x v_y \Delta t & v_x v_z \Delta t \\ v_y v_x \Delta t & v_y\left(\Delta y + v_y \Delta t\right) & v_y v_z \Delta t \\ v_z v_x \Delta t & v_z v_y \Delta t & v_z\left(\Delta z + v_z \Delta t\right) \end{bmatrix}. \qquad (2.25)$$

Fanchi (1983) also derived the expression for numerical dispersion when the finite difference scheme is explicit in time. For that case, the numerical dispersion is expressed as

$$\vec{\vec{D}}_{num} = \frac{1}{2}\begin{bmatrix} v_x\left(\Delta x - v_x\Delta t\right) & -v_x v_y \Delta t & -v_x v_z \Delta t \\ -v_y v_x \Delta t & v_y\left(\Delta y - v_y \Delta t\right) & -v_y v_z \Delta t \\ -v_z v_x \Delta t & -v_z v_y \Delta t & v_z\left(\Delta z - v_z \Delta t\right) \end{bmatrix}. \quad (2.26)$$

Numerical dispersion can be suppressed by higher-order transmissibility weighting schemes, e.g. two-point upstream weighting. However the numerical dispersion from these higher-order schemes may not be Fickian (Stalkup 1998). Settari and Aziz (1972) also showed that the order of accuracy of a second order differential equation reduces when using variable grid-block sizes in finite difference approximation. The presence of heterogeneity also reduces the order of local truncation error (Yang 1990). Therefore the level of dispersion in highly complex flows may not be known. However, there is a potential of using dispersion resulting from large grid block sizes to match the actual physical mixing during miscible displacement (Haajizadeh *et al.* 2000, Garmeh and Johns 2010).

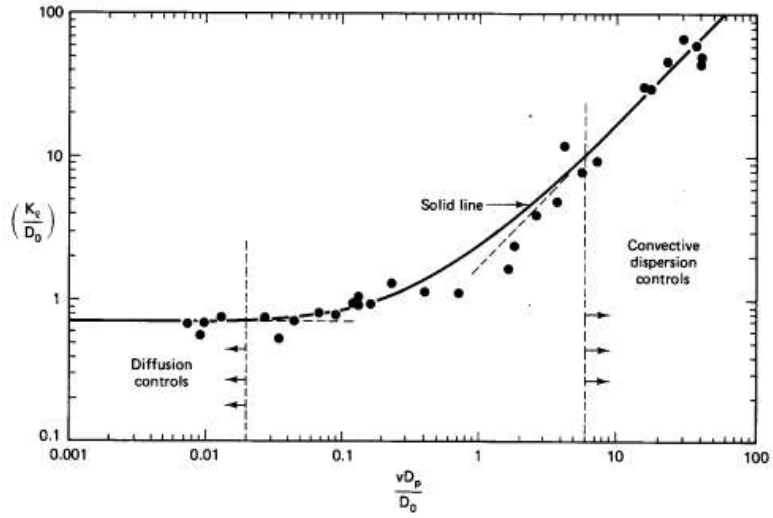

Figure 2.1: Longitudinal dispersion coefficients in permeable flow (from Perkins and Johnston, 1963)

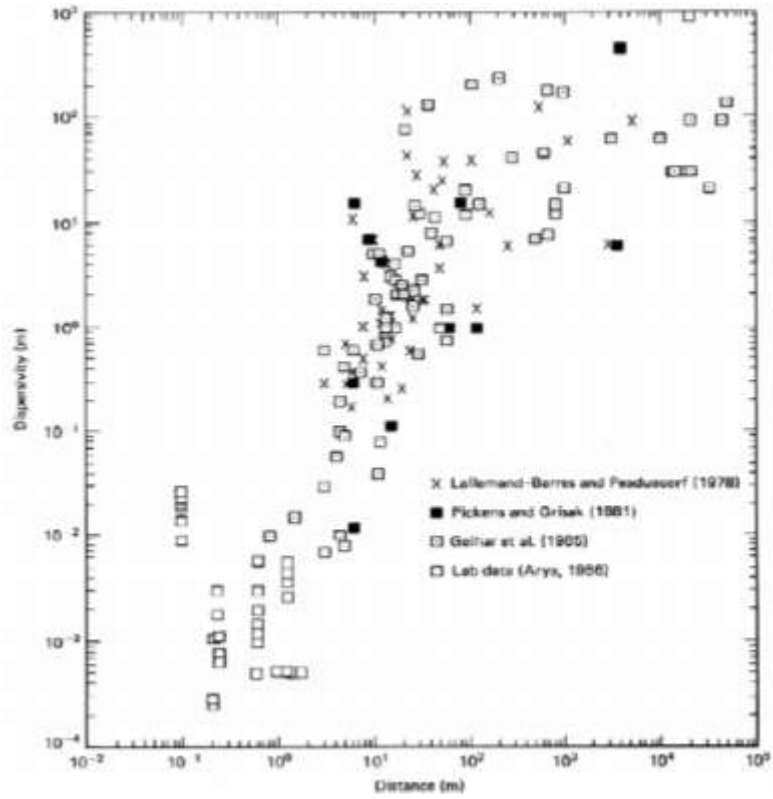

Figure 2.2: Field and laboratory measured dispersivities (from Arya *et al.* 1988).

Chapter 3: Investigation of Anisotropic Mixing in Miscible Displacements

This chapter investigates anisotropic mixing in miscible displacements. We present an instantaneous finite-volume source solution for the two-dimensional CDE and the procedure to estimate longitudinal and transverse dispersivity from local concentration profiles from FCM simulations. The simulations were conducted with CMG-GEM ® (Computer Modeling Group, 2010).

3.1 ANALYTICAL MODEL

The two-dimensional CDE for first-contact miscible flow, with the assumption of constant velocity and dispersion coefficient in both longitudinal and transverse direction is,

$$\frac{\partial C}{\partial t} + v_x \frac{\partial C}{\partial x} + v_y \frac{\partial C}{\partial y} = D_L \frac{\partial^2 C}{\partial x^2} + D_T \frac{\partial^2 C}{\partial y^2} \tag{3.1}$$

where v_x and v_y are the interstitial velocity in x and y directions respectively. D_L and D_T are the longitudinal and transverse dispersion coefficients, respectively. The off-diagonal dispersion coefficient of the dispersion tensor is assumed to be negligible since velocity is considered dominant in the longitudinal direction.

Most work in hydrology focuses on uniform flow where the velocity in the longitudinal direction (v_x) dominates and the velocity in the transverse direction (v_y) is small. The two-dimensional CDE equation for uniform flow can therefore be expressed as,

$$\frac{\partial C}{\partial t} + v \frac{\partial C}{\partial x} = D_L \frac{\partial^2 C}{\partial x^2} + D_T \frac{\partial^2 C}{\partial y^2} \tag{3.2}$$

where v is the average interstitial velocity of the groundwater (Bruggeman 1999).

Bruggeman (1999) gave the solution to the two-dimensional CDE equation for an instantaneous point source solution of strength m_i and initial concentration C_o in an infinite medium with uniform flow, subject to the following initial and boundary conditions,

$$C(x,y,0)=\begin{cases} C_o & x=0; y=0 \\ 0 & other\ x\ \&\ y \end{cases} \tag{3.3a}$$

$$C,\frac{\partial C}{\partial y}=0, \qquad y=\pm\infty \tag{3.3b}$$

$$C,\frac{\partial C}{\partial x}=0, \qquad x=\pm\infty \tag{3.3c}$$

The analytical solution obtained by Bruggeman (1999) is expressed as,

$$C(x,y,t)=\frac{C_o A}{4\pi t\sqrt{D_L D_T}}\exp\left\{-\frac{(x-vt)^2}{4D_L t}-\frac{y^2}{4D_T t}\right\} \tag{3.4}$$

where the solute strength (*mi*) is estimated using the base area (*A*) of the solute source multiplied by the initial solute source concentration (C_o) and expressed as,

$$m_i = AC_o \tag{3.5}$$

It is impractical to generate a point source using a finite difference type simulator. An approximate point source can be generated if the grid-block sizes are small. However, for the purpose of this research, it is reasonable to have a finite width and finite length source. This can be easily achieved by integrating the two-dimensional CDE solution (equation (3.4)) in both x- and y- directions. Equation (3.4) can be expressed as

$$C(x,y,t)=\frac{C_0 xy}{4\pi t\sqrt{D_L D_T}}\exp\left[-\frac{(x-vt)^2}{4D_L t}\right]\exp\left[-\frac{y^2}{4D_T t}\right]. \tag{3.6}$$

Integrating from y_1 to y_2 we obtain the finite width source. Using the integral relationship,

$$\int \exp\left(-ax^2\right)dx = \frac{\sqrt{\pi}}{2\sqrt{a}}erf\left(x\sqrt{a}\right) \tag{3.7}$$

we obtain the instantaneous finite width source solution for the two-dimensional CDE considering uniform flow,

$$C(x,y,t)=\frac{C_0 x}{4\sqrt{\pi t D_L}}\exp\left[-\frac{(x-vt)^2}{4D_L t}\right]\left\{erf\left(\frac{y_2-y}{\sqrt{4D_T t}}\right)-erf\left(\frac{y_1-y}{\sqrt{4D_T t}}\right)\right\} \qquad (3.8)$$

where y_1 and y_2 represent the base and the top of the width of the solute source. To extend the finite width instantaneous source solution to a finite volume instantaneous solution, equation (3.8) is integrated in the x-direction. Using the integral relationship from equation (3.7), we obtain,

$$C(x,y,t)=\frac{C_0}{4}\left\{erf\left(\frac{x_2-x+vt}{\sqrt{4D_L t}}\right)-erf\left(\frac{x_1-x+vt}{\sqrt{4D_L t}}\right)\right\}\left\{erf\left(\frac{y_2-y}{\sqrt{4D_T t}}\right)-erf\left(\frac{y_1-y}{\sqrt{4D_T t}}\right)\right\} \qquad (3.9)$$

where x_1, x_2, y_1 and y_2 represents the coordinates of the solute source. Equation (3.9) can be used to analyze and represent solute concentration profiles in a homogenous medium with uniform velocity in the longitudinal direction and negligible velocity in the transverse direction.

3.1.1 Two-dimensional CDE with anisotropic velocity

The growth of the solute plume is affected by local velocity variations and this significantly impacts the level of dispersion in porous medium. The two-dimensional CDE considering anisotropic velocity is given in equation (3.1). Clearly and Ungs (1978) gave the solution to equation (3.1) for a continuous injection of a strip (finite width) source in an infinite medium subject to the following initial and boundary conditions,

$$C(x,y,t)=\begin{cases} C_o & x=0 \;\; y_1 \le y \le y_2 \\ 0 & \textit{anywhere else} \end{cases} \qquad (3.10a)$$

$$\frac{\partial C}{\partial y} = 0, \qquad y = \pm\infty \tag{3.10b}$$

$$\frac{\partial C}{\partial x} = 0, \qquad x = \infty \ . \tag{3.10c}$$

Clearly and Ungs (1978) solution is expressed as,

$$C(x,y,t) = \frac{C_o x}{4\sqrt{\pi D_L}} \exp\left(\frac{v_x x}{2D_L}\right) \int_{\tau=0}^{t} \tau^{-3/2} \exp\left(\frac{-v_x^2 \tau}{4D_L} - \frac{x^2}{4D_L \tau}\right) \cdot \left\{ erf\left(\frac{y_2 - y}{\sqrt{4D_T \tau}} + \frac{v_y}{2}\sqrt{\frac{\tau}{D_T}}\right) - erf\left(\frac{y_1 - y}{\sqrt{4D_T \tau}} + \frac{v_y}{2}\sqrt{\frac{\tau}{D_T}}\right)\right\} d\tau \tag{3.11}$$

where τ is a dummy variable for integration. Equation (3.11) must be evaluated numerically using Gaussian quadrature (Wexler 1989). Equation (3.11) can be differentiated with respect to time to obtain the solution for an instantaneous finite width source with anisotropic velocity. The analytical solution for an instantaneous finite width source can therefore be expressed as,

$$C(x,y,t) = \frac{C_0 x}{4\sqrt{\pi t D_L}} \exp\left[-\frac{(x - v_x t)^2}{4D_L t}\right] \left\{ erf\left(\frac{y_2 - y}{\sqrt{4D_T t}} + \frac{v_y}{2}\sqrt{\frac{t}{D_T}}\right) - erf\left(\frac{y_1 - y}{\sqrt{4D_T t}} + \frac{v_y}{2}\sqrt{\frac{t}{D_T}}\right)\right\} \tag{3.12}$$

Equation (3.12) can easily be extended to account for a finite volume instantaneous source solution by integrating with respect to length in the x-direction. The analytical solution for a two-dimensional CDE with instantaneous finite width and length source is therefore given as,

$$C(x,y,t) = \frac{C_0}{4}\left\{ erf\left(\frac{x_2 - x + v_x t}{\sqrt{4D_L t}}\right) - erf\left(\frac{x_1 - x + v_x t}{\sqrt{4D_L t}}\right)\right\} \cdot \left\{ erf\left(\frac{y_2 - y}{\sqrt{4D_T t}} + \frac{v_y}{2}\sqrt{\frac{t}{D_T}}\right) - erf\left(\frac{y_1 - y}{\sqrt{4D_T t}} + \frac{v_y}{2}\sqrt{\frac{t}{D_T}}\right)\right\} \ . \tag{3.13}$$

The full derivation of equation (3.13) is detailed in Appendix A. Equation (3.13) is used to investigate anisotropic mixing for FCM simulations under varying conditions.

Assuming small time steps and negligible diffusion, the longitudinal and transverse dispersion coefficients (including numerical dispersion) can be expressed in terms of their respective dispersivities (α) as,

$$D_L = \alpha_L \frac{v_x^2}{|v|} + \alpha_T \frac{v_y^2}{|v|} + \frac{1}{2} v_x \Delta x \tag{3.14a}$$

$$D_T = \alpha_L \frac{v_y^2}{|v|} + \alpha_T \frac{v_x^2}{|v|} + \frac{1}{2} v_y \Delta y . \tag{3.14b}$$

An estimate of the average solute particle velocity is required to estimate dispersion in heterogeneous media. The local velocity of each grid-block from finite difference simulation is not the same as the average travel velocity of the particle. The average velocity of the particle is dependent on the local velocities along the path of the solute particle, which maybe tortuous based on heterogeneity.

We used the average particle travel time, determined from the local concentration profile to determine the average solute particle velocity. The mean speed of the particle can be estimated using the time of arrival of the center of mass of the solute plume at the target cell from the source cell. For a Gaussian concentration distribution, the average travel time is the time at the peak concentration (Figure 3.1).

The average solute travel velocity between the target grid block at which dispersion is being estimated and the source grid block, which initially contains the solute is approximated as the ratio of the distance between the two grid blocks and the average solute particle travel time. The velocity is usually positive in the longitudinal direction since flow is dominant in that direction, but the prevailing direction of the average velocity in the transverse direction depends on the average local transverse velocity of the flow regions around the source and target cells and can be locally negative.

Analogously, the average solute velocity for a continuous solute source can be determined from the time estimated from at the advection front (where dimensionless concentration is typically 0.5) and the distance travelled from the solute source.

3.1.2 Validation of two-dimensional CDE solution

Equation (3.13) was validated by fitting the analytical model (equation (3.13)) to the solute concentration profile in a homogenous reservoir with specified input dispersivity. A two-dimensional homogenous reservoir is initially saturated with a resident fluid, except for a single grid block, which is initially at 100 percent concentration of the solute at the same density and viscosity as the resident fluid. To minimize boundary effects, the solute source is placed 10 ft away from the injection well. The solute and the resident fluid are first contact miscible. The reservoir model has 50 grid blocks in the longitudinal direction and 100 grid-blocks in the transverse direction. The grid-block sizes in the longitudinal and transverse directions are 1.0 ft and 0.5 ft respectively. A uniform flow field is generated in the reservoir model by placing a constant rate injection and production wells at the inlet and outlet boundaries. A schematic of the model is shown in Figure 3.2.

Since the reservoir model is homogenous, the observed spreading of the solute is entirely the result of input dispersivity and numerical dispersion. The input longitudinal dispersivity is 1.0 feet, while the input transverse dispersivity is 0.5 feet. The average time step size in the simulation model is 0.1 day, average velocities v_x is 0.296 ft/day and v_y is 0 ft/day. From Fanchi (1983) the numerical dispersivities are 0.515 feet and 0 feet, in the longitudinal and transverse direction, respectively. The total dispersion for a homogenous model is the sum of the numerical dispersion and input dispersion.

Therefore, the total longitudinal dispersivity is 1.52 feet, while the total transverse dispersivity is 0.5 feet.

The analytical model was fitted to the local (grid block) concentration profile by minimizing the sum of the square of residuals between solute concentration from the simulation and analytical model by varying longitudinal and transverse dispersivities. An excellent match was obtained between the analytical model and the local concentration profile (Figure 3.3). The estimated dispersivities from the analytical model are comparable to the total longitudinal and transverse dispersivities in the simulation model (Figure 3.4).

Since the simulation model is homogenous with a constant total longitudinal and transverse dispersivity, the analytical model can also be fitted to the global solute concentration profiles at various times. A good match of the global solute concentration distribution is obtained with the analytical model (Figure 3.5). Figure 3.5 shows the lower half of the concentration distribution, since the concentration distribution is symmetric.

The estimated dispersivities from the analytical model at various times are comparable to the total longitudinal and transverse dispersivities in the simulation model (Figure 3.6).

3.2 EFFECT OF PERMEABILITY HETEROGENEITY ON ANISOTROPIC MIXING

Heterogeneous medium results in a spatially varying velocity field that enhances mechanical dispersion. This variation in velocities result in increased mixing (Jha *et al.* 2006). The effect of heterogeneity on dispersion was investigated by studying the effect of stochastically generated permeability distribution on dispersion.

All simulations were conducted using CMG-GEM® simulator for a two-dimensional medium undergoing a FCM displacement. Stochastic permeability fields were generated by FFTSIM (Jennings *et al.* 2000). The inputs for FFTSIM include autocorrelation lengths (in both x- and y-directions), Dykstra-Parsons coefficient (V_{DP}) and mean permeability. The simulation models consist of a single grid block with an initial 100 percent solute concentration in a steady flow field. To minimize boundary effects, the solute source is placed 10 feet away from the injector. The spreading of the solute is monitored and local concentration fitted to the 2-D analytical model by varying the dispersivities. The velocity flow fields of the simulation models were maintained at steady state with constant injection and production rates. The simulation models have 64 grid-blocks in x-directions and 128 grid-blocks in y-directions. The grid-block sizes in x- and y-directions are 1.0 ft. and 0.5 ft., respectively. Except otherwise stated, there is no input dispersivity in the simulation models.

Qualitative insight into anisotropic mixing was inferred by superimposing solute concentration contours on streamlines of the simulation models. Streamlines are lines that are everywhere tangential to a velocity field (Datta-Gupta and King 2007). For incompressible flow, streamlines give the path fluid particles travel as they move through porous media. In miscible displacements solute mixes along streamlines and across adjacent streamlines because of varying concentration gradients.

Streamlines are usually traced based on the concept of time of flight (TOF) (Datta-Gupta and King 2007). The TOF indicates the time necessary for an injected particle to reach a particular point. We traced streamlines for different permeability realizations based on the underlying steady velocity field using an algorithm proposed by Pollock (1988). The method uses the velocity field generated from finite-difference models to trace the simulation model streamlines. The method assumes that velocities

vary linearly from the entry point to the exit point of the grid-block. Therefore for steady state systems, the exit point of the particles can be computed and the travel path of the particles traced through a multi-dimensional field.

3.2.1 Dispersion in uncorrelated medium

Uncorrelated medium have randomly distributed permeability. We compared three uncorrelated models with V_{DP} of 0.4, 0.6 and 0.8. Increasing V_{DP} indicates increasing heterogeneity.

The local solute concentration profile from simulation was matched with the analytical model (equation (3.13)). Figure 3.7 compares the concentration profiles from the analytical solution and simulation. The estimated local dispersivities were used to generate the solute concentration distribution at different days. The concentration distribution from the analytical model is comparable with the simulation solute concentration contour (Figure 3.8).

Estimated longitudinal dispersivity increases with distance and level of heterogeneity (Figure 3.9). The estimated longitudinal dispersivity also approaches asymptotic values. Estimated transverse dispersivity also increases with increasing level of heterogeneity, however with more fluctuations (Figure 3.10a). The fluctuations in the transverse dispersivity are caused by local changes in the dominant flow direction in the medium.

The plot of the ratio of transverse to longitudinal dispersivity shows a declining trend with longitudinal distance (Figure 3.10b). This indicates that as the finite volume source transverses the medium, longitudinal dispersion becomes increasingly dominant due to the prevailing flow direction. The magnitude of the transverse dispersivity is

determined by concentration gradients in the transverse direction and macroscopic heterogeneity. At high levels of heterogeneity (V_{DP} = 0.8), the average ratio of transverse to longitudinal dispersivity is about unity showing significant mixing of the solute in the transverse direction.

The solute concentration map was superimposed on the model streamlines (Figure 3.11). The streamlines are traced based on the algorithm by Pollock (1988) using the steady-state velocity field of the simulation model. Though the solute particles move and spread across and along streamlines, Figure 3.11 shows that changes in the dominant flow direction enhances mixing and is indicative of the level of mixing. There is an observable difference in the shape and dilution of the solute plume with increasing heterogeneity.

Increasing the level of heterogeneity amplifies the change in flow directions and creates high flow regions (with concentrated number of streamlines) that enhance spreading. If a medium is very heterogeneous and there are concentration gradients in the transverse direction, there is a potential for significant transverse dispersion. The transverse dispersion could be as large as the longitudinal dispersion as shown when V_{DP} = 0.8. The effect of increased transverse dispersion is to lower the solute concentration as it mixes and to cause solute particles to be present at points in the transverse section much farther than the initial solute source.

3.2.2 Dispersion in correlated medium

Using FFTSIM we generated simulation models in which the dimensionless autocorrelation lengths are 25 and 10 percent in the x- and y-directions respectively. The

level of the autocorrelation lengths indicates the spatial relationship of the permeability field. The higher the value of the autocorrelation lengths, the more layered the model.

The local solute concentration profile from simulation was matched with the analytical model (equation (3.13)). Figure 3.12 compares the concentration profiles from analytical solution and simulation. The solute concentration distributions at various times were generated using estimated local dispersivities at various points. The concentration distributions from the analytical model are comparable with the simulation solute concentration map (Figure 3.13).

The results show that longitudinal dispersivity increases with distance traveled and with increasing heterogeneity (Figure 3.14). Increasing level of heterogeneity not only increases mixing but also enhances convective spreading as shown when V_{DP} equals 0.8. When convection dominates, mixing reduces. The effect of convective spreading is for solute particles to spread as they travel faster in high permeability streaks with little change in their concentration. Convective spreading will ultimately result in early breakthrough of the solute. Mixing is not uniformly increasing along the medium when convective spreading dominates as can be seen when $V_{DP} = 0.8$.

Estimated transverse dispersion fluctuates along the medium due to variations in the dominant flow paths in the medium (Figure 3.15). Transverse dispersion still tends to be higher with increasing level of heterogeneity. Transverse dispersion also tends to be constant along correlated regions as seen in Figure 3.15.

The solute concentration map was superimposed on the simulation model streamlines (Figure 3.16). The effect of autocorrelation on the streamlines is obvious as high flow regions, with high concentration of streamlines are visible. Though solute mixes across and along streamlines, the dominant flow paths control the movement of the

solute plume. At high levels of heterogeneity (V_{DP} = 0.8), high flow regions causes the solute to channel through the medium minimizing mixing.

Increasing level of heterogeneity (V_{DP}) causes some of the solute to be trapped in low velocity regions. Figure 3.17 shows trapped solute plume, after the solute has already broken through to the production well. This trapped or delayed solute plume is the source of the tailing and asymmetry noticed in effluent concentrations at the production well.

We also considered five different realizations of the permeability fields using the same input autocorrelation lengths, mean permeability and V_{DP}. Figure 3.18 shows the streamlines of some of the realizations indicating that different permeability realizations have different flow structures. These different flow structures or patterns determine the growth of the solute plume and the level of dispersion. The flow structure of the first realization is shown in Figure 3.16c.

Figures 3.19 and 3.20 show the estimated dispersivities. The estimated longitudinal dispersivity (Figure 3.19) for all the five realizations increases with distance but they develop differently from each other due to the different flow structure in each realization. Estimated longitudinal dispersivity also converged to about the same peak value for the different realizations. Figure 3.20 show that transverse dispersivity is quite different for each realization. This difference is because the level of transverse dispersion is more dependent on the structure of the flow paths, which is quite different for each realization as seen in Figure 3.18.

Care must be taken in planning miscible enhanced oil recovery injection to avoid a high permeability streak. High permeability regions results in convective spreading of the miscible solute which minimizes mixing. This may be noticed in field applications with early solvent breakthrough and early production of high concentrations of the solvent.

3.2.3 Effect of cross flow on dispersion

Cross flow refers to flow across layers of different flow characteristics. We model cross flow with different levels of permeability anisotropy ratio (k_v/k_h). A k_v/k_h of zero indicates no cross flow while k_v/k_h of 1 indicates significant cross flow.

Good matches of the local solute concentration profiles were obtained for the different levels of permeability anisotropy ratio (Figure 3.21). The estimated dispersivities were also used to generate the solute concentration maps at various times, which compares favorably to the simulation concentration maps (Figure 3.22).

Results show that cross flow is required for transverse dispersion to be significant (Figures 3.23 and 3.24). When there is no cross flow (kv/kh = 0.0), the solute is forced to travel along a single horizontal streamline or a single layer and longitudinal dispersion is essentially numerical with little physical dispersion (Figure 3.23). The grid-block size in the simulation model is 1.0 ft. Therefore the numerical dispersivity is about 0.5 ft. There is also negligible transverse dispersion when there is no cross-flow (kv/kh = 0.0). As cross-flow increases dispersion increases.

The effect of cross flow on solute plume growth and dispersion can also be visualized from the solute concentration map superimposed on the simulation streamline (Figure 3.25). When there is no cross-flow, the solute plume stays along a particular streamline in a single layer and solute concentration equilibrates instantaneously across the layer. Therefore longitudinal dispersivity approaches an asymptotic value with little growth and transverse dispersion is negligible. As cross flow increases, solute particles dilute across streamlines increasing transverse dispersion. The combination of transverse dispersion and variation in flow paths also results in increasing longitudinal dispersion.

3.2.4 Effect of flow barrier along solute path on dispersion

The effect of a flow barrier in the simulation model on dispersion was investigated by creating a no-flow region (permeability = 0.0) along the path of the solute plume. Local dispersivities were estimated with the analytical model. The analytical model was able to match favorably the local solute concentration map (Figure 3.26). The match at long time (99 days) was better than early times (39 days) due to the presence of the flow barrier affecting the effective length travelled. The average velocity of the solute is determined using the distance between source and target grid blocks. Therefore the presence of a flow barrier introduces an extra length that is not captured. As the travel distance increases the effect of the barrier on the estimated velocity reduces. Analogous to the time of flight in streamline simulation, the average arrival time determined from the local solute profile captures the extra distance traveled by the solute around the barrier minimizing the error in the estimated velocity.

The solute plume was forced to travel around the flow barriers as can be seen when the solute concentration map was superimposed on the simulation streamlines (Figure 3.27). The presence of the flow barrier results in increased longitudinal dispersion (Figure 3.28), as the barrier creates an increased contact area for the solute. There was an initial reduction in transverse dispersion due to the presence of the flow barrier, as the solute spreads and navigates around the barrier (Figure 3.29).

3.2.5 Effect of input dispersivity on dispersion

Some conventional compositional simulators allows for input dispersivity, which is sometimes used as a history matching parameter. We investigated the effect of input longitudinal and transverse dispersivity in an uncorrelated medium. An uncorrelated

medium was used to minimize the effect of correlated regions on the estimated dispersivity.

Good matches were obtained for the simulation local solute concentration profiles by the analytical model (Figure 3.30). The estimated local dispersivities were also used to generate the solute concentration maps, which compare well with the simulation concentration contours (Figure 3.31).

Results show that the effect of input longitudinal dispersivity is to add to the original total longitudinal dispersivity in the medium. This is shown in Figure 3.32, where the average estimated longitudinal dispersivity increased from 0.56 ft to 0.91 ft with an increase of input longitudinal dispersivity from 0.0 ft. to 0.5 ft. The effect of the input longitudinal dispersivity is to cause increased mixing in the longitudinal direction as can be seen when the solute concentration map is superimposed on the model streamlines at similar times (Figure 3.34). Figure 3.34 shows that the solute plume is more dilute for the case with input longitudinal dispersivity, as the peak dimensionless concentration reduced from $5x10^{-3}$ to $3x10^{-3}$. The input longitudinal dispersivity does not change the flow structure (streamline pattern and distribution). There is only a slight change in the transverse dispersivity with input longitudinal dispersivity (Figure 3.33).

The effect of input transverse dispersivity is amplified spreading in the transverse direction that is far greater than the input value. The average transverse dispersivity increased from 0.58 ft to 2.6 ft with an increase of input transverse dispersivity from 0.0 ft to 0.5 ft (Figure 3.35). There is a slight reduction in longitudinal dispersivity probably due to the dominance of transverse dispersion (Figure 3.36).

As the solute particles spreads to a new transverse position, the input local transverse dispersivity causes the solute to spread further in the transverse direction amplifying the effect of input transverse dispersivity (Figure 3.37). The estimated

transverse dispersivity is greater than the longitudinal dispersivity indicating that transverse spreading dominates.

We also considered flow where the model has input longitudinal and transverse dispersivity of 0.5 ft. The effect of transverse dispersivity dominates, with nearly no change in the longitudinal dispersivity (Figures 3.38 and 3.39). Therefore care must be taken in using dispersivity, especially transverse dispersivity as a history matching parameter.

3.2.6 Effect of autocorrelation lengths on dispersion

We investigated the effect of increasing autocorrelation in the longitudinal direction for dimensionless correlation lengths (L_{XD}) of 0.25, 0.5 and 5 at the same dimensionless autocorrelation in the y-direction (L_{YD}) of 0.1. The larger value of 5 indicates a layered model. All the models were of the same heterogeneity level of V_{DP} equal to 0.6. The simulation model used has 512 grid blocks in the longitudinal direction and 64 grid blocks in the transverse direction. The grid block sizes in the x- and y-directions are 0.5 ft and 1.0 ft respectively.

Local concentration profiles were fitted to the analytical model with good matches (Figure 3.40). The estimated local dispersivities from analytical model were also used to generate the solute concentration maps at various times. The generated concentration maps were comparable to simulation concentration maps (Figure 3.41).

In the correlated longitudinal region, longitudinal dispersivity increases (with respect to longitudinal distance) at about a constant slope until it enters a new region where the slope changes. The level of mixing in the next correlated region depends on the velocity variation in that region. The gross level of mixing in all the correlated

longitudinal regions is equivalent as shown in Figure 3.42, but the manner in which they develop is different.

The estimated transverse dispersivity for different dimensionless autocorrelation lengths in the longitudinal direction tends to reduce with increasing correlation in the longitudinal direction (Figure 3.43). When the dimensionless longitudinal autocorrelation is 0.5, the longitudinal dispersivity initially increases at a steep slope initially and the slope changes as it enters another region of correlation. Figure 3.43 shows that the transverse dispersivity also develops differently based on the prevailing autocorrelation structure.

We also considered changes in the autocorrelation in the y-direction (L_{YD}) of 0.05, 0.1 and 0.5 at the same dimensionless autocorrelation of 0.25 in the x-direction. Increasing autocorrelation in the transverse direction reduces longitudinal dispersion as concentrations in the transverse direction equilibrate more efficiently along a continuous section in the transverse direction (Figure 3.44). The change in the transverse dispersion is not significant with changes in correlation in the transverse direction (Figure 3.45), as the estimated dispersivities fluctuate about a similar average value.

3.3 CONCLUSIONS

We proposed a two-dimensional model for analyzing local anisotropic mixing. The analytical model was validated and a procedure to use the model for heterogeneous media was shown. Both longitudinal and traverse dispersion changes with travel distance. Transverse dispersion can exceed longitudinal dispersion when there are significant changes in the dominant flow direction and there exist large concentration gradients in the transverse direction.

Dispersion was also shown to increase with increasing heterogeneity. Heterogeneity can also lead to increased convective spreading and to some solute being trapped in slow fluid velocity regions. Different stochastic permeability realizations that have the same correlation lengths, mean permeability and Dykstra-Parsons coefficient may have different flow structures and hence dispersion.

Viscous cross flow, modeled as k_v/k_h ratio, significantly affects transverse dispersion. If there is no cross flow transverse dispersion is negligible and growth of longitudinal dispersion is minimized. The effect of input dispersivity in a compositional finite-difference simulator is to increase mixing in the respective direction. The effect of input longitudinal dispersivity adds to the existing longitudinal dispersivity. Input transverse dispersivity can result in a significant increase in transverse spreading.

The effect of longitudinal autocorrelation in the x-direction permeability is to create regions where longitudinal dispersion increases at different rates. The effect of autocorrelation in the transverse direction is to reduce the longitudinal dispersion. The reduction in the longitudinal dispersion is caused by faster equilibration of the concentrations in the transverse direction.

The limitation of using an instantaneous solute source to analyze dispersion is that it is dominated by local effects in the flow medium. Also since the current analytical model is limited to infinite mediums, a large part of the reservoir model is not sampled and thus a complete effect of the medium heterogeneity on dispersion cannot be determined. Therefore there is the need to explore the use of continuous solute sources and analytical models that account for the lateral boundaries of the flow medium.

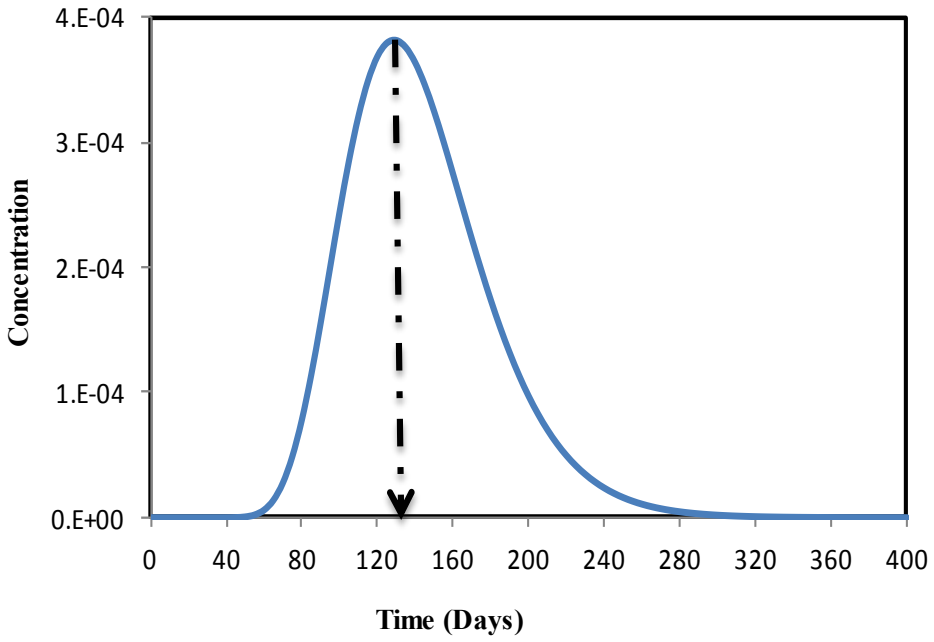

Figure 3.1: Local solute concentration history showing the average travel time (indicated by arrow).

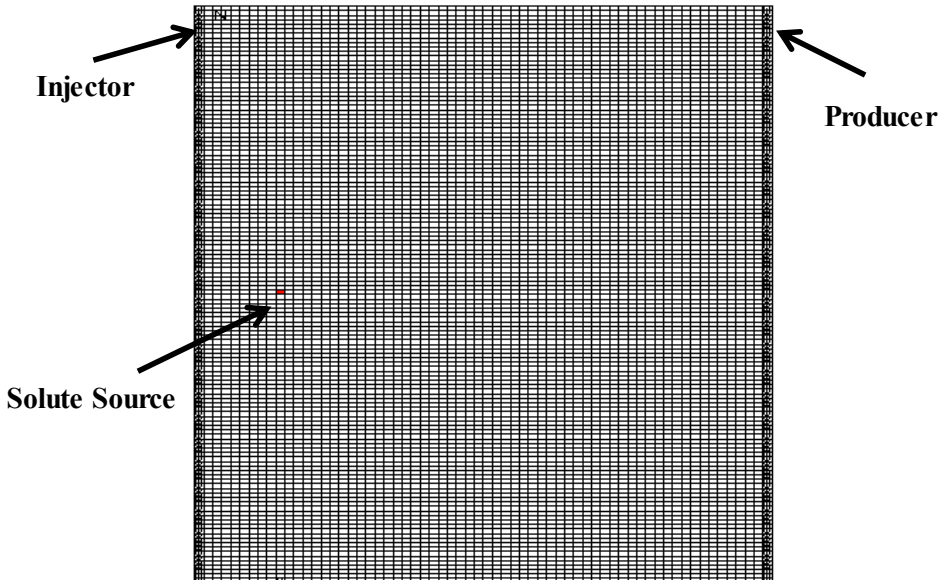

Figure 3.2: Simulation model showing injection and production wells at the lateral boundaries and solute source placed some distance from injection well. The top and bottom of the model are no-flow boundaries.

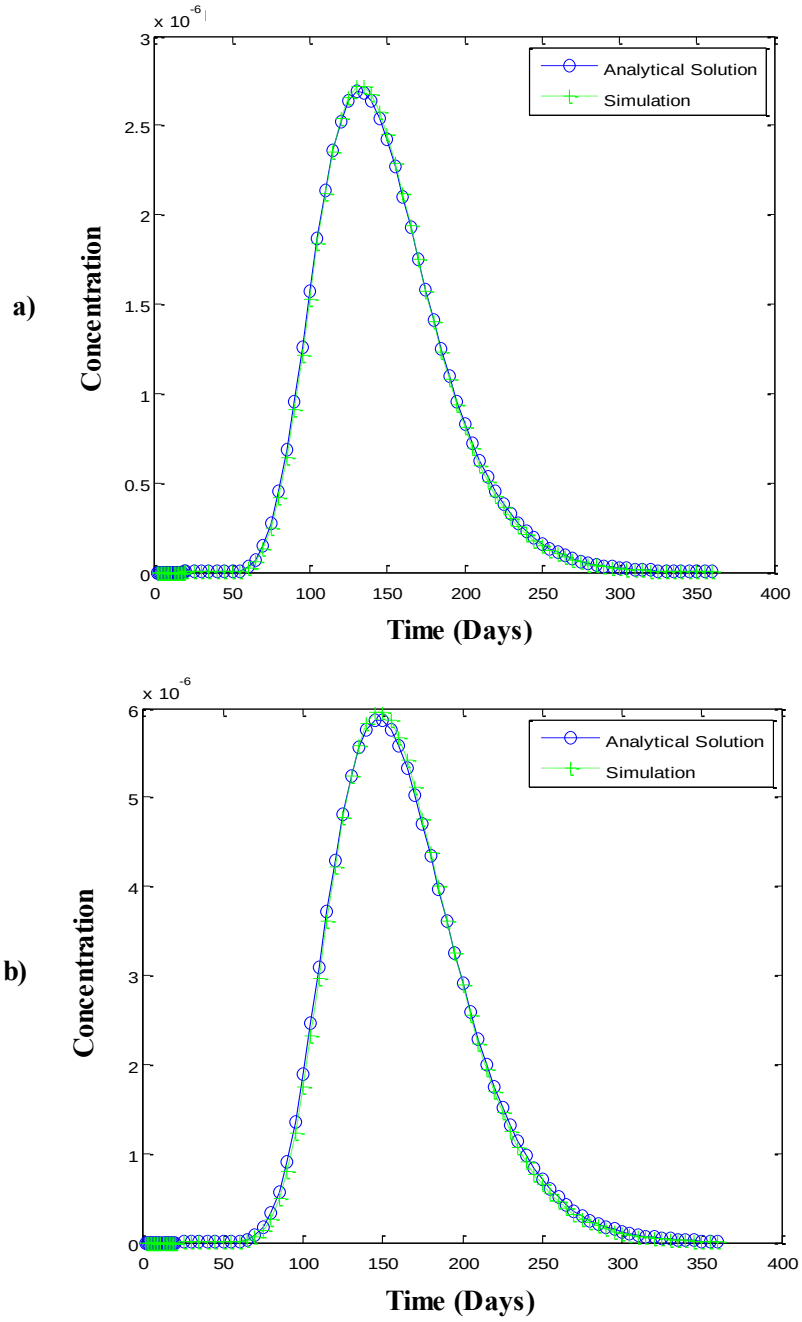

Figure 3.3: Example match of the analytical solution to simulation concentration histories at (a) x = 24 ft and y = 4.75 ft and (b) x = 31 ft and y = 44.75 ft for homogenous model. The input longitudinal and transverse dispersivity are 1.0 ft and 0.5 ft respectively.

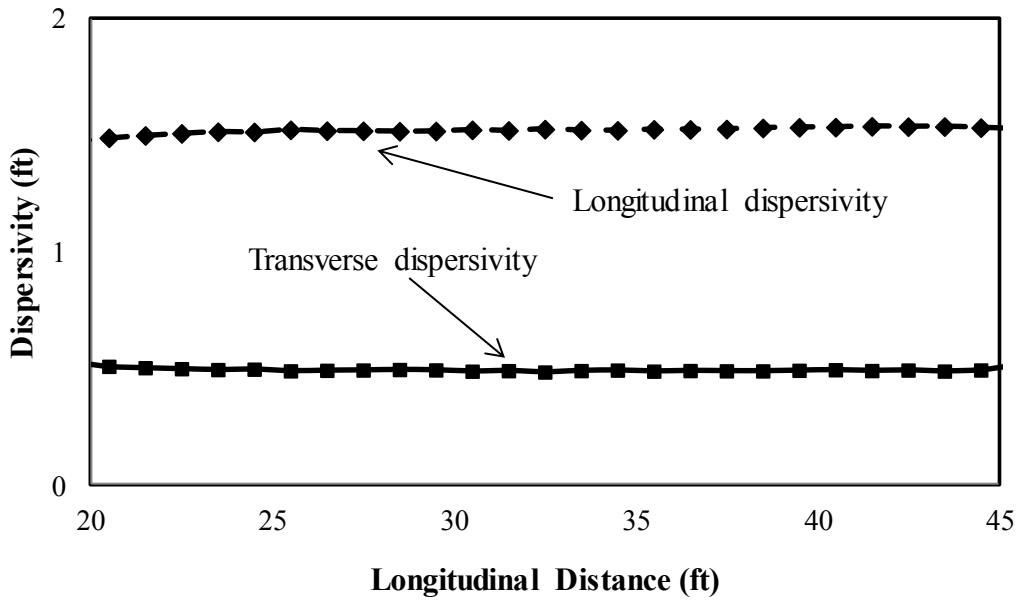

Figure 3.4: Matched longitudinal and transverse dispersivities averaged across vertical cross-sections.

a)

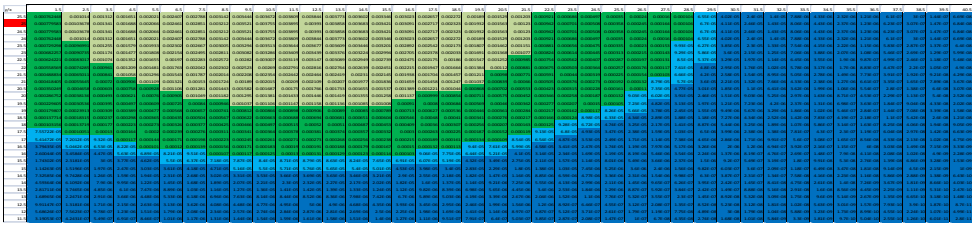

b)

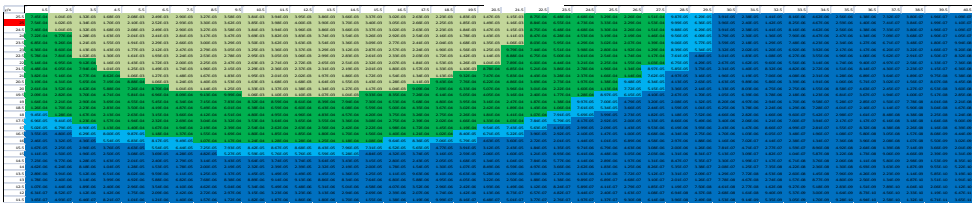

c)

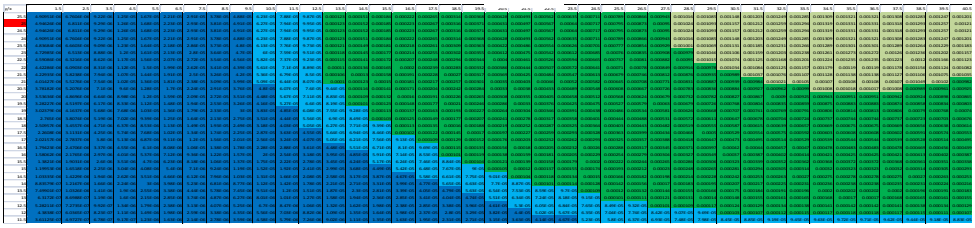

d)

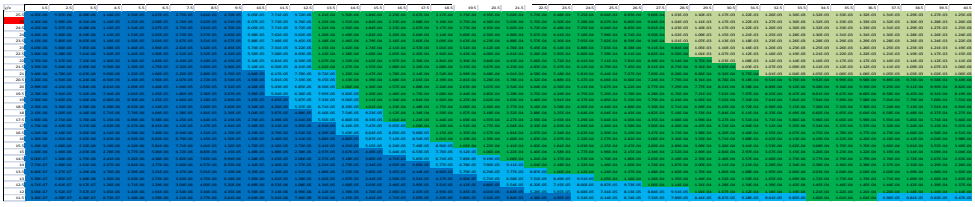

e)

0	to	0.00005	
0.00005	to	0.0001	
0.0001	to	0.001	
0.001	to	0.01	
0.01	to	0.1	
0.1	to	0.3	
0.3	to	0.6	
0.6	to	1	

Figure 3.5: Global solute concentration distribution across the 2D model at various times from (a) the analytical model at 40 days (b) the simulation model at 40 days (c) the analytical model at 120 days (d) the simulation model at 120 days and (e) the color legend for the figures. The red grid on the left shows the initial position of the solute.

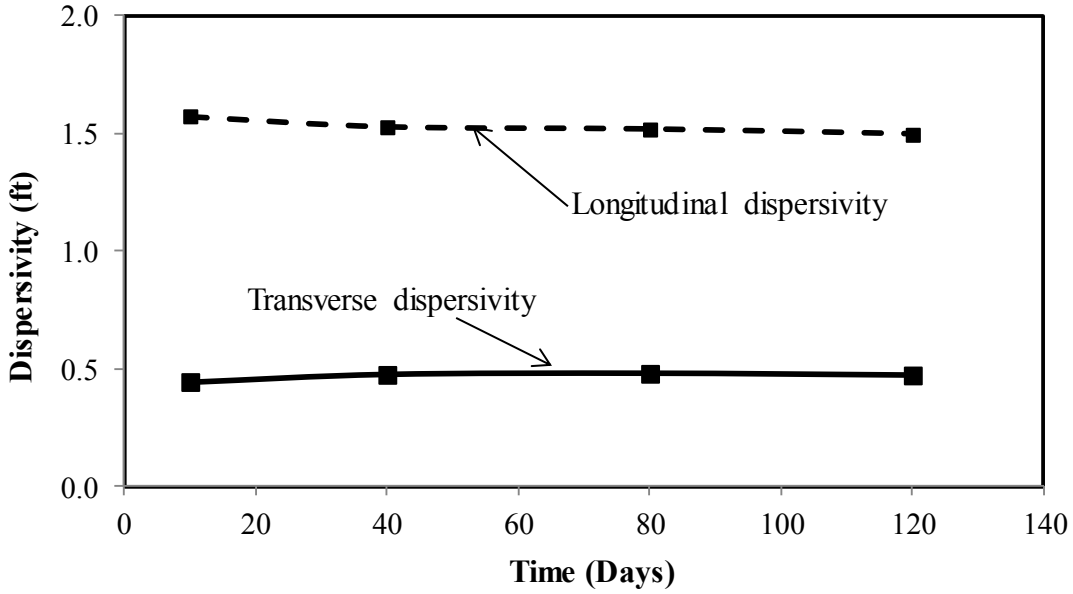

Figure 3.6: Estimated longitudinal and transverse dispersivity from global concentration at different times for a homogenous reservoir model with total longitudinal and transverse dispersivities of 1.5 ft. and 0.5 ft. respectively.

a)

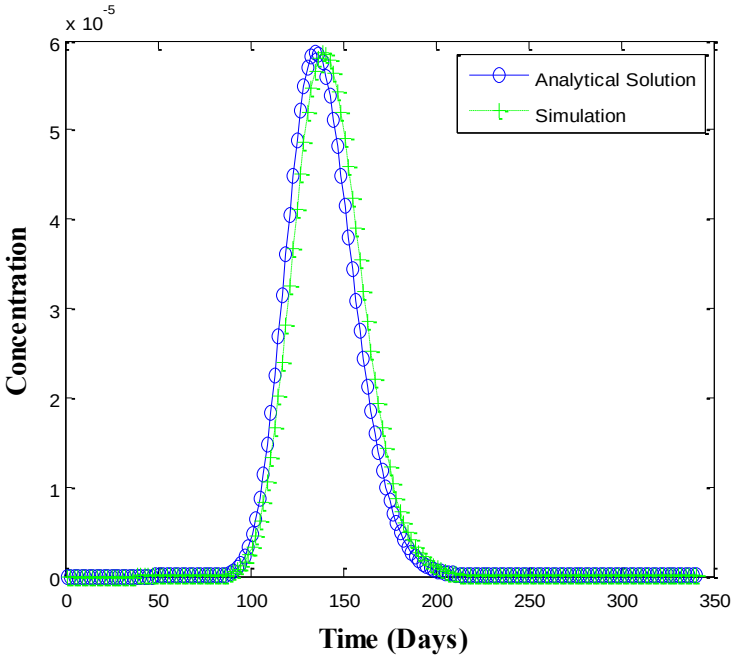
x 10^-5
Concentration
Time (Days)
Analytical Solution
Simulation
0
1
2
3
4
5
6
0
50
100
150
200
250
300
350

b)

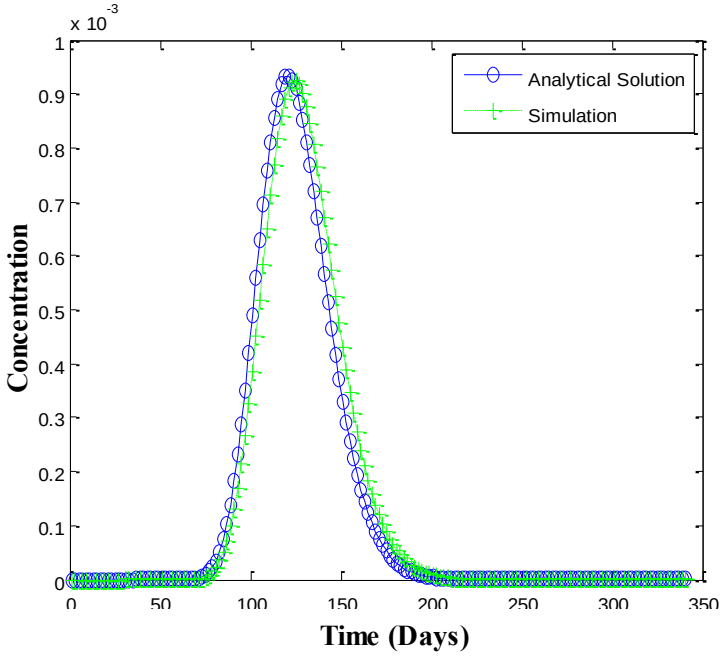
x 10^-3
Concentration
Time (Days)
Analytical Solution
Simulation
0
0.1
0.2
0.3
0.4
0.5
0.6
0.7
0.8
0.9
1
0
50
100
150
200
250
300
350

c)

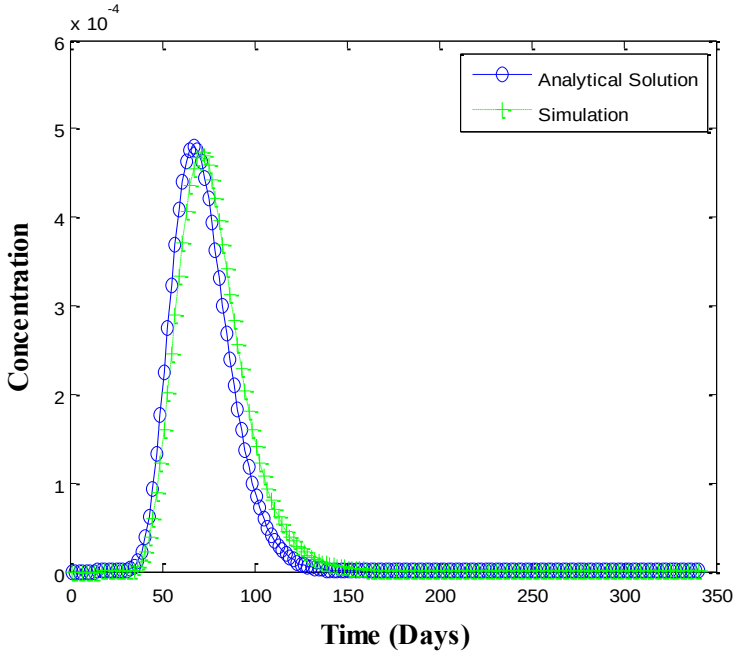

Figure 3.7: Comparison of the solute concentrations history from simulation and analytical models for various levels of heterogeneity for uncorrelated permeability medium (L_{XD} = 0.0, L_{YD} = 0.0) at various points (a) V_{DP} = 0.4, x = 52.5 ft, y = 37.75 ft (b) V_{DP} = 0.6, x = 43.5 ft, y = 37.25 ft and (c) V_{DP} = 0.8, x = 50.5, y = 38.75 ft.

a)

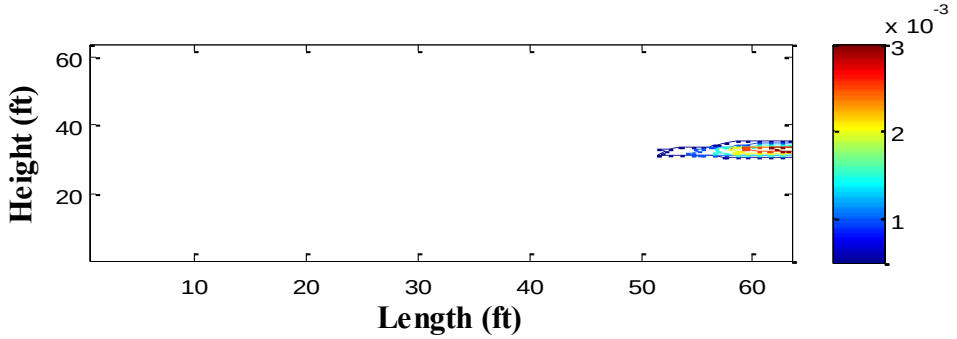
Height (ft)
60
40
20
10
20
30
40
50
60
Length (ft)
x 10^-3
3
2
1

b)

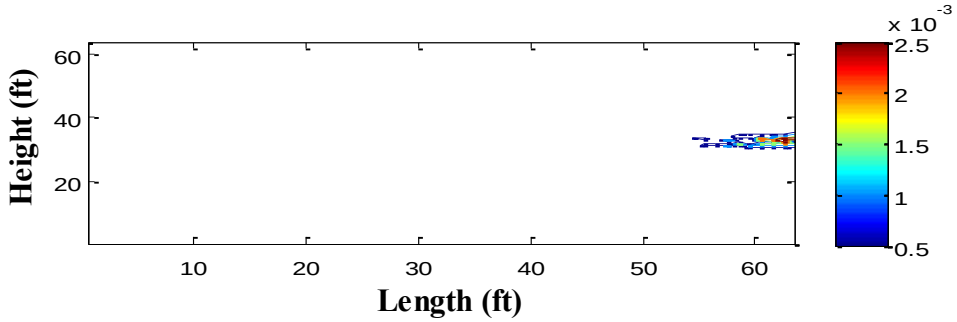
Height (ft)
60
40
20
10
20
30
40
50
60
Length (ft)
x 10^-3
2.5
2
1.5
1
0.5

c)

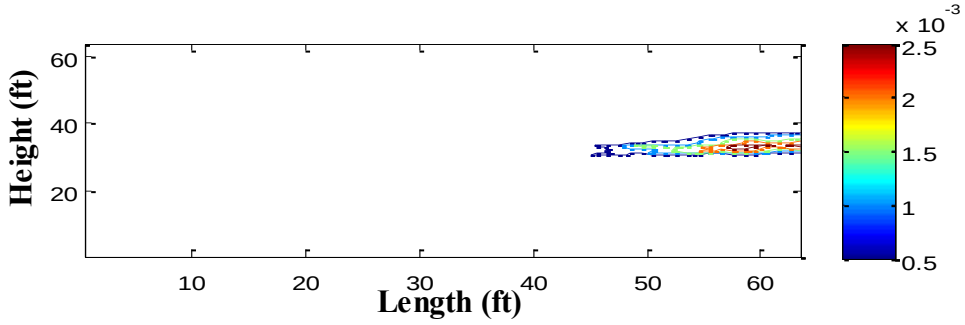
Height (ft)
60
40
20
10
20
30
40
50
60
Length (ft)
x 10^-3
2.5
2
1.5
1
0.5

d)

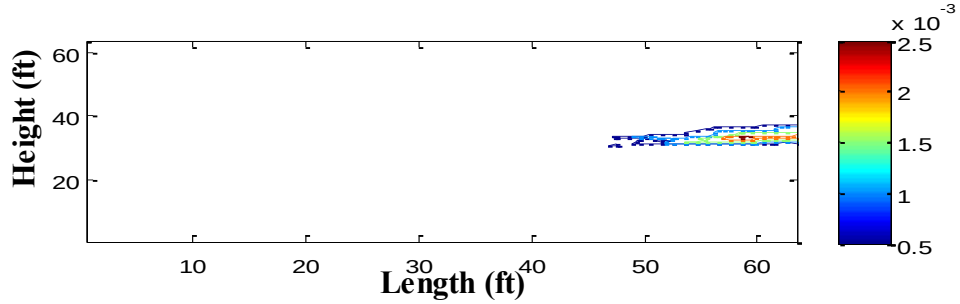
Height (ft)
60
40
20
10
20
30
40
50
60
Length (ft)
x 10^-3
2.5
2
1.5
1
0.5

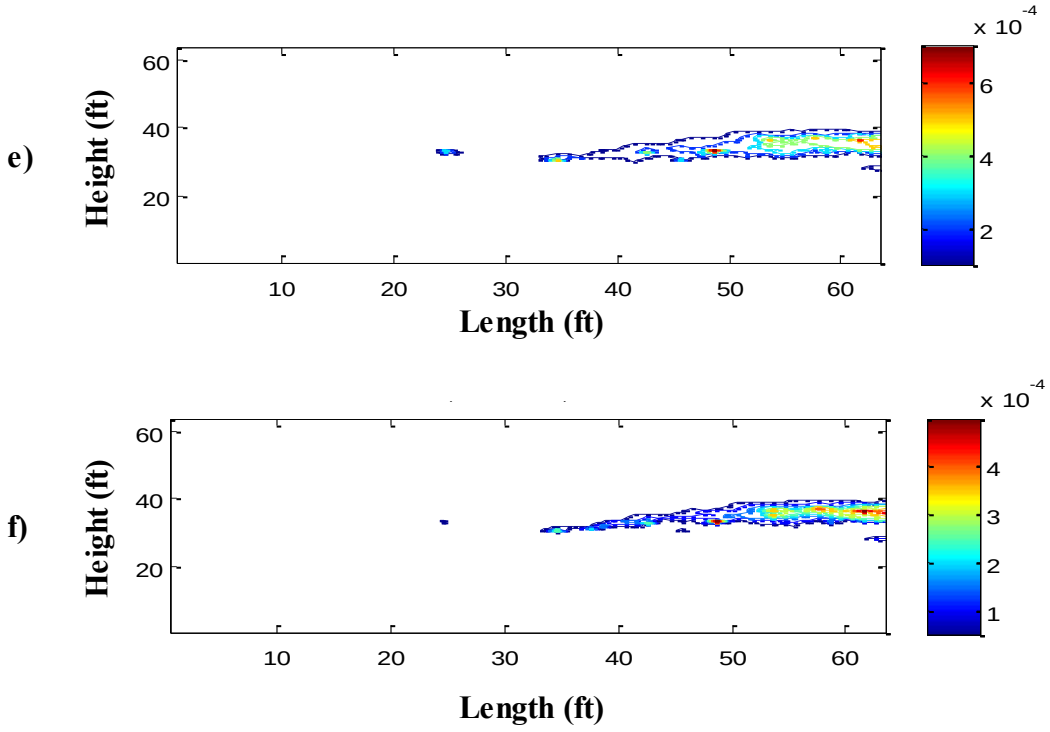

Figure 3.8: Global solute concentration distribution showing comparable profiles between the simulation model and analytical models for various levels of heterogeneity for uncorrelated permeability medium (L_{XD} = 0.0, L_{YD} = 0.0) at various times (a) simulation profile for V_{DP} = 0.4 at 159 days (b) analytical model profile for V_{DP} = 0.4 at 159 days (c) simulation profile for V_{DP} = 0.6 at 159 days (d) analytical model profile for V_{DP} = 0.6 at 159 days (e) simulation profile for V_{DP} = 0.8 at 99 days (f) analytical model profile for V_{DP} = 0.8 at 99 days.

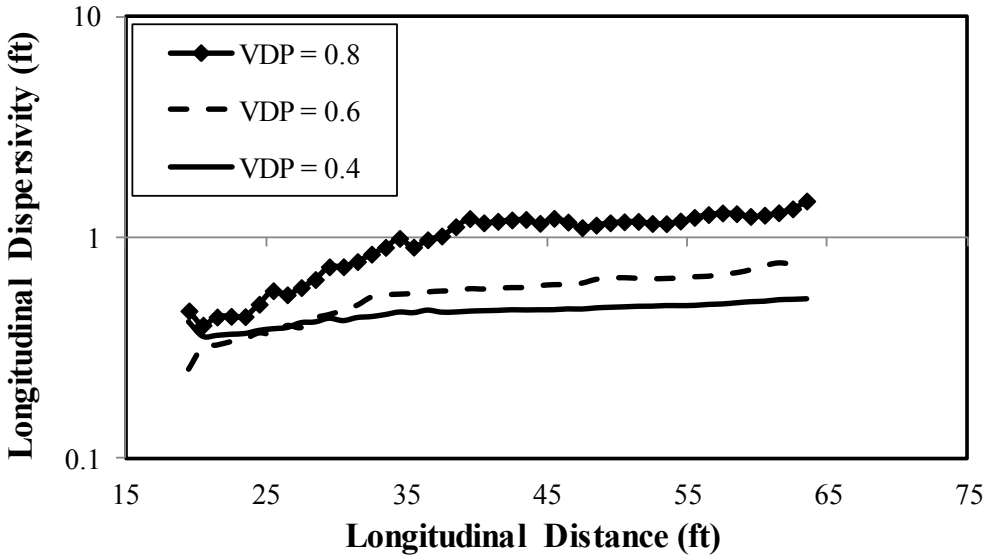

Figure 3.9: Average longitudinal dispersivity for uncorrelated medium with increasing levels of heterogeneity.

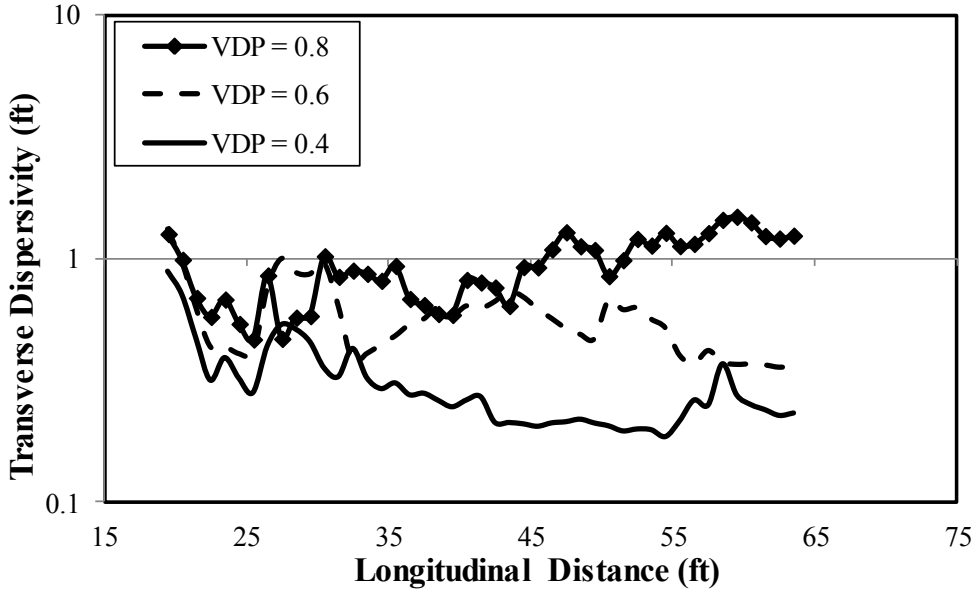

Figure 3.10a: Average transverse dispersivity for uncorrelated medium with increasing levels of heterogeneity.

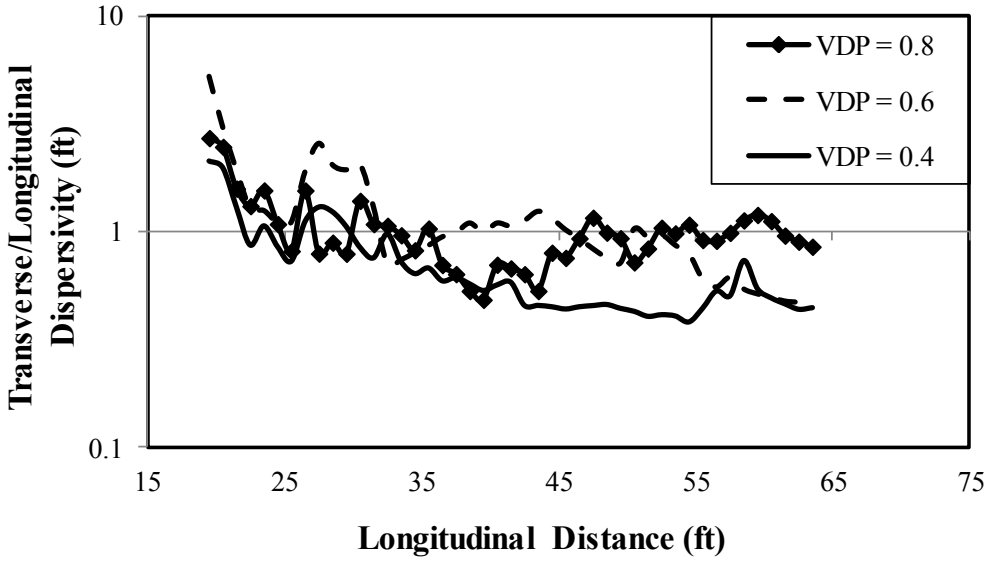

Figure 3.10b: Ratio of transverse to longitudinal dispersivity with longitudinal distance for uncorrelated medium with increasing levels of heterogeneity.

a)

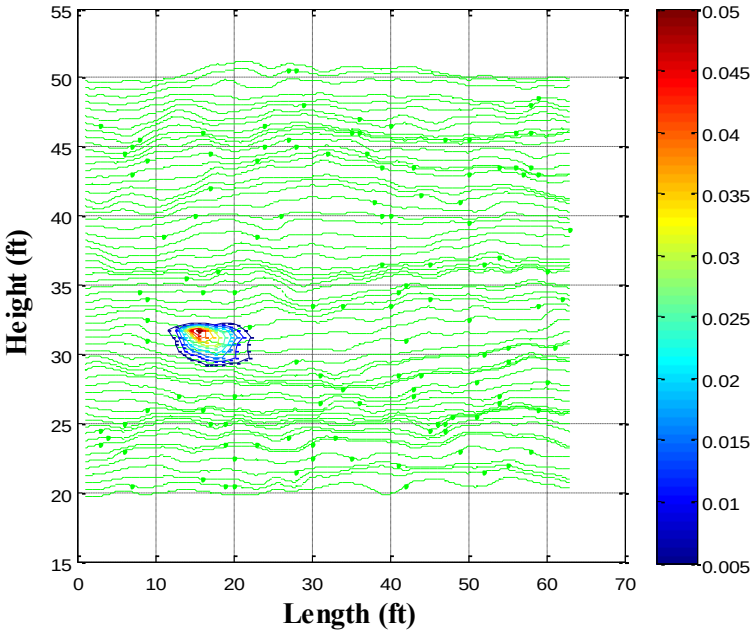
Height (ft)
Length (ft)
55
50
45
40
35
30
25
20
15
0
10
20
30
40
50
60
70
0.05
0.045
0.04
0.035
0.03
0.025
0.02
0.015
0.01
0.005

b)

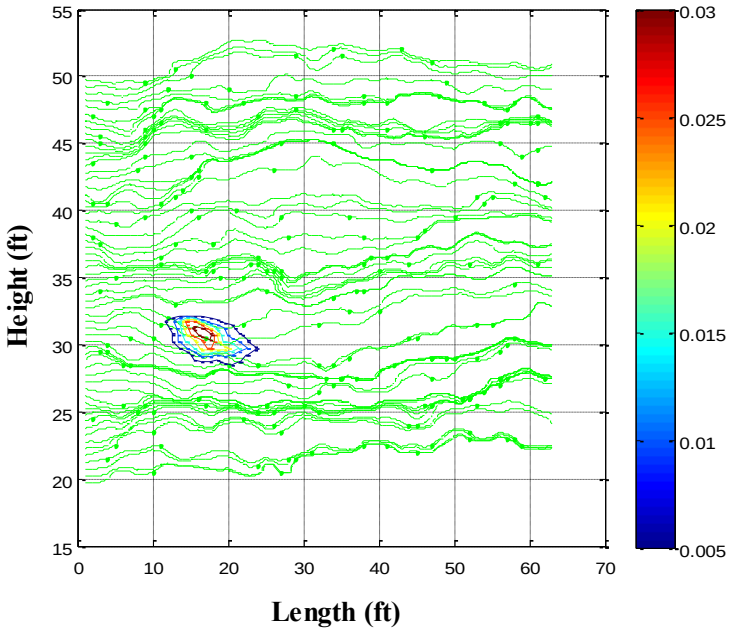
Height (ft)
Length (ft)
55
50
45
40
35
30
25
20
15
0
10
20
30
40
50
60
70
0.03
0.025
0.02
0.015
0.01
0.005

c)

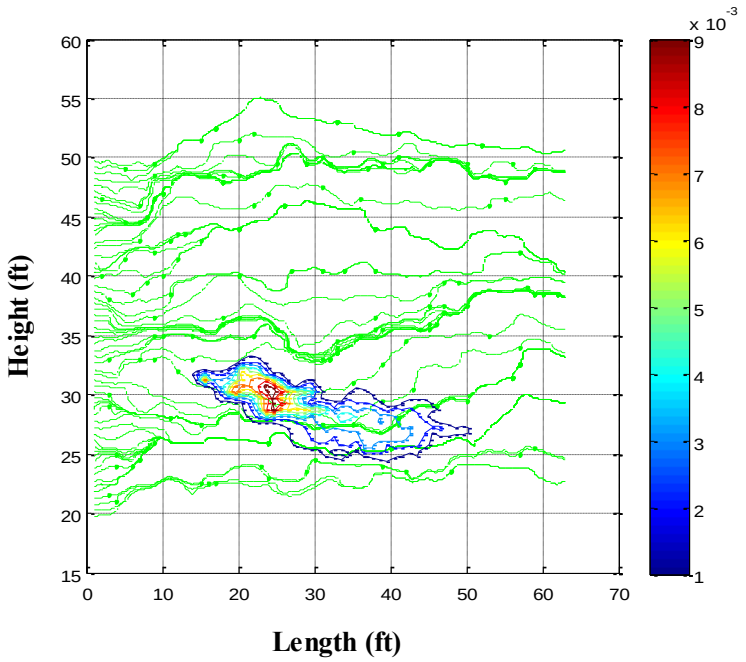

Figure 3.11: Concentration distribution at 19 days superimposed on model streamlines (green lines) for uncorrelated medium (a) $V_{DP} = 0.4$ (b) $V_{DP} = 0.6$ and (c) $V_{DP} = 0.8$.

a)

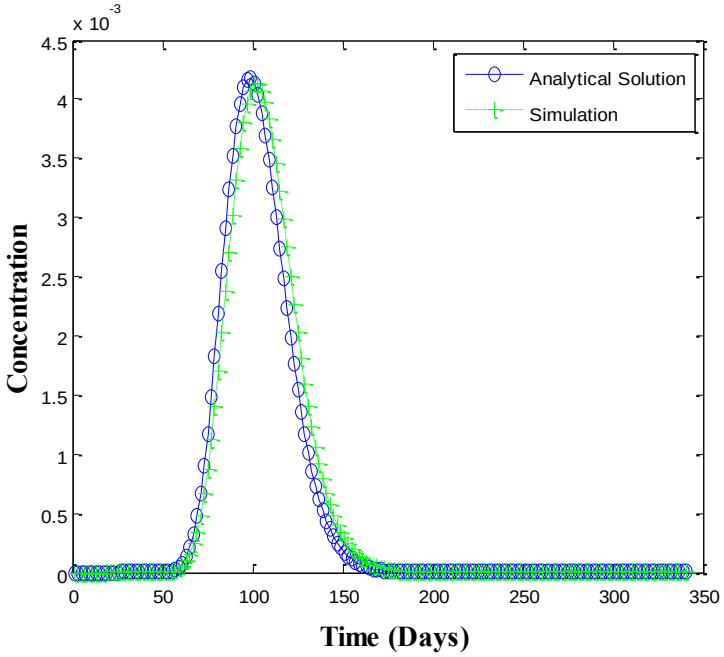
x 10^-3
4.5
4
3.5
3
2.5
2
1.5
1
0.5
0
0
50
100
150
200
250
300
350
Concentration
Time (Days)
Analytical Solution
Simulation

b)

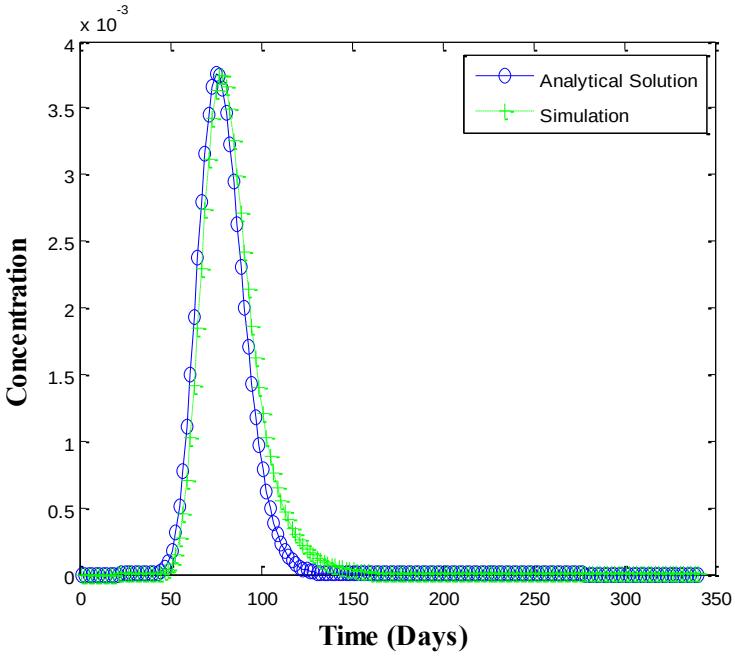
x 10^-3
4
3.5
3
2.5
2
1.5
1
0.5
0
0
50
100
150
200
250
300
350
Concentration
Time (Days)
Analytical Solution
Simulation

c)

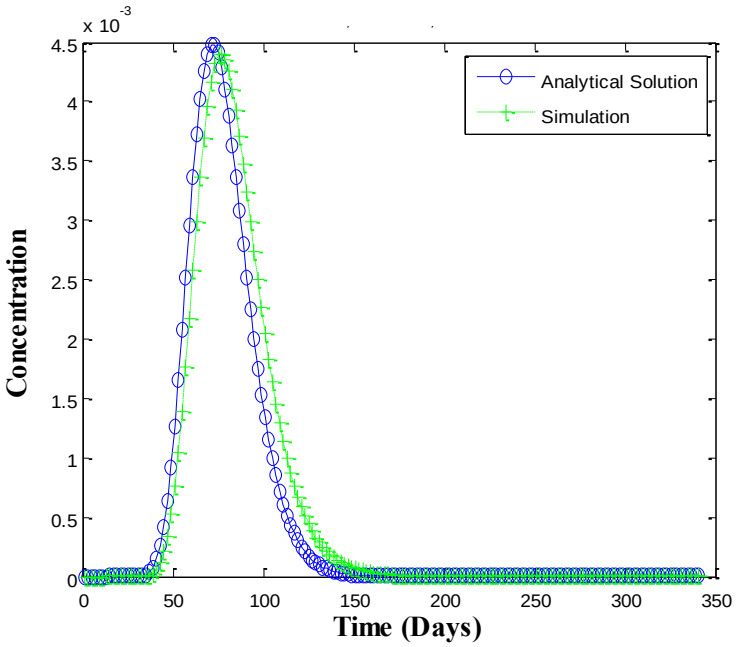

Figure 3.12: Comparison of the solute concentration histories from simulation and analytical models for various levels of heterogeneity for correlated permeability medium (L_{XD} = 0.25, L_{YD} = 0.1) at various points (a) V_{DP} = 0.4, x = 28.5 ft, y = 34.25 ft (b) V_{DP} = 0.6, x = 35.5 ft, y = 34.25 ft and (c) V_{DP} = 0.8, x = 25.5 ft, y = 31.25 ft.

a)

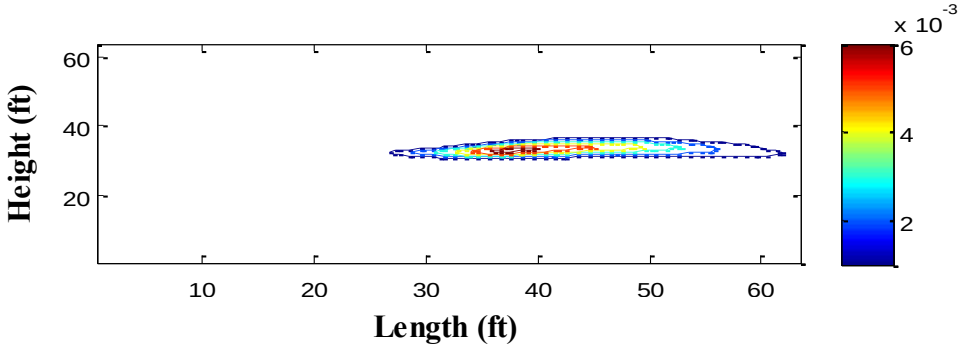
x 10^-3
6
4
2
Height (ft)
60
40
20
10
20
30
40
50
60
Length (ft)

b)

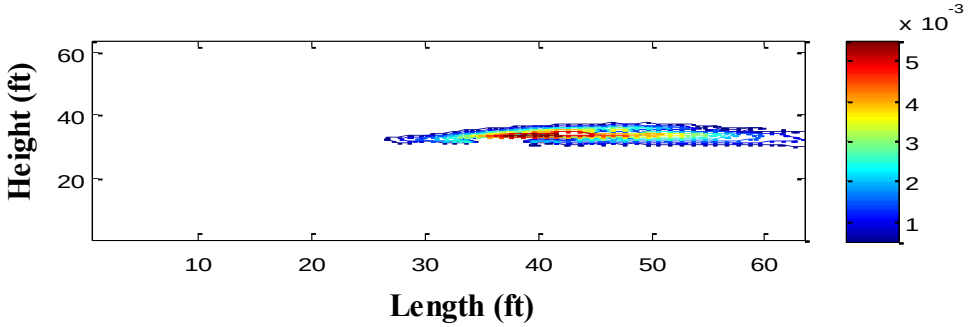
x 10^-3
5
4
3
2
1
Height (ft)
60
40
20
10
20
30
40
50
60
Length (ft)

c)

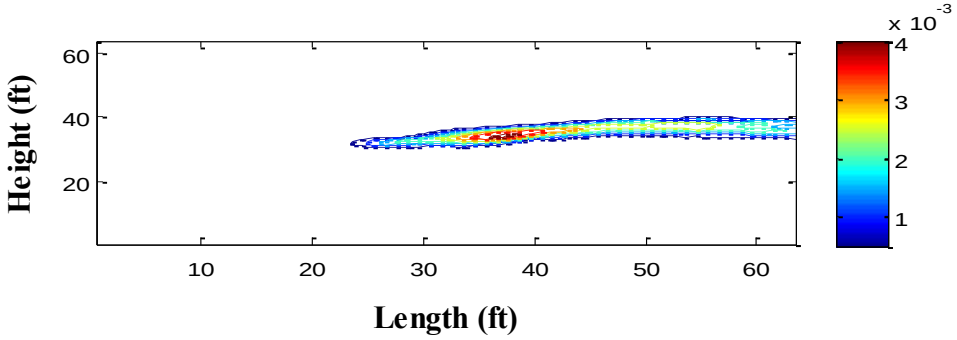
x 10^-3
4
3
2
1
Height (ft)
60
40
20
10
20
30
40
50
60
Length (ft)

d)

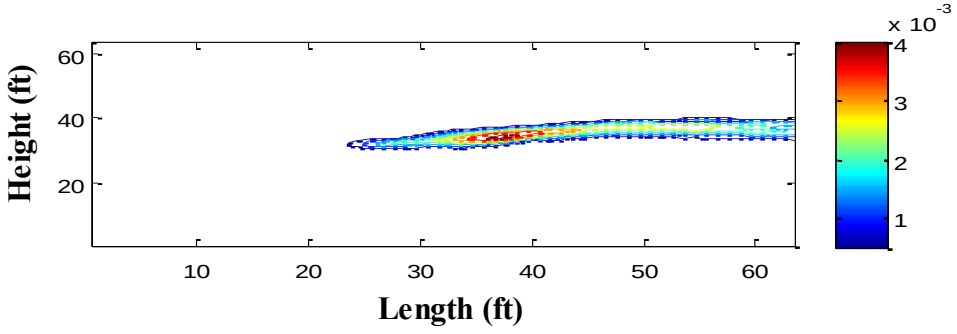
x 10^-3
4
3
2
1
Height (ft)
60
40
20
10
20
30
40
50
60
Length (ft)

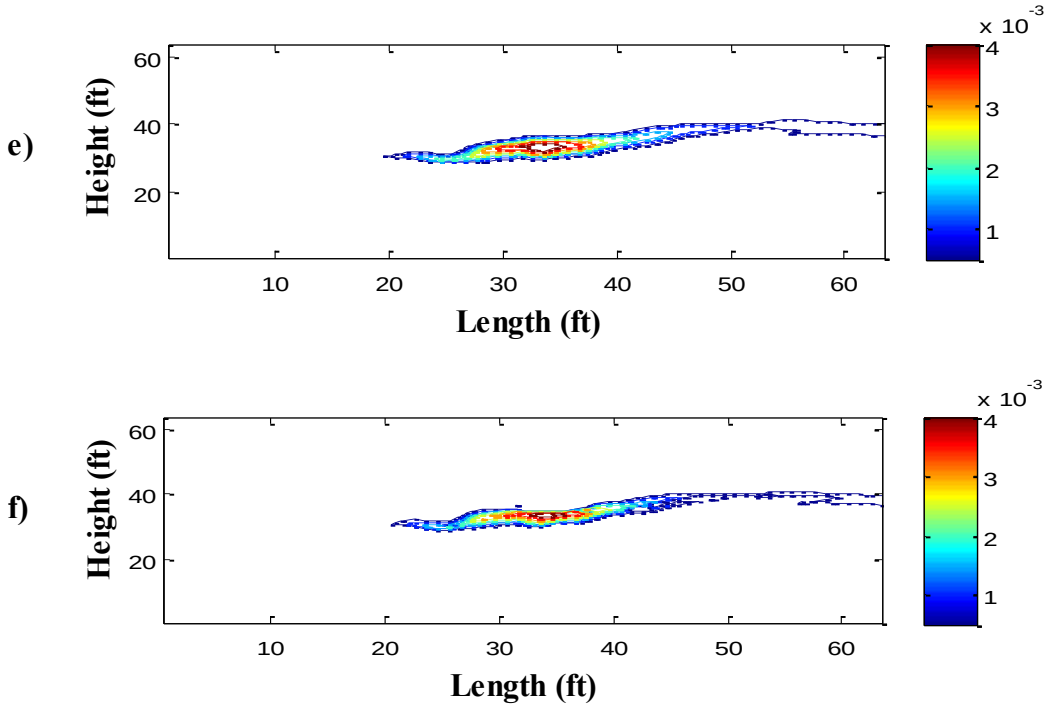

Figure 3.13: Global solute concentration maps showing comparable profiles between the simulation model and analytical models for various levels of heterogeneity for correlated permeability medium (L_{XD} = 0.25, L_{YD} = 0.1) at various times (a) simulation profile for V_{DP} = 0.4 at 99 days (b) analytical model profile for V_{DP} = 0.4 at 99 days (c) simulation profile for V_{DP} = 0.6 at 99 days (d) analytical model profile for V_{DP} = 0.6 at 99 days (e) simulation profile for V_{DP} = 0.8 at 99 days (f) analytical model profile for V_{DP} = 0.8 at 99 days.

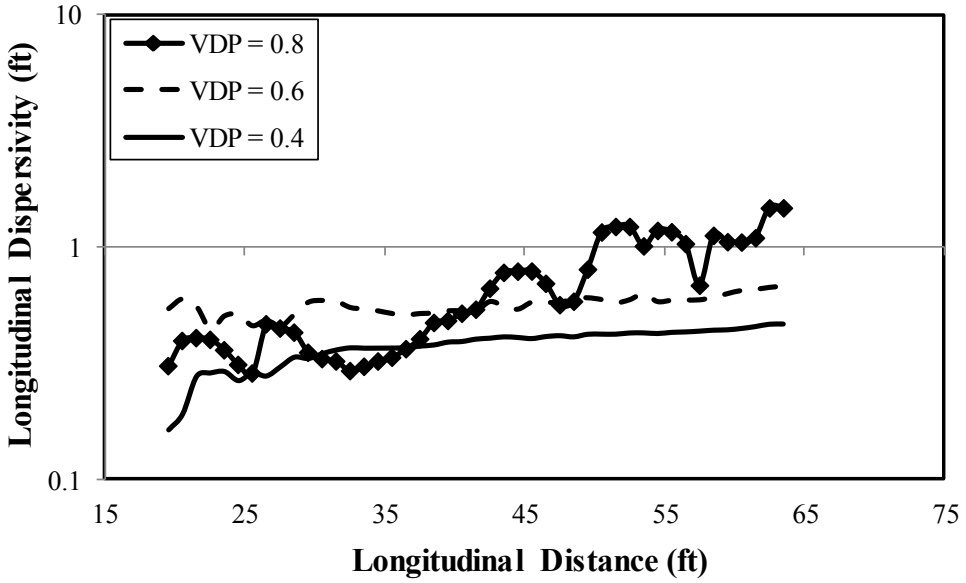

Figure 3.14: Average longitudinal dispersivity for correlated medium (L_{XD} = 0.25, L_{YD} = 0.1) with increasing level of heterogeneity.

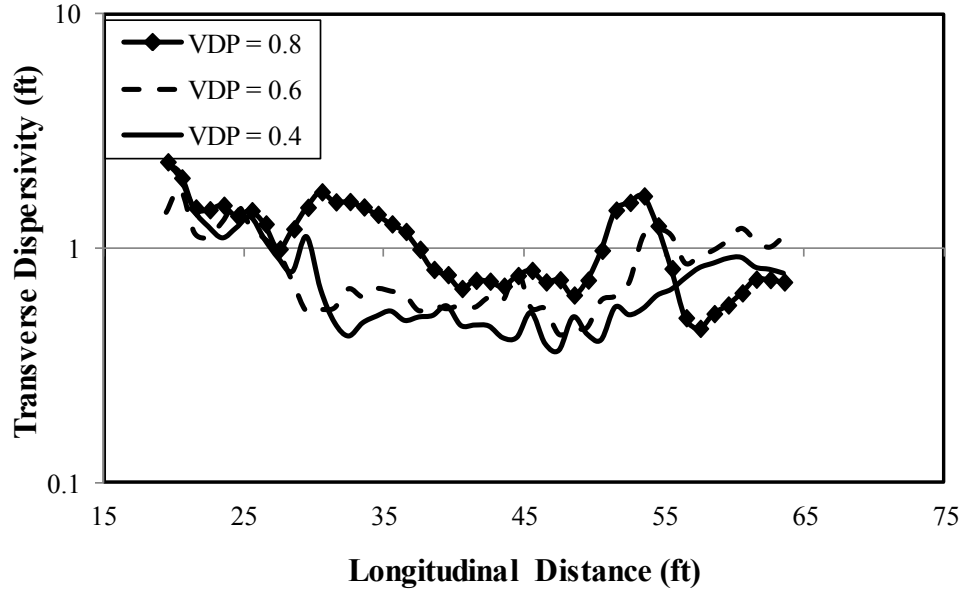

Figure 3.15: Average transverse dispersivity for correlated permeability medium (L_{XD} = 0.25, L_{YD} = 0.1) with increasing level of heterogeneity.

a)

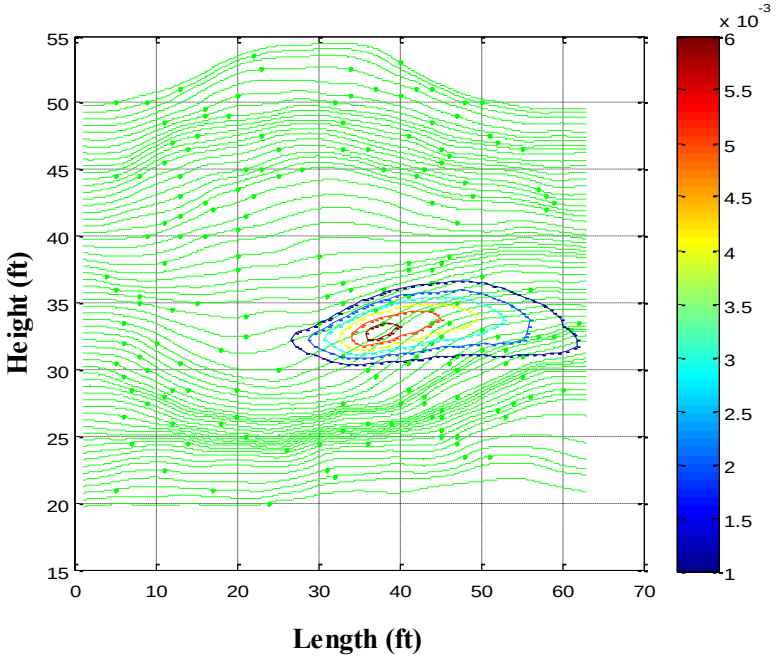

b)

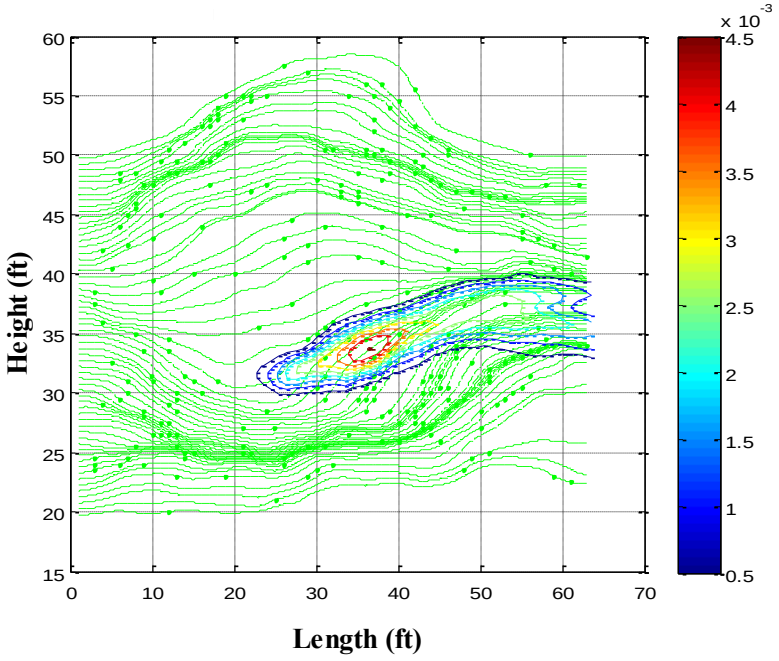

c)

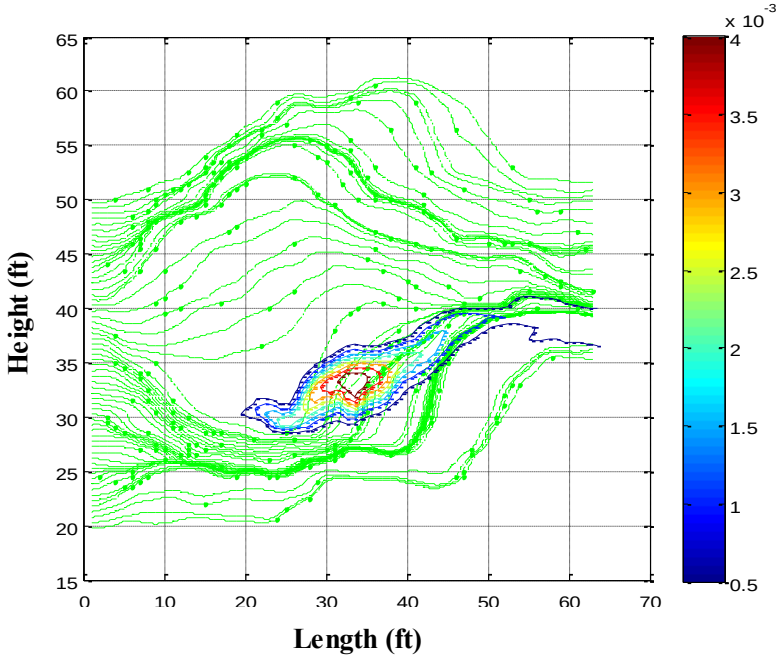

Figure 3.16: Concentration distribution at 99 days superimposed on model streamlines (green lines) for correlated medium (L_{XD} = 0.25, L_{YD} = 0.1) for various levels of heterogeneity (a) V_{DP} = 0.4 (b) V_{DP} = 0.6 and (c) V_{DP} = 0.8.

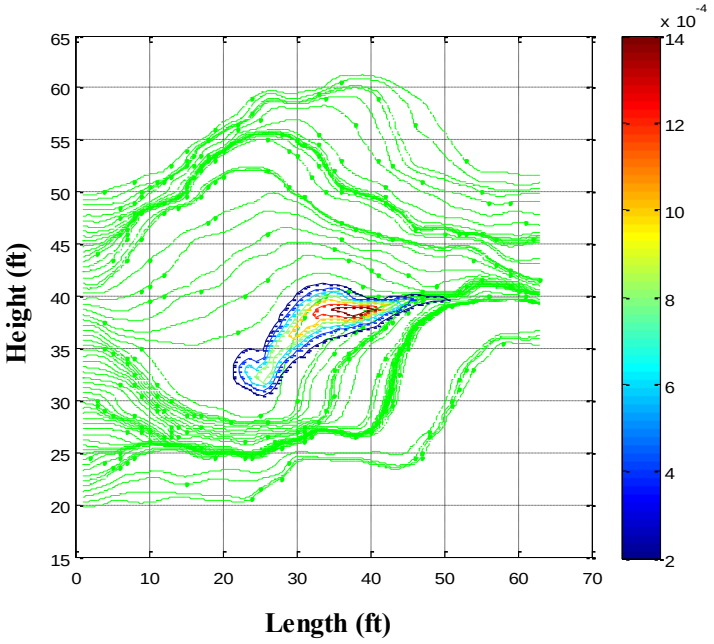

Figure 3.17: Concentration distribution for correlated permeability medium (L_{XD} = 0.25, L_{YD} = 0.1) with V_{DP} = 0.8 at 239 days showing trapped solute plume in low flow region.

a)

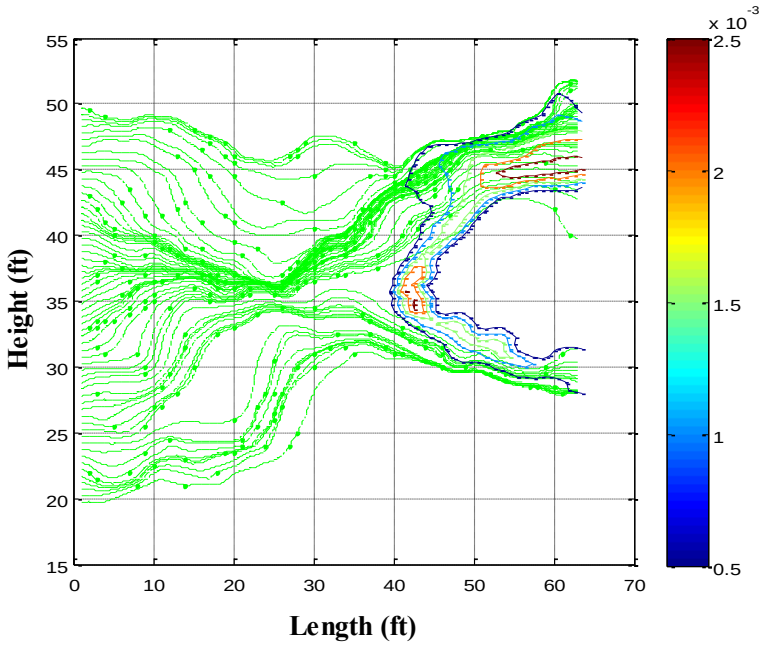
x 10^-3
2.5
2
1.5
1
0.5
55
50
45
40
35
30
25
20
15
0
10
20
30
40
50
60
70
Height (ft)
Length (ft)

b)

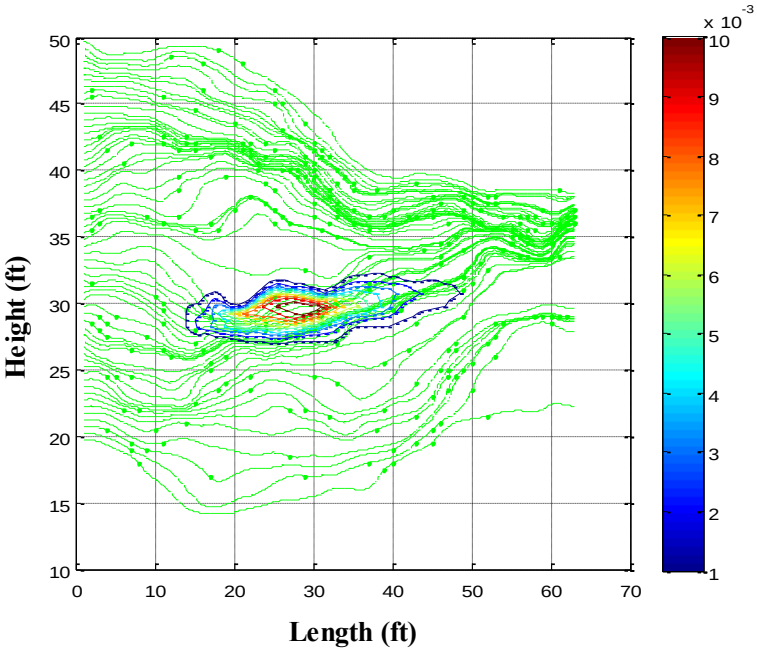
x 10^-3
10
9
8
7
6
5
4
3
2
1
50
45
40
35
30
25
20
15
10
0
10
20
30
40
50
60
70
Height (ft)
Length (ft)

c)

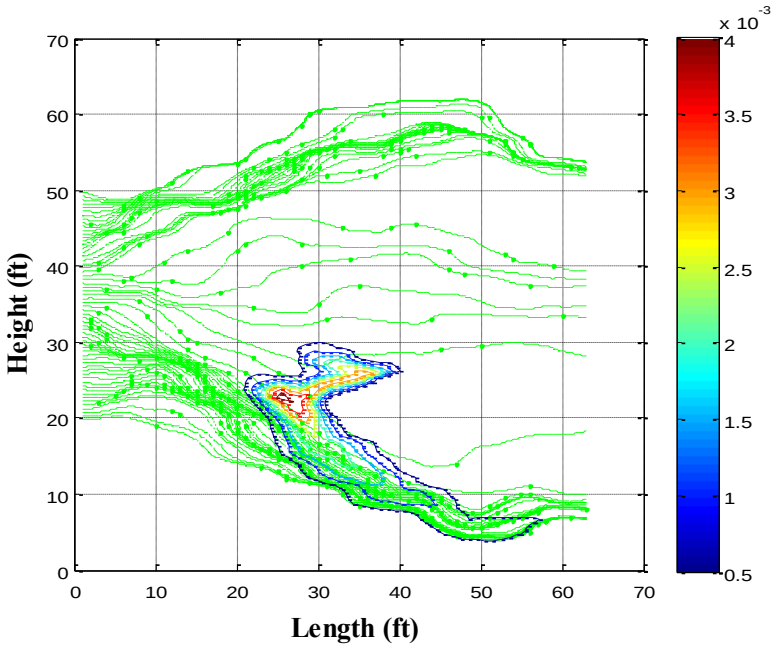

d)

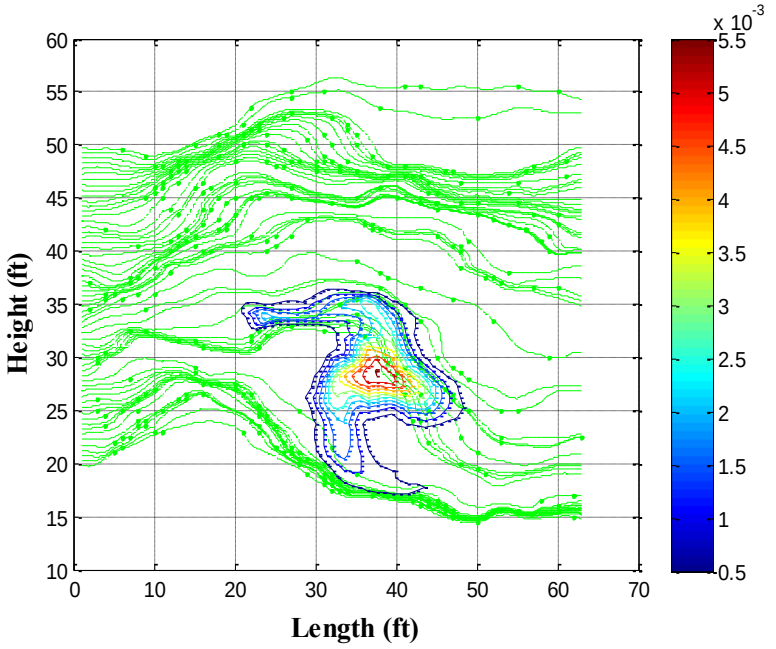

Figure 3.18: Solute concentration maps superimposed on simulation model streamlines (green lines) for different permeability realizations with same permeability correlations (L_{XD} = 0.25, L_{YD} = 0.1), mean permeability (200 mD) and V_{DP} = 0.8 at 88 days (a) realization 2 (b) realization 3 (c) realization 4 and (d) realization 5.

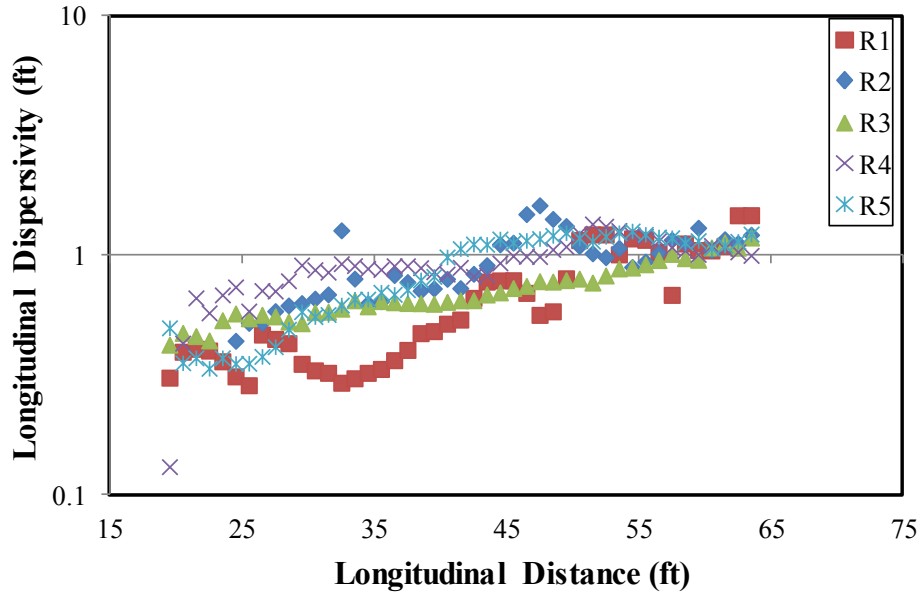

Figure 3.19: Average longitudinal dispersivity for five different realizations (R1:R5) with same permeability autocorrelation (0.25 in x-direction and 0.1 in y-direction), mean permeability (200 mD) and V_{DP} = 0.8.

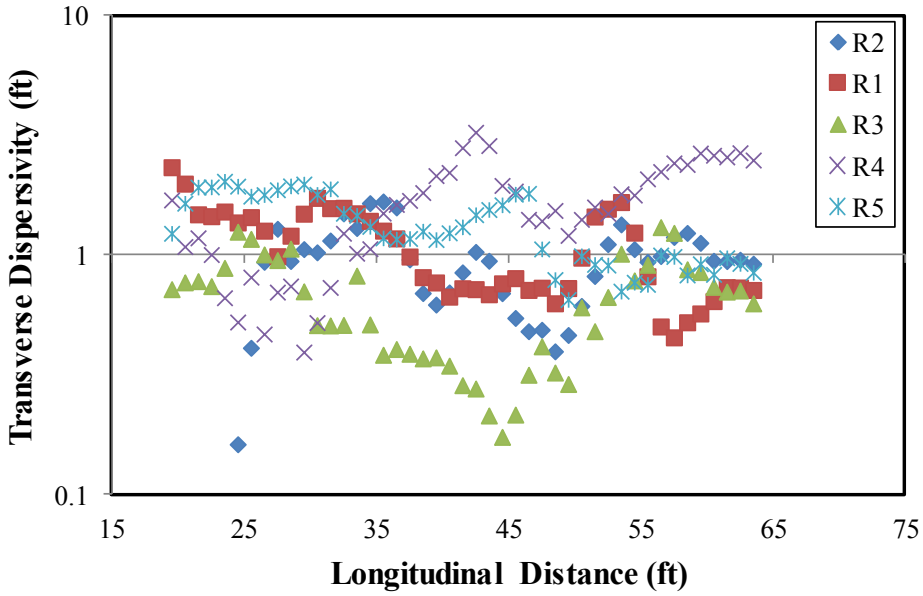

Figure 3.20: Average transverse dispersivity for five different realizations (R1:R5) with same permeability autocorrelation (0.25 in x-direction and 0.1 in y-direction), mean permeability and V_{DP} = 0.8.

a)

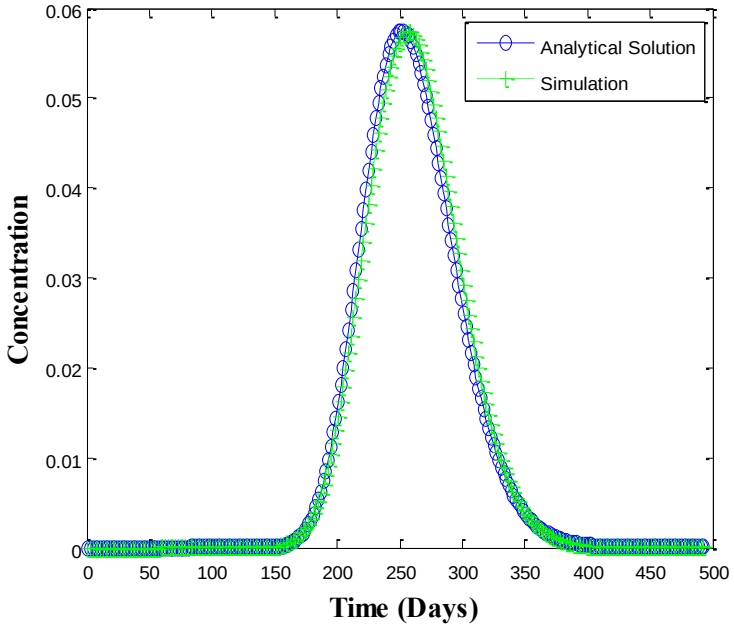
Analytical Solution
Simulation
Concentration
Time (Days)
0.06
0.05
0.04
0.03
0.02
0.01
0
0 50 100 150 200 250 300 350 400 450 500

b)

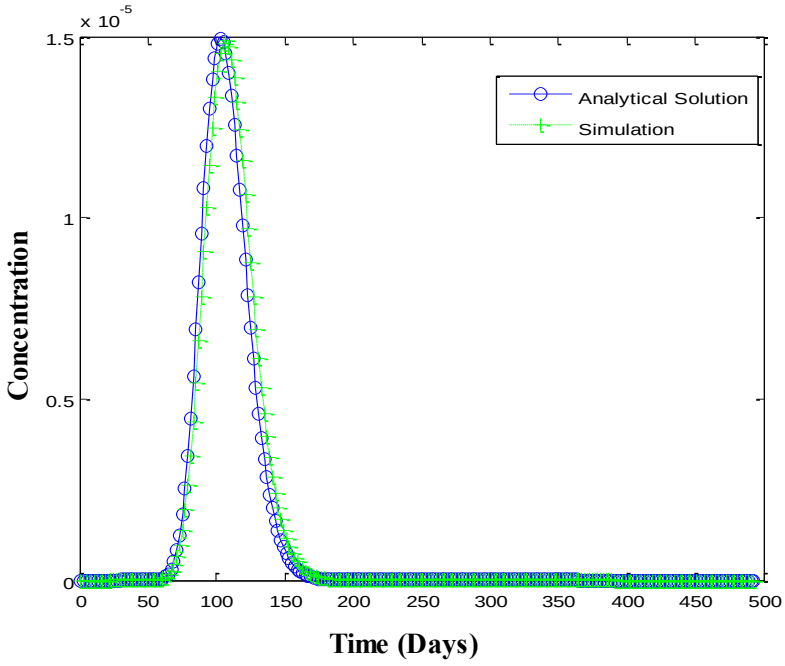
x 10^-5
Analytical Solution
Simulation
Concentration
Time (Days)
1.5
1
0.5
0
0 50 100 150 200 250 300 350 400 450 500

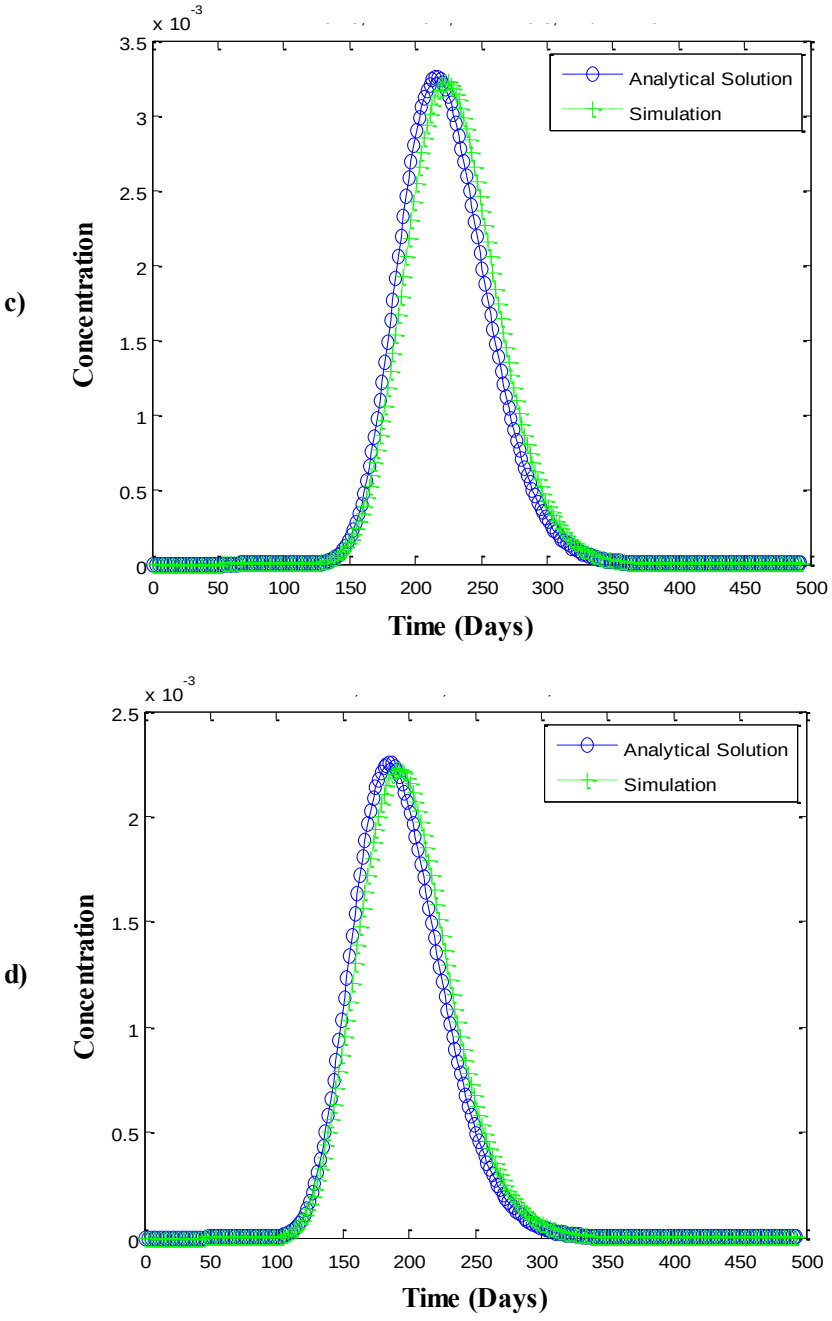

Figure 3.21: Comparison of the solute concentration histories from simulation and analytical models for same level of heterogeneity (V_{DP} = 0.6) and correlation lengths (L_{XD} = 0.25, L_{YD} = 0.1) at different kv/kh ratios (a) kv/kh = 0.0, x = 49.5ft, y = 31.75 ft (b) kv/kh = 0.01, x = 39.5 ft, y = 28.25 ft and (c) kv/kh = 0.1, x = 52.5 ft, y = 35.75 ft and (d) kv/kh = 0.2, x = 46.5 ft, y = 37.25 ft

a)

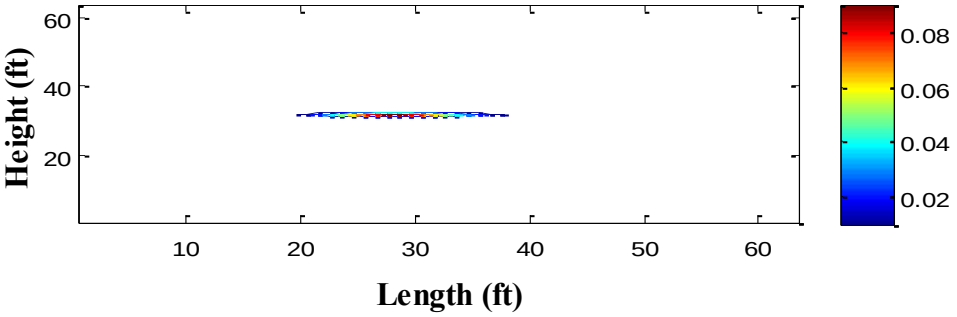
Height (ft)
60
40
20
10
20
30
40
50
60
Length (ft)
0.08
0.06
0.04
0.02

b)

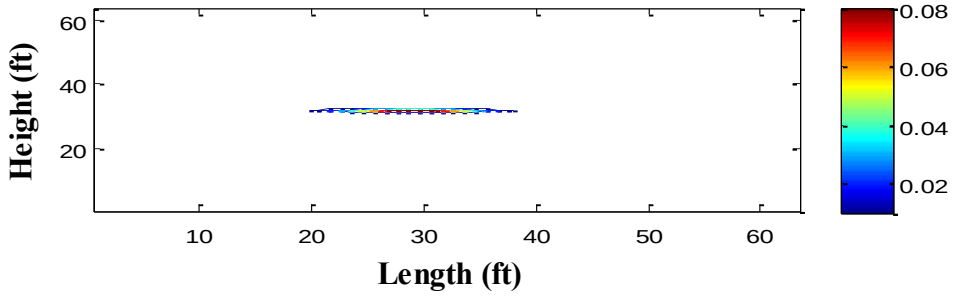
Height (ft)
60
40
20
10
20
30
40
50
60
Length (ft)
0.08
0.06
0.04
0.02

c)

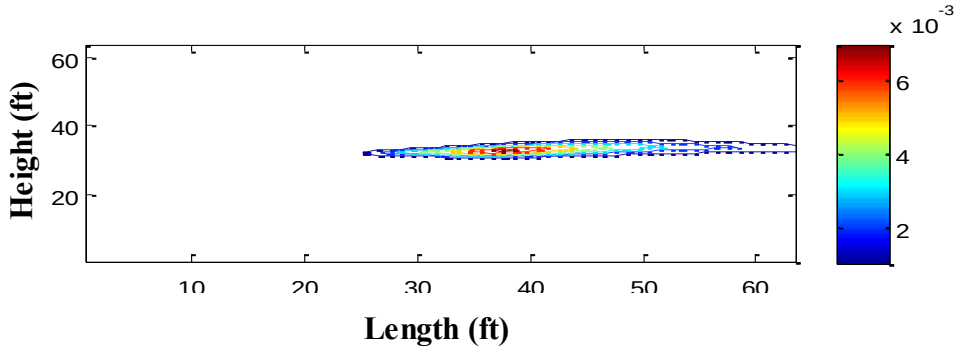
Height (ft)
60
40
20
10
20
30
40
50
60
Length (ft)
x 10^-3
6
4
2

d)

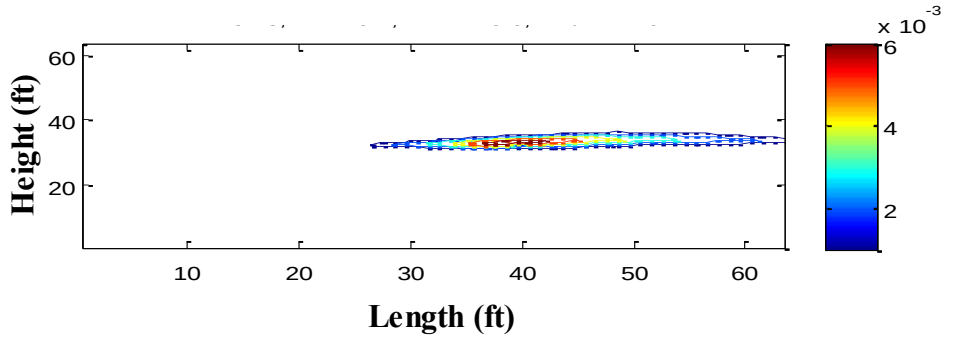
Height (ft)
60
40
20
10
20
30
40
50
60
Length (ft)
x 10^-3
6
4
2

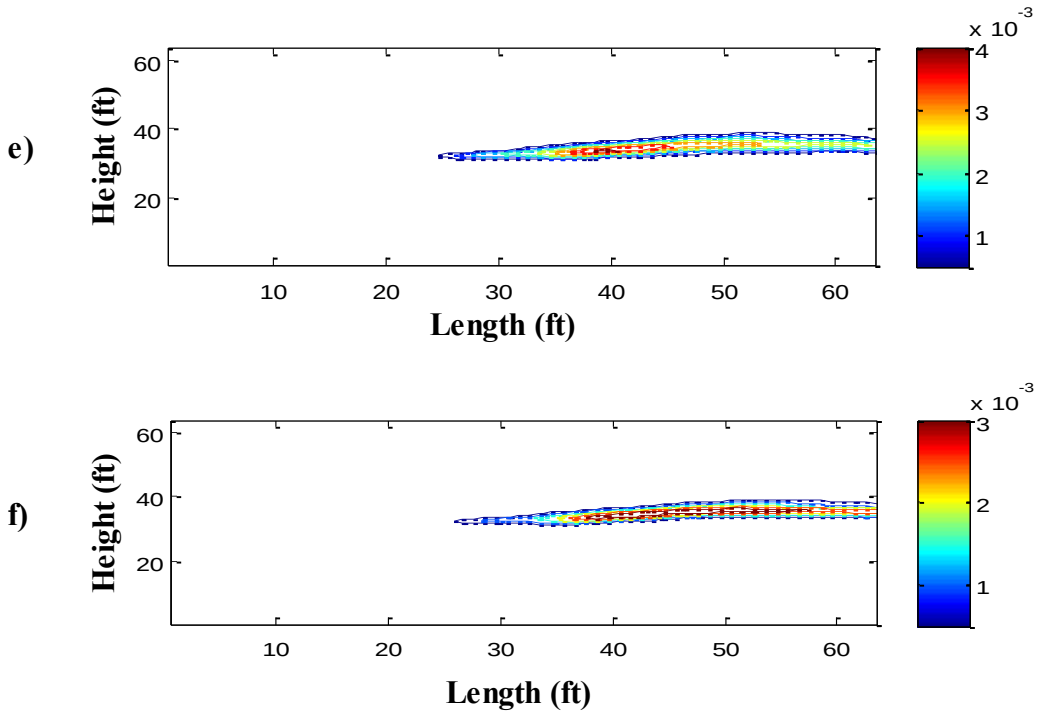

Figure 3.22: Global solute concentration maps showing comparable profiles between the simulation model and analytical models for same level of heterogeneity (V_{DP} = 0.6) with same permeability correlation lengths (L_{XD} = 0.25, L_{YD} = 0.1) at different permeability anisotropy ratios (a) simulation profile for kv/kh = 0.0 at 99 days (b) analytical model profile for kv/kh = 0.0 at 99 days (c) simulation profile for kv/kh = 0.1 at 159 days (d) analytical model profile for kv/kh = 0.1 at 159 days (e) simulation profile for kv/kh = 0.2 at 159 days (f) analytical model profile for kv/kh = 0.2 at 159 days.

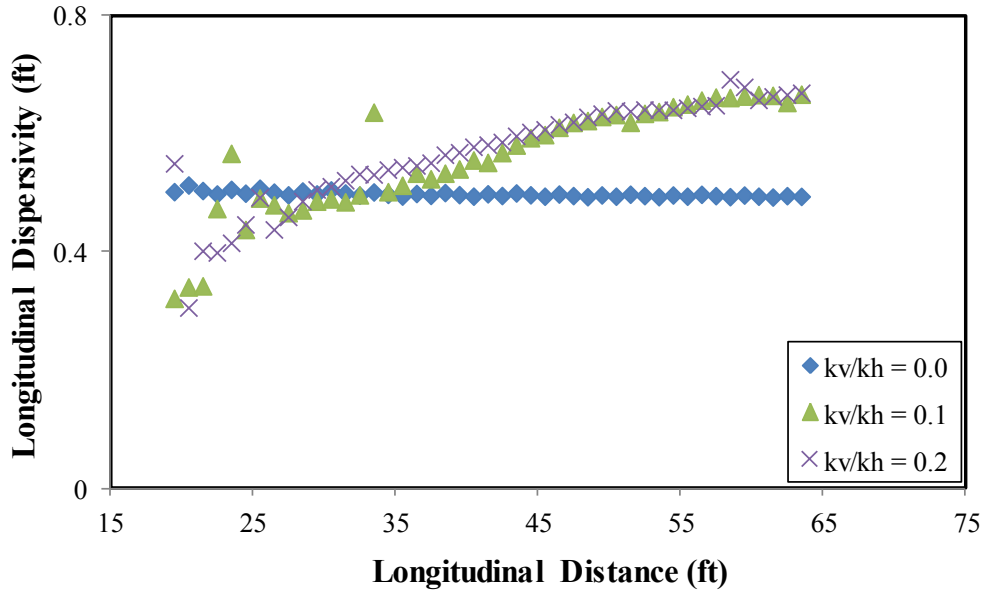

Figure 3.23: Average longitudinal dispersivity at various levels of cross-flow (kv/kh) for same level of heterogeneity (V_{DP} = 0.6) and permeability correlation lengths (L_{XD} = 0.25, L_{YD} = 0.1)

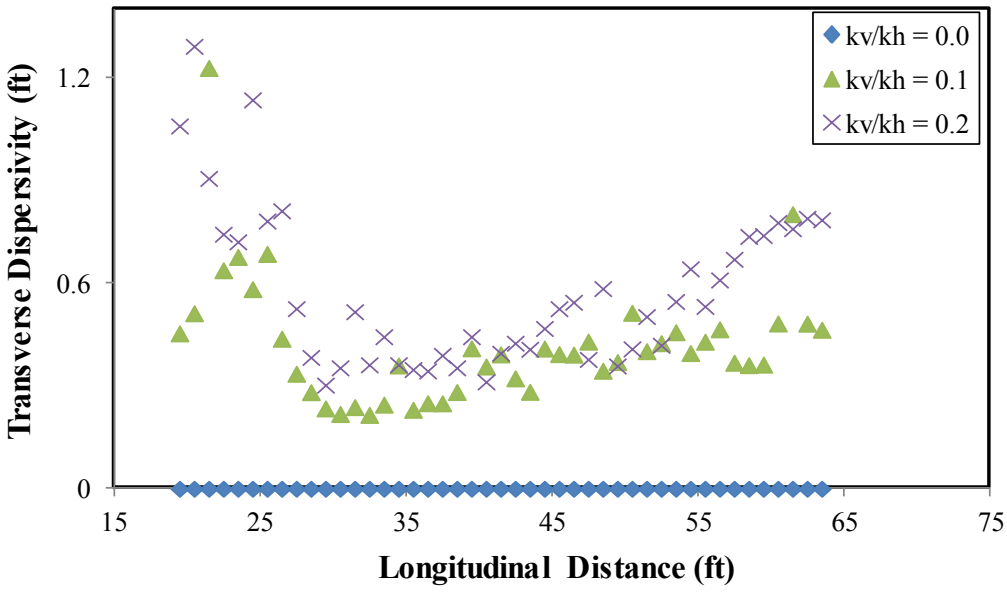

Figure 3.24: Average transverse dispersivity at various levels of cross-flow (kv/kh) for same level of heterogeneity (V_{DP} = 0.6) and permeability correlation lengths (L_{XD} = 0.25, L_{YD} = 0.1)

a)

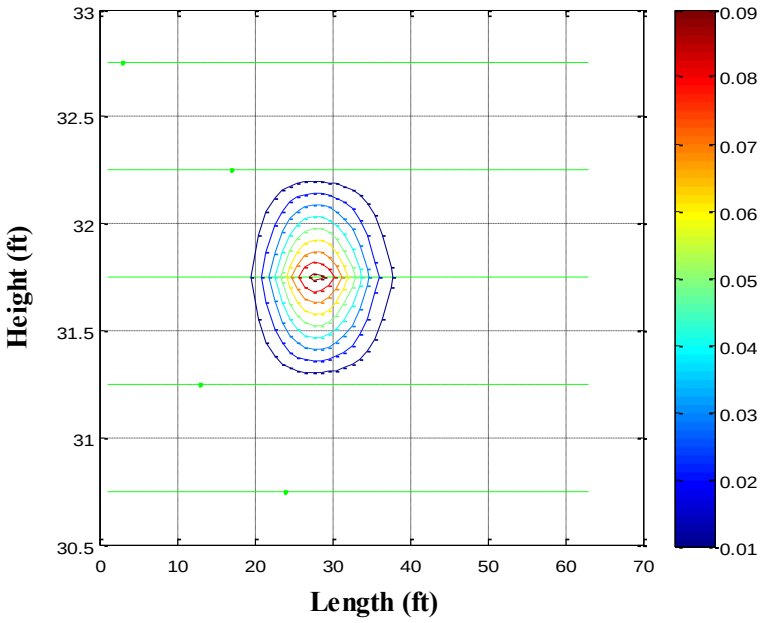
Height (ft)
Length (ft)
33
32.5
32
31.5
31
30.5
0
10
20
30
40
50
60
70
0.09
0.08
0.07
0.06
0.05
0.04
0.03
0.02
0.01

b)

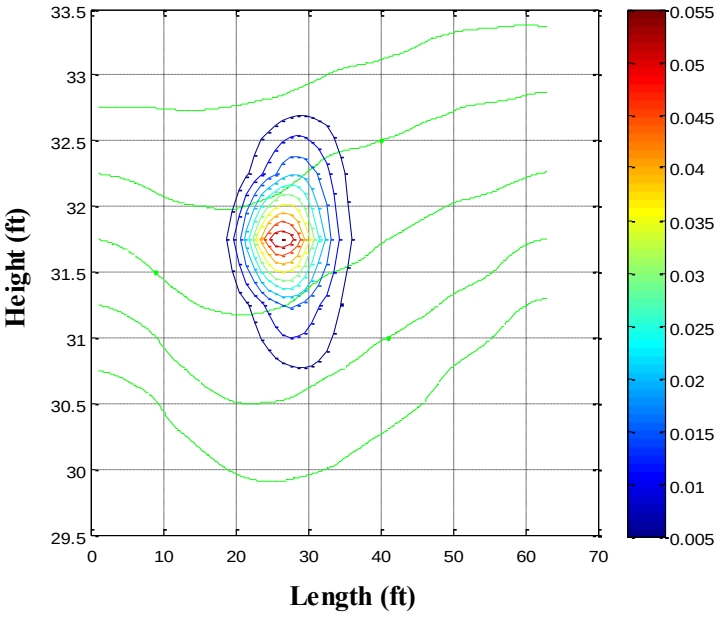
Height (ft)
Length (ft)
33.5
33
32.5
32
31.5
31
30.5
30
29.5
0
10
20
30
40
50
60
70
0.055
0.05
0.045
0.04
0.035
0.03
0.025
0.02
0.015
0.01
0.005

c)

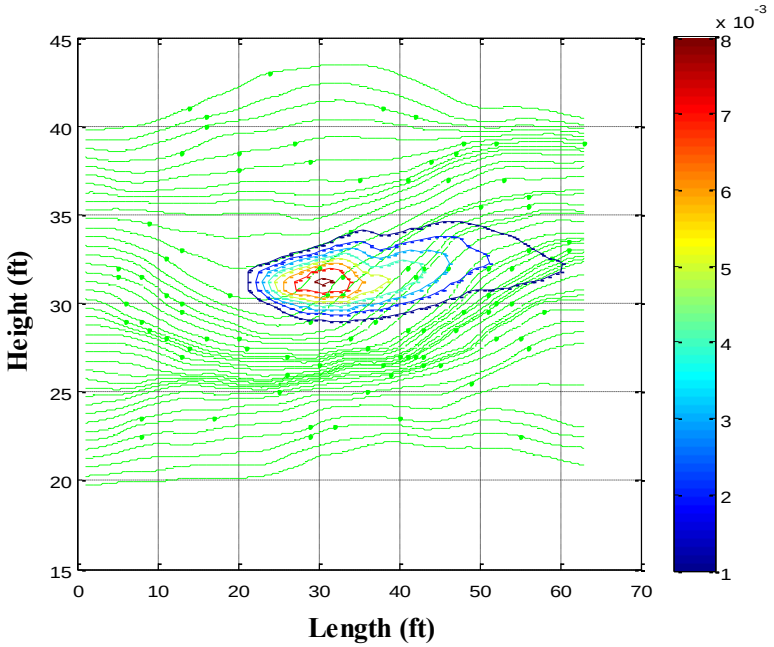

Figure 3.25: Solute concentration distribution superimposed on simulation streamlines (green lines) for same level of heterogeneity (V_{DP} = 0.6) and permeability correlation lengths (L_{XD} = 0.25, L_{YD} = 0.1) with varying levels of cross flow at 99 days (a) kv/kh = 0.0 (b) kv/kh = 0.01 and (c) kv/kh = 0.2.

a)

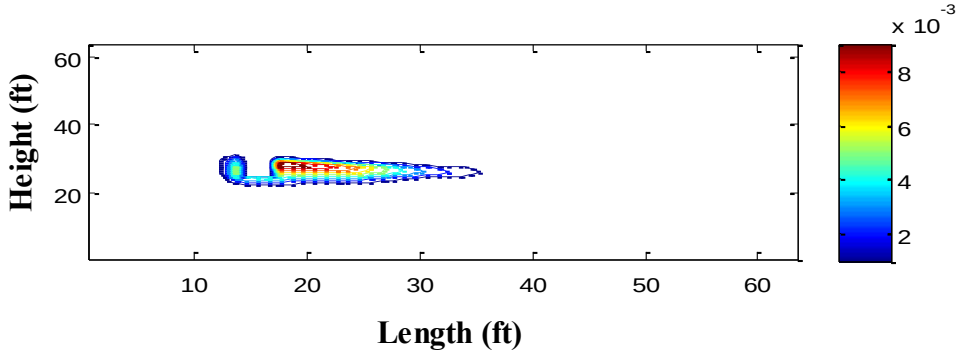

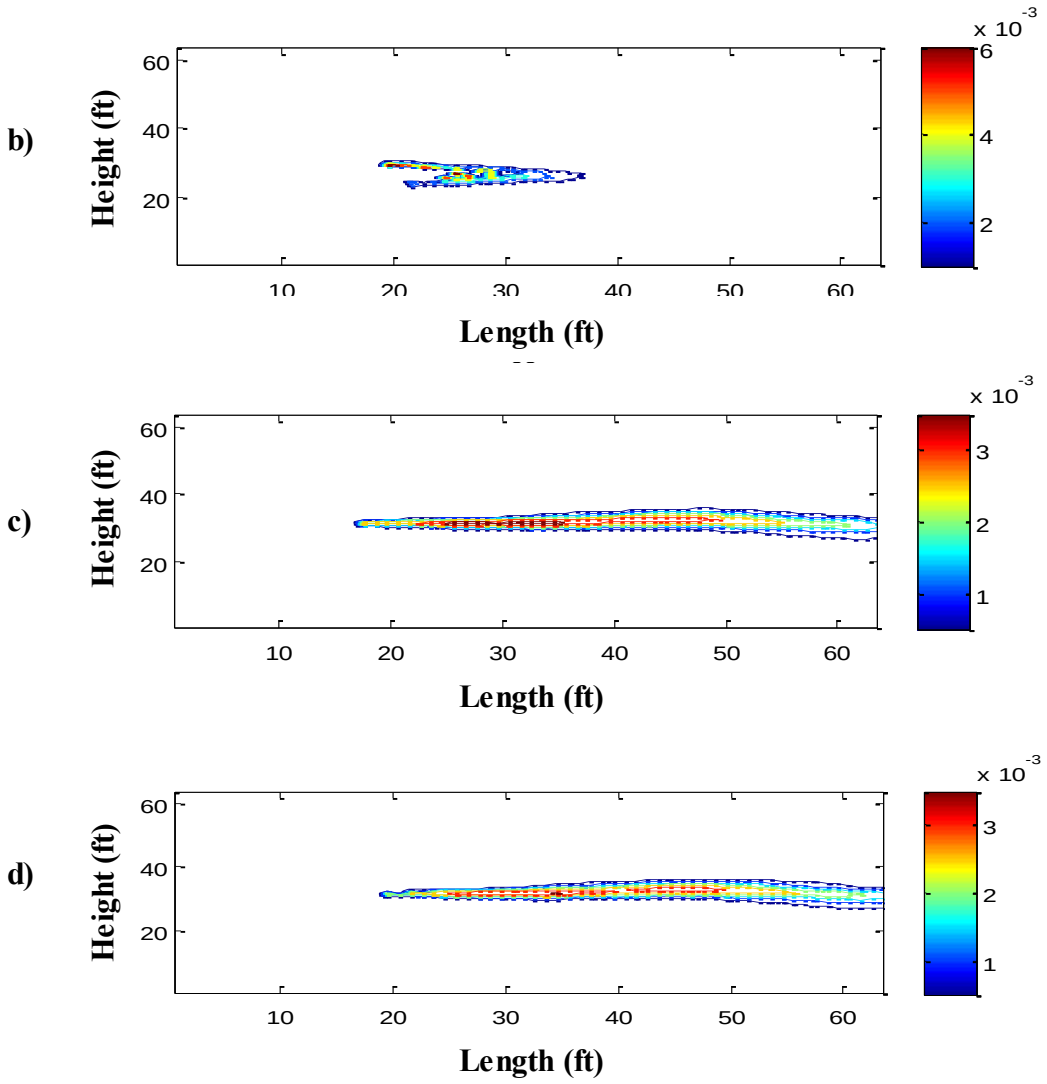

Figure 3.26: Solute concentration map for a simulation models and analytical model with similar V_{DP} = 0.4, mean permeability and permeability correlation lengths (L_{XD} = 0.25, L_{YD} = 0.1) at various times (a) simulation model at 39 days (b) analytical model at 39 days (c) simulation model at 99 days and (d) analytical model at 99 days.

a)

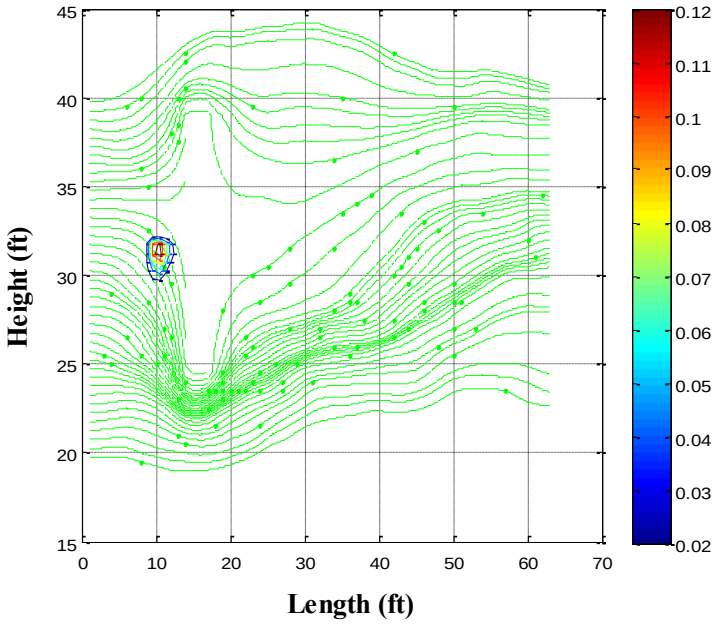
Height (ft)
Length (ft)
45
40
35
30
25
20
15
0
10
20
30
40
50
60
70
0.12
0.11
0.1
0.09
0.08
0.07
0.06
0.05
0.04
0.03
0.02

b)

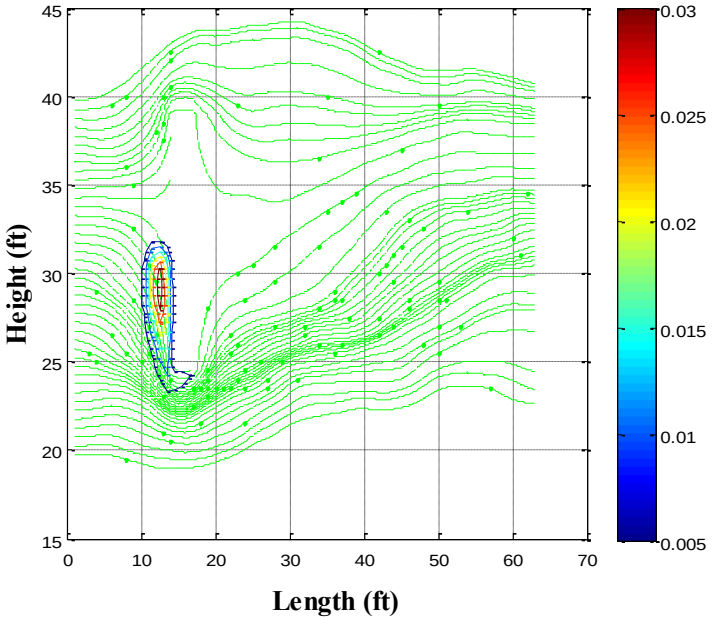
Height (ft)
Length (ft)
45
40
35
30
25
20
15
0
10
20
30
40
50
60
70
0.03
0.025
0.02
0.015
0.01
0.005

c)

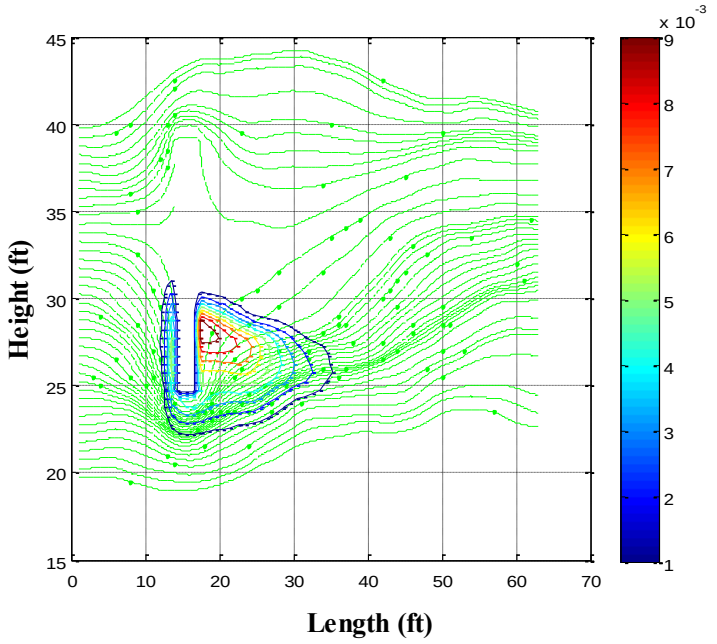

d)

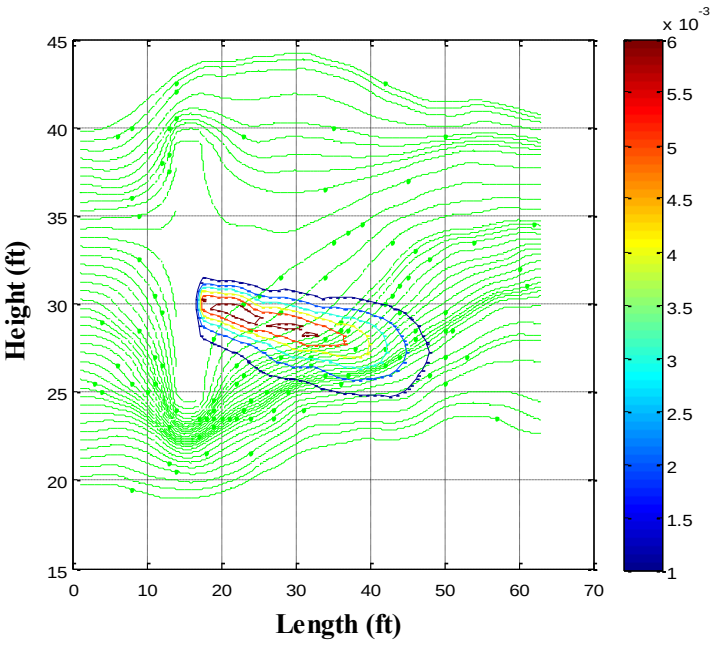

Figure 3.27: Solute concentration distribution superimposed on simulation model streamlines (green lines) for same level of heterogeneity (V_{DP} = 0.4) and correlation lengths (L_{XD} = 0.25, L_{YD} = 0.1) with a no flow barrier along the path of the solute plume for various times (a) 5 days (b) 19 days (c) 39 days and (d) 59 days.

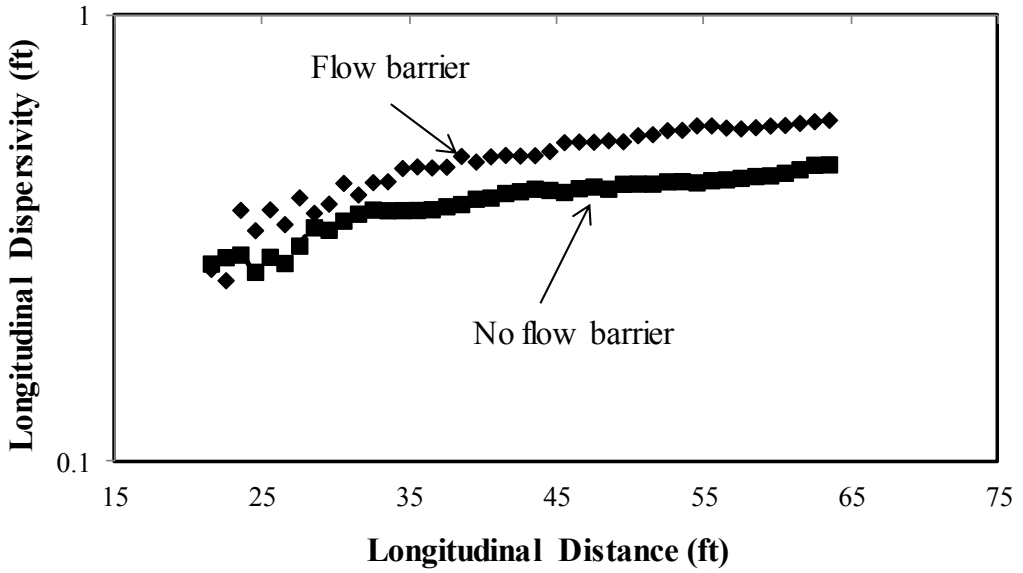

Figure 3.28: The effect of flow barrier on estimated longitudinal dispersivity for a simulation model with $V_{DP} = 0.4$ and similar dimensionless correlation lengths ($L_{XD} = 0.25$, $L_{YD} = 0.1$)

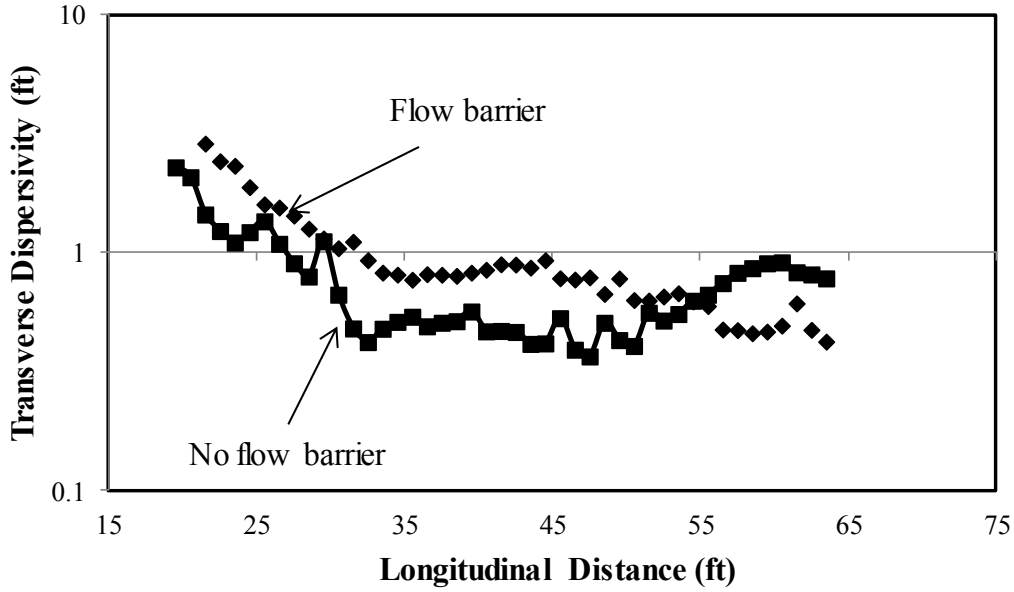

Figure 3.29: The effect of flow barrier on estimated transverse dispersivity for a simulation model with $V_{DP} = 0.4$ and similar dimensionless correlation lengths ($L_{XD} = 0.25$, $L_{YD} = 0.1$).

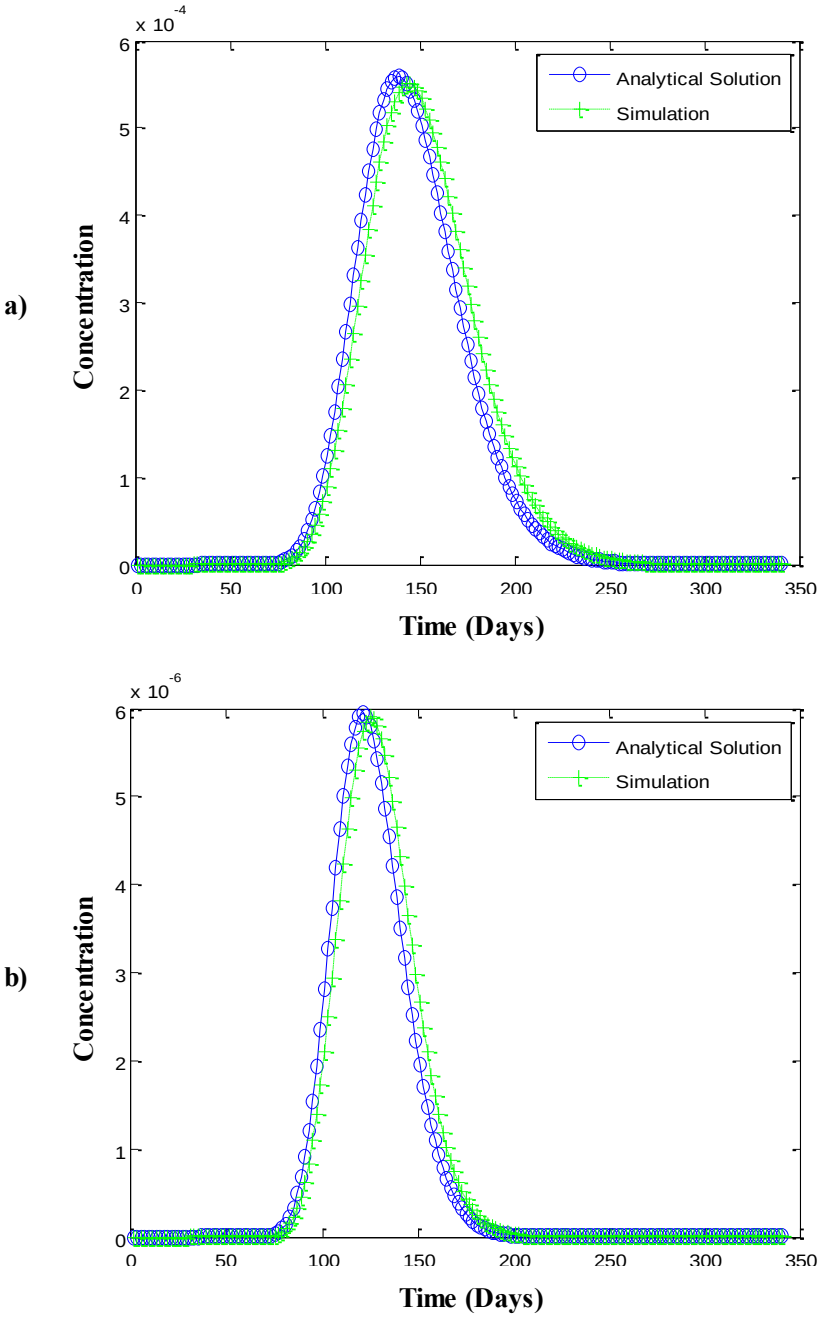

Figure 3.30: Comparison of local solute concentrations history from simulation model and analytical model for same level of heterogeneity (V_{DP} = 0.6) and uncorrelated permeability medium (L_{XD} = 0.0, L_{YD} = 0.0) at different input dispersivities (α_L and α_T) (a) input α_L = 0.5, x = 49.5ft, y = 37.25 ft and (b) input α_T = 0.5, x = 48.5 ft, y = 53.75 ft.

a)

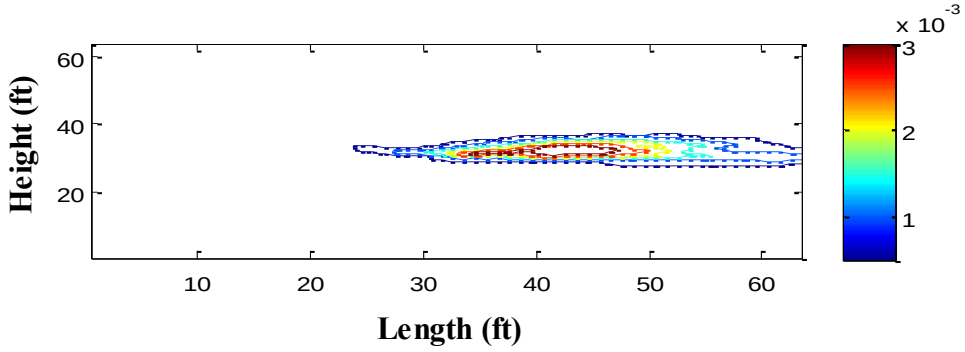
x 10^-3
3
2
1
60
40
20
Height (ft)
10
20
30
40
50
60
Length (ft)

b)

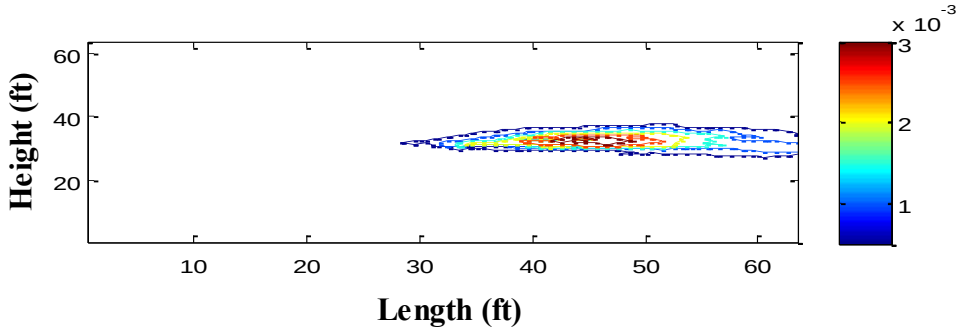
x 10^-3
3
2
1
60
40
20
Height (ft)
10
20
30
40
50
60
Length (ft)

c)

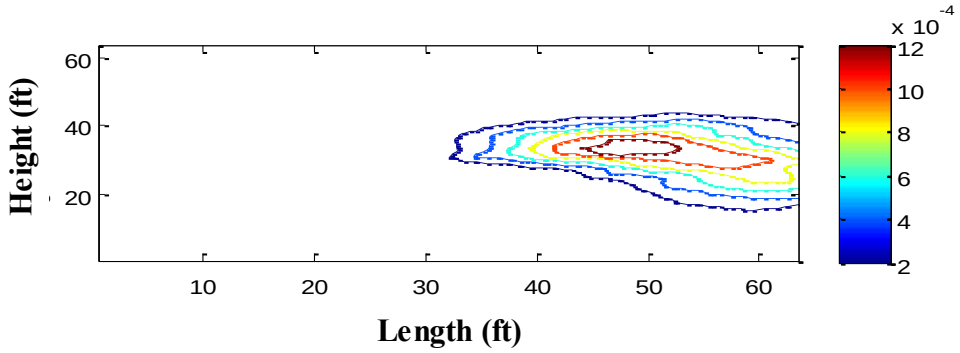
x 10^-4
12
10
8
6
4
2
60
40
20
Height (ft)
10
20
30
40
50
60
Length (ft)

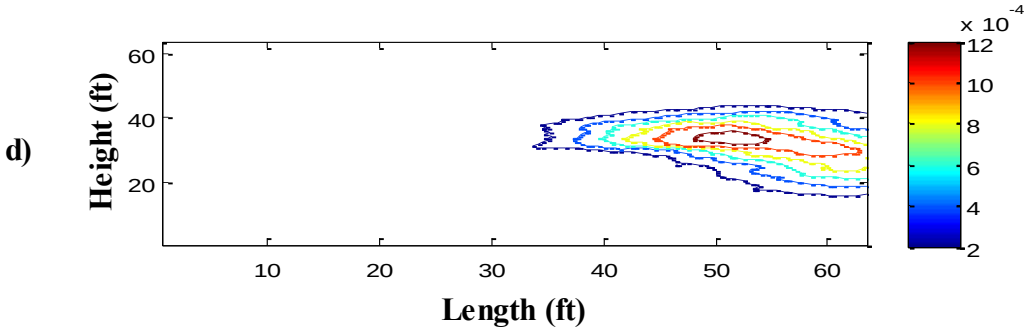

Figure 3.31: Solute concentration maps for simulation models and analytical model with similar V_{DP} = 0.6, mean permeability and correlation length for different input dispersivities at 99 days (a) simulation model with input longitudinal dispersivity of 0.5 ft (b) analytical model with input longitudinal dispersivity of 0.5 ft (c) simulation model with input transverse dispersivity of 0.5 ft and (d) analytical model with input transverse dispersivity at 0.5 ft.

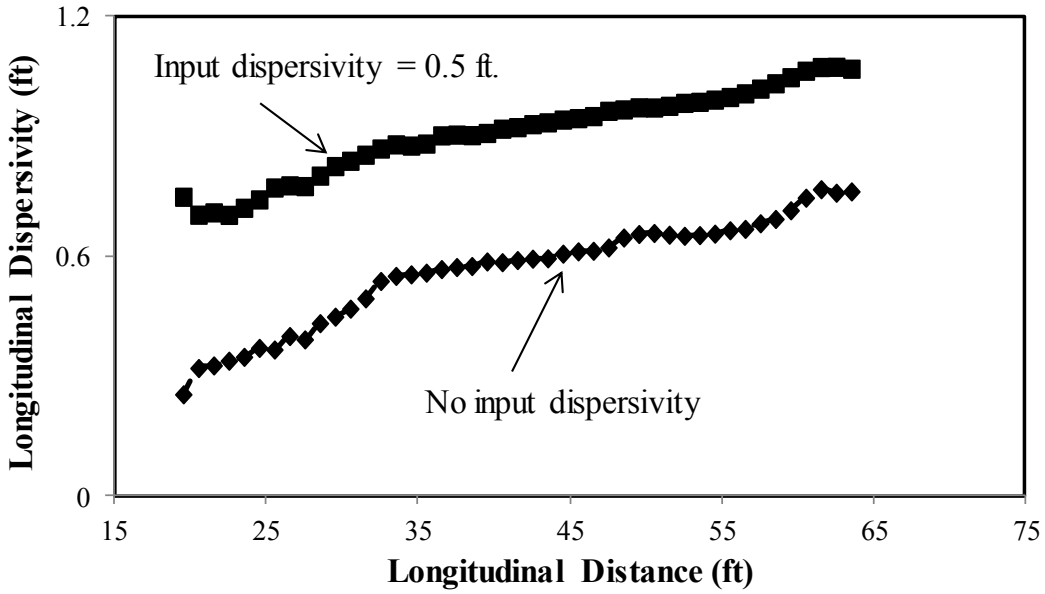

Figure 3.32: Estimated longitudinal dispersivity with and without input longitudinal dispersivity for an uncorrelated medium with V_{DP} = 0.6.

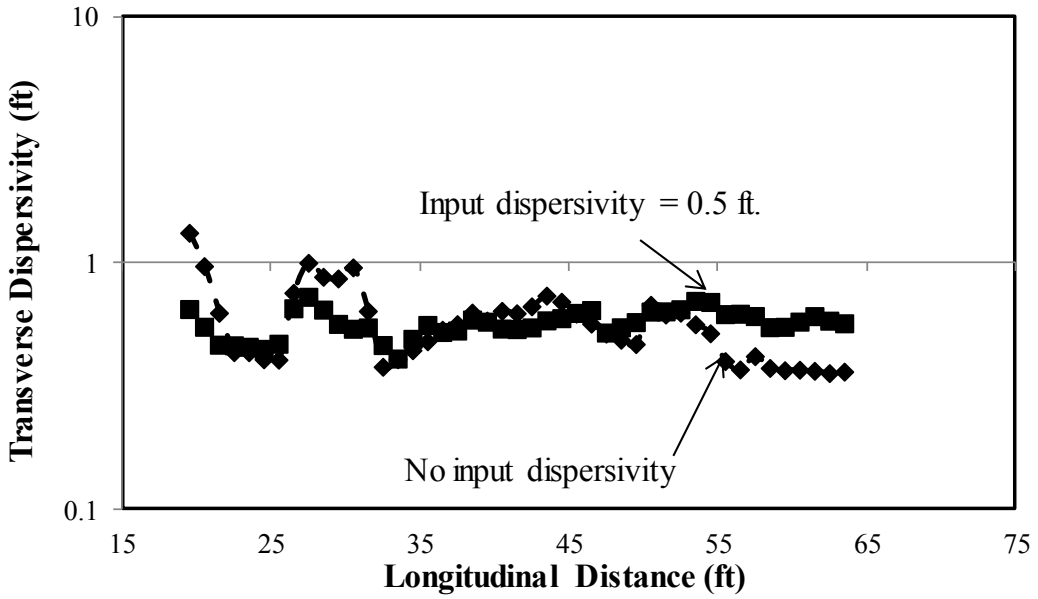

Figure 3.33: Estimated transverse dispersivity with and without input longitudinal dispersivity for an uncorrelated medium with $V_{DP} = 0.6$.

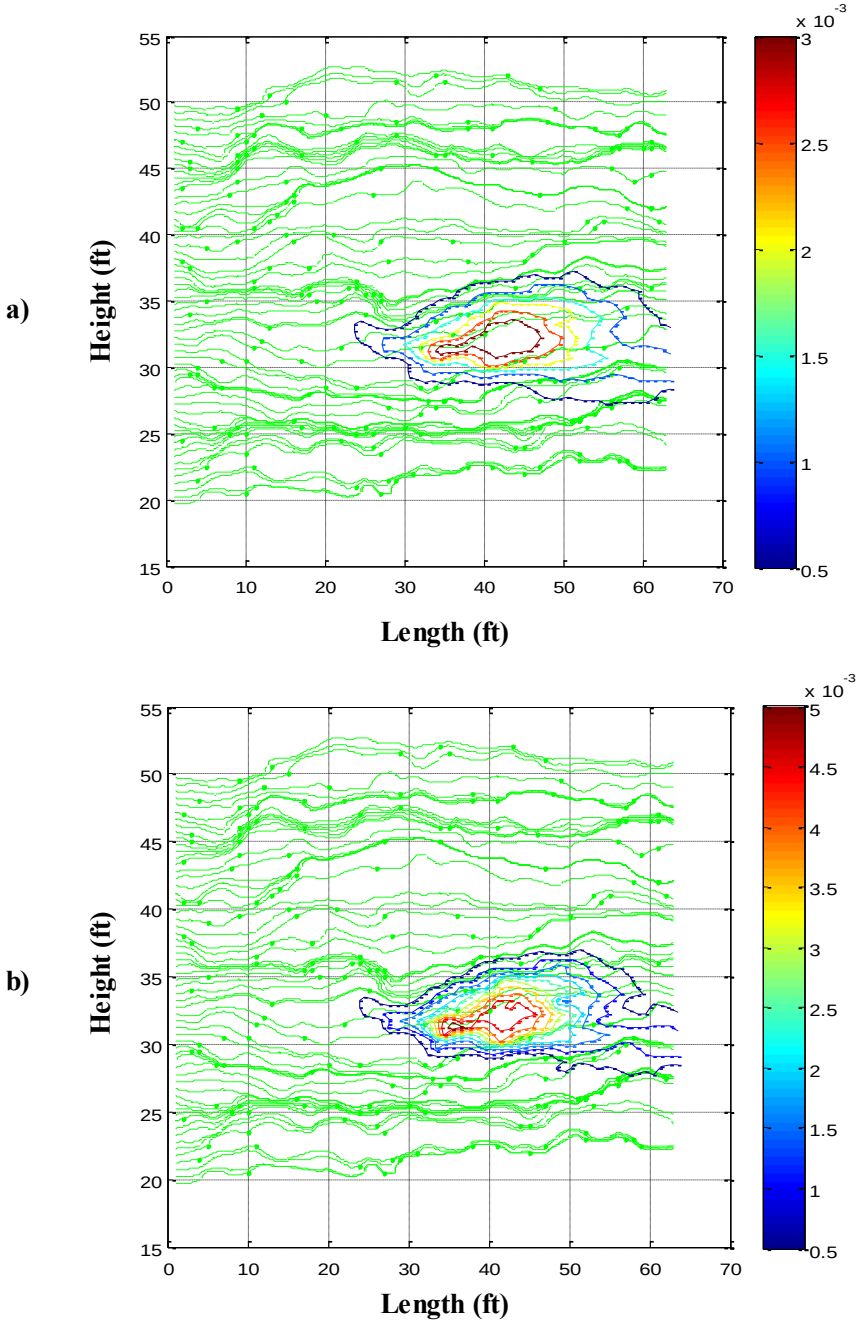

Figure 3.34: Solute concentration map at 99 days superimposed on the model streamlines (green lines) for an uncorrelated medium with $V_{DP} = 0.6$ (a) with input longitudinal dispersivity of 0.5 ft and (b) with no input dispersivity.

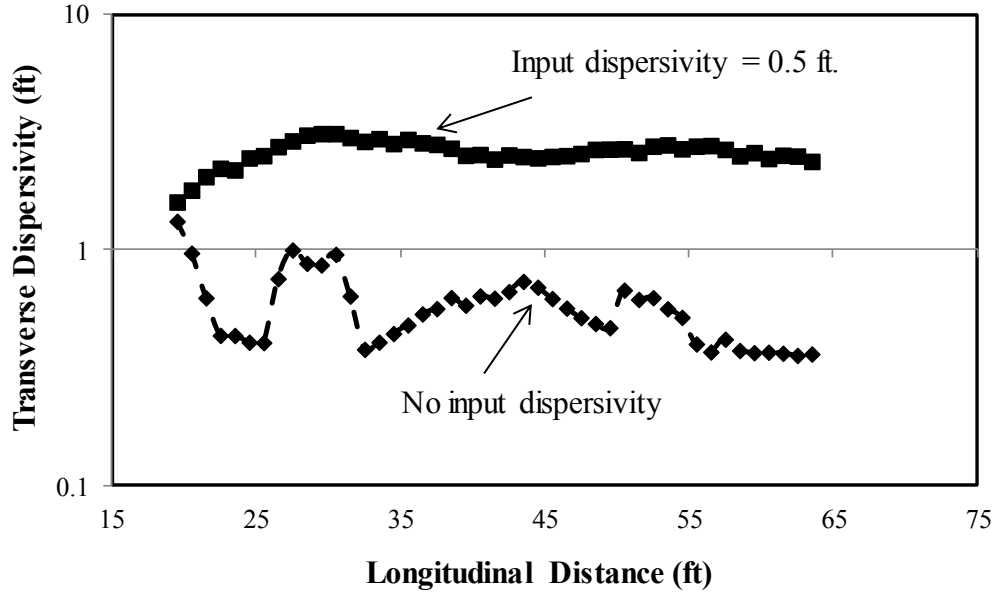

Figure 3.35: Estimated transverse dispersivity with and without input transverse dispersivity for an uncorrelated medium with $V_{DP} = 0.6$.

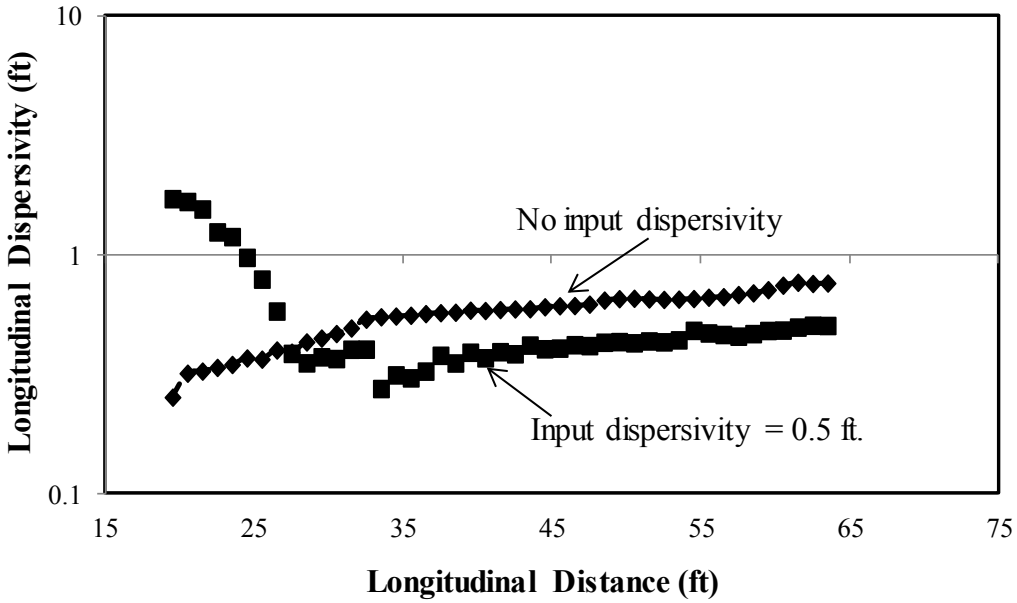

Figure 3.36: Estimated longitudinal dispersivity with and without input transverse dispersivity for an uncorrelated medium with $V_{DP} = 0.6$.

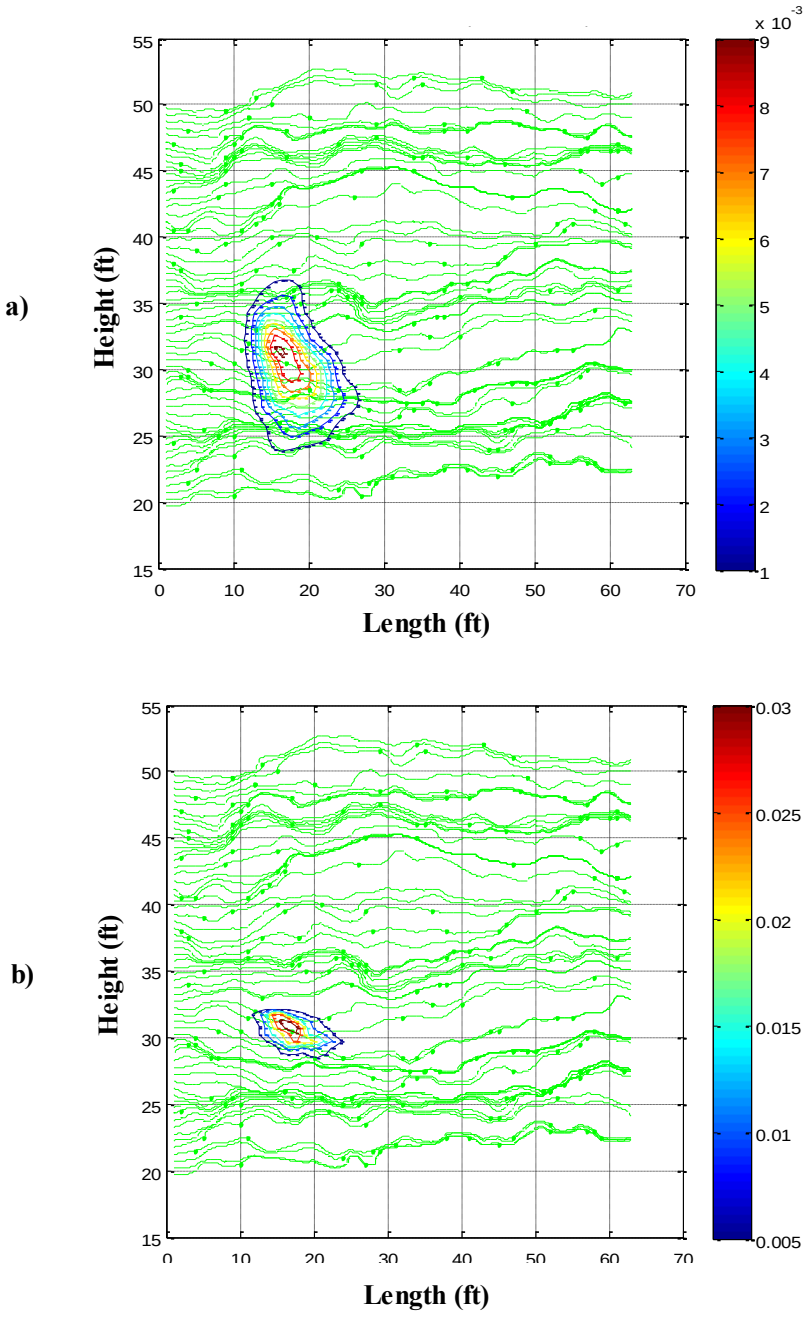

Figure 3.37: Solute concentration map at 19 days superimposed on the model streamlines (green lines) for an uncorrelated medium with $V_{DP} = 0.6$ (a) with input transverse dispersivity of 0.5 ft and (b) with no input dispersivity.

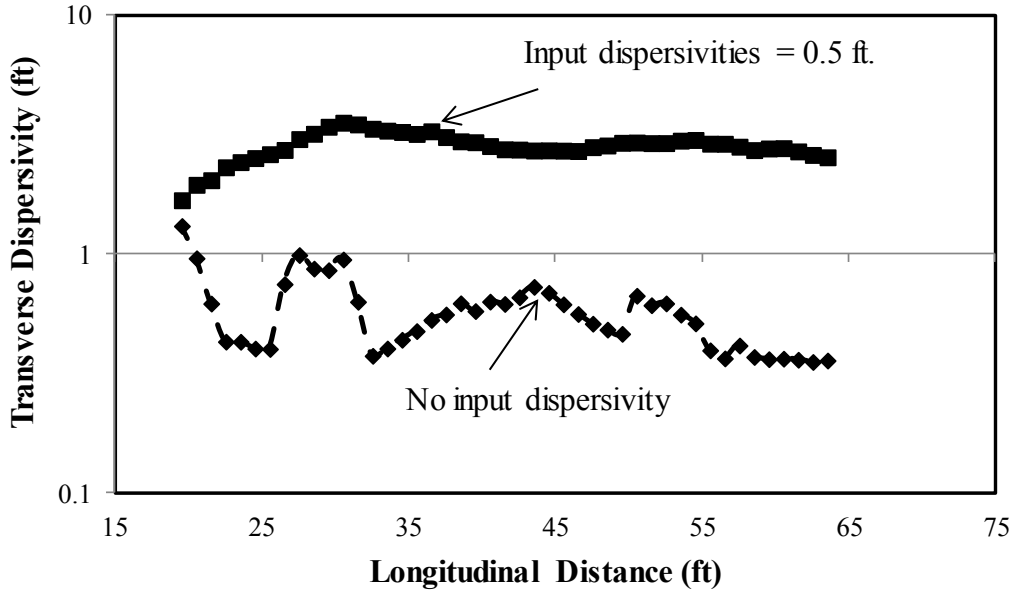

Figure 3.38: Estimated transverse dispersivity for cases with and without combined input of longitudinal and transverse dispersivity for an uncorrelated medium with $V_{DP} = 0.6$.

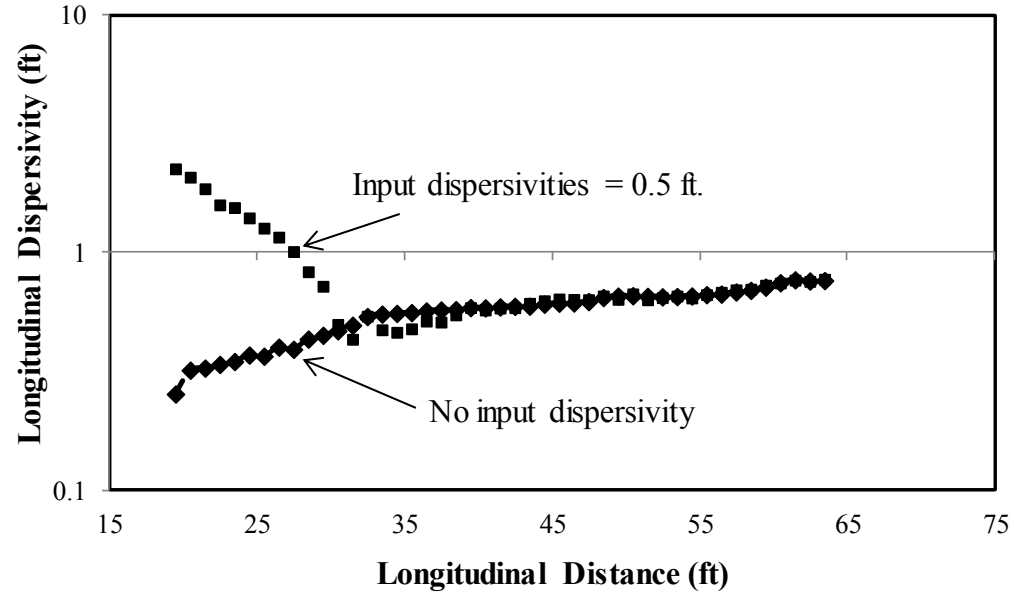

Figure 3.39: Estimated longitudinal dispersivity for cases with and without combined input of longitudinal and transverse dispersivity for an uncorrelated medium with $V_{DP} = 0.6$.

a)

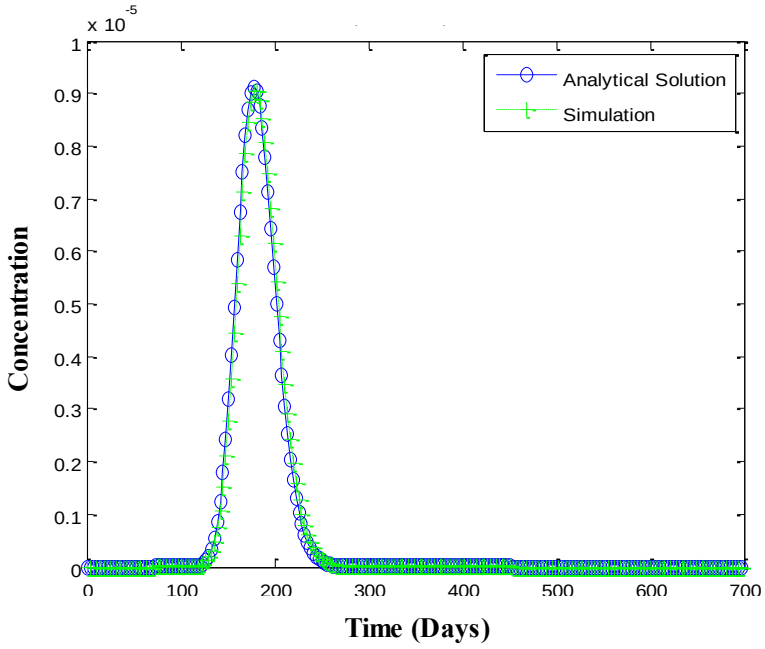
x 10^-5
Analytical Solution
Simulation
Concentration
Time (Days)
0
0.1
0.2
0.3
0.4
0.5
0.6
0.7
0.8
0.9
1
0
100
200
300
400
500
600
700

b)

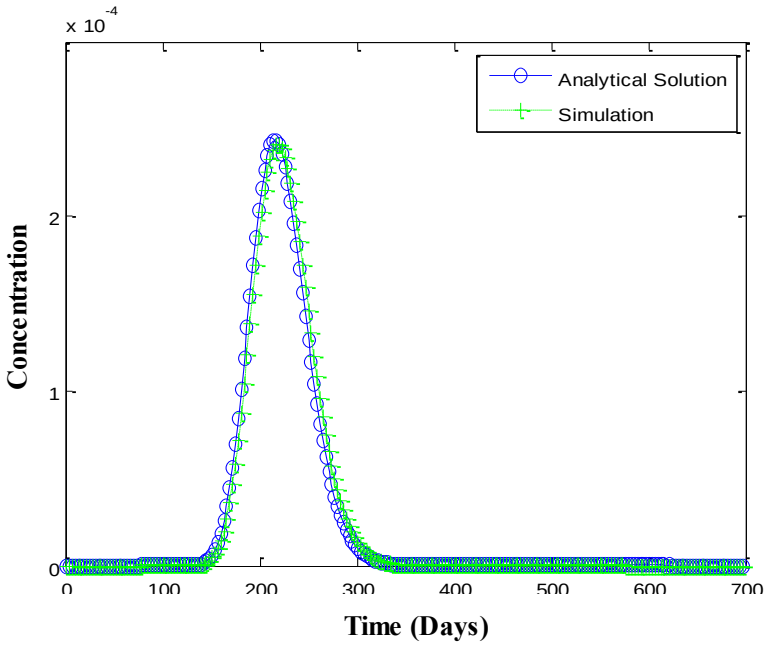
x 10^-4
Analytical Solution
Simulation
Concentration
Time (Days)
0
1
2
0
100
200
300
400
500
600
700

c)

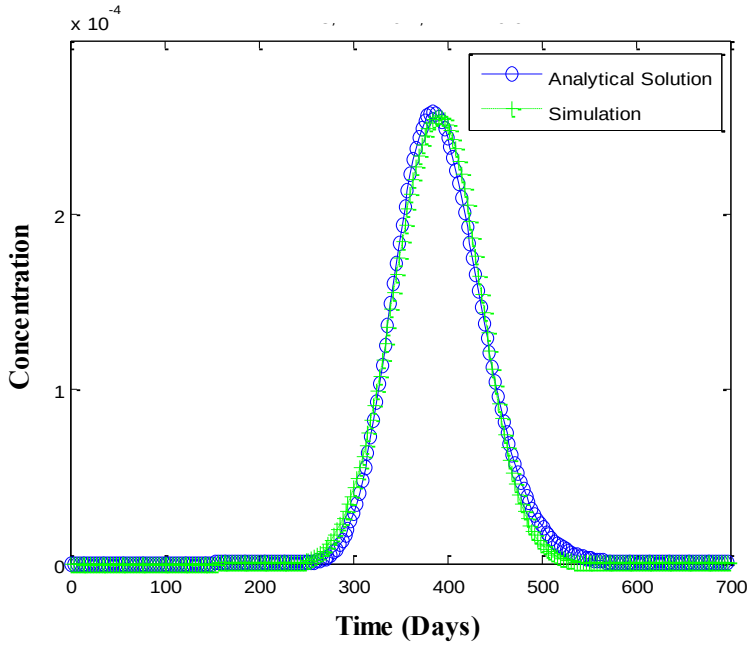

Figure 3.40: Comparison of the local solute concentration history between simulation and analytical models for $V_{DP} = 0.6$ for different dimensionless correlation lengths (a) $L_{XD} = 0.5$, $L_{YD} = 0.1$, x = 185 ft and y = 47.5 ft (b) $L_{XD} = 0.25$, $L_{YD} = 0.1$, x = 158 ft and y = 41.5 ft and (c) $L_{XD} = 5$, $L_{YD} = 0.1$, x = 225 ft and y = 23.5 ft.

a)

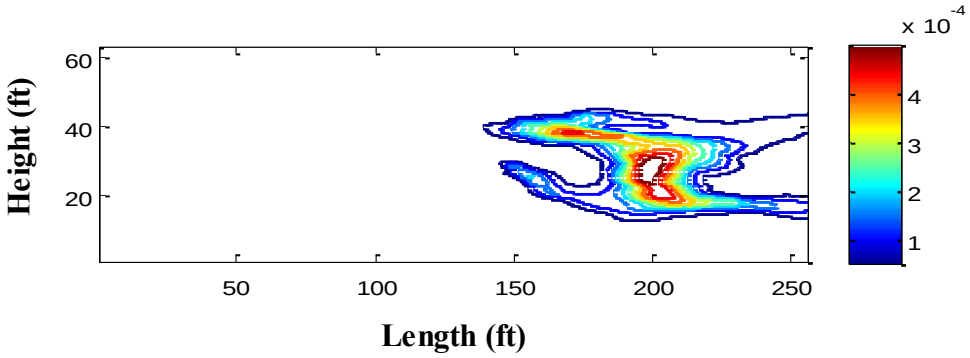
x 10^-4
Height (ft)
60
40
20
50
100
150
200
250
Length (ft)
4
3
2
1

b)

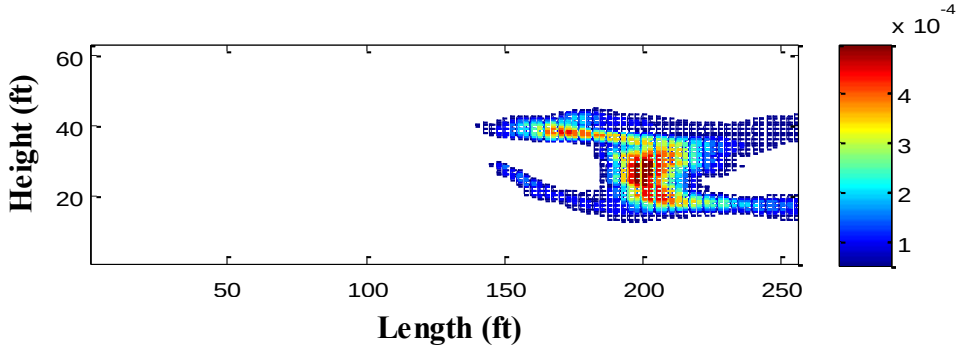
x 10^-4
Height (ft)
60
40
20
50
100
150
200
250
Length (ft)
4
3
2
1

c)

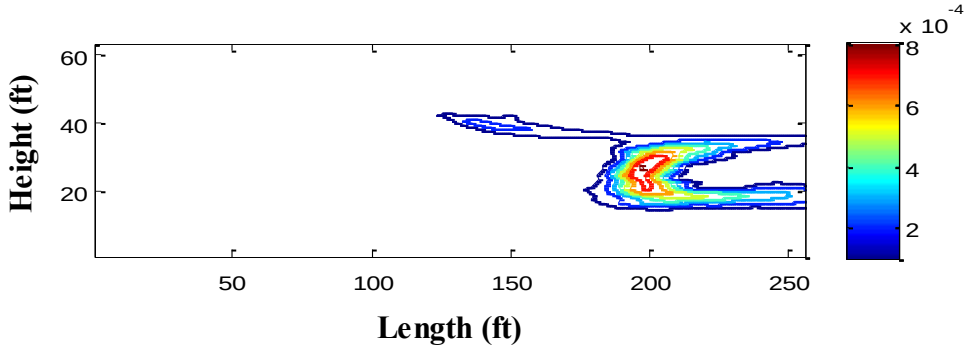
x 10^-4
Height (ft)
60
40
20
50
100
150
200
250
Length (ft)
8
6
4
2

d)

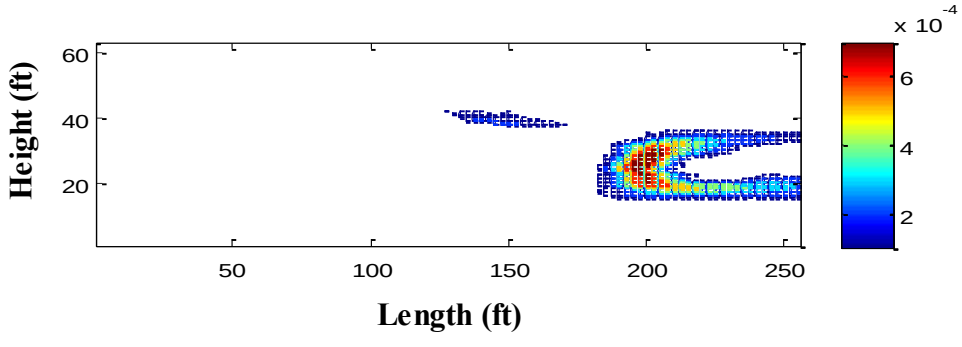
x 10^-4
Height (ft)
60
40
20
50
100
150
200
250
Length (ft)
6
4
2

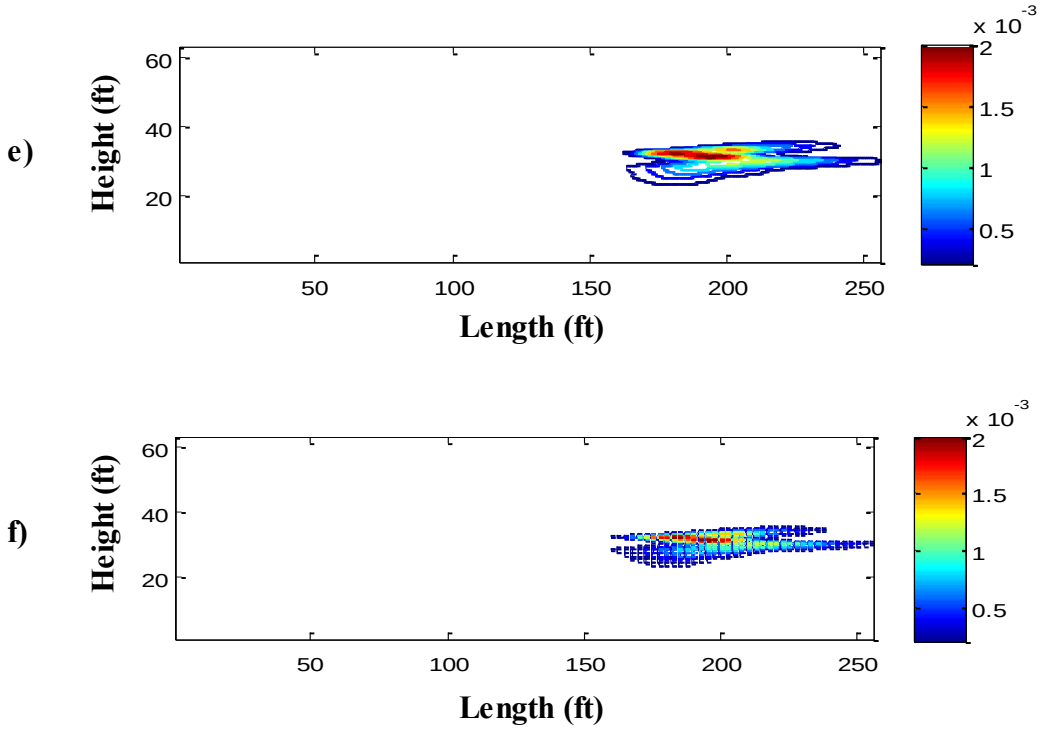

Figure 3.41: Solute concentration distributions with similar V_{DP} = 0.6, mean permeability and dimensionless correlation in the transverse direction (L_{YD} = 0.1) at 238 days with different dimensionless correlation lengths in the longitudinal direction (L_{XD}) (a) simulation model with L_{XD} = 0.25 (b) analytical model with L_{XD} = 0.25 (c) simulation model with L_{XD} = 0.5 (d) analytical model with L_{XD} = 0.5 (e) simulation model with L_{XD} = 5.0 and (f) analytical model with L_{XD} = 5.0.

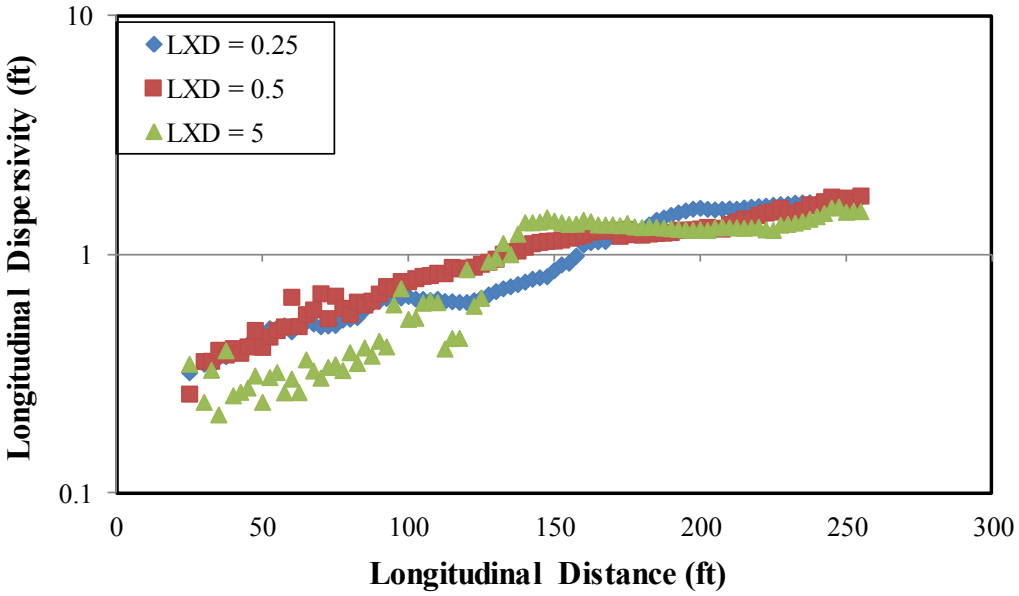

Figure 3.42: Estimated longitudinal dispersivity for different correlation lengths in the longitudinal direction at constant transverse correlation length (L_{YD} = 0.1) and V_{DP} = 0.6.

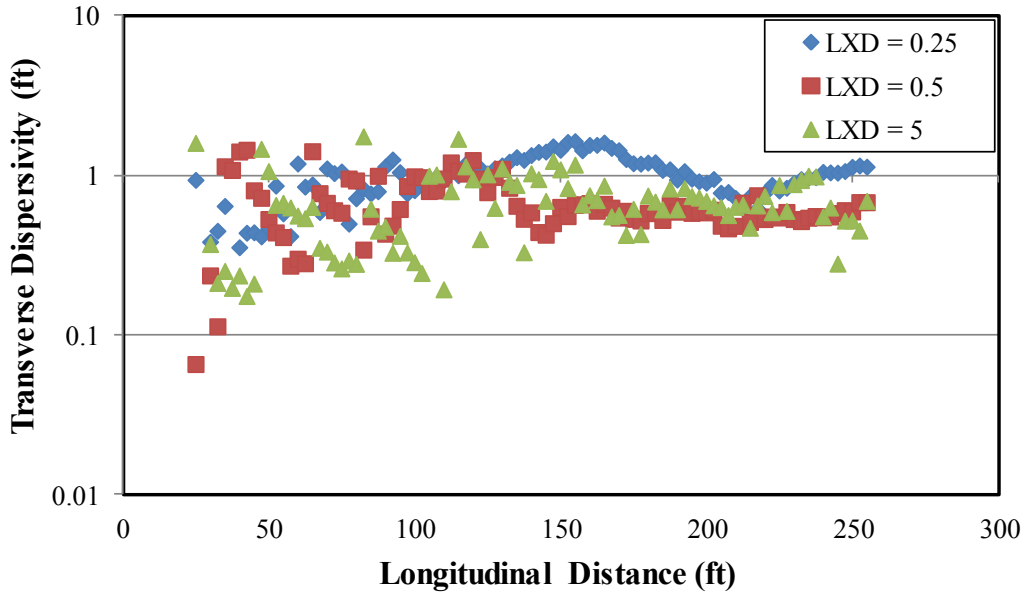

Figure 3.43: Estimated transverse dispersivity for different correlation lengths in the longitudinal direction at constant transverse correlation length (L_{YD} = 0.1) and V_{DP} = 0.6.

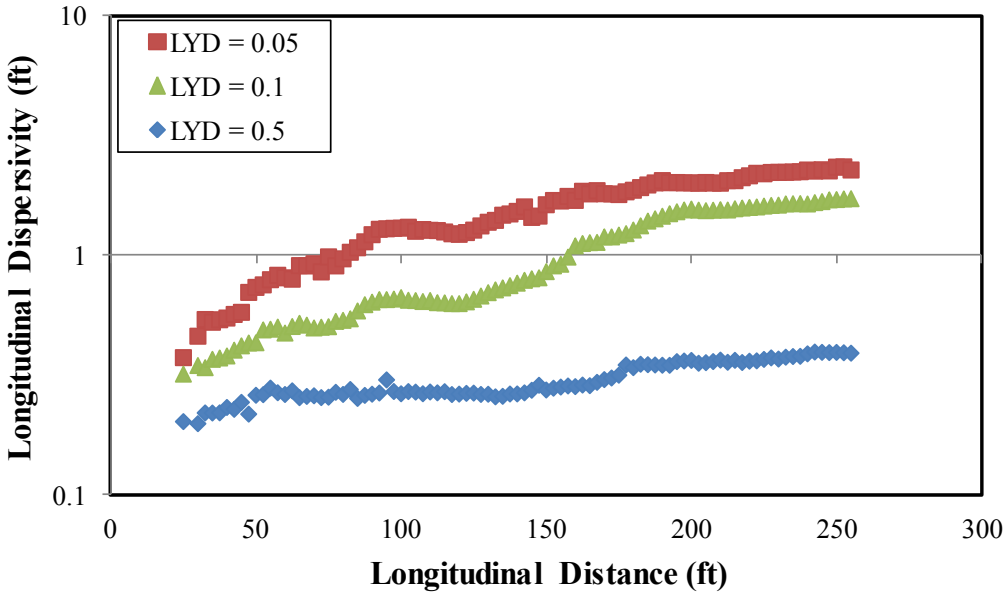

Figure 3.44: Estimated longitudinal dispersivity for different correlation lengths in the transverse direction at constant longitudinal correlation length (L_{XD} = 0.25) and V_{DP} = 0.6.

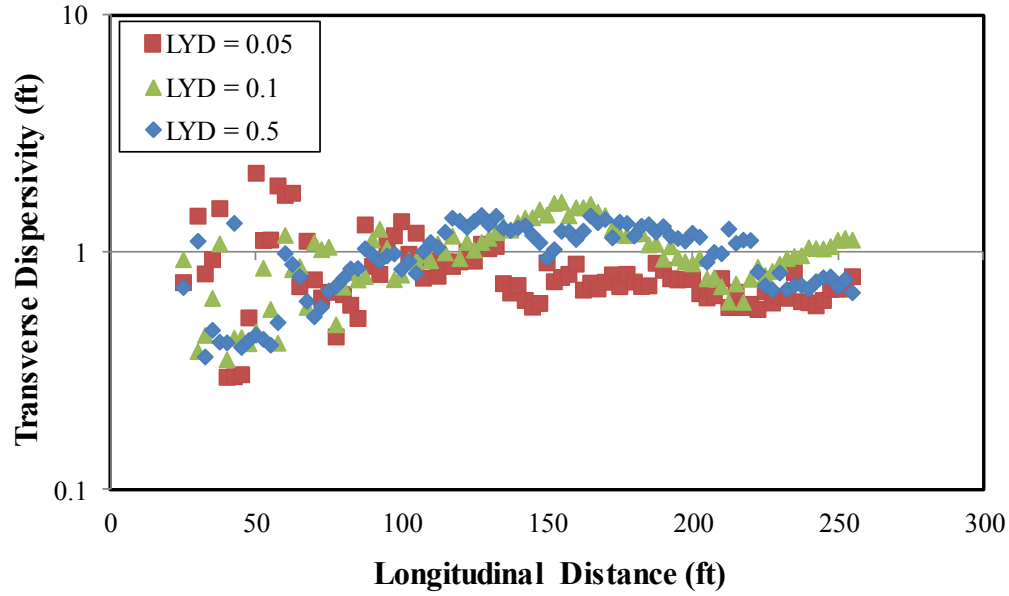

Figure 3.45: Estimated transverse dispersivity for different correlation lengths in the transverse direction at constant longitudinal correlation length (L_{XD} = 0.25) and V_{DP} = 0.6.

Chapter 4: Determination of Longitudinal and Transverse Dispersion in Large Scale Media

This chapter presents an approach to determine longitudinal and transverse dispersion in a large scale media using continuous injection of the solute while accounting for no flow lateral boundaries. The approach uses the analytical solution of the two-dimensional convection dispersion equation to simultaneously determine the longitudinal and transverse dispersivity from local (grid-block) concentration profiles. The approach builds on the experimental framework proposed by Blackwell (1962) to determine transverse dispersivity with continuous injection of the solute.

The effects of stochastic permeability distribution and cross-flow on dispersion were investigated. Dispersion was confirmed to be scale dependent and to increase with increasing heterogeneity. The effect of autocorrelation in the longitudinal direction is to increase longitudinal dispersion while minimizing transverse dispersion. Results show that increasing autocorrelation in the transverse direction minimizes both longitudinal and transverse dispersion. The resulting effect of increasing autocorrelation in the transverse direction is to minimize channeling, by stabilizing the mixing zone.

4.1 Analytical solution of Convection-Dispersion Equations

The two-dimensional CDE, assuming constant velocity and constant dispersion coefficients in longitudinal and transverse directions was expressed in equation (3.1) as,

$$\frac{\partial C}{\partial t} + v_x \frac{\partial C}{\partial x} + v_y \frac{\partial C}{\partial y} = D_L \frac{\partial^2 C}{\partial x^2} + D_T \frac{\partial^2 C}{\partial y^2} \tag{3.1}$$

where D_L and D_T are the longitudinal and transverse dispersion coefficients, respectively.

The analytical solution was derived using integral transforms for a semi-infinite length, finite height and a continuous injection of the solute subject to the following boundary and initial conditions given by Wexler (1989),

$$C,\ \frac{\partial C}{\partial y}=0, \qquad y=0, y=W \tag{4.1a}$$

where W is the height of the flow medium.

$$C,\ \frac{\partial C}{\partial x}=0, \qquad x=\infty \tag{4.1b}$$

$$C(0,y,t)=C_0 \quad at \quad Y_1<y<Y_2 \tag{4.1c}$$

where Y_1 and Y_2 are lower and upper dimension of the solute source

$$C(x,y,0)=0. \tag{4.1d}$$

The derived analytical solution for two-dimensional CDE, with the above initial and boundary constraints is expressed as,

$$C(x,y,t)=\frac{C_0}{W}\sum_{n=0}^{\infty}L_nP_n\cos(\eta y)\exp\left[\frac{v_x x}{2D_L}+\frac{v_y y}{2D_T}\right]\cdot \left\{\exp[-x\gamma]erfc\left[\frac{x-2D_L t\gamma}{2\sqrt{D_L t}}\right]+\exp[x\gamma]erfc\left[\frac{x+2D_L t\gamma}{2\sqrt{D_L t}}\right]\right\} \tag{4.2}$$

where

$$L_n=\begin{cases}\frac{1}{2} & n=0\\ 1 & n>0\end{cases}$$

$$P_n=\begin{cases}I_{y,v_y=0,n=0} & v_y=0, n=0\\ I_{y,v_y\neq 0,n=0} & v_y\neq 0, n=0\\ I_{y,n>0} & n>0\end{cases}$$

$$\gamma=\left(\eta^2\frac{D_T}{D_L}+\frac{v_x^2}{4D_L^2}+\frac{v_y^2}{4D_L D_T}\right)^{1/2}$$

$$\eta=\frac{n\pi}{W}$$

$$I_{y,v_y=0,n=0} = Y_2 - Y_1$$

$$I_{y,v_y\neq 0,n=0} = \frac{2D_T}{v_y}\left\{\exp\left[\frac{-v_y Y_1}{2D_T}\right] - \exp\left[\frac{-v_y Y_2}{2D_T}\right]\right\}$$

$$I_{y,n>0} = \frac{1}{\left(\frac{v_y}{2D_T}\right)^2 + \eta^2}\left\{\begin{array}{l}\exp\left[\frac{-v_y Y_2}{2D_T}\right]\left(\eta\sin\left(\eta Y_2\right) - \frac{v_y\cos\left(\eta Y_2\right)}{2D_T}\right) \\ -\exp\left[\frac{-v_y Y_1}{2D_T}\right]\left(\eta\sin\left(\eta Y_1\right) - \frac{v_y\cos\left(\eta Y_1\right)}{2D_T}\right)\end{array}\right\}.$$

The full derivation of equation (4.2) is detailed in Appendix B. Equation (4 .2) reduces to the solution obtained by Wexler (1989), when the velocity in the transverse direction (v_y) is zero. In most applications, the flow is dominant in the longitudinal direction (x-direction in this case) and the velocity in the transverse direction is negligible. However, if there is a gradient in the transverse direction, velocity in the y-direction may become significant. For the cases considered in this chapter, the flow is dominant in the longitudinal direction.

The infinite series in equation (4.2) converge slowly. The larger the number of terms (n) used to represent the infinite series the more accurate the solution (Wexler 1989). We used 400 summations in this research, though a minimum of a 100 summations is suggested by Wexler (1989).

The average solute velocity can be estimated from the local solute concentration profile. The average solute velocity is obtained from the ratio of the distance from the solute source and the arrival time of the center of mass of the solute at target grid block. The arrival time of the center of mass of the solute cell can be estimated from the local solute concentration profile (Figure 4.1).

4.1.1 Model validation

The analytical solution (equation (4.2)) was validated by matching the local concentration profiles of a homogenous model that has a known input dispersivity with the analytical solution. For a homogenous model, the observed dispersion is only due to input and numerical dispersivity. Fanchi (1983) derived the expression for the numerical dispersion coefficient, for an upstream weighting implicit backward difference scheme. The expressions for numerical longitudinal and transverse dispersion coefficient is expressed as,

$$D_L = \frac{1}{2} v_x \left(\Delta x + v_x \Delta t \right) \tag{4.3a}$$

$$D_T = \frac{1}{2} v_y \left(\Delta y + v_y \Delta t \right) . \tag{4.3b}$$

For homogenous model with a fully-penetrating injection well at one end of the lateral boundary and a fully-penetration producing well at the outlet of the medium, the transverse velocity (v_y) is negligible. The total longitudinal dispersivity is a sum of the input longitudinal dispersivity and numerical dispersivity, which has a magnitude of about half of the grid-block size, since the time step is small (~0.1 ft/day). The total transverse dispersivity is the input transverse dispersivity since there is no numerical transverse dispersion since the transverse velocity (v_y) is negligible for a homogenous model.

The grid-block sizes of our simulation model in x- and y-directions are both 2.0 ft. The model has 128 grid-blocks in the x-direction and 32 grid-blocks in the y-direction. The input dispersivity in the longitudinal direction is 0.5 ft, while there is no input dispersivity in the transverse direction. The total longitudinal dispersivity is about 1.5 ft (input and numerical), while transverse dispersivity is negligible. We used the analytical solution to match the simulation local concentration profiles by varying both longitudinal

and transverse dispersivities. The objective is to minimize the sum of the square of residuals between the local solute concentration from simulation and the analytical model. A good match of the local simulation profile was obtained with the analytical solution (Figure 4.2). From the analytical solution the longitudinal dispersivity was estimated to be 1.5 ft (Figure 4.3), validating the analytical solution. The injection and producing well are fully-penetrating, therefore the solute concentration equilibrates across the cross-section and transverse dispersion is negligible (Figure 4.4).

4.1.2 Transverse dispersion

Experimental determination of transverse dispersion is considered challenging because longitudinal dispersion must be minimized before transverse dispersion can be determined (Hassinger and Dale 1963). Two classical approaches to determine transverse dispersivity experimentally are the work of Perkins and Johnson (1963) and Blackwell (1962). Garmeh and Johns (2010) used mathematical approximations to estimate transverse dispersion, using estimated longitudinal dispersivity from one-dimensional CDE and the velocity anisotropy ratio (v_y/v_x).

The approach of Blackwell (1962) involves co-injection of two miscible fluids into a central core area and annulus area of the core. The experiment is such that one fluid can be injected and produced through the central core area and another fluid injected into and produced from the annulus area of the core. The goal is to ensure dominance of radial dispersion compared to axial dispersion. Transverse dispersion is estimated from the effluent concentration after steady state is reached. Steady state is reached when the concentration of the effluent stream becomes constant. The objective of this set-up is to

ensure that the transport of solute from the annulus area to the central core results primarily from transverse dispersion and not convection.

Alkindi *et al.* (2011) utilized the Blackwell approach to experimentally determine transverse dispersion in a sand-pack. They injected the first fluid into one half of the sand pack at the same rate as the other fluid, which was injected into the other half of the sand pack. The two fluids are first contact miscible. After a while a steady state mixing zone is developed and the effluent concentration at the outlet of the core becomes constant. Figure 4.5 shows a schematic of the experimental set-up used for their analysis.

At steady state it is assumed that longitudinal dispersion is negligible and transverse dispersion prevails. Therefore the CDE reduces to,

$$v_x \frac{\partial C}{\partial x} = D_T \frac{\partial^2 C}{\partial y^2}. \tag{4.4}$$

Equation (4.4) was solved using method of separation of variables subject to the following boundary conditions,

$$\frac{\partial C}{\partial y} = 0 \qquad y = 0, w \tag{4.5a}$$

$$C = 1 \qquad 0 \le y \le w_1,\ x = 0 \tag{4.5b}$$

$$C = 0 \qquad w_1 \le y \le w,\ x = 0 \tag{4.5c}$$

where w_1 is the width of the solute injector and w is the width of the model. Alkindi *et al.* (2011) gave the solution to equation (4.4) subject to the above boundary conditions as,

$$C(x,y) = \frac{w_1}{w} + \frac{2}{\pi}\left[\sum_{n=1}^{\infty}\frac{1}{n}\cos\left(\frac{n\pi y}{w}\right)\sin\left(\frac{n\pi w_1}{w}\right)\exp\left(-D_T\frac{n^2\pi^2 x}{w^2 v_x}\right)\right]. \tag{4.6}$$

Equation (4.6) can be used to generate a relationship between stabilized concentrations at steady-state for various levels of transverse dispersion. Transverse dispersivity is the proportionality constant between the transverse dispersion coefficient and velocity. Figure 4.6 shows a relationship between fractional concentration and

transverse dispersivity based on equation (4.6) for a sample problem (where $w_1 = 32$, $w = 64$, $v_x = 0.46$ ft/day and $n = 500$). Figure 4.6 can be used to determine the level of transverse dispersion based on the steady state fractional concentration at given points in the medium. Figure 4.6 also shows that the transverse dispersivity becomes invariant to fractional concentration at the mid-point of the model (in this case NY = 32), where the fractional concentration is 0.5.

FCM simulations were conducted using a model similar to Alkindi *et al.* (2011). The two fluids (oil and solute) used in the simulations are first contact miscible and of equal viscosity and density. The model was initially saturated with oil. There are two injection wells and two production wells at the lateral boundary of the model. The first injection and production wells penetrated the first half of the model, while the second wells penetrated the lower half. The solute is injected in the first half of the model, while the other miscible fluid (oil) is injected at the lower half of the model. The injection continues until a steady mixing zone develops. When a steady mixing zone is attained, the local and effluent concentration becomes constant.

The set-up is validated by considering a homogenous model with 128 grid-blocks in x-direction and 64 grid-blocks in the y-direction. The grid-block size in both directions is 1.0 ft. The specified input longitudinal and transverse dispersivity are 1.0 ft and 0.5 ft respectively. Figure 4.7 shows the solute concentration distribution in the simulation model after a steady mixing-zone is attained.

The stabilized mixing zone is increasing from the inlet of the model to the outlet of the model indicating that transverse dispersion develops along the length of the medium and is not instantaneously asymptotic. This development is due to the fact that transverse dispersion has to develop in the presence of convection in the dominant flow

direction and longitudinal dispersion. Therefore transverse dispersion requires some time to fully develop. This observation is similar to experimental observation (Figure 4.5).

The dominant flow direction in the simulation model is the x-direction and there is negligible velocity in the transverse direction. Therefore the movement of the solute from the top layer to bottom layer is due entirely to transverse dispersion. However, since there is flow in the longitudinal direction the solute is also mixing in the longitudinal direction. This is the limitation of the Alkindi *et al.* (2011) solutions, since it focuses only on transverse dispersion. The effect of both longitudinal and transverse dispersion can be quantified by using equation (4.2) to describe the local solute concentration profile.

The local concentration profile is fitted to the analytical solution (equation (4.2)) by adjusting the longitudinal and transverse dispersivity and minimizing the sum of the square of the residuals of the concentration between the simulation and the analytical solution. The average solute velocity can be determined from the mid-point of the local concentration profile (Figure 4.1). For the homogenous model, the longitudinal velocity is constant. A good fit was obtained between the analytical solution and the local concentration profiles as shown in Figure 4.8. The average sum of the square of the residuals for all the sampled points is 0.02, showing a good fit between the analytical solution and the simulation concentrations.

The dispersivities from the analytical solution are comparable to the expected total longitudinal dispersivity of 1.5 ft and a transverse dispersivity of 0.5 ft (Figure 4.9). The cross-section average of estimated dispersivity was conducted between layers where transverse dispersion is dominant (layers 15 to 35). Transverse dispersion is significant where the local (grid-block) steady maximum concentration is less than 0.9 and greater than 0.1. The transverse dispersivity develops along the longitudinal direction as the

mixing zone develops. This observation is shown in the estimated transverse dispersivity as it rises from zero to 0.5 ft (Figure 4.9).

A second simulation case was conducted to validate that the analytical solution (equation (4.2)) can predict the total dispersivity in a porous medium. We consider a homogenous medium with 1.0 ft grid-block size in both x- and y-directions and an input longitudinal and transverse dispersivity of 1.0 ft and 1.5ft respectively. Therefore the total longitudinal dispersivity in the model is 1.5 ft., while the total transverse dispersivity is also 1.5 ft, since the transverse velocity is zero. Figure 4.10 shows that the increase in the input transverse dispersivity results in a more pronounced mixing zone at steady-state.

The analytical solution was used to match the local (grid-block) solute concentration profile. Good matches were obtained as shown in Figure 4.11. The estimated dispersivities from the analytical solution are comparable to the total longitudinal dispersivity of 1.5 ft and total transverse dispersivity of 1.5 ft. The average dispersivities were averaged across the entire cross-section, since the mixing zone extends across the model. The average estimated transverse dispersivity is comparable to the total transverse dispersivity in the simulation model (Figure 4.12).

To verify that the spreading of the solute from the top layer to the bottom layer is due entirely to dispersion and not convection, we conducted simulations using the same set-up in a homogenous model with no input dispersivity. Since there is no transverse dispersion, no solute should cross to the lower layer of the model. Figure 4.13 shows that indeed no solute crosses over to the lower layer of the homogenous model when there was no input dispersivity, confirming that the spread of the solute to the lower part of the model requires transverse dispersion. The estimated longitudinal dispersivity is

comparable to the numerical longitudinal dispersivity of 0.5 ft, based on the grid-block size of 1.0 ft (Figure 4.14). The estimated transverse dispersivity is negligible.

4.2 EFFECT OF HETEROGENEITY ON DISPERSION

The local velocity variation caused by spatially varying permeability distribution, results in increased mixing (Jha *et al.* 2006, Adepoju *et al.* 2013). Yang (1990) also showed that the presence of heterogeneity can increase the order of the truncation error in finite difference schemes. The effect of heterogeneity on longitudinal and transverse dispersivity is studied in this section.

FFTSIM (Jennings *et al.* 2000) was used to generate stochastic permeability fields. Autocorrelation lengths (in both x- and y-directions), Dykstra-Parsons coefficient (V_{DP}) and the mean permeability are inputs into FFTSIM. Two levels of heterogeneity were considered (V_{DP} = 0.6 and V_{DP} = 0.9), with uncorrelated permeability distribution. Increasing V_{DP} indicate greater level of heterogeneity. No input dispersivity was included in the simulation for the heterogeneous model. The simulation model has 128 grid-blocks in the longitudinal (x-direction) and 32 grid-blocks in the transverse direction (y-direction). The model is initially saturated with oil and a first contact miscible solute of equal density and viscosity is continuously injected into the top half of the model. The oil is also continuously injected into the lower part of the model. The grid-blocks sizes are 1 ft in both directions.

The analytical solution was fitted to the local concentration profile by adjusting the longitudinal and transverse dispersivity. A good match was obtained between the analytical solution and local simulation concentration profiles for all cases considered

(Figure 4.15). The average sum of the square of residuals for all sampled points in the three realizations of $V_{DP} = 0.6$ is 0.034, while that for $V_{DP} = 0.9$ is 0.049.

The steady state mixing zone for the two levels of heterogeneity is shown in Figure 4.16. The local and spatial velocity variations causes the solute to mix and spread in both longitudinal and transverse directions. As shown in Figure 4.16, the size of the steady state mixing zone increases with increasing level of heterogeneity. An increase in the size of the stabilized mixing zone indicates a higher level of transverse dispersion.

Three different realizations of each level of heterogeneity were generated and compared. Each realization has different flow structures as shown in chapter 3 and thus different levels of dispersion. The effect of the difference in the flow structure in each realization can be visualized in the nature of the developed steady state mixing zone in each realization (Figures 4.17 and 4.18).

Estimated dispersivity for all the different realizations and different levels of heterogeneity shows that dispersivity is scale dependent and increase with increasing distance (Figures 4.19 and 4.20). Figures 4.19 and 4.20 also show that dispersion increases with increasing level of heterogeneity. Dispersion also develops differently for each permeability realization for the same level of heterogeneity. The difference in dispersion for different realizations is more pronounced with greater level of heterogeneity ($V_{DP} = 0.9$ compared $V_{DP} = 0.6$).

4.2.1 Effect of Autocorrelation Lengths on Dispersion

Permeability distributions are typically spatially correlated because of the nature of geological deposition. Autocorrelation is a means of quantifying the extent of spatial correlation in the permeability field. Autocorrelation lengths in the transverse direction

are typically smaller than the autocorrelation lengths in the longitudinal direction. Correlation lengths in both directions are a measure of autocorrelation. Dimensionless correlation lengths (L_{XD} and L_{YD}) indicate the range in which the permeability distribution is spatially correlated with respect to the distance in the direction. A dimensionless correlation length greater than 1, indicate a more layered medium.

The effect of autocorrelation lengths on dispersion was investigated by varying the dimensionless correlations in the longitudinal direction (L_{XD} = 0.25; L_{XD} = 0.5 and L_{XD} = 5) while the dimensionless autocorrelation in the transverse direction is uncorrelated (L_{YD} = 0). The simulation model was set-up to estimate both longitudinal and transverse dispersivity and there was no input dispersivity in the models. The analytical solution was fitted to the local solute concentration profile to estimate the longitudinal and transverse dispersivity simultaneously. Good matches were obtained for the simulation models using the analytical solution (Figure 4.21).

The results show that increasing correlation in the longitudinal direction increases longitudinal dispersion as the solute travels along continuous layers. Transverse dispersion reduces with increasing correlation in the longitudinal direction due to solute channeling through continuous layers with lesser proclivity to disperse across layers causing early breakthrough of the solute (Figures 4.22 and 4.23). While Figure 4.22 shows increased longitudinal dispersion and spreading as the solute travels through the medium, Figure 4.23 shows a reduction in transverse dispersion as a result of increased correlation in the longitudinal direction.

The estimated longitudinal dispersivity can be seen to increase with increasing correlation in the longitudinal direction (Figure 4.24), while transverse dispersion decreases (Figure 4.25). The practical implication of this, for example, in miscible

displacements is that solute may be channeling through high permeability streaks with little spreading transversely.

The effect of autocorrelation in the transverse direction was also investigated with various levels of autocorrelation the transverse direction (L_{YD} = 0.0, L_{YD} = 0.2, L_{YD} = 0.5). The model is uncorrelated in the longitudinal direction (L_{XD} = 0.0). The increase in transverse autocorrelation results in continuous permeability sections in the transverse direction. The solute quickly equilibrates over these sections, minimizing channeling through the medium (Figure 4.26). As the solute equilibrates over the transverse section, both longitudinal and transverse dispersion are minimized. Figure 4.27 shows that transverse dispersion is also minimized (reduced width of the mixing zone) with increasing autocorrelation in the transverse direction. The estimated longitudinal and transverse dispersivity confirms that as the autocorrelation in the transverse direction increases, both longitudinal and transverse dispersion reduces (Figures 4.28 and 4.29).

The advantage of a thick continuous transverse section in large-scale miscible application is that the mixing zone gets quickly equilibrated over the section, resulting in a mixing front that is more stable and less susceptible to channeling.

We obtained similar results when the autocorrelation is varied in one direction and there is a prevailing autocorrelation in the other direction. Figure 4.30 shows that with increasing autocorrelation in the longitudinal direction, longitudinal dispersion increases while transverse dispersion decreases, with prevailing autocorrelation in the transverse direction. Figure 4.31 shows increasing autocorrelation in the transverse direction reduces both longitudinal and transverse dispersion, with prevailing autocorrelation in the longitudinal direction.

4.2.2 Effect of Cross-flow on Dispersion

The effect of cross-flow between layers on dispersion is investigated with different levels of permeability anisotropy ratio (kv/kh). No cross-flow is modeled with a kv/kh of zero and the level of cross-flow between layers increases with increasing kv/kh ratio. The analytical solution was fitted to the local solute concentration profile to estimate the longitudinal and transverse dispersivity simultaneously. Good matches were obtained for the simulation models by the analytical solution (Figure 4.32). The average sum of the square of residuals from the matches for kv/kh equals 0.0, 0.01, 0.5 and 1.0 are 0.0035, 0.086, 0.096 and 0.071 respectively.

Results show that there is minimal longitudinal dispersion when there is no cross-flow, even though the V_{DP} of the model is 0.9 (Figure 4.33a). The effect of no cross-flow is that solute only travels in a single layer, where the concentration quickly equilibrates resulting in negligible transverse dispersion and minimized longitudinal dispersion. As the cross-flow increases, longitudinal and transverse dispersion increases as solute can spread across layers and increase their contact area with resident fluid (Figure 4.33). Figure 4.33 also shows that a small level of cross-flow (kv/kh = 0.01) can result in significant longitudinal mixing when compared to no cross-flow (kv/kh = 0.0).

The stabilized mixing zone for the different cross-flow cases shows that there is negligible transverse dispersion when there is no cross flow (Figure 4.34). Transverse dispersion increases with increasing cross-flow. Estimated dispersivities from the analytical solution confirm that increasing cross-flow increase both longitudinal and transverse dispersion (Figures 4.35 and 4.36).

4.3 CONCLUSIONS

This chapter presented an approach to determine longitudinal and transverse dispersion in large scale media. We used the analytical solution of the two-dimensional CDE to simultaneously determine longitudinal and transverse dispersivity from local concentration profile in finite-difference compositional simulators. The method was validated by estimating comparable dispersivities with simulation models of known dispersivities.

Sensitivity analysis of stochastic permeability distributions confirm that dispersion increases with heterogeneity and is scale dependent. Results also show that the effect of increasing autocorrelation in the longitudinal direction is to increase longitudinal dispersion as solute travels through more continuous layers, while reducing transverse dispersion. The effect of increasing autocorrelation in the transverse direction is to reduce dispersion in both longitudinal and transverse directions. This reduction is due to solute concentration equilibrating in continuous sections resulting in a more stable mixing zone and reduced solute channeling. Cross-flow was also shown to significantly affect dispersion. As cross-flow increases, dispersion increases.

The next chapter introduces how the estimated longitudinal and transverse dispersivities can be used to determine the level of coarsening during upscaling for miscible displacement. A formalism to determine the maximum grid-block size that will maintain equivalent dispersion between fine scale models and the corresponding upscaled model will be explored.

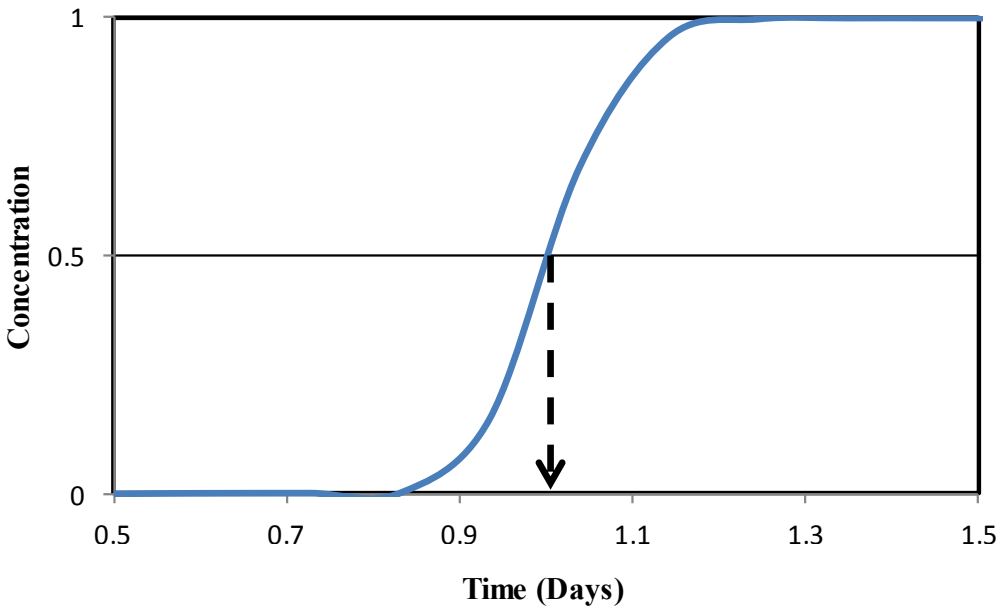

Figure 4.1: Estimation of the average arrival time of the center of mass of the solute at the target grid block. The dashed arrow points at the average arrival time.

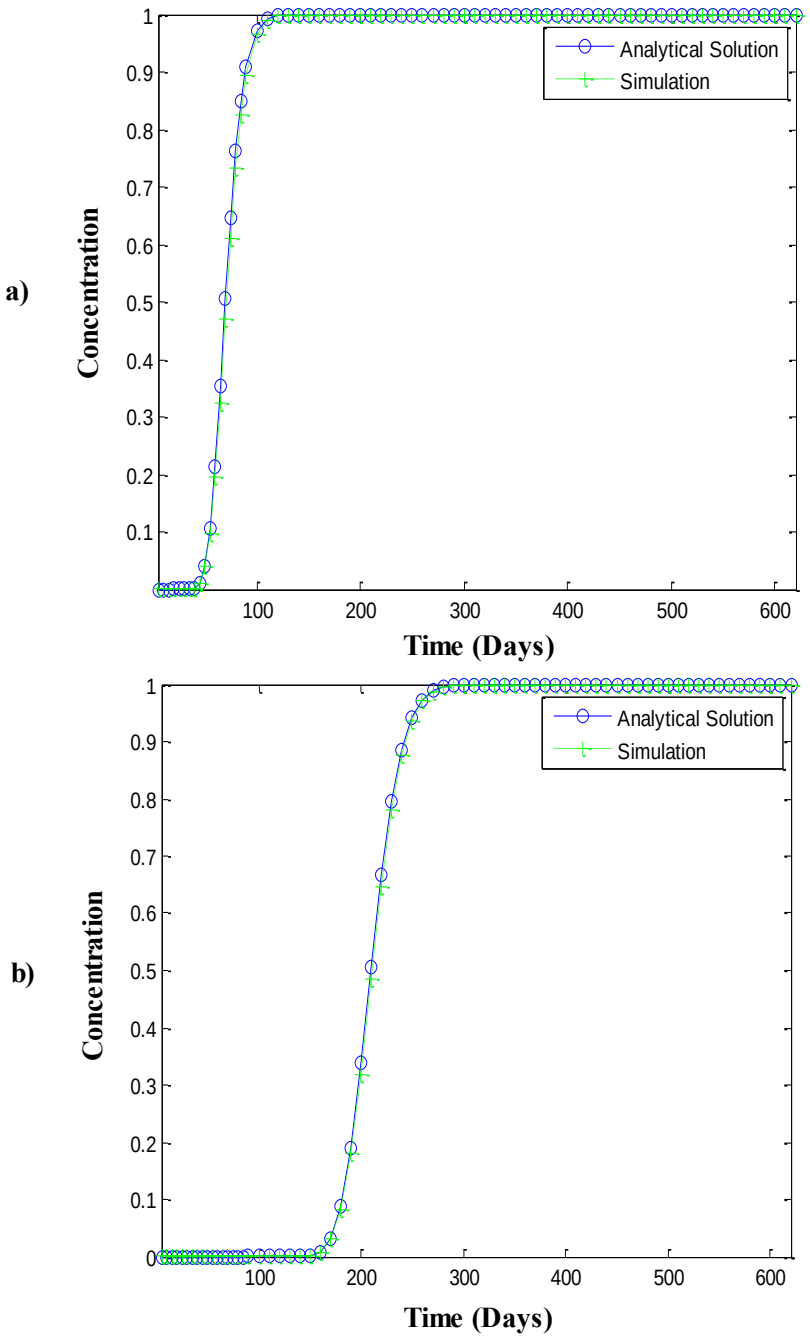

Figure 4.2: A match of the analytical solution to the local concentration history from simulation model at different points (a) x = 81 ft, y = 41 ft and (b) x = 241 ft, y = 41 ft.

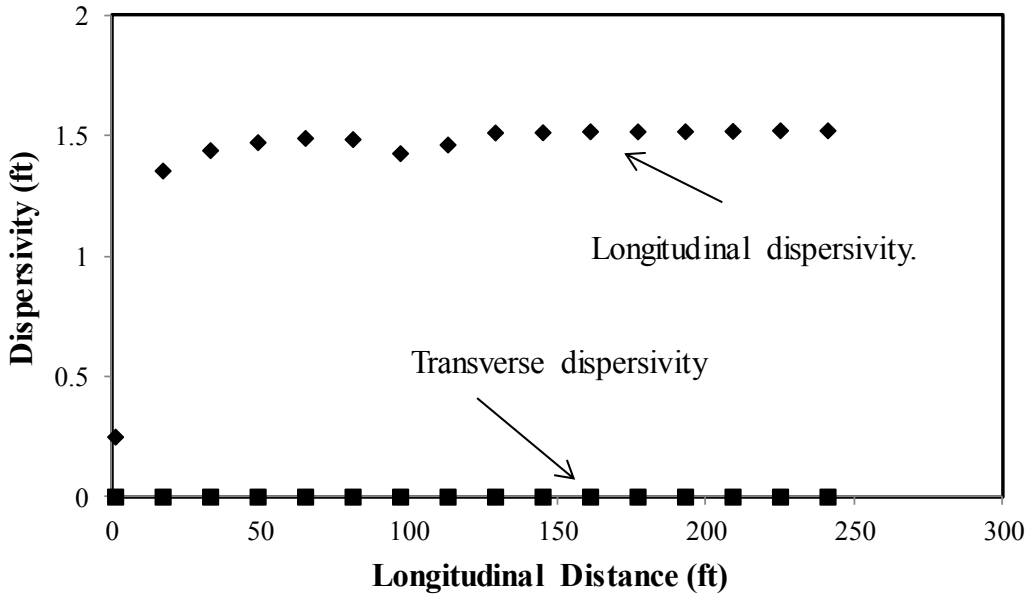

Figure 4.3: Estimated longitudinal and transverse dispersivity for a homogenous model with grid block size of 2.0 ft and input longitudinal dispersivity of 0.5 ft.

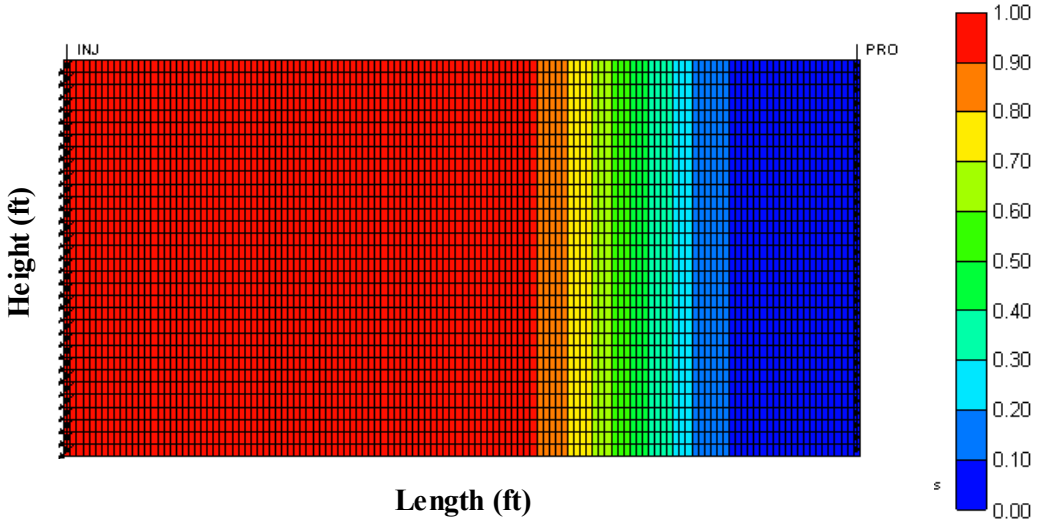

Figure 4.4: Simulation solute concentration distribution showing equilibrated concentration across model cross-section.

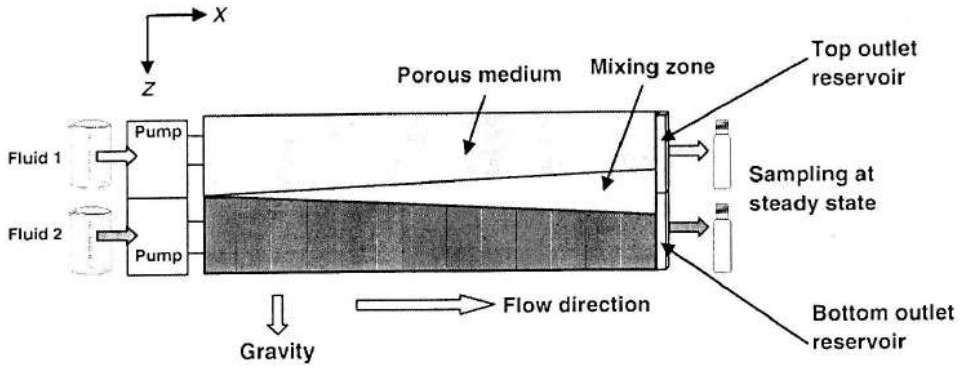

Figure 4.5: Schematic of the experimental setup to determine transverse dispersion (from Alkindi *et al.* (2011)).

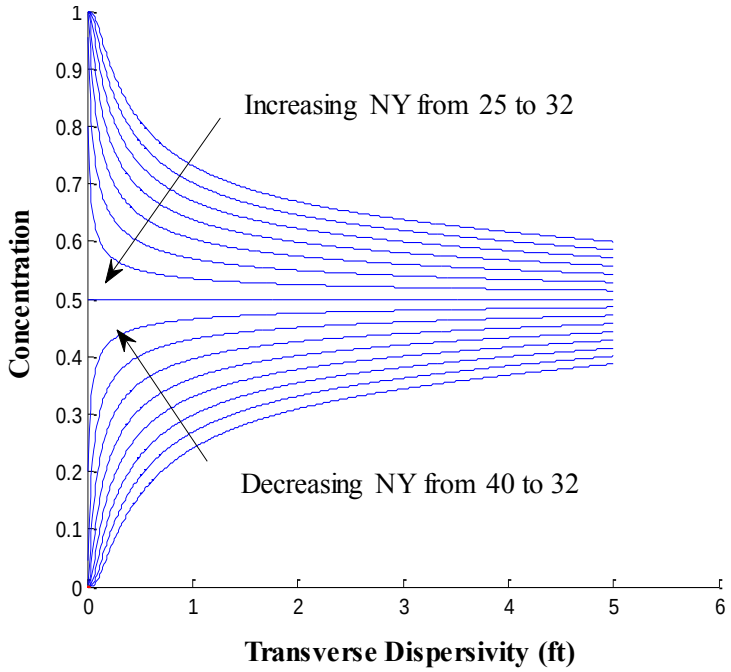

Figure 4.6: Concentration versus transverse dispersivity generated from equation (4.6) for a particular point in x-direction (NX = 64) and various points along the y-direction (NY = 25:40).

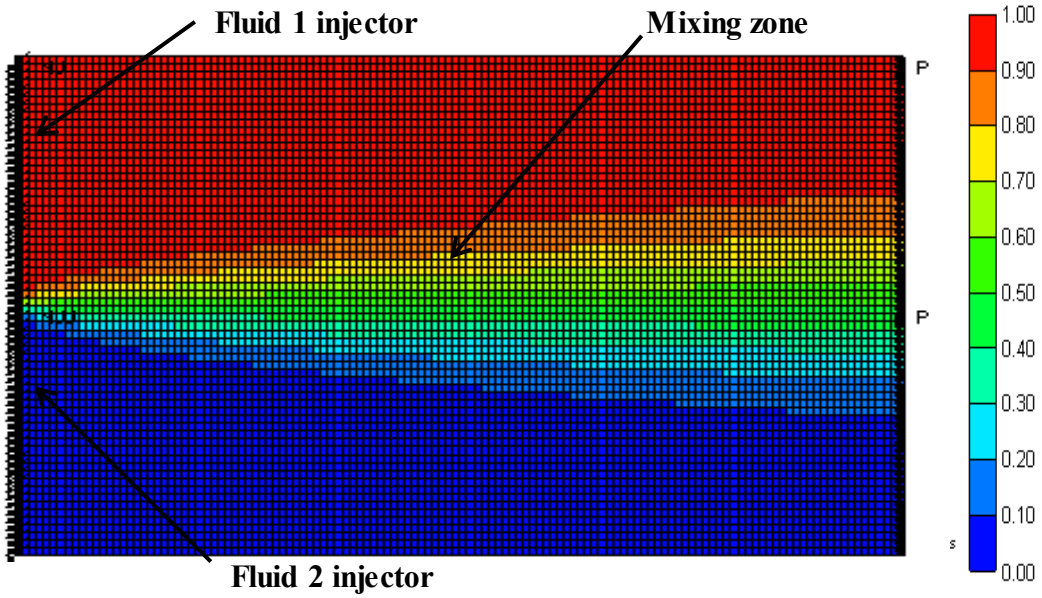

Figure 4.7: Solute concentration map showing fluid 1 injector and the fluid 2 injector and the prevailing mixing zone at steady state for a homogenous model with input longitudinal (1.0 ft) and transverse dispersivity (0.5 ft).

a)

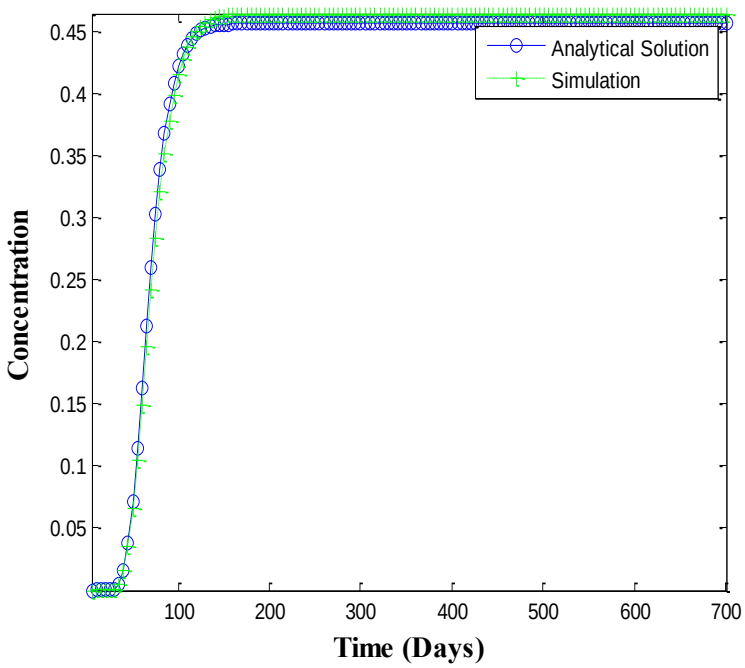

b)

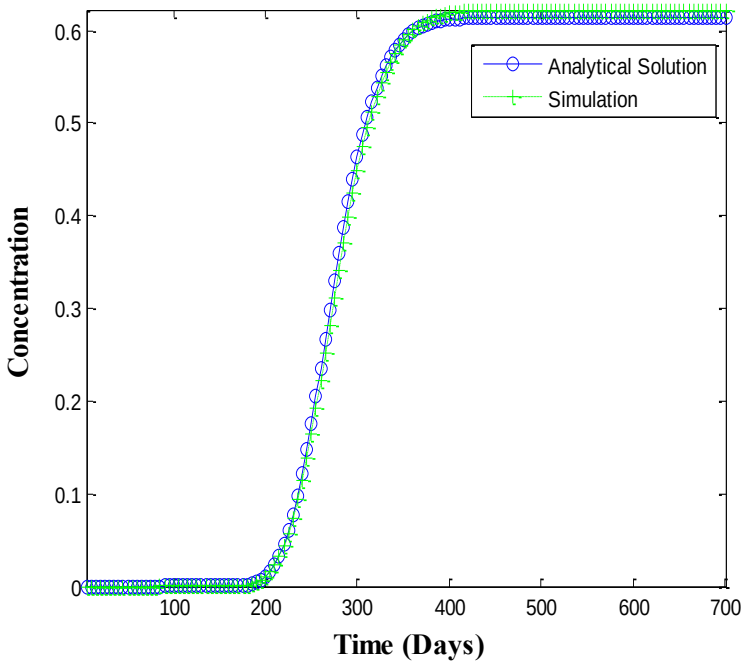

Figure 4.8: Local concentration histories at different points showing a good comparison between the analytical solution and simulation results for homogenous model with input longitudinal and transverse dispersivities of 1.0 ft and 0.5 ft respectively (a) x = 31.5 ft, y = 32.5 ft and (b) x = 127.5 ft, y = 28.5 ft. The average sum of the square of the residuals for all the sampled points is 0.02.

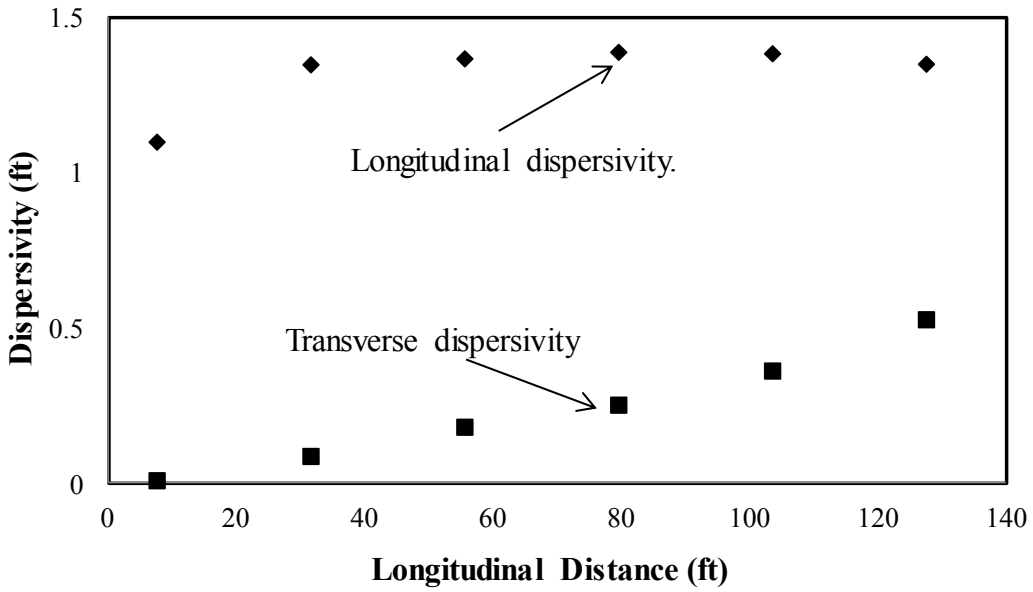

Figure 4.9: Estimated longitudinal and transverse dispersivity for a homogenous model with input longitudinal dispersivity of 1.0 ft and input transverse dispersivity of 0.5 ft.

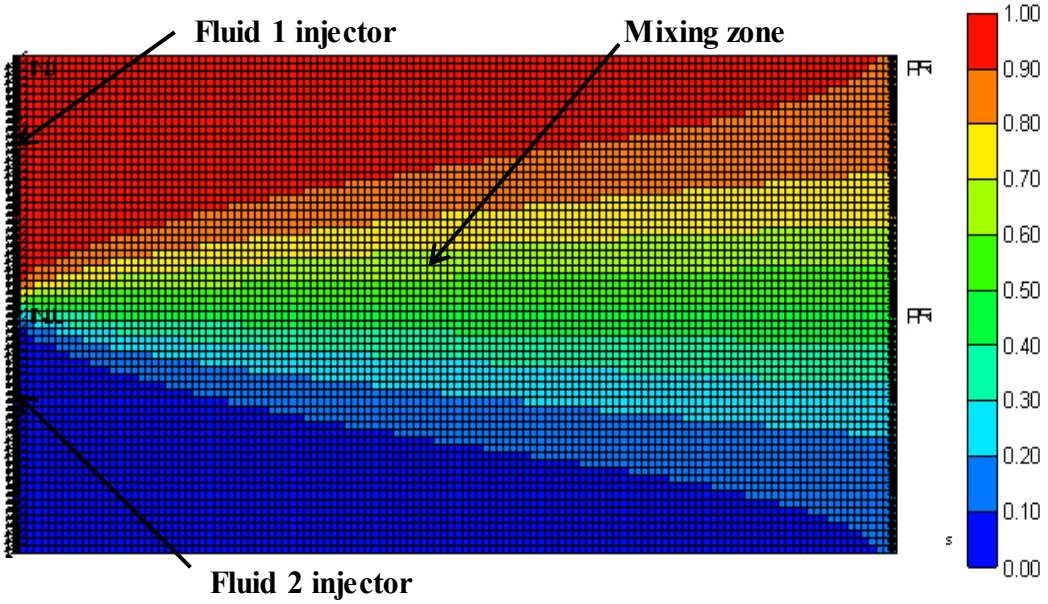

Figure 4.10: Solute concentration map showing fluid 1 injector and fluid 2 injector and the prevailing mixing zone for a homogenous model with input longitudinal (1.0 ft) and transverse dispersivity (1.5 ft).

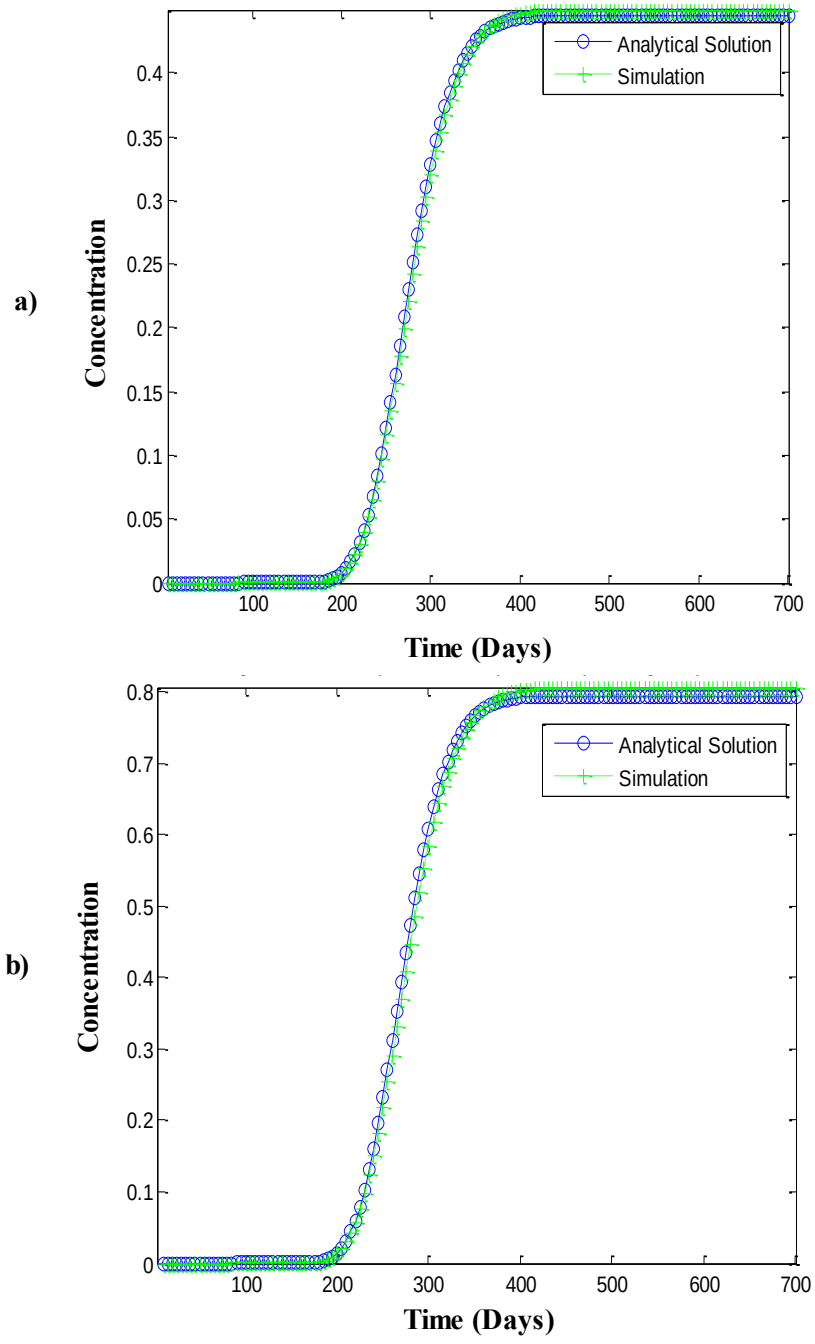

Figure 4.11: Local concentration profiles at different points in the model showing a good fit between the analytical solution and simulation results for homogenous model with input longitudinal and transverse dispersivities of 1.0 ft and 1.5 ft respectively (a) x = 127.5 ft, y = 34.5 ft and (b) x = 127.5 ft, y = 14.5 ft. The average sum of the square of the residuals for all the sampled points is 0.019.

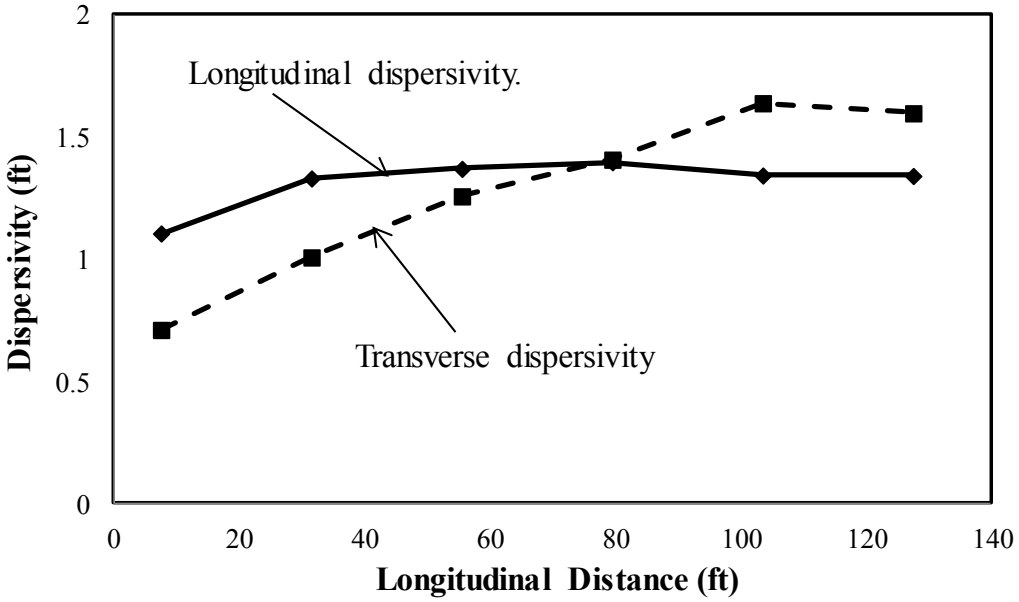

Figure 4.12: Estimated longitudinal and transverse dispersivity for a homogenous model with total longitudinal dispersivity of 1.5 ft and input transverse dispersivity of 1.5 ft.

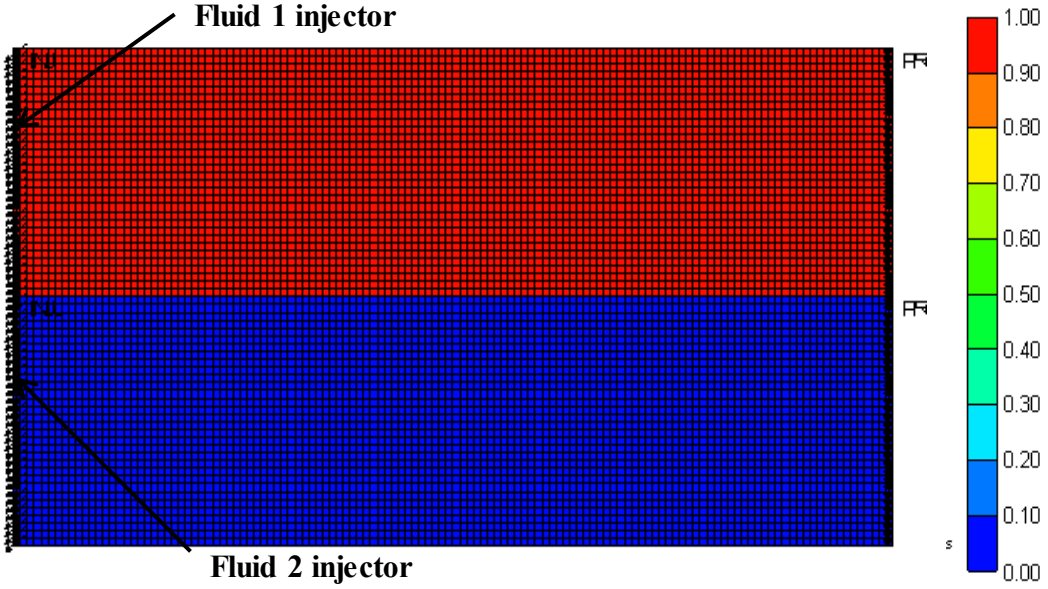

Figure 4.13: Solute concentration map showing fluid 1 and fluid 2 injectors and no mixing zone for a homogenous model with zero input longitudinal and transverse dispersivity.

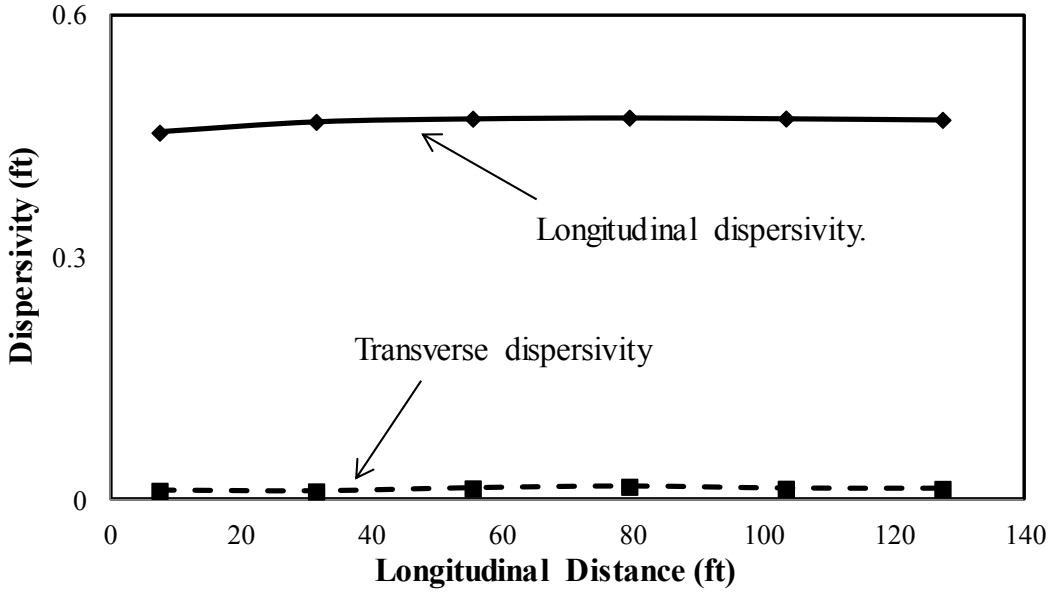

Figure 4.14: Estimated longitudinal and transverse dispersivity for a homogenous model with no input longitudinal and transverse dispersivity in the simulation model.

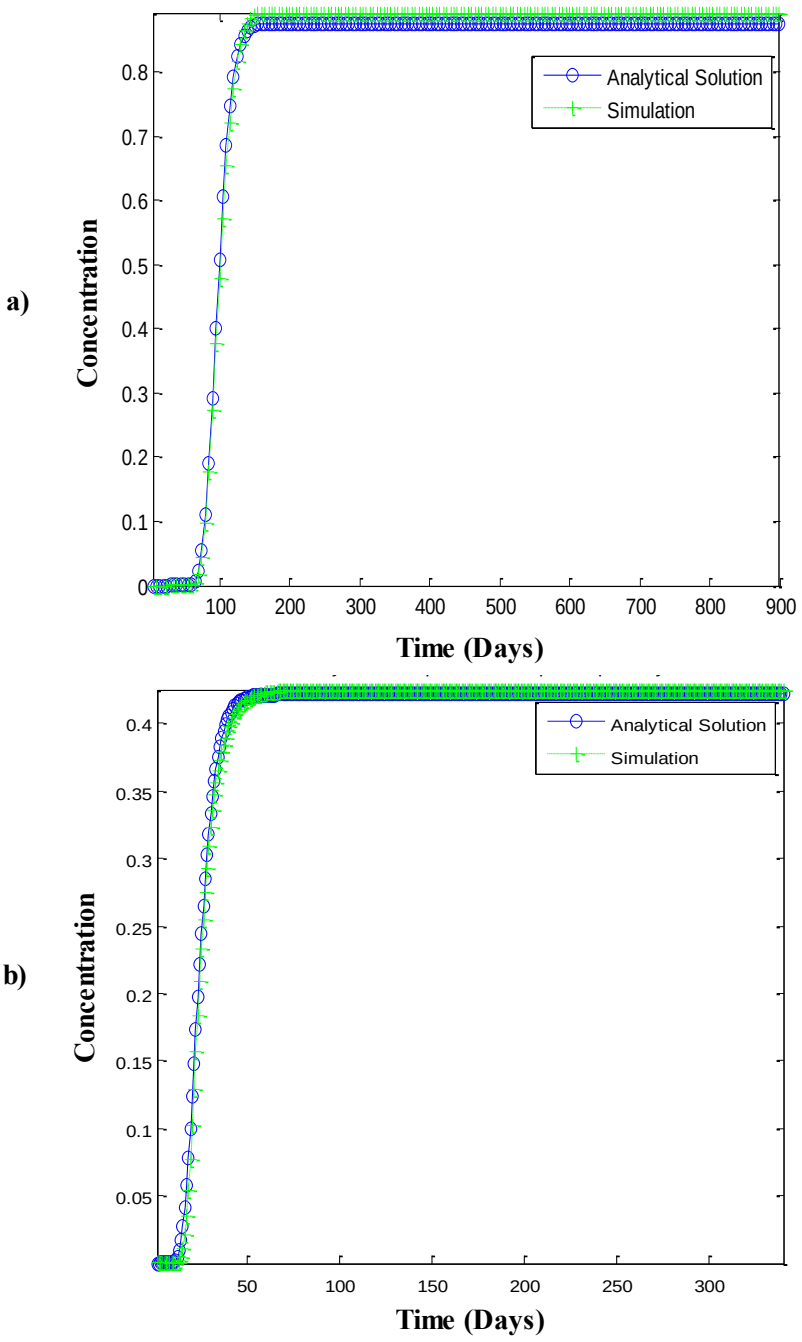

Figure 4.15: A match of the analytical solution to local simulation concentration history for uncorrelated medium for (a) VDP = 0.6 at x = 79.5 ft, y = 10.5 ft and (b) VDP = 0.9 at x = 127.5 ft, y = 20.5 ft.

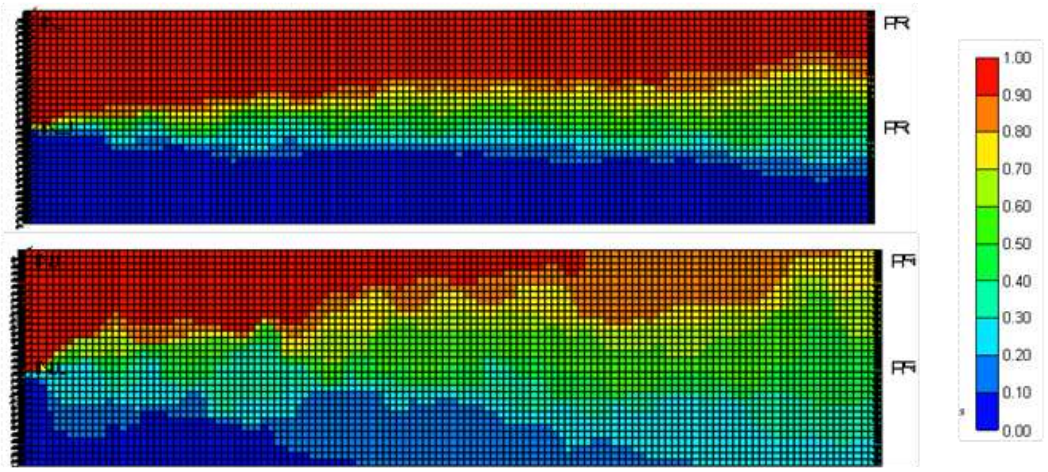

Figure 4.16: Solute concentration map at steady state showing the developed mixing zone for an uncorrelated medium at different levels of heterogeneity (top: V_{DP} = 0.6 and bottom: V_{DP} = 0.9).

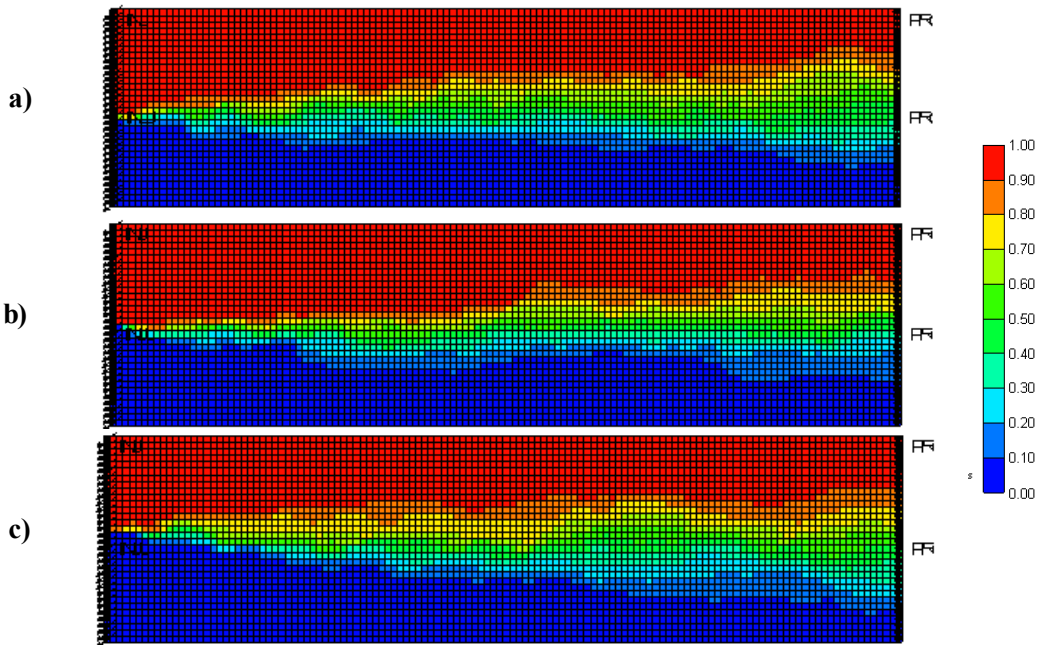

Figure 4.17: Solute concentration showing developed mixing zone at steady state for three different realizations for an uncorrelated medium with V_{DP} = 0.6 (a) realization 1, (b) realization 2 and (c) realization 3.

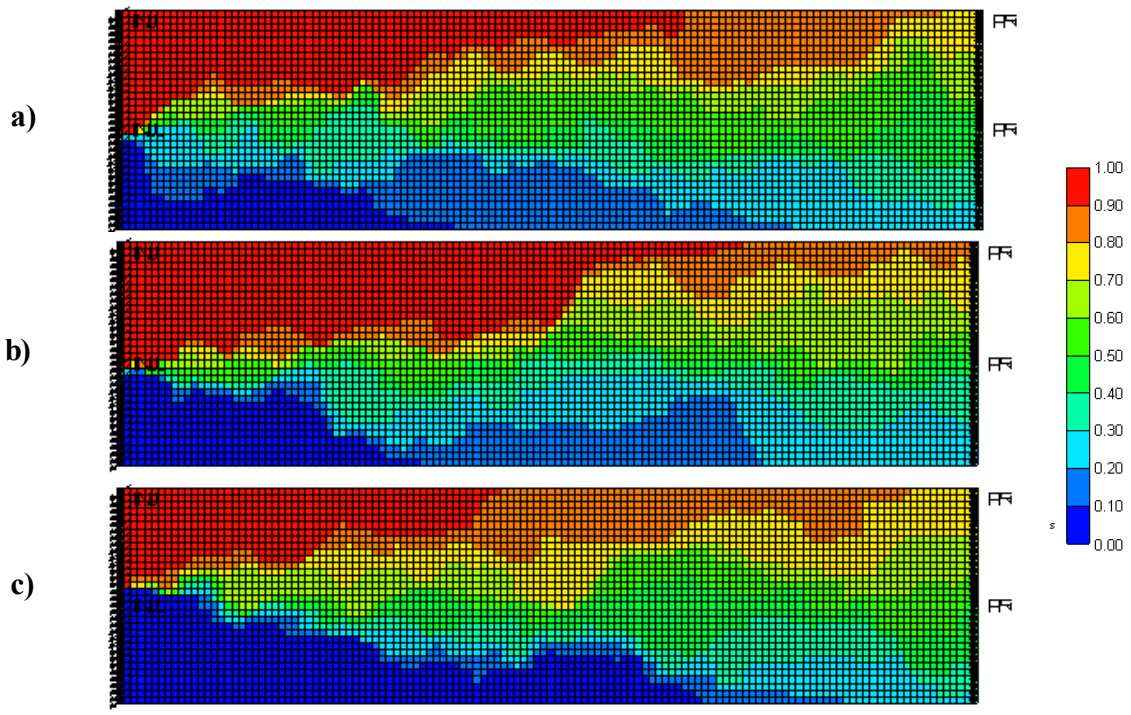

Figure 4.18: Solute concentration showing developed mixing zone at steady state for three different realizations for an uncorrelated medium with $V_{DP} = 0.9$ (a) realization 1, (b) realization 2 and (c) realization 3.

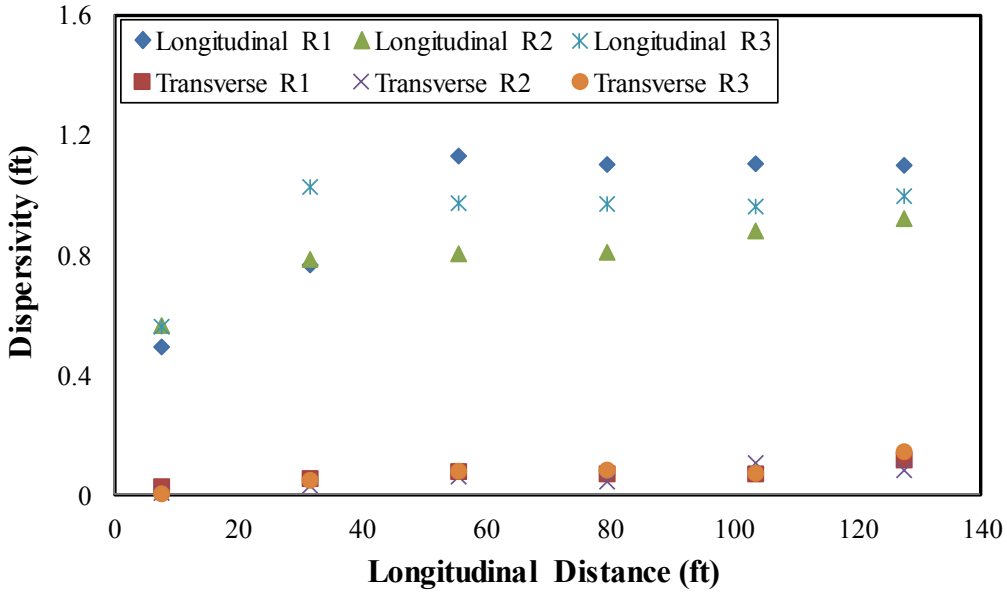

Figure 4.19: Estimated longitudinal and transverse dispersivity for three realizations (R1, R2 and R3) for an uncorrelated medium with $V_{DP} = 0.6$.

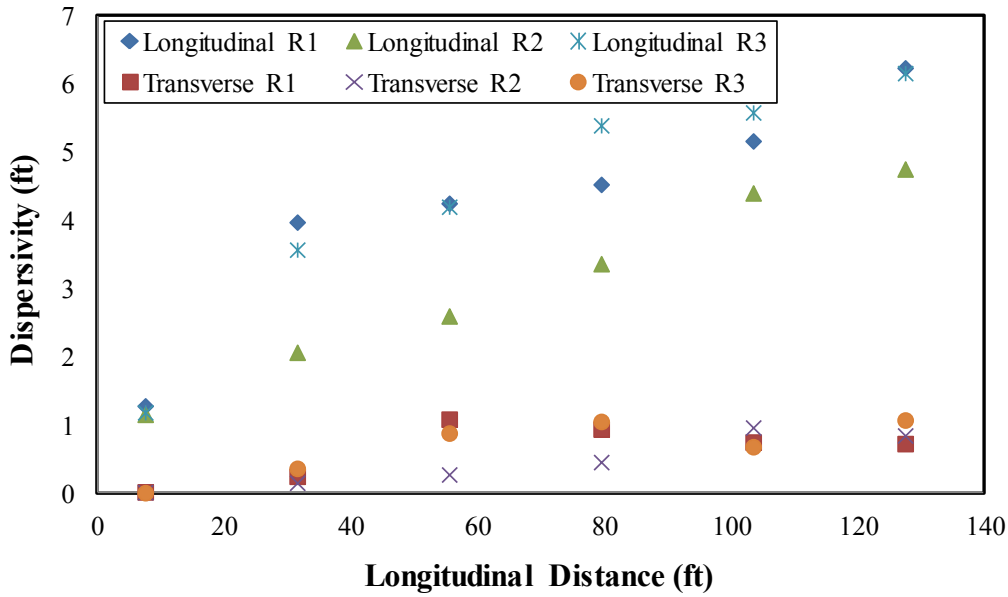

Figure 4.20: Estimated longitudinal and transverse dispersivity for three realizations (R1, R2 and R3) of an uncorrelated medium with $V_{DP} = 0.9$.

a)

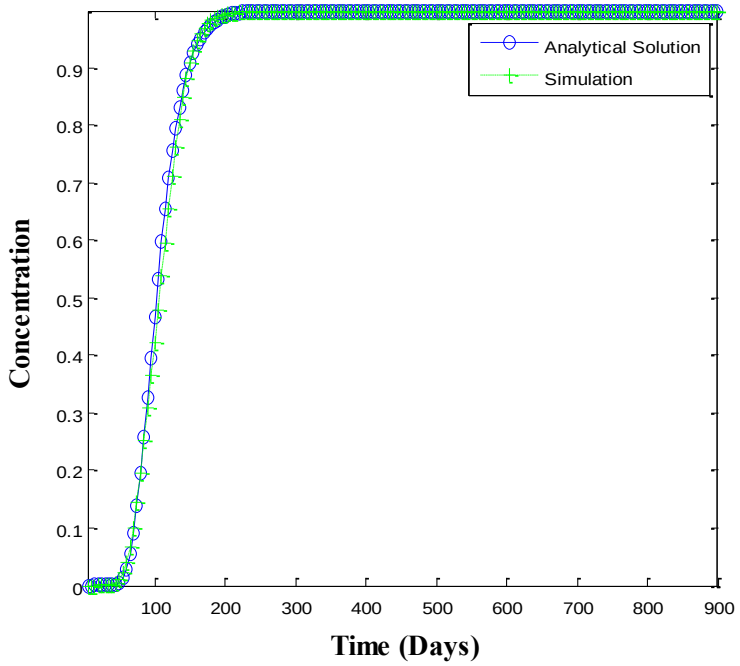
Analytical Solution
Simulation
Concentration
Time (Days)
0
0.1
0.2
0.3
0.4
0.5
0.6
0.7
0.8
0.9
100
200
300
400
500
600
700
800
900

b)

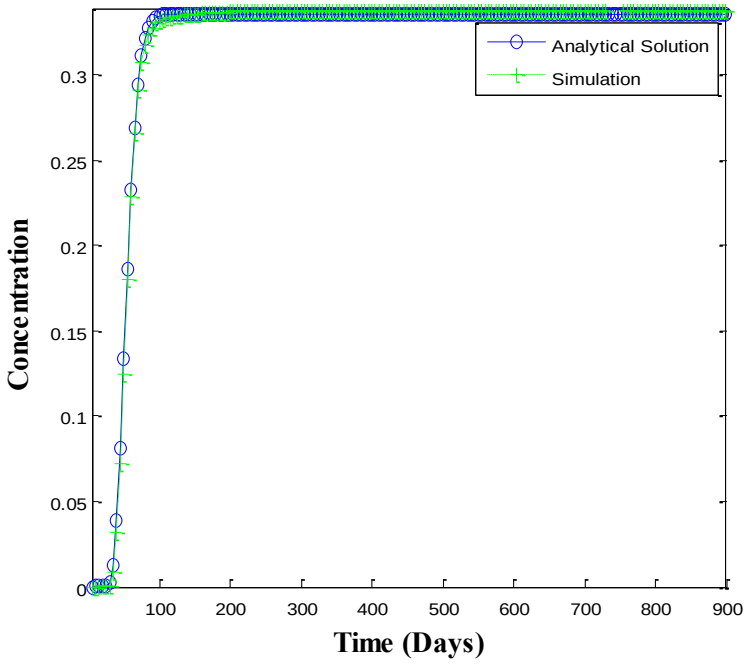
Analytical Solution
Simulation
Concentration
Time (Days)
0
0.05
0.1
0.15
0.2
0.25
0.3
100
200
300
400
500
600
700
800
900

c)

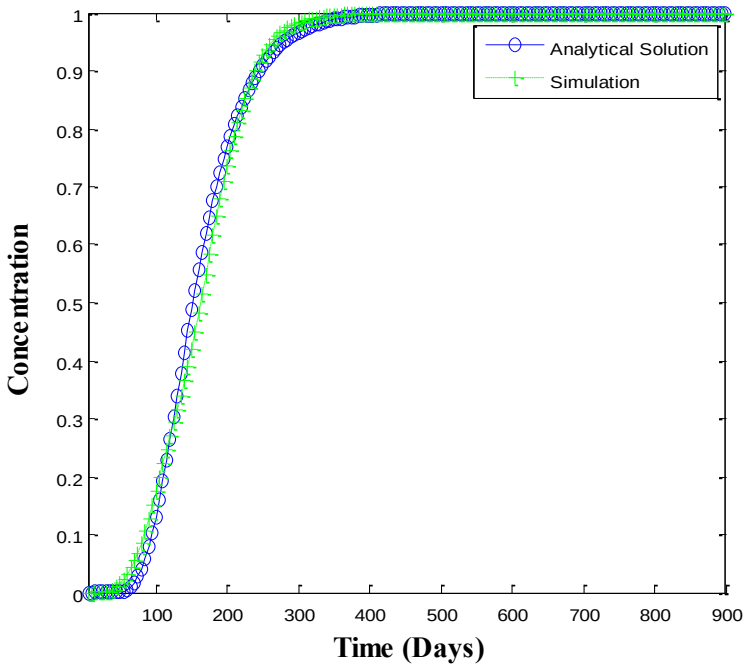

Figure 4.21: Comparison of the analytical solution to local simulation concentration histories for V_{DP} = 0.6 for different levels of spatial correlation (a) L_{XD} = 0.25, L_{YD} = 0.0 at x = 79.5 ft, y = 8.5 ft; the average sum of square of residuals for sampled points is 0.062 (b) L_{XD} = 0.5, L_{YD} = 0.0 at x = 79.5 ft, y = 18.5 ft; the average sum of square of residuals for sampled points is 0.101 and (c) L_{XD} = 5, L_{YD} = 0.0 at x = 79.5 ft, y = 8.5 ft; the average sum of square of residuals for sampled points is 0.169.

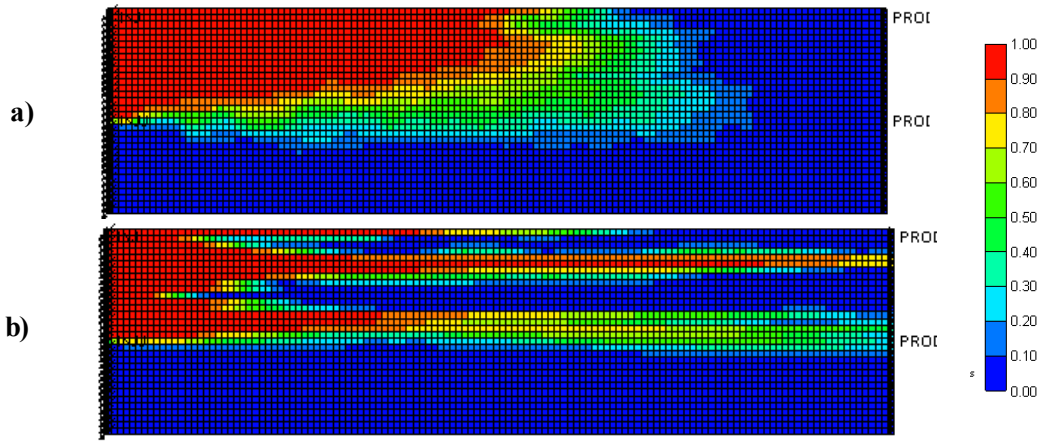

Figure 4.22: Solute concentration distribution at 95 days showing the effect of increasing longitudinal correlation length on dispersion for V_{DP} = 0.6 (a) L_{XD} = 0.0 and (b) L_{XD} = 5.0

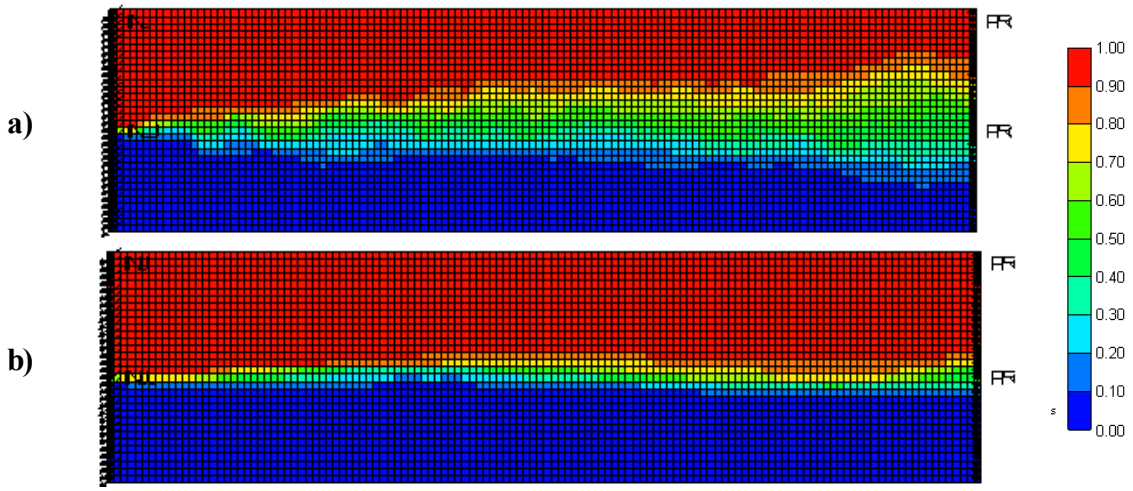

Figure 4.23: Solute concentration showing steady state mixing zone for different longitudinal correlation length for V_{DP} = 0.6 (a) L_{XD} = 0.0 and (b) L_{XD} = 5.0.

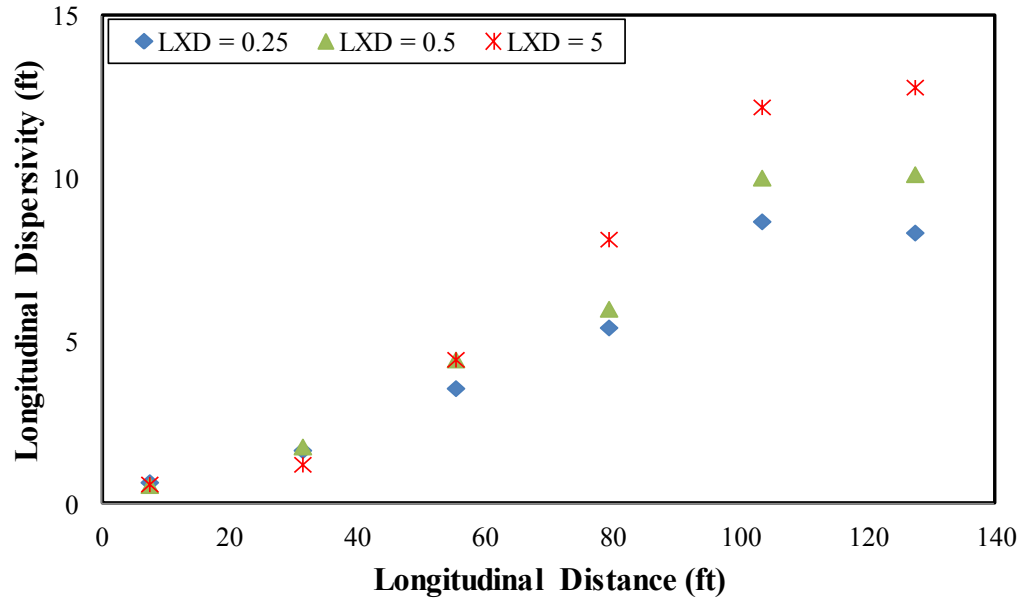

Figure 4.24: Estimated longitudinal dispersivities for various autocorrelation lengths in the longitudinal direction. The model is uncorrelated in the transverse direction and $V_{DP} = 0.6$.

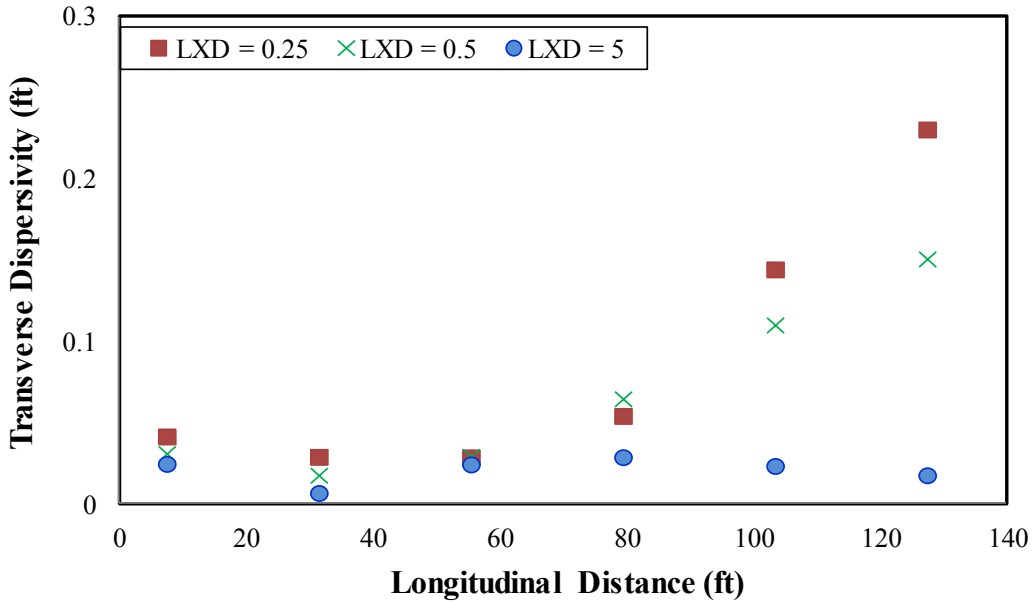

Figure 4.25: Estimated transverse dispersivities for various autocorrelation lengths in the longitudinal direction. The model is uncorrelated in the transverse direction ($L_{YD} = 0$) and $V_{DP} = 0.6$.

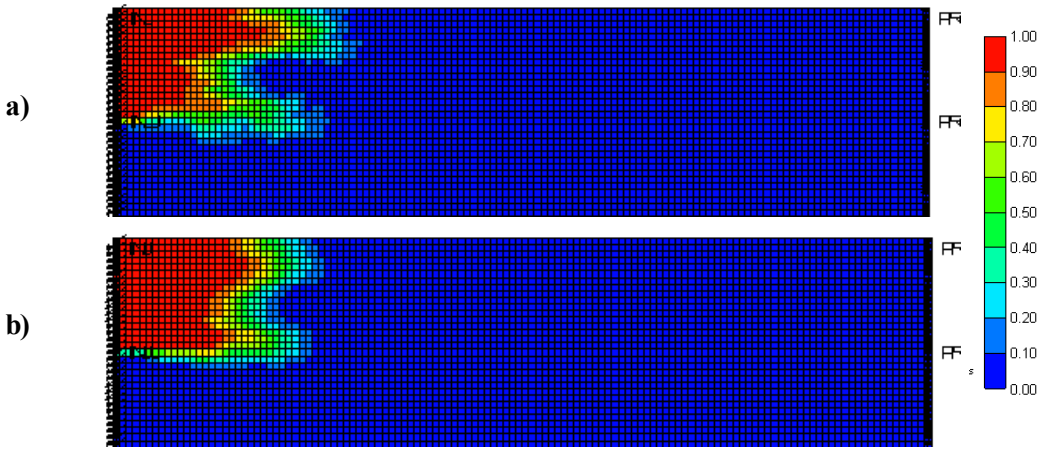

Figure 4.26: Solute concentration at 30 days showing the effect of increasing transverse correlation length on dispersion for V_{DP} = 0.6 (a) L_{YD} = 0.0 and (b) L_{YD} = 0.5.

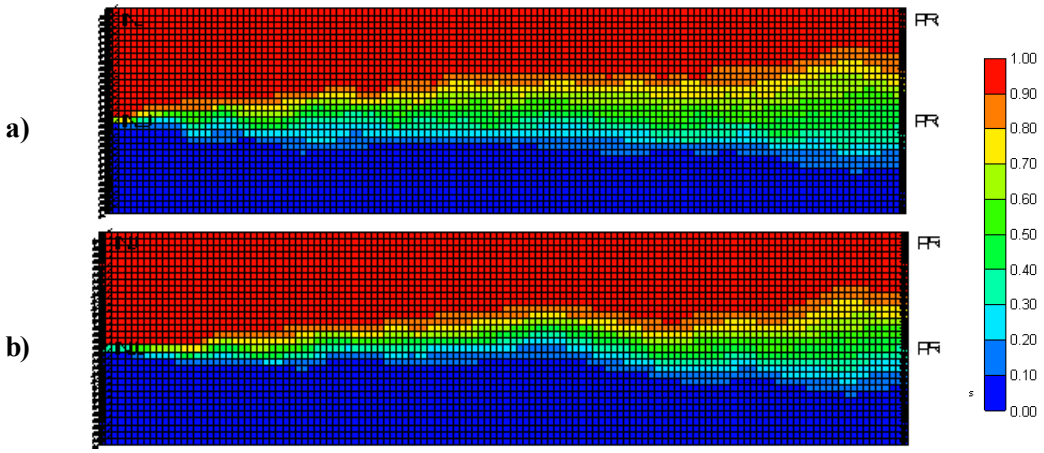

Figure 4.27: Solute concentration showing steady state mixing zone for different transverse correlation length for V_{DP} = 0.6 (a) L_{XD} = 0.0, L_{YD} = 0.0 and (b) L_{XD} = 0.0, L_{YD} = 0.5.

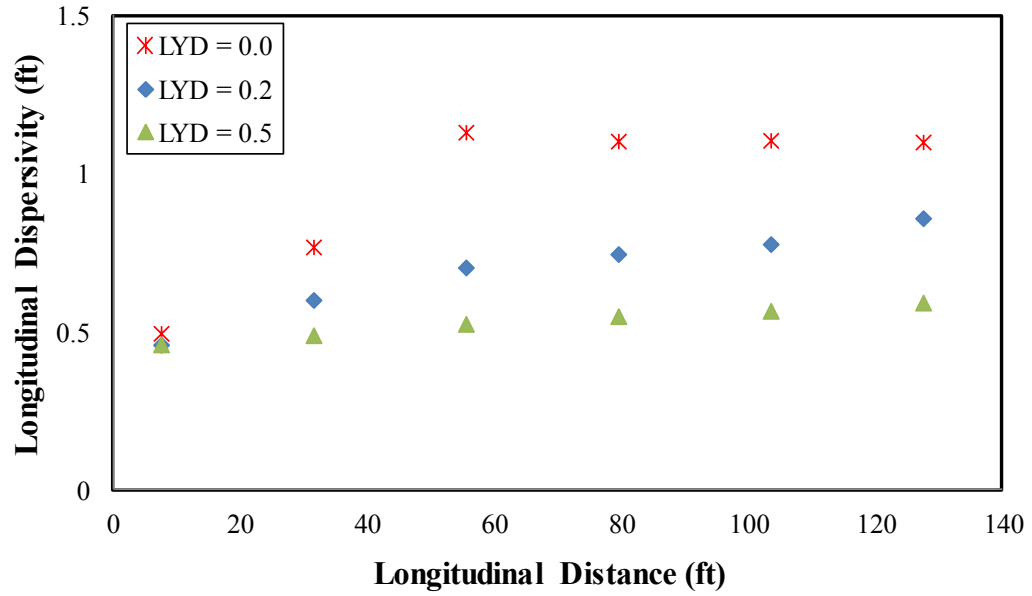

Figure 4.28: Estimated longitudinal dispersivities for various autocorrelation lengths in transverse direction. The model is uncorrelated in the longitudinal direction and $V_{DP} = 0.6$.

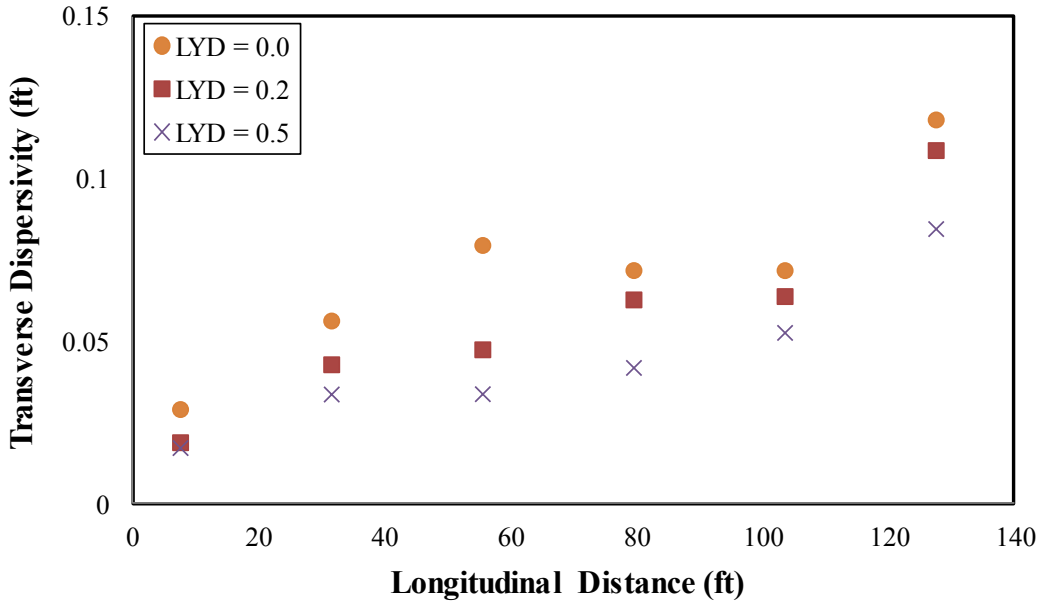

Figure 4.29: Estimated transverse dispersivities for various autocorrelation lengths in transverse direction. The model is uncorrelated in the longitudinal direction and $V_{DP} = 0.6$.

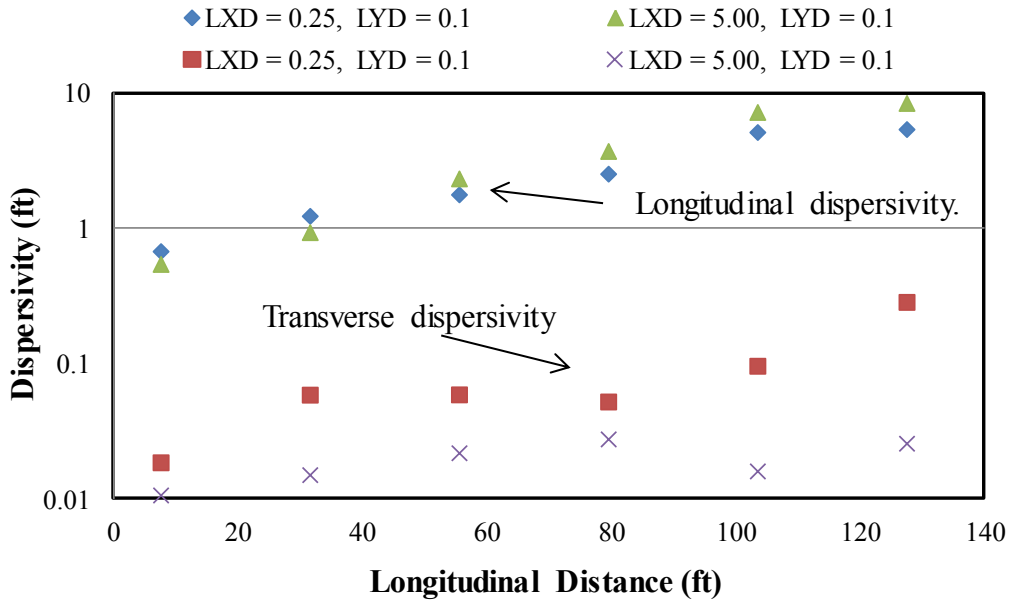

Figure 4.30: Estimated longitudinal and transverse dispersivities for various autocorrelation lengths in longitudinal direction. The autocorrelation length in the transverse direction (L_{YD}) is 0.1 and V_{DP} = 0.6.

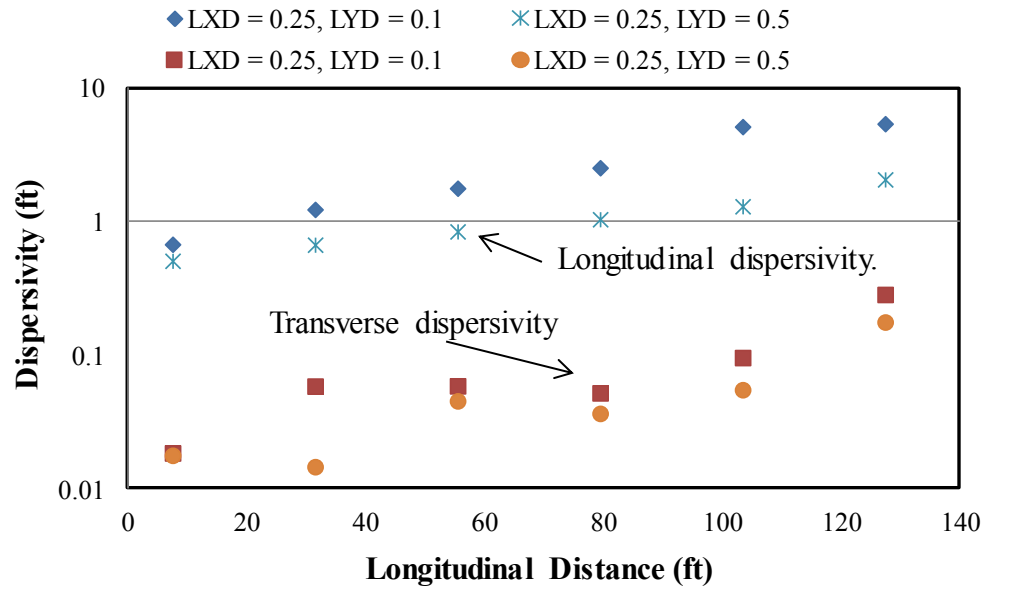

Figure 4.31: Estimated longitudinal and transverse dispersivities for various autocorrelation lengths in transverse direction. The autocorrelation length in longitudinal direction (L_{XD}) is 0.25 and V_{DP} = 0.6.

a)

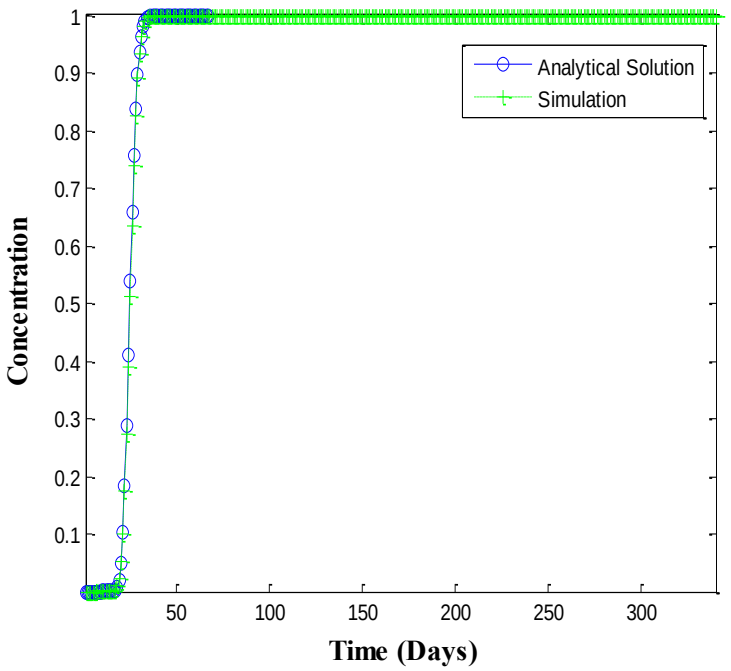

b)

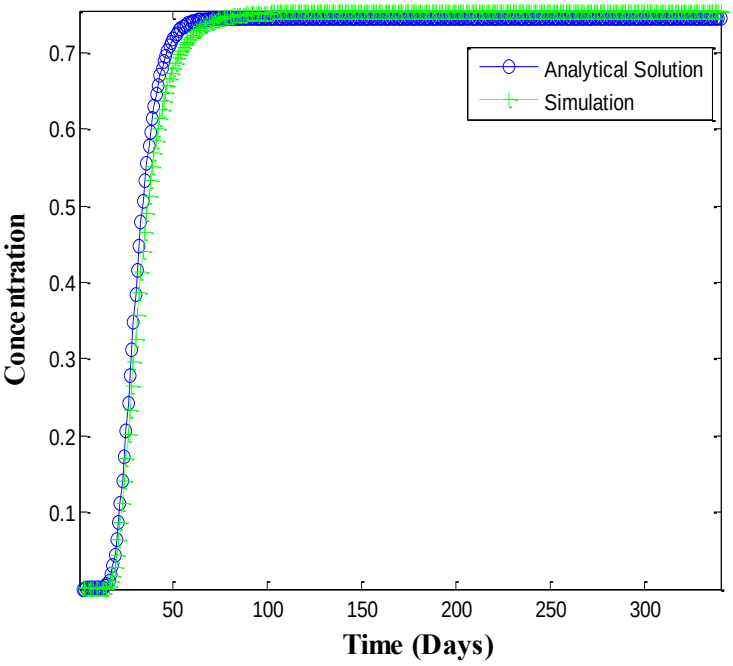

Figure 4.32: A match of the analytical solution to local simulation concentration histories for V_{DP} = 0.9 and uncorrelated model for different permeability anisotropy ratios (kv/kh) (a) kv/kh = 0.0 at x = 79.5 ft, y = 14.5 ft and (b) kv/kh = 1.0 at x = 127.5 ft, y = 4.5 ft.

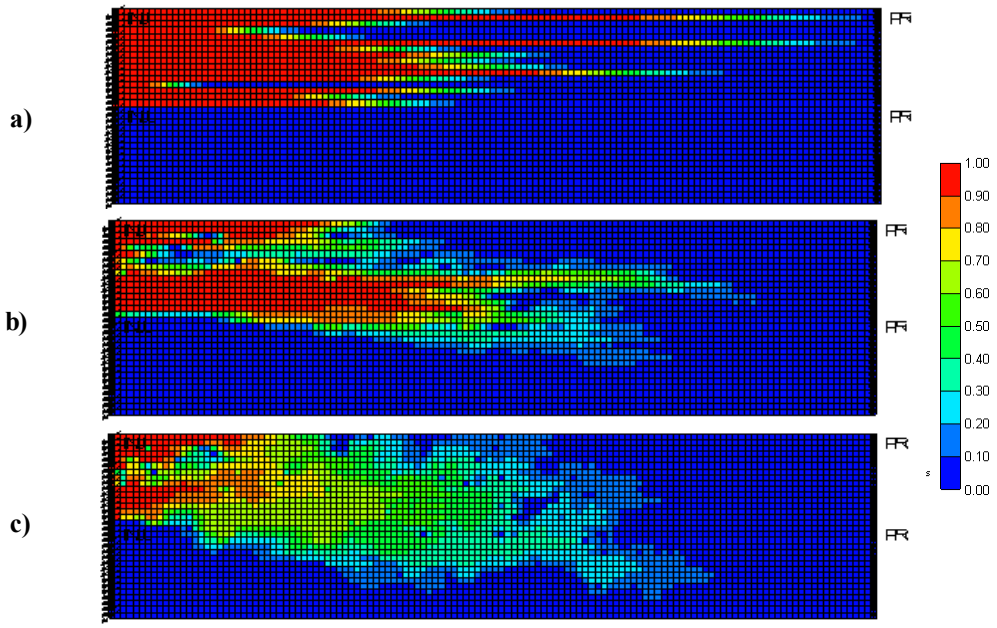

Figure 4.33: Solute concentration at 12 days showing the effect of increasing cross-flow on dispersion for V_{DP} = 0.9 (a) kv/kh = 0.0, (b) kv/kh = 0.01 and (c) kv/kh = 1.0.

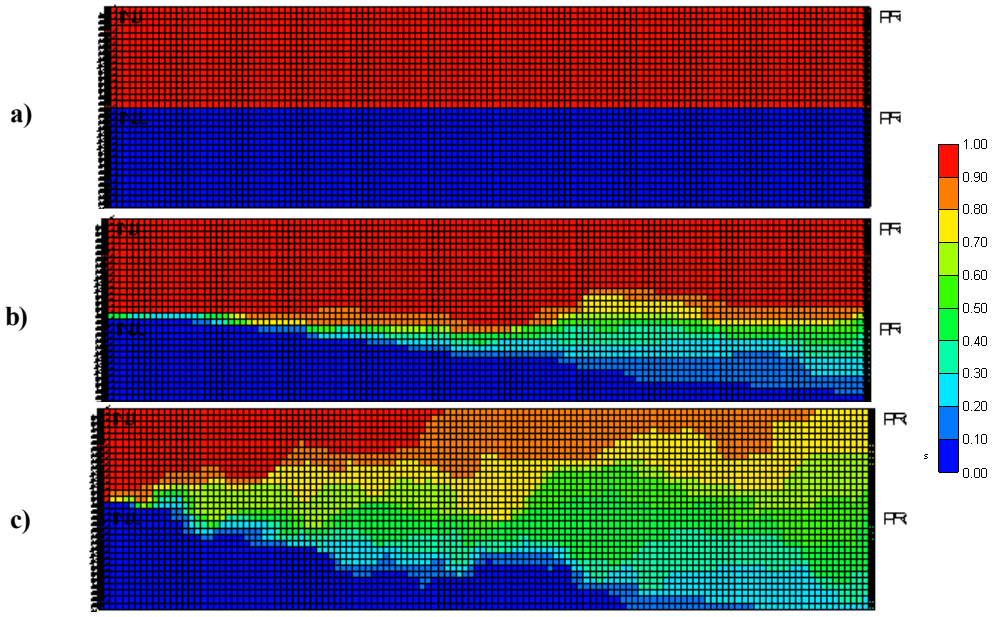

Figure 4.34: Solute concentration showing steady state mixing zone for cases with increasing cross-flow for V_{DP} = 0.9 (a) kv/kh = 0.0, (b) kv/kh = 0.01 and (c) kv/kh = 1.0.

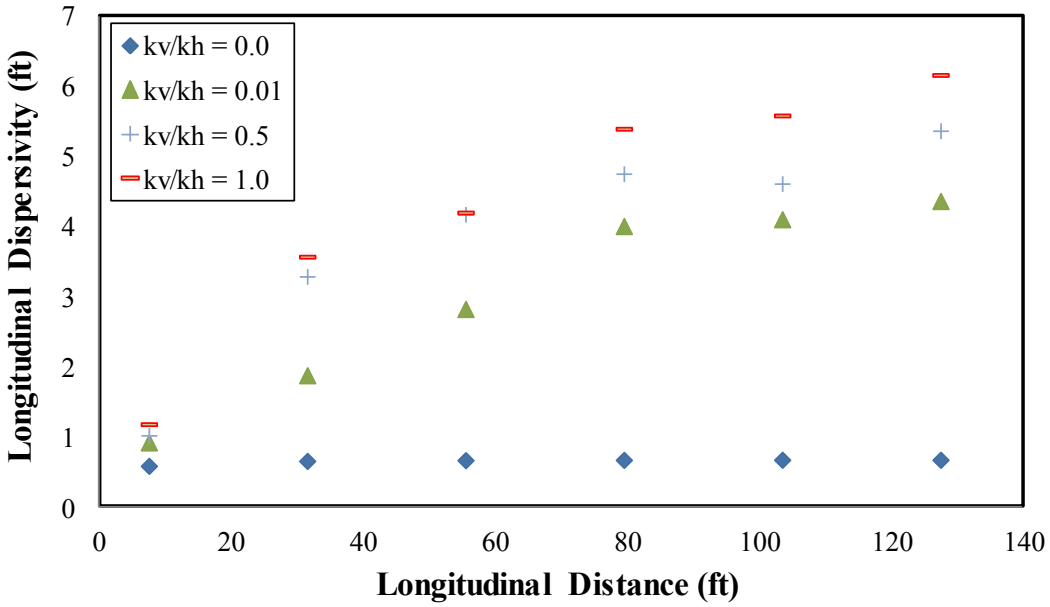

Figure 4.35: Estimated longitudinal dispersivity for various levels of cross-flow (kv/kh). The model is uncorrelated in both directions and V_{DP} = 0.9.

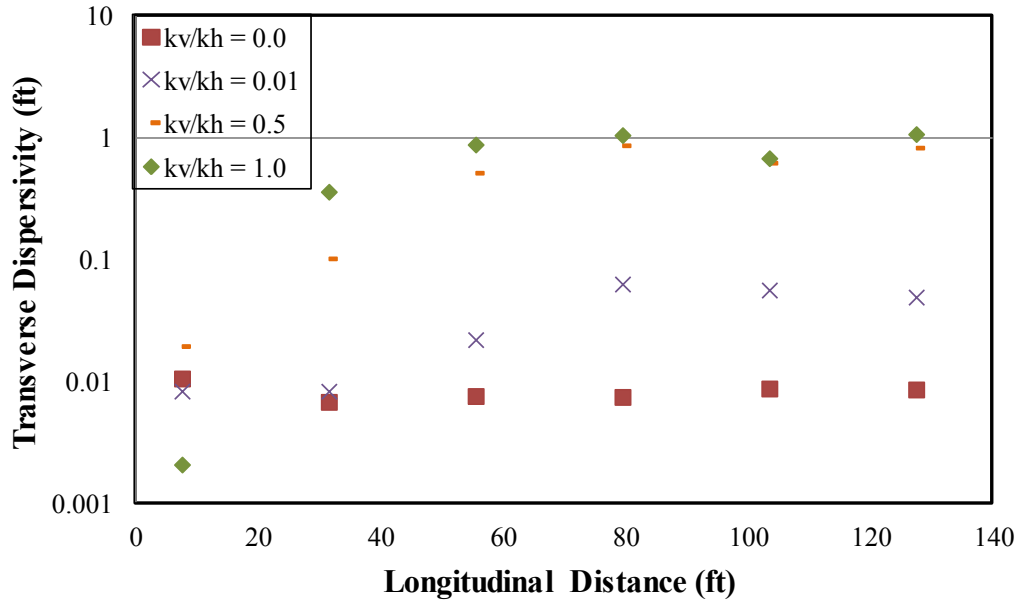

Figure 4.36: Estimated transverse dispersivity for various levels of cross-flow (kv/kh). The model is uncorrelated in both directions and V_{DP} = 0.9.

Chapter 5: Upscaling Miscible Displacements

In this chapter, we present the mathematical formalism and approach to determine the maximum grid-block size that maintains equivalent mixing between fine and upscaled coarse models. We extend the approach to reservoir models with different permeability distributions. Non-uniform coarsening scheme was proposed for media with different permeability distributions. The upscaling method was also extended to multi-contact miscible displacement with comparable recovery between the fine and upscaled models.

5.1 INTRODUCTIONS

Fine scale geological models contain detailed reservoir properties, but they may be too computationally intensive for routine reservoir simulations. Upscaling coarsens the fine scale model to obtain a smaller coarse model while attempting to maintain fine scale behavior. The process of coarsening the fine scale model homogenizes the reservoir model, thereby resulting in reduction of local velocity variations. The reduction in velocity variations results in reduction in local mixing. However, the increased grid-block size in the coarse model increases numerical dispersion. Therefore, there is need to ensure equivalent level of mixing in both fine and upscaled models.

Oil recovery in a multicontact miscible flood depends on the level of reservoir mixing or dispersion that occurs as gas displaces oil. One advantage of dispersion during a miscible flood is that larger grid blocks can be used to match the high level of physical mixing that occurs in fine-scale models and to maintain accuracy of the oil recovery prediction.

Conventional upscaling focuses on petrophysical (permeability) upscaling without consideration of mixing, especially for miscible displacement. Garmeh and Johns (2010)

proposed an iterative procedure to determine the maximum grid-block size required during upscaling for miscible displacements. We used the computed longitudinal and transverse dispersivity to determine *a-priori* the maximum grid block size required during upscaling without iteration.

5.2 MATHEMATICAL FORMALISM

The objective is to utilize the estimated longitudinal and transverse dispersion from fine scale model to estimate the maximum grid-block size that will generate equivalent dispersion at the coarse scale. This approach uses finite difference compositional simulator and assumes that the prevailing numerical dispersion can be estimated using the expression by Fanchi (1983).

The longitudinal dispersion coefficient (including numerical dispersion) assuming small time steps sizes and dominance of dispersion over diffusion is given as

$$D_L = \alpha_L \frac{v_x^2}{|v|} + \alpha_T \frac{v_y^2}{|v|} + \frac{1}{2} v_x \Delta x \,. \qquad (3.14a)$$

The goal is to have an equivalent level of dispersion for both the fine and upscaled models. That is,

$$D_L\big|_f = D_L\big|_u \qquad (5.1)$$

where subscript ‘f’ refers to fine scale and ‘u’ refers to upscaled models respectively.

The total longitudinal (α_{Lf}) and transverse (α_{Tf}) dispersivity for the fine scale model at x_D (dimensionless distance) equal to one is estimated using the procedure in chapter 4. Since upscaling homogenizes the medium and reduces the physical dispersion, the maximum grid block size (Δx_u) that would generate equivalent dispersion can thus be inferred. The maximum grid-block size that will generate equivalent mixing as the fine scale model can be described as,

$$\Delta x_u = \frac{2}{v_x}\left(\alpha_{Lf}\frac{v_x^2}{|v|} + \alpha_{Tf}\frac{v_y^2}{|v|}\right). \tag{5.2}$$

Assuming the flow is dominant in the x-direction $\left(v_y <<< v_x\right)$, equation (5.2) can be simplified to,

$$\Delta x_u = 2\alpha_{Lf}\,. \tag{5.3}$$

Therefore, the estimated longitudinal dispersivity of the fine scale model can be used to determine the maximum grid-block size in the longitudinal direction during upscaling.

Similarly, the maximum grid-block size in the transverse direction can be determined. The transverse dispersion coefficient is given in equation (3.14b) as;

$$D_T = \alpha_L\frac{v_y^2}{|v|} + \alpha_T\frac{v_x^2}{|v|} + \frac{1}{2}v_y\Delta y\,. \tag{3.14b}$$

The maximum upscaled grid-block size that will have equivalent dispersivities as the fine scale model can be expressed as,

$$\Delta y_u = \frac{2}{v_y}\left(\alpha_{Lf}\frac{v_y^2}{|v|} + \alpha_{Tf}\frac{v_x^2}{|v|}\right). \tag{5.4}$$

Assuming the flow is dominant in the x-direction, equation (5.4) can be simplified to,

$$\Delta y_u = 2\alpha_{Tf}\left(\frac{v_x}{v_y}\right). \tag{5.5}$$

Therefore, the estimated transverse dispersivity of the fine scale model and the velocity anisotropy ratio $\left(\frac{v_y}{v_x}\right)$ can be used to determine the maximum grid-block size in the transverse direction during upscaling. The log-averaged velocities (v_x and v_y) are obtained from the fine scale model.

5.2.1 Upscaling first contact miscible (FCM) displacements

The developed mathematical formalism (equations (5.3) and (5.5)) was used to determine the maximum grid-block size in both longitudinal and transverse directions for several FCM simulations. The single-phase pressure solver upscaling algorithm with harmonic permeability averaging was used for the upscaling, where the effluent flux from the fine scale grid-blocks is matched to the coarse scale grid-blocks to determine the equivalent grid-block permeability (Begg *et al.* 1989).

5.2.1.1 Case 1: V_{DP} = 0.6, L_{XD} = 0.25 and L_{YD} = 0.1

The reservoir model to be upscaled has 128 grid-blocks in the x-direction and 32 grid-blocks in the y-direction and a V_{DP} of 0.6. The grid-block size of the model is 1.0 ft in each direction. The reservoir model dimensionless correlation lengths in the x- and y-directions are 0.25 and 0.1 respectively. The estimated dispersivity in the longitudinal and transverse directions, using the procedure explained in chapter 4 is 5.39 ft and 0.25 ft respectively. Using equations (5.3) and (5.5), the maximum grid-block sizes that will generate equivalent mixing in the longitudinal and transverse directions are 10.78 ft and 5.93 ft respectively. Since the fine scale model can only be coarsened to an even number of grid-blocks (2, 4, 8, 16 etc), the recommended upscaled model dimension is 16x8. Equations (5.2) and (5.4) also gave comparable upscaled grid blocks sizes of 10.75 ft and 6.81 ft in the x- and y-directions respectively.

Table 5.1 shows that the recommended upscaled model (16 X 8) has a comparable recovery as the fine scale model. Further coarsening results in significant deviation from the fine scale model results as shown by the result of the 16 X 4 model.

It must be stated that less coarsening in either or both directions than the recommended maximum can also generate comparable results to the fine scale model as

can be seen with the 16 X 16 model. Other levels of coarsening that will give a comparable result to the fine scale model can be iteratively determined by reducing the level of coarsening in either direction.

The concentration distribution of the fine scale model and the coarse scale model at different pore-volumes injected (PVI) are comparable showing good representation of the fine scale model by the upscaled coarse model (Figure 5.1). Figure 5.2 shows that the recovery profile of the fine and upscaled model are also comparable. The recovery profile of a coarser model (16 X 4) was not comparable to the fine scale model. The simulation time for the upscaled model is 0.9 minutes compared to 32 minutes for the fine scale model.

5.2.1.2 Case 2: V_{DP} = 0.6, L_{XD} = 0.0 and L_{YD} = 0.0

The reservoir model to be upscaled has 128 grid-blocks in the x-direction and 32 grid-blocks in the y-direction and a V_{DP} of 0.6. The grid-block size of the model is 1.0 ft in each direction. The reservoir model permeability distribution is uncorrelated. The lack of correlation in the permeability distribution results in reduced physical dispersion in the fine scale model, resulting in limited opportunity for upscaling.

The estimated dispersivity in the longitudinal and transverse directions is 1.10 ft and 0.12 ft respectively. Using equations (5.3) and (5.5), the maximum grid-block sizes that will generate equivalent mixing in the longitudinal and transverse directions are 2.20 ft and 1.96 ft. respectively. Therefore, the recommended upscaled model dimension is 64 X 16. Equations (5.2) and (5.4) also gave comparable upscaled grid blocks sizes of 2.19 ft and 2.21 ft in the x- and y-directions respectively.

Table 5.2 shows that the recommended upscaled model (64 X 16) has a comparable recovery as the fine scale model. Further coarsening results in significant deviation from the fine scale model results as shown by the recovery of the 16 X 16 model.

The solute concentration map of the fine scale model and the coarse scale model for the uncorrelated model at different PVI are comparable showing good representation of the fine scale model by the upscaled coarse model (Figure 5.3). Further coarsening will result in excessive numerical dispersion that will not mimic the behavior of the fine scale model as shown in Figure 5.3.

Figure 5.4 shows that the recovery profile of the fine and upscaled model are also comparable. The simulation time for the upscaled model is 7.5 minutes compared to 37.98 minutes for the fine scale model.

5.2.1.3 Case 3: V_{DP} = 0.9, L_{XD} = 0.0 and L_{YD} = 0.0

The reservoir model to be upscaled in this case has 128 grid-blocks in the x-direction and 32 grid-blocks in the y-direction with a V_{DP} of 0.9. The grid-block size of the model is 1.0 ft in each direction. The reservoir model permeability distribution is uncorrelated. The lack of correlation in the permeability distribution results in reduced physical dispersion in the fine scale model, however the higher level of heterogeneity causes an increase in physical mixing compared to case 2 above.

The estimated dispersivity in the longitudinal and transverse directions is 6.16 ft and 1.07 ft respectively. Using equations (5.3) and (5.5), the maximum grid-block sizes that will generate equivalent mixing in the longitudinal and transverse directions are 12.32 ft and 7.23 ft. respectively. This implies that the upscaled grid-block sizes should

not exceed this maximum. Therefore, the recommended upscaled model dimension is 16 X 8 with grid-block size of 8 ft in x-direction and 4 ft in y-direction. However, equations (5.2) and (5.4) estimated the maximum grid blocks sizes as 12.00 ft and 10.43 ft in the x- and y-directions respectively. This will result in an upscaled model dimension of 16 X 4 with grid-block size of 8 ft in x-direction and 8 ft in y-direction. This 16 X 4 upscaled model though more coarse also gives comparable results to the fine scale model (Table 5.3).

Table 5.3 shows that the both suggested upscaled models (16 X 8 and 16 X 4) gives comparable recovery as the fine scale model. Further coarsening results in significant deviation from the fine scale model results as shown by the recovery of the 8 X 16 model.

Figure 5.5 shows that the two suggested upscaled models maintains the gross behavior of the fine scale model at different pore volume injected. The upscaled models display equivalent spreading of the solute as the fine scale models. Figure 5.6 shows that the recovery profile of the fine and upscaled models are also comparable.

5.2.1.4 Case 4: V_{DP} = 0.6, L_{XD} = 5.0 and L_{YD} = 0.0

We also extended the approach to a layered model, with dimensionless longitudinal correlation length of 5.0. The dimension reservoir model to be upscaled is 128 X 32 with 1.0 ft of grid-block size in each direction. As shown in chapter 4, solute channels through layers, with increased spreading and dilution in the longitudinal direction and minimized spreading in the transverse direction.

The estimated longitudinal dispersivity is 12.8 ft, while the transverse dispersivity is 0.02 ft. The estimated average velocity anisotropy ratio (v_y/v_x) is 0.02. Therefore the

estimated maximum upscaled grid block sizes are 25.6 ft and 1.97 ft in x- and y-directions respectively using equations (5.3) and (5.5). Comparable maximum grid-blocks sizes of 25.6 ft and 2.43 ft were estimated using equations (5.2) and (5.4). Therefore the suggested upscaling scheme is 8x16 with a grid-block size of 16 ft in the x-direction and 2 ft in the y-direction.

Figure 5.7 shows that the suggested upscaled model (8 X 16) compares favorably with the fine scale model (128 X 32). The total dispersion in the upscaled model was able to replicate the spreading and dilution across the layered medium of the fine scale model. The recovery from the fine scale and upscaled model are also comparable as shown in Figure 5.8.

5.2.2 Upscaling multi-contact contact miscible (MCM) displacements

Miscible enhanced oil recovery such as high pressure CO_2 flooding are mostly multi-contact miscible. The objective here is to use the estimated longitudinal and transverse dispersivity from FCM simulations to estimate the maximum grid block size that will give equivalent mixing between fine and coarse models used for miscible displacement. Dispersivity from FCM simulations with similar scaling characteristics as the MCM floods is expected to have similar levels of dispersion because the effect of relative permeability on dispersion is small and there is good mass transfer between phases in the MCM floods (Garmeh and Johns 2010). As the floods become more immiscible, mixing becomes less significant and the accuracy of the approach reduces.

The reservoir model shown in case 1 above with dimensions 128 X 32 and V_{DP} = 0.6 was upscaled for a high pressure CO_2 flood. The reservoir model has dimensionless correlation lengths of 0.25 and 0.1 in the longitudinal and transverse directions

respectively. As shown in Table 5.1 the suggested upscaled model is 16 X 8 with grid-block sizes of 8 ft in the x-direction and 4 ft in the y-direction. The oil composition (Table 5.4) and reservoir model properties (Table 5.5) used for the CO_2 flood were adapted from Woods *et al.* (2008). The viscosity ratio, which is one of the scaling groups affecting dispersion, was maintained to be slightly favorable such that it will be similar to the viscosity ratio used in the FCM simulation. The effect of adverse mobility ratio on dispersion and upscaling will be shown in the next example.

We conducted the CO_2 flood on the fine (128 X 32) and upscaled (16 X 8) model. Figures 5.9 shows comparable recovery plots between the two models. The oil saturation map at 0.34 PVI shows comparable swept volume between the fine and upscaled models (Figure 5.10). This shows that dispersion estimated from FCM simulations can be used to estimate maximum grid-block sizes for MCM simulations with similar scaling groups.

Most miscible gases used in enhanced oil recovery have less viscosity compared to the resident oil resulting in unfavorable viscosity ratio (>1). Unfavorable viscosity ratio causes solute to channel through high permeability regions resulting in minimal mixing. The effect of viscosity ratio and other scaling factors affecting FCM displacements have to be considered in the estimation of fine scale model dispersivities.

A miscible flood with CO_2 viscosity of 0.07 cp was used to displace resident oil of viscosity 1.59 cp (Table 5.6). The reservoir model has similar permeability distribution as the earlier case. A FCM simulation with similar viscosity ratio was used to estimate the longitudinal and transverse dispersivity of the fine scale model (128 X 32). The estimated longitudinal and transverse dispersivity is 2.65 ft and 0.09 ft respectively. Though the model has the same permeability distribution (V_{DP} = 0.6, L_{XD} = 0.25 and L_{YD} = 0.1) as case 1 above, adverse viscosity ratio has reduced the level of dispersion in the model. The estimated maximum grid-block sizes in the x- and y-directions are 5.31 ft and

2.12 ft respectively. Therefore, the suggested upscaled model dimension is 32 X 16 with grid-block sizes of 4 ft in x-direction and 2 ft in y-direction.

The upscaled model (32 X 16) oil saturation and CO_2 concentration maps compares favorably with the fine scale model (128 X 32) (Figures 5.11 and 5.12). Figures 11 and 12 also show that using a coarser model (16 X 8) does not give comparable swept volume as the fine scale model. The oil recovery plots from the upscaled and fine scale model are also comparable (Figure 5.13). The results show that the estimated dispersivities from FCM simulation can be used to determine the maximum grid-block sizes for MCM simulations, as long as they share similar scaling parameters. The complete dimensionless scaling parameters for FCM simulations and their effect on dispersion will be covered in the next chapter.

5.2.3 Upscaling Reservoir Models with Different Sets of Permeability Distributions

Geological deposition can result in a reservoir with different sequences of heterogeneity and/or correlation lengths. Each set of permeability distributions may have different levels of dispersion. This situation is mimicked by combining two models of the same heterogeneity but different correlation lengths. The objective here is to use the knowledge about each set of permeability distributions to constrain the upscaling process. This will lead to non-uniform coarsening of the upscaled grid-block sizes. The non-uniform coarsening approach was evaluated with FCM simulations.

Simulation models with permeability distributions shown in case 1 (V_{DP} = 0.6, L_{XD} = 0.25, L_{YD} = 0.1) and case 2 (V_{DP} = 0.6, L_{XD} = 0.0, L_{YD} = 0.0) are combined to form a third model with dimensions of 256 X 32 (Figure 5.14). The dispersivities and the recommended upscale schemes of case 1 and case 2 simulation models are detailed in

Tables 5.1 and 5.2. The objective is to use that information to coarsen the combined simulation model (256 X 32).

The recommended upscaling model dimension for the first half of the combined simulation model is 64 X 16 (case 2), while the recommended upscaling model dimension for the second part of the combined simulation model is 16 X 16 (case1). The maximum upscaled model dimension for case 2 is 16 X 8, but the simulator cannot handle different number of grid-blocks in transverse direction for the same model. It was also confirmed that 16 X 16 is a good upscaled model for case 1 (see Table 5.1).

Therefore the non-uniform coarsening scheme for the upscaled model will be of dimension 80 X 16, with the first half having a grid-block size of 2 ft in x-direction, while the second half will have a grid block size of 8 ft in x-direction. The upscaled model will have grid-block size of 2 ft in the y-direction.

The solute concentration map for the fine (256 X 32) and the upscaled model (80 X 16) are comparable (Figure 5.15). The solute concentration map shows that a good vertical sweep in the first half of the model due to the randomness of the permeability distribution and solute channeling in the second half of the model due to increased layering. The recovery from the FCM simulations of the fine and upscaled model are also comparable (Figure 5.16). The results show that non-uniform coarsening scheme can be employed to upscaled models with different permeability structures.

Alternatively, the dispersivities of the fine scale model (256 X 32) can be computed and the maximum upscaled grid block size estimated. The computed longitudinal and transverse dispersivities for the combined fine scale simulation model are 2.18 ft and 0.08 ft respectively. Using equations (5.3) and (5.5), the maximum grid-block sizes that will generate equivalent mixing in the longitudinal and transverse directions are 4.36 ft and 1.64 ft respectively. Therefore the recommended upscaled

model dimension using uniform coarsening is 64 X 16 with 4 ft in the x-direction and 2 ft in the y-direction. Table (5.7) shows that the recovery from both the non-uniform coarsening scheme (80 X 16) and uniform coarsening scheme (64 X 16) are comparable to the fine scale model (256 X 32). The solute concentration map and recovery of the uniform coarsening upscaling scheme (64 X 16) compares favorably with the fine scale model (Figure 5.17).

The non-uniform coarsening approach was also considered for a combination of layered medium with an uncorrelated medium. The layered medium permeability distribution is detailed in case 4 ($V_{DP} = 0.6$, $L_{XD} = 5.0$, $L_{YD} = 0.1$) and the uncorrelated medium permeability distribution is given in case 2 ($V_{DP} = 0.6$, $L_{XD} = 0.0$, $L_{YD} = 0.0$). The resulting fine scale model (256 X 32) is shown in Figure 5.18.

The recommended upscaling model dimension for the first half of the combined simulation model is 8 X 16 (case 4), while the recommended upscaling model dimension for the second part of the combined simulation model is 64 X 16 (case1). Therefore the non-uniform coarsening scheme for the upscaled model will be of dimension 72 X 16, with the first half having a grid-block size of 16 ft in x-direction, while the second half will have a grid block size of 2 ft in x-direction. The upscaled model will have grid-block sizes of 2 ft in the y-direction. The solute concentration map and recovery show that the non-uniform coarsened upscaled model compares favorably with the fine scale model (Figure 5.19). The solute concentration map also shows that solute channeling through the layered medium in the first part of the model and increased vertical sweep in the later part of the simulation model.

The use of variable grid-block sizes can increase the truncation error associated with the finite difference discretization. We are proposing different grid-blocks sizes for different permeability distributions. Therefore the use of variable grid-block sizes is

localized to the junction of the sets of uniform grid-blocks. In Appendix D, we showed that the form of numerical dispersion for variable grid-block sizes is similar to physical dispersion. However the order of the truncation error decreases from second order to first order with variable grid-blocks. Therefore caution must be exercised in the use of non-uniform grid-blocks and the accuracy of the resulting solution should always be verified.

5.3 CONCLUSIONS

This chapter presents the mathematical formalism and procedure to utilize the estimated longitudinal and transverse dispersivities to determine the maximum upscaled grid block sizes. The procedure was validated with several cases of FCM simulations showing that the suggested upscaled models compares favorably with the fine scale models.

The upscaling procedure was also successfully extended for MCM displacements. The main criteria for using dispersivities from FCM simulations to determine maximum grid block sizes for MCM simulations is that both simulations must have similar scaling factors. The complete set of scaling factors affecting FCM simulations and consequently dispersion will be discussed in the next chapter.

Finally the upscaling procedure was extended to reservoir models with regions of different permeability distributions. Non-uniform and uniform coarsening schemes were recommended for the different regions. The proposed upscaled models were shown to replicate sweep and recovery of the fine scale model.

	α_L	α_T	α_T/α_L	Δx (feet)	Δy (feet)	v_y/v_x	Recovery % (@1 PV)
128 X 32	5.39	0.25	0.05	1	1	0.08	75.61
16 X 4	4.72	0.78	0.16	8	8	0.07	81.70
16 X 8	5.56	0.45	0.08	8	4	0.06	76.93
16 X 16	6.68	0.29	0.04	8	2	0.05	74.94

Table 5.1: Fine and upscaled parameters for case $V_{DP} = 0.6$, $L_{XD} = 0.25$ and $L_{YD} = 0.1$.

	α_L	α_T	α_T/α_L	Δx (feet)	Δy (feet)	v_y/v_x	Recovery % (1 PV)
128X32	1.10	0.12	0.11	1	1	0.12	94.06
64 X 16	1.42	0.13	0.09	2	2	0.08	93.53
32 X 16	2.27	0.08	0.04	4	2	0.04	92.06
16 X 16	3.66	0.06	0.02	8	2	0.02	89.74

Table 5.2: Fine and upscaled parameters for case $V_{DP} = 0.6$, $L_{XD} = 0.0$ and $L_{YD} = 0.0$.

	α_L	α_T	α_T/α_L	Δx (feet)	Δy (feet)	v_y/v_x	Recovery % (1 PV)
128 X 32	6.16	1.07	0.17	1	1	0.30	85.93
16 X 4	5.85	1.36	0.23	8	8	0.06	86.05
16 X 8	6.72	0.76	0.11	8	4	0.08	84.75
8 X 16	7.52	0.13	0.02	16	2	0.05	81.63

Table 5.3: Fine and upscaled parameters for case $V_{DP} = 0.9$, $L_{XD} = 0.0$ and $L_{YD} = 0.0$.

Components	Mole Fraction
CO2	0
C1	0.0885
C2 - C3	0.1742
C4 - C6	0.1944
C7 - C16	0.3138
C17 - C29	0.1549
C30+	0.0742

Table 5.4: Oil composition for CO_2 flood (adapted from Woods *et al.* 2008).

Properties	Values
MMP (psi)	1800
Reservoir Pressure (psi)	4500
Soi	0.55
Swr	0.20
End-Point krw	0.22
End-Point kro	0.43
End-Point krg	0.30
Oil Viscosity (cp)	1.59
CO_2 Viscosity (cp)	1.32
Water Viscosity (cp)	1.00
Oil Density (lb/ft^3)	81.50
CO_2 Density (lb/ft^3)	79.80

Table 5.5: Fluid and reservoir properties for CO_2 flood – Case 1 (adapted from Woods *et al.* 2008 with favorable mobility ratio).

Properties	Values
MMP (psi)	1800
Reservoir Pressure (psi)	4500
Soi	0.55
Swr	0.20
End-Point krw	0.30
End-Point kro	0.80
End-Point krg	0.66
Oil Viscosity (cp)	1.59
CO_2 Viscosity (cp)	0.07
Water Viscosity (cp)	0.62
Oil Density (lb/ft^3)	54.30
CO_2 Density (lb/ft^3)	49.00

Table 5.6: Fluid and reservoir properties for CO_2 flood with unfavorable mobility ratio (adapted from Woods *et al.* 2008).

	α_L	α_T	α_T/α_L	Δx (feet)	Δy (feet)	v_y/v_x	Recovery % (@1 PV)
256 X 32	2.18	0.08	0.04	1	1	0.10	87.54
64 X 16	4.45	0.06	0.01	4	2	0.05	87.61
80 X 16	3.58	0.22	0.06	~3.2	2	0.07	87.77

Table 5.7: Estimated dispersion and FCM recovery for simulation model with different sets of permeability distributions.

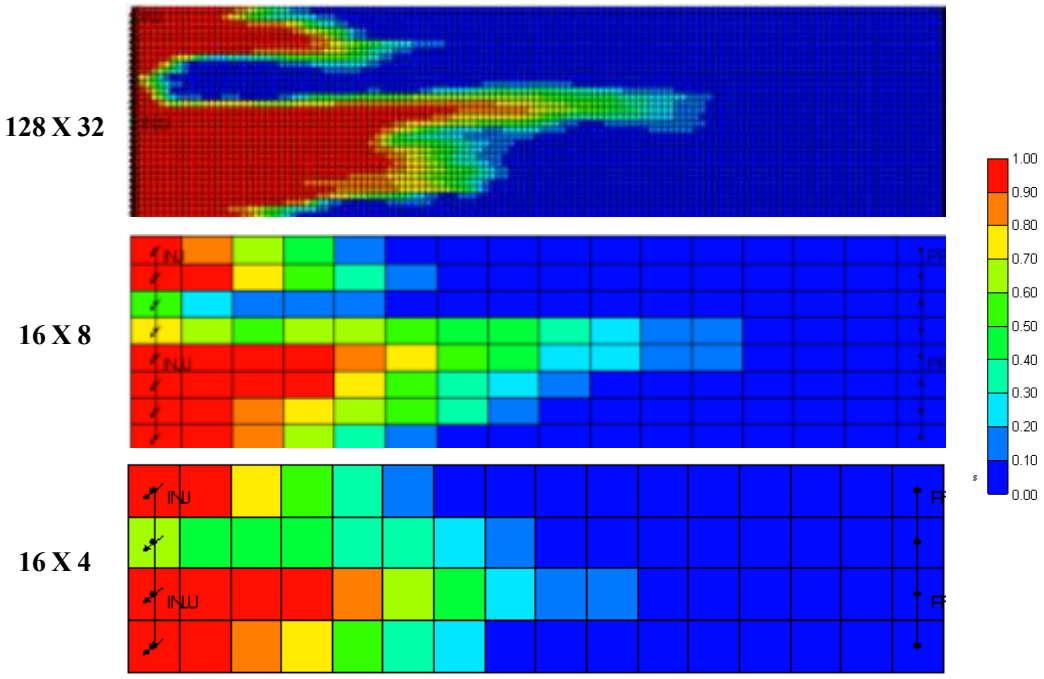

Figure 5.1: Solute concentration at 0.3 pore volume injected for fine scale model (128 X 32), recommended upscaled model (16 X 8) and a coarser model (16 X 4) for case V_{DP} = 0.6, L_{XD} = 0.25 and L_{YD} = 0.1.

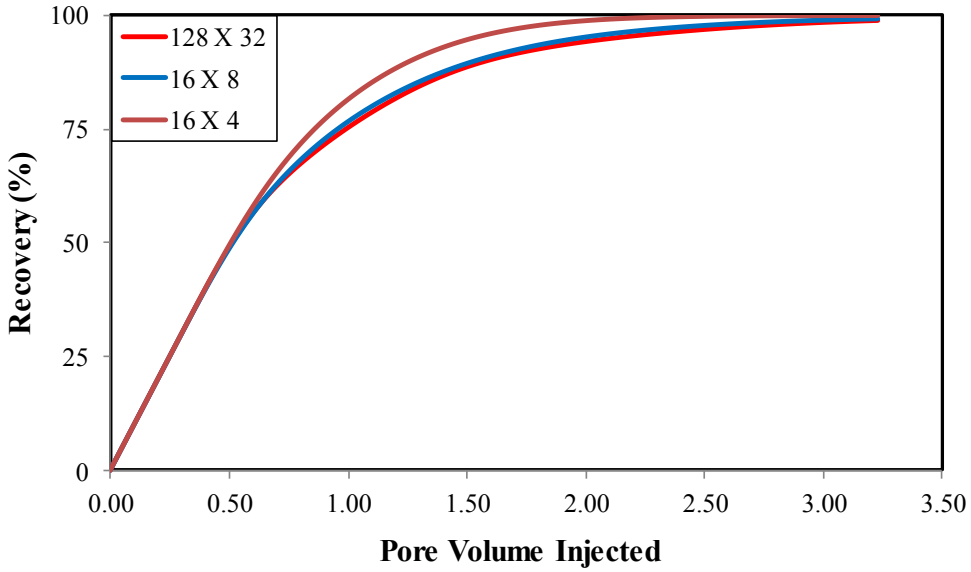

Figure 5.2: Recovery plots for fine scale model (128 X 32), recommended upscaled model (16 X 8) and a coarser model (16 X 4) for case V_{DP} = 0.6, L_{XD} = 0.25 and L_{YD} = 0.1.

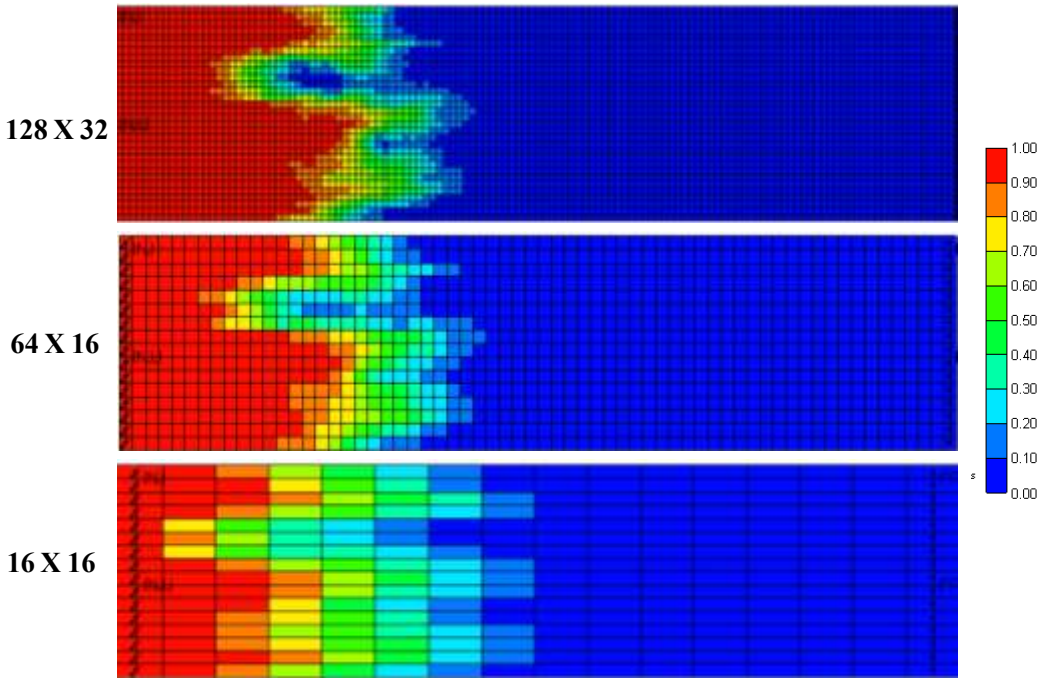

Figure 5.3: Solute concentration distribution at 0.3 pore volume injected for fine scale model (128 X 32), recommended upscaled model (64 X 16) and a coarser model (16 X 16) for case $V_{DP} = 0.6$, $L_{XD} = 0.0$ and $L_{YD} = 0.0$.

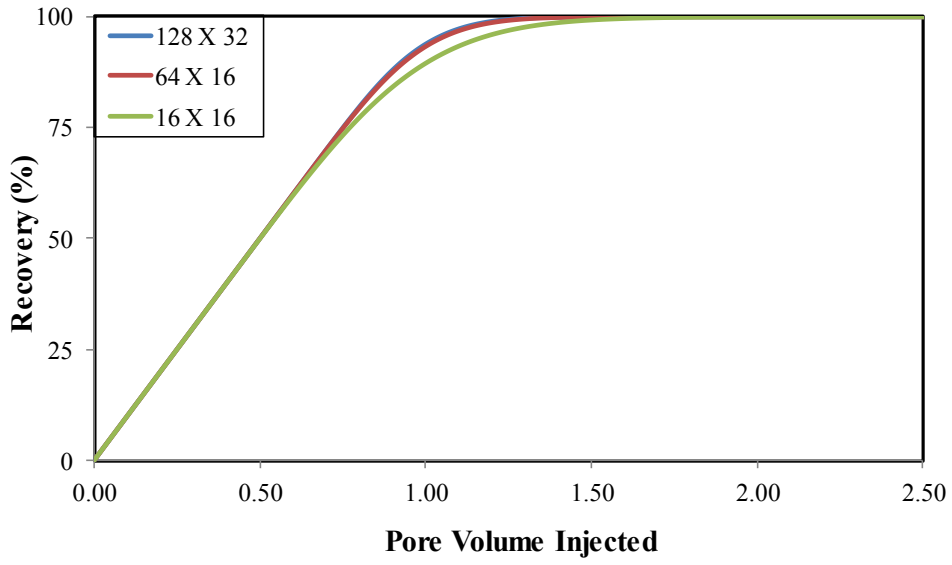

Figure 5.4: Recovery plots from FCM simulations for fine scale model (128 X 32), recommended upscaled model (64 X 16) and a coarser model (16 X 16) for case $V_{DP} = 0.6$, $L_{XD} = 0.0$ and $L_{YD} = 0.0$.

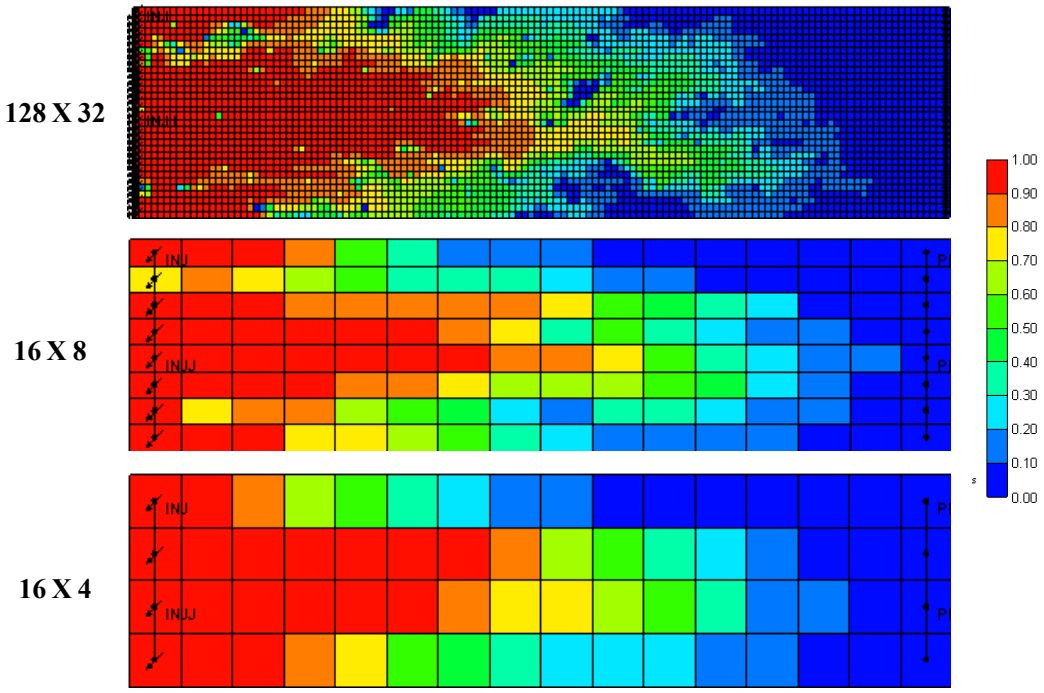

Figure 5.5: Solute concentration at 0.5 pore volume injected for fine scale model (128 X 32) and the two suggested upscaled models (16 X 8 and 16 X 4) for case $V_{DP} = 0.9$, $L_{XD} = 0.0$ and $L_{YD} = 0.0$.

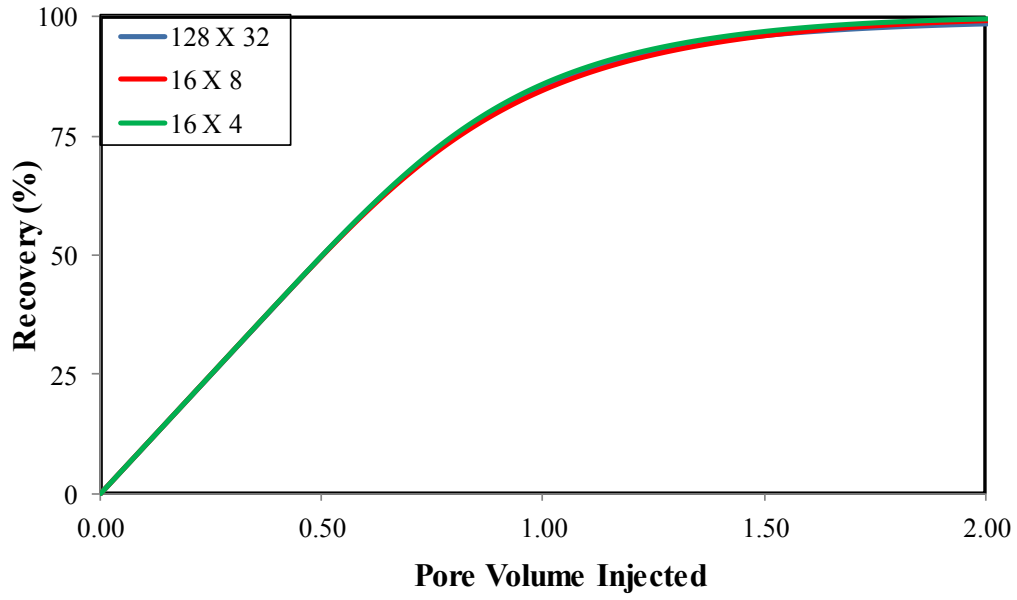

Figure 5.6: Recovery plots for fine scale model (128 X 32) and the upscaled models (16 X 8 and 16 X 4) for case $V_{DP} = 0.9$, $L_{XD} = 0.0$ and $L_{YD} = 0.0$.

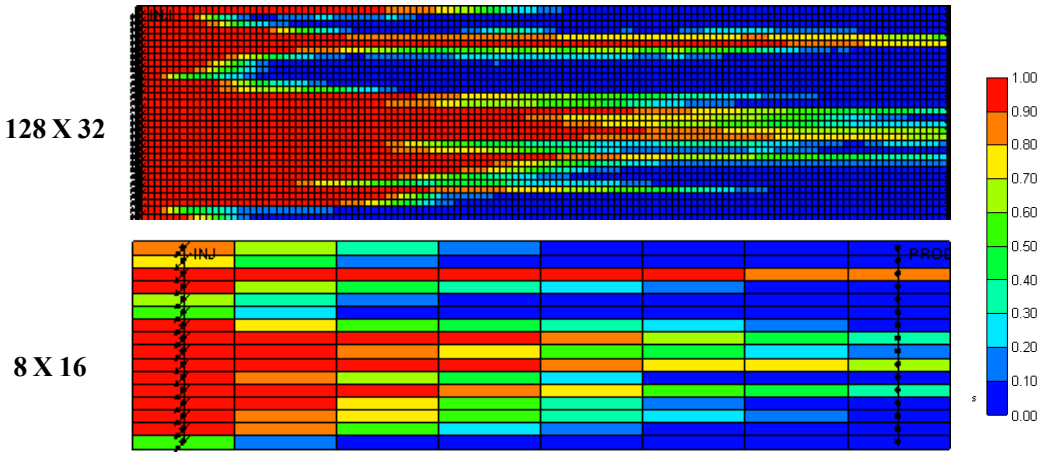

Figure 5.7: Solute concentration at 0.5 pore volume injected for fine scale model (128 X 32) and suggested upscaled models (8 X 16) for case V_{DP} = 0.6, L_{XD} = 5.0 and L_{YD} = 0.0.

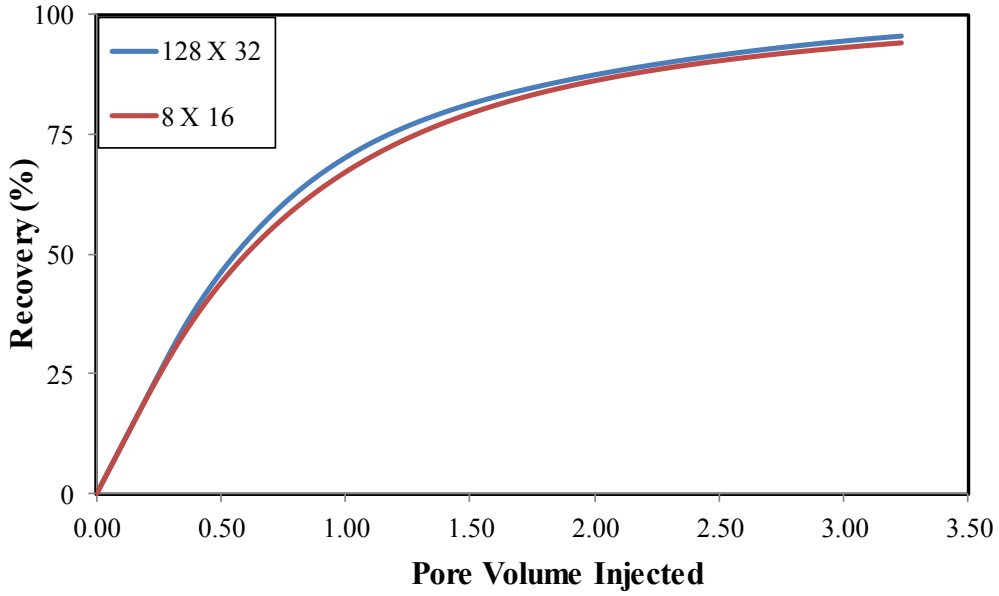

Figure 5.8: Recovery plots for fine scale model (128 X 32) and the upscaled models (8 X 16) for case V_{DP} = 0.6, L_{XD} = 5.0 and L_{YD} = 0.0.

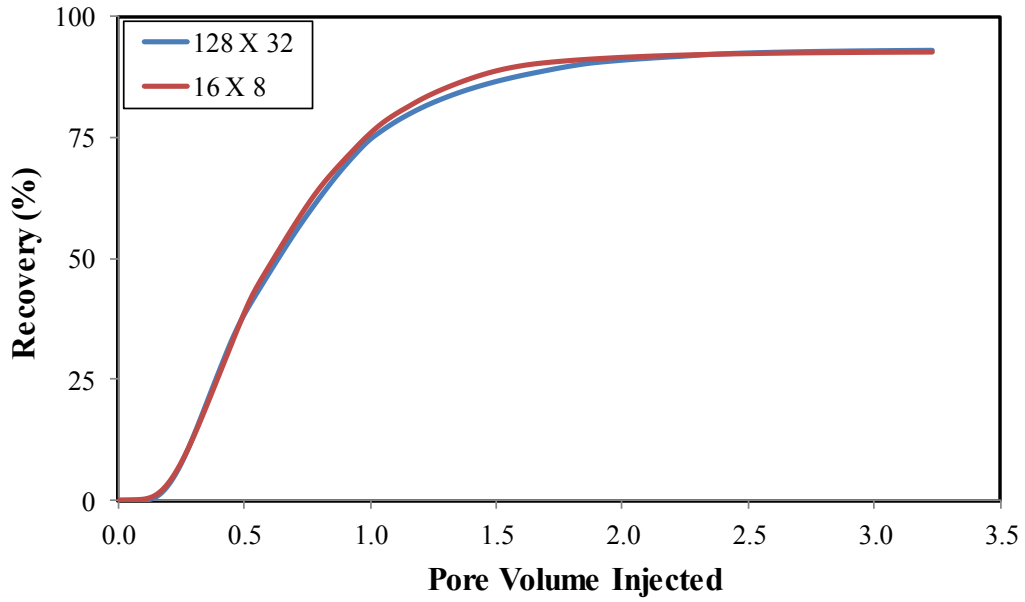

Figure 5.9: Oil recovery from CO_2 flood for fine scale model (128 X 32) and the upscaled model (16 X 8) with V_{DP} = 0.6, L_{XD} = 0.25 and L_{YD} = 0.1 and viscosity ratio = 1.2.

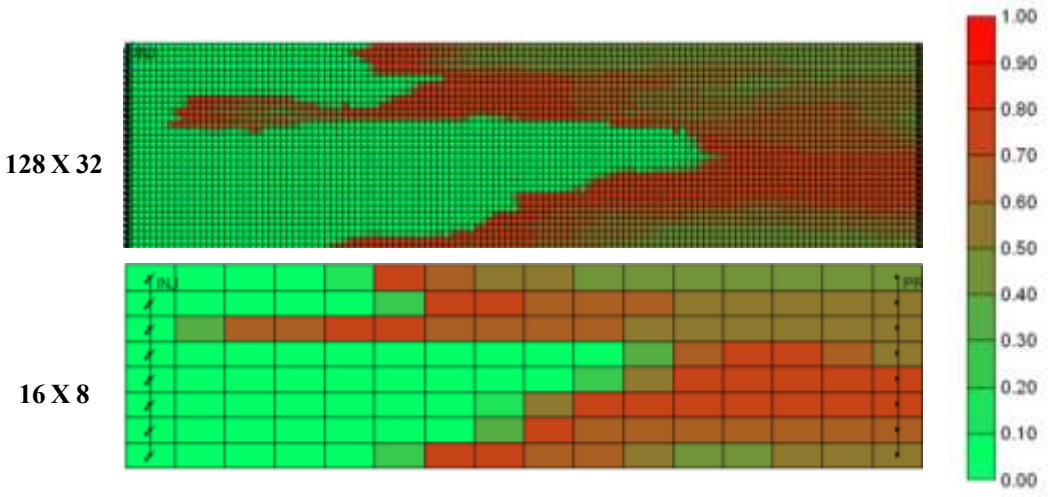

Figure 5.10: Oil saturation map at 0.34 pore volume injected showing comparable swept volume for the fine scale model (128 X 32, top) and the suggested upscaled model (16 X 8, bottom) for case V_{DP} = 0.6, L_{XD} = 0.25 and L_{YD} = 0.1 with viscosity ratio = 1.2.

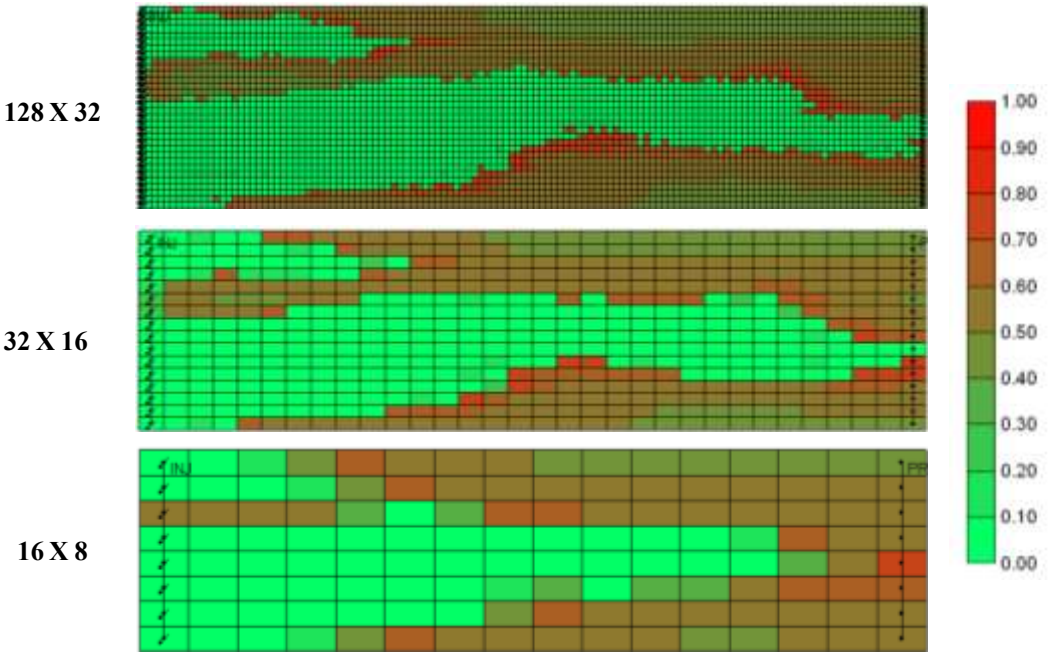

Figure 5.11: Oil saturation map at 0.34 pore volume injected for the fine scale model (128 X 32), recommended upscaled model (32 X 16) and a coarser model (16 X 8) for viscosity ratio = 22.7 with $V_{DP} = 0.6$, $L_{XD} = 0.25$ and $L_{YD} = 0.1$.

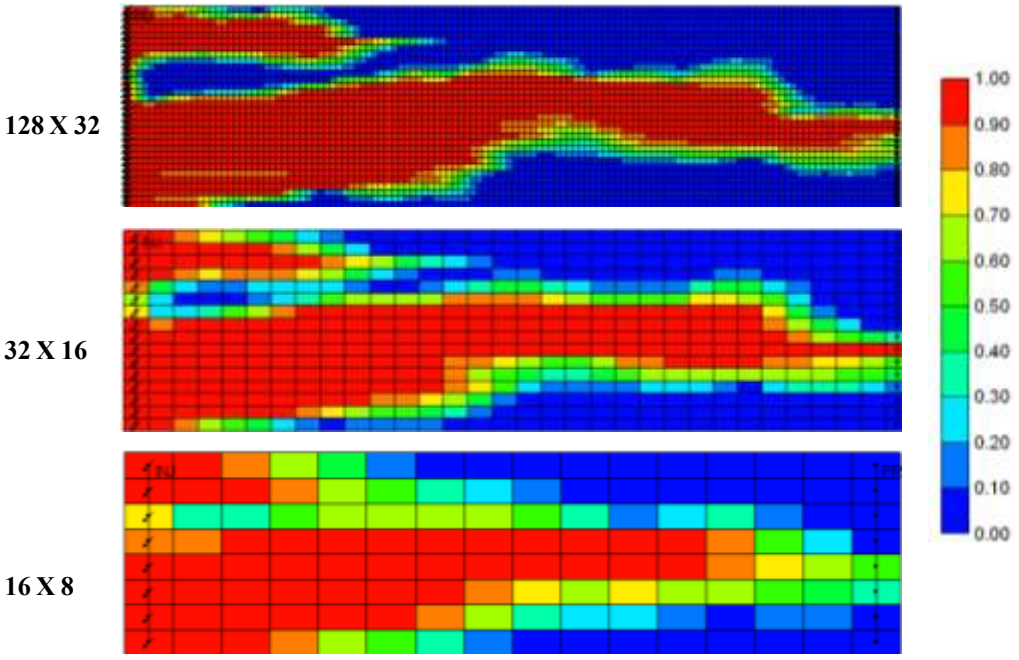

Figure 5.12: CO_2 concentration map at 0.34 pore volume injected for the fine scale model (128 X 32), recommended upscaled model (32 X 16) and a coarser model (16 X 8) for viscosity ratio = 22.7 with V_{DP} = 0.6, L_{XD} = 0.25 and L_{YD} = 0.1.

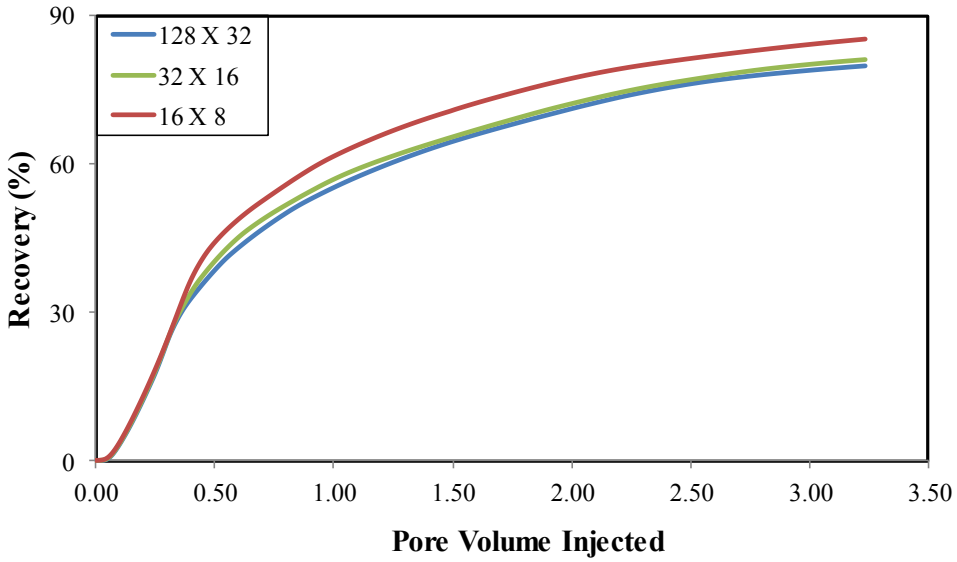

Figure 5.13: Oil recovery for a CO_2 flood from the fine scale model (128 X 32), recommended upscaled model (32 X 16) and a coarser model (16 X 8) for viscosity ratio = 22.7 with V_{DP} = 0.6, L_{XD} = 0.25 and L_{YD} = 0.1.

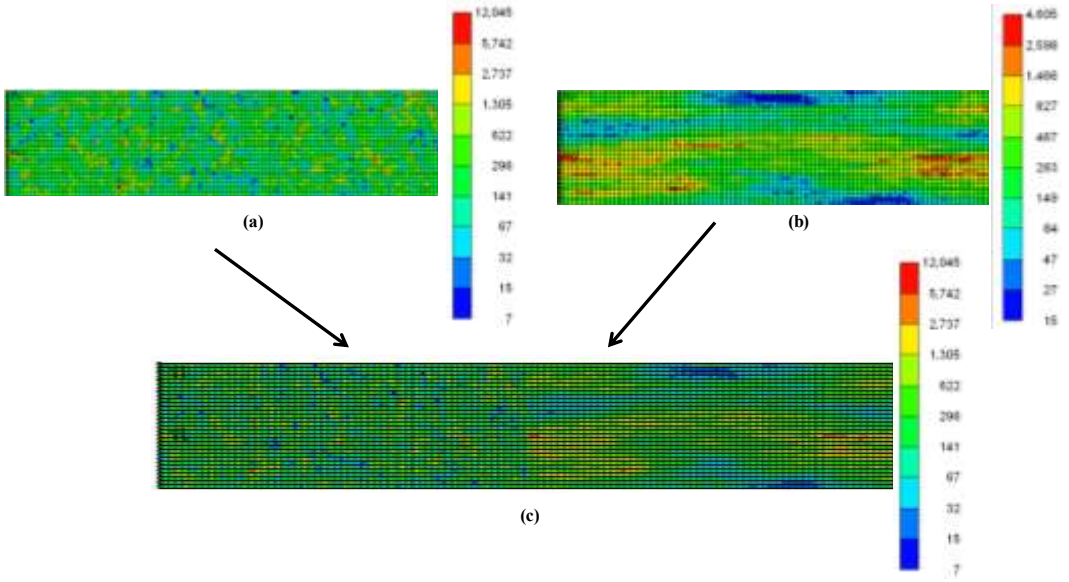

Figure 5.14: Permeability (mD) distribution of combined model and its component simulations models (a) 128 X 32 model with V_{DP} = 0.6, L_{XD} = 0.0 and L_{YD} = 0.0 (b) 128 X 32 model with V_{DP} = 0.6, L_{XD} = 0.25 and L_{YD} = 0.1 and (c) combined model with dimensions 256 X 32.

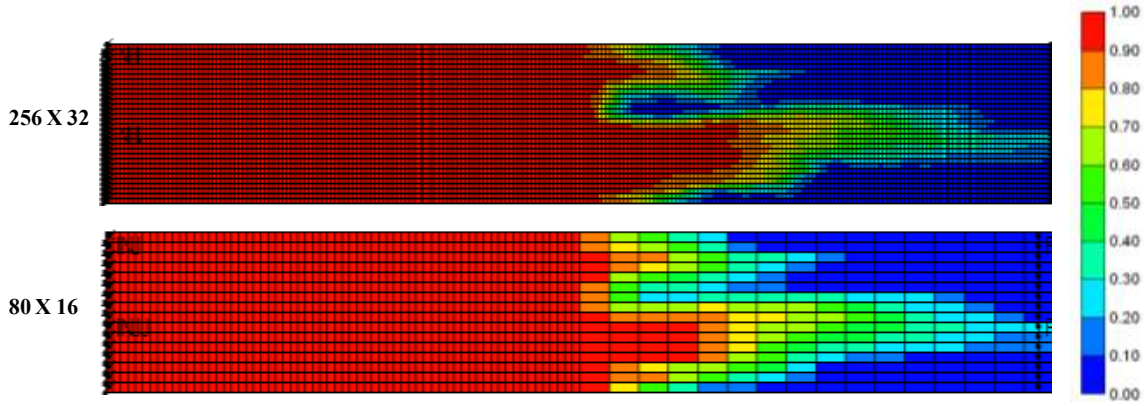

Figure 5.15: Solute concentration map at 0.7 pore volume injected for the fine scale simulation model (256 X 32) and the non-uniformly coarsened upscaled model (80 X 16).

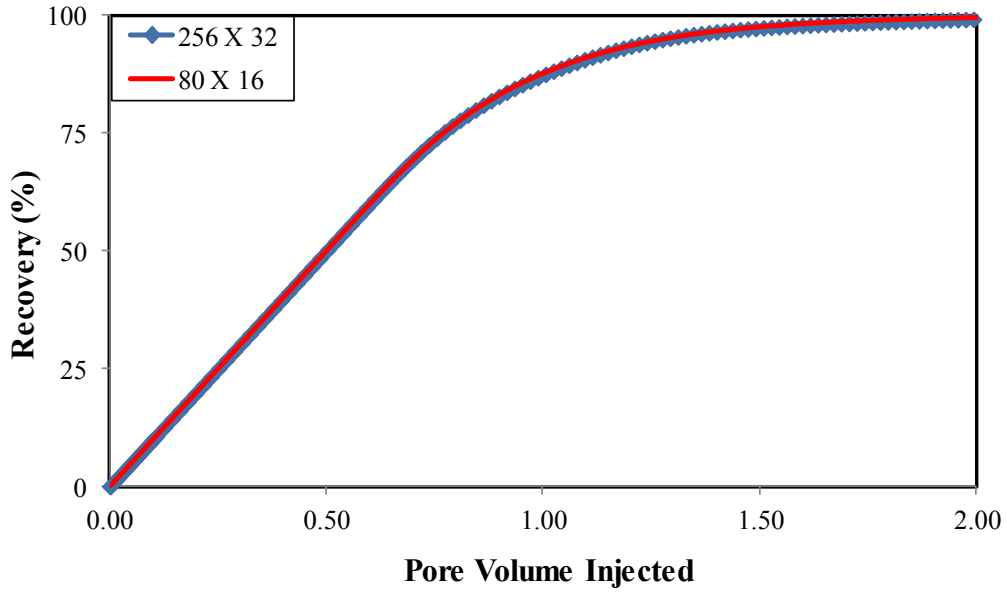

Figure 5.16: Recovery from FCM simulations fine scale simulation model (256 X 32) and the non-uniform coarsened upscaled model (80 X 16).

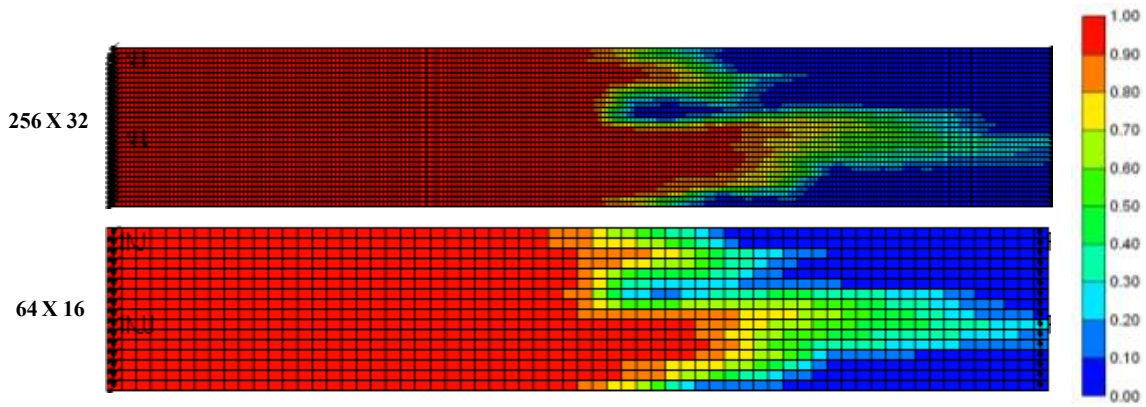

Figure 5.17a: Solute concentration map at 0.7 pore volume injected for the fine scale simulation model (256 X 32) and the uniform coarsened upscaled model (64 X 16).

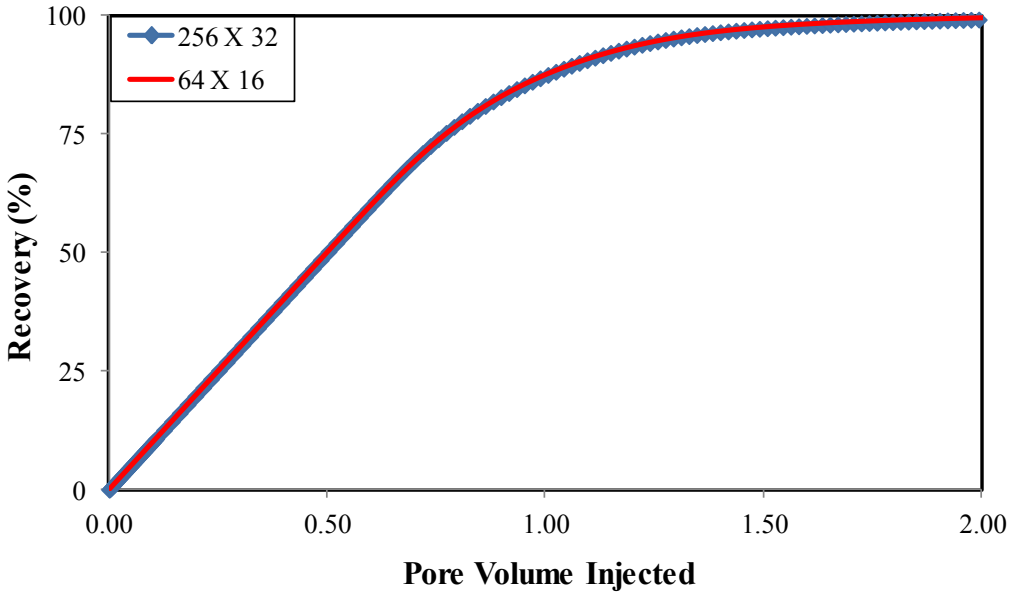

Figure 5.17b: Recovery from FCM simulations fine scale simulation model (256 X 32) and uniformly coarsened upscaled model (64 X 16).

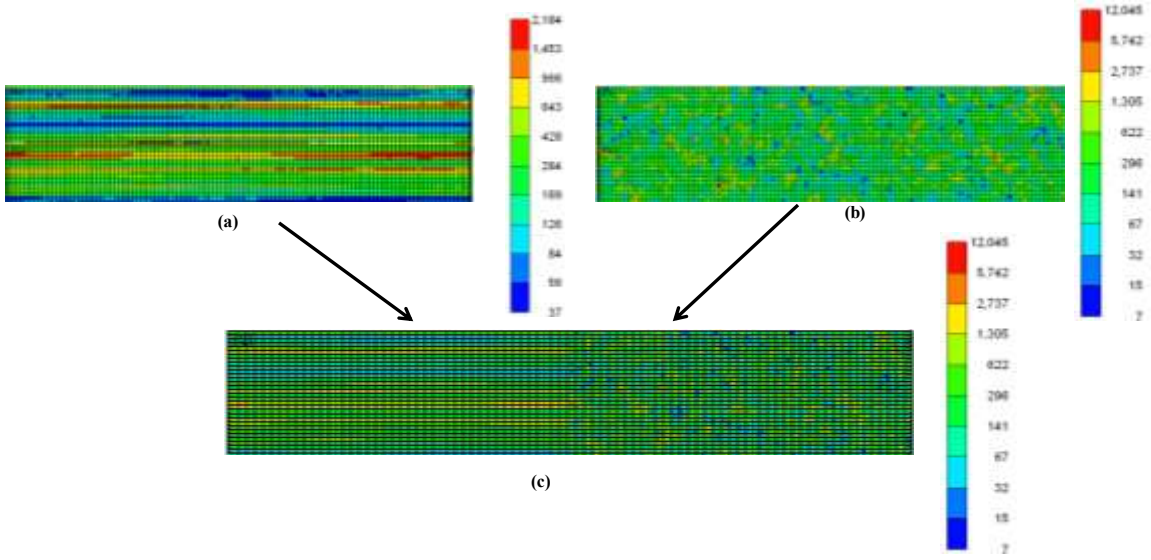

Figure 5.18: Permeability (mD) distribution of combined model and her component simulations model (a) 128 X 32 model with V_{DP} = 0.6, L_{XD} = 5.0 and L_{YD} = 0.0 (b) 128 X 32 model with V_{DP} = 0.6, L_{XD} = 0.0 and L_{YD} = 0.0 and (c) combined model with dimensions 256 X 32.

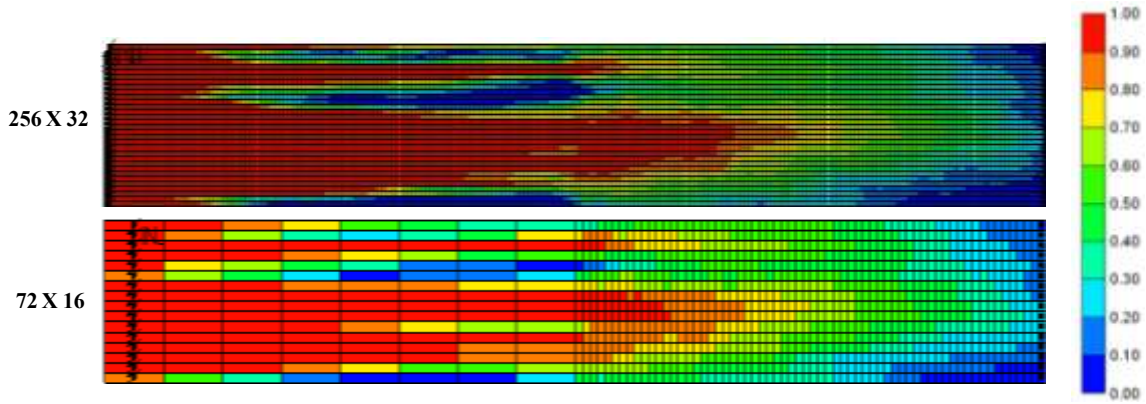

Figure 5.19a: Solute concentration map at 0.65 pore volume injected for the fine scale simulation model (256 X 32) and the non-uniform coarsened upscaled model (72 X 16).

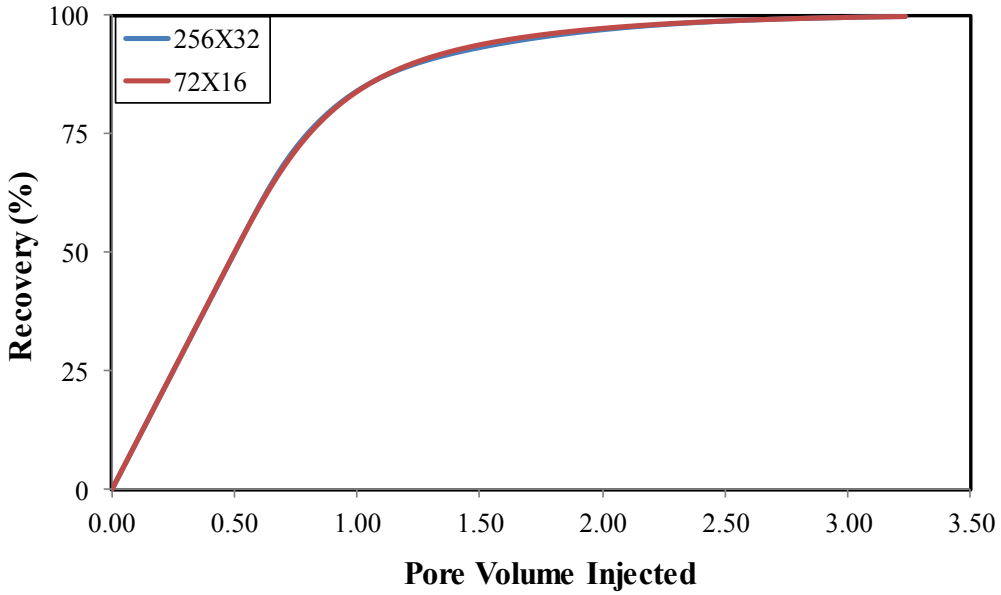

Figure 5.19b: Recovery from FCM simulations fine scale simulation model (256 X 32) and non-uniformly coarsened upscaled model (72 X 16).

Chapter 6: Effect of FCM Displacements Dimensionless Scaling Groups on Dispersion

This chapter presents the scaling groups affecting FCM displacements. The impact of each scaling group on longitudinal and transverse dispersion was investigated. Experimental design was then utilized to develop a response surface function for dispersivity based on the significance of the scaling groups.

Garmeh and Johns (2010) developed a response surface function for longitudinal dispersivity based on a set of FCM displacement scaling groups. In this chapter, we present the complete FCM scaling groups including buoyancy number, density number and dip angle. We also present the impact of these scaling groups on transverse dispersivity.

6.1 INTRODUCTION

Scaling analysis helps to relate the behavior of geometrically similar systems irrespective of scale (Li and Lake 1995, Shook *et al.* 1998). Systems are considered geometrically similar, if they can be described by similar set of physical laws, spatial orientations and they have similar boundary conditions (Rapoport 1955, Greenkorn *et al*. 1965).

Dimensionless scaling groups are usually obtained from either dimensional analysis or inspectional analysis. Dimensional analysis generates dimensionless scaling groups using the knowledge of all pertinent variables influencing the system, though the governing equations may not be known (Rapoport 1955). Inspectional analysis is more robust compared to dimensional analysis because it uses the governing equations and

imposed boundary conditions to generate dimensionless scaling groups (Shook *et al*. 1992, Gharbi *et al.* 1998, Ghanbarnezhad Moghanlo 2012).

Dispersion is scale dependent, as dispersion obtained from field data is orders of magnitude larger than those measured in the laboratory (Greenkorn and Cala 1968, Arya *et al.* 1988). Heterogeneity and permeability autocorrelations have also been shown to affect dispersion in chapters 3 and 4.

Using inspectional analysis, the complete set of dimensionless scaling group affecting FCM displacements is presented.

6.2 FCM DISPLACEMENTS SCALING GROUPS

Inspectional analysis was utilized to determine the complete scaling groups affecting FCM displacements. The governing equations for FCM displacements assuming incompressible flow includes the conservation equation, continuity equation and other auxiliary equations such as Darcy's equation and mixing rule for viscosity and density.

The CDE is a statement of conservation of mass. Assuming no chemical reaction and adsorption, the CDE is expressed as,

$$\phi\frac{\partial C}{\partial t}+\nabla\cdot\left(\vec{u}C\right)-\nabla\cdot\phi\left(\vec{\vec{D}}\nabla C\right)=0 \tag{6.1}$$

where C is the solute concentration (mass/unit volume of solution), ϕ is the porosity, $\vec{u}$ is the Darcy velocity vector and $\vec{\vec{D}}$ is the dispersion tensor. The continuity equation for steady state flow is given by,

$$\nabla.\vec{u}=0\,. \tag{6.2}$$

The Darcy velocity vector $\vec{u}$ is define by Darcy's law as,

$$\vec{u}=\frac{k}{\mu_m}\left(\nabla P\right). \tag{6.3}$$

The mixture viscosity (μ_m) and mixture density (ρ_m) are defined by quarter and linear mixing rules respectively (Gharbi *et al.* 1998, Garmeh and Johns 2010). The definition of the mixing rule and other boundary conditions used to define the scaling groups is detailed in Appendix C. Appendix C also details the derivation of the scaling groups using inspectional analysis.

The inspectional analysis yields seven dimensionless scaling groups that affect FCM displacements. Three heterogeneity factors, Dykstra-Parsons coefficient (V_{DP}) and the autocorrelation lengths in the longitudinal and transverse directions, are added to account for permeability variation and distribution.

6.2.1 Validation of Scaling Groups

The scaling groups that are derived are Peclet number (N_{pe}), transverse dispersion number (N_D), effective aspect ratio (R_L), viscosity ratio (V_o), buoyancy number (N_g), density number (N_ρ), dip angle (N_α). The heterogeneity factors included are the Dykstra Parson Coefficient (V_{DP}), and dimensionless horizontal (L_{XD}) and vertical correlation lengths (L_{YD}).

Validating scaling groups from inspectional analysis may be unnecessary if the governing and auxiliary equations are complete (Shook *et al.* 1992). The derived scaling groups were validated by comparing three simulation models with the same scaling group values, but different reservoir and fluid properties. The reservoir and fluid properties were chosen such that they will result in the same scaling group values. Table 6.1 shows the values of the scaling groups and their different input parameters used for the validation.

FCM simulations were conducted using each of the simulations models by injection of two pore volumes of solute across the model (fully perforated) from one end and the solute is produced at the same rate from the other end of the model. The simulations were performed with CMG GEM® simulator. All the simulation models have 128 grid cells in the y-direction and 32 grid blocks in the x-direction. The top and bottom layer are no-flow boundaries. The local longitudinal and transverse dispersivity is estimated using equation (4.2). The estimated dispersivities were averaged across the cross-section and normalized with the length of the medium.

Figure 6.1 shows the solute concentration map at 0.5 PVI. The solute concentration maps show that the flow behaviors in the models are similar for each case, though some of the input parameters are different. The three models show gravity override due to the high buoyancy number (N_g = 1.0). The estimated normalized longitudinal dispersivity is also similar across the length of the simulation models (Figure 6.2). The estimated transverse dispersivity is negligible for each case as the solute is injected and equilibrates across the entire cross-section. The recovery from the three cases is also comparable showing that the behavior of different simulation models with the same scaling groups are similar (Figure 6.3).

6.2.2 Scaling Group Definition and Sensitivity Analysis

One of the advantages of inspectional analysis over dimensionless analysis is that the physical significance of derived scaling groups are readily apparent (Gharbi *et al.* 1998). This section gives the definition of each scaling groups and their impact on longitudinal and transverse dispersivity, while keeping all other scaling groups constant. Except otherwise stated all simulations in this section are FCM displacements with 128

grids in the x-direction and 32 grid-blocks in the y-directions. The simulations were conducted with the CMG-GEM® simulator.

Peclet Number: The Peclet number (N_{pe}) is inversely proportional to dispersion and gives the ratio of the characteristic time a particle will be transported by dispersion compared to convection in the same direction. The Peclet number is mathematically expressed as,

$$N_{pe} = \frac{v_x L}{D_L} \tag{6.4}$$

where v_x is the average pore velocity in the longitudinal direction and L is the length of the medium in the same direction. The expression for longitudinal dispersion coefficient (D_L) (see equation 3.14a) can be substituted into equation (6.4) to obtain (Garmeh and Johns 2010),

$$N_{pe} = \frac{2L}{2\alpha_L + 2\alpha_T \left(\frac{v_z}{v_x}\right)^2 + \Delta x} \tag{6.5}$$

Since flow is dominant in the x-direction, the log average of the velocity anisotropy $\left(v_z / v_x\right)$ is small. Thus the Peclet number in numerical simulation can be estimated from the input dispersivity (α_L and α_T) and grid-block size in the longitudinal direction (Δx).

The effect of increasing Peclet number is to reduce dispersion. The 2-D solute concentration map from FCM simulation of two different Peclet numbers (N_{pe} = 256 and N_{pe} =64) shows that reducing Peclet number increases both longitudinal and transverse dispersion (Figure 6.4). Figure 6.4 shows more pronounced mixing when N_{pe} = 64 compared to when N_{pe} = 256. The estimated average dispersivities (both longitudinal and transverse) confirm that as the Peclet number reduces dispersion increases (Figures 6.5 and 6.6).

The inverse of the Peclet number gives an estimate of the effect of the input Peclet number on the estimated normalized longitudinal dispersivity.

$$N_{pe} = \frac{v_x L}{D_L} = \frac{v_x L}{\alpha_L v_x} = \frac{L}{\alpha_L} = \frac{1}{\alpha_{LD}} \tag{6.6}$$

If the inverse of the Peclet number is subtracted from the estimated normalized dispersivity, the two cases (Npe = 256 and Npe = 64) should have similar levels of physical dispersion in the longitudinal direction, as all the scaling factors are now equal. Figure 6.7 confirms that the normalized longitudinal dispersivity collapses to one curve after subtracting the inverse of their respective Peclet number.

*Transverse Dispersion Number: Transverse d*ispersion number (N_D) indicates the ratio of transverse dispersion to longitudinal dispersion. A large value of dispersion number indicates high level of transverse dispersion, which will result in more mixing along the cross-section perpendicular to the flow direction. Large transverse dispersion may result in a stabilized mixing zone that reduces displacement instability such as channeling, as the solute concentration is equilibrated across the simulation cross-section. The dispersion number is expressed as,

$$N_D = \frac{L}{H}\sqrt{\frac{D_T}{D_L}} \tag{6.7}$$

The dispersion number can be mathematically simplified by substitution of the definition of the dispersion coefficients (Garmeh and Johns 2010).

$$N_D = \frac{L}{H}\sqrt{\frac{2\alpha_L\left(\frac{v_z}{v_x}\right)^2 + 2\alpha_T + \left(\frac{v_z}{v_x}\right)\Delta z}{2\alpha_L + 2\alpha_T\left(\frac{v_z}{v_x}\right)^2 + \Delta x}} \tag{6.8}$$

The dispersion number in the simulation model can thus be estimated from the input dispersivities, grid-block sizes and the log-averaged velocity anisotropy.

Three simulation models with different dispersion numbers (N_D = 1.0, N_D = 10.0 and N_D = 100.0) were considered. The large dispersion number case (N_D = 100.0) was achieved by using a large input dispersivity of 678 ft compared to 0 ft when N_D = 1.0 and 7 ft when N_D = 10.0. Such a large input dispersivity is impractical but shows the asymptotic behavior of the transverse dispersion number.

The solute concentration map from the 2-D simulations at 0.4 PVI (Figure 6.8) shows pronounced mixing across the cross-section of the model as the dispersion number increases. For the case (N_D = 100), the solute concentration is fully equilibrated across the entire cross-section, due to large transverse dispersion. This is analogous to vertical equilibrium as the concentration gradient in the transverse direction is negligible.

The effect of increasing dispersion number is to increase the transverse dispersion. Increasing dispersion number also enhances longitudinal dispersion as the longitudinal dispersion increases and approach asymptotic value faster with increasing dispersion number (Figures 6.9 and 6.10).

Effective aspect ratio: The effective aspect ratio gives the ratio between the time for the fluid to cross the reservoir in the longitudinal direction compared to the time required to cross the reservoir in the transverse direction (Lake 1989). As the effective aspect ratio increases, cross-flow increases and so does dispersion. At aspect ratios greater than 10, vertical equilibrium can be assumed. At vertical equilibrium, the sum of all fluid driving forces in the transverse direction is zero (Lake 1989, Shook *et al.* 1992). The effective aspect ratio is given as

$$R_L = \left[\frac{L}{H} \sqrt{\frac{k_z}{k_x}} \right]. \quad (6.9)$$

At effective aspect ratio of zero, there is no cross-flow and there is negligible dispersion. Three different values of aspect ratio were considered (R_L = 0.0, R_L = 0.1 and R_L = 10).

The solute concentration maps (Figure 6.11) shows that when the effective aspect ratio is zero, solute dispersion is limited to a single layer. As the effective cross-flow increases (R_L = 0.1), dispersion increases as the solute can now dilute across layers. It is also noted that only a small level of cross flow is required for transverse dispersion to be active, though dispersion will increase with increasing cross-flow. Estimated longitudinal and transverse dispersion show that increasing effective aspect ratio increases dispersion (Figures 6.12 and 6.13).

Viscosity ratio: Viscosity ratio is the ratio of the oil viscosity (μ_o) to the solute viscosity (μ_s). Viscosity ratios greater than 1.0 is considered unfavorable as it causes the solute to channel through high permeability regions. The viscosity ratio is defined as,

$$V_o = \left[\frac{\mu_o}{\mu_s} \right] \quad (6.10)$$

Two cases of viscosity ratios were considered (V_o = 0.6 and V_o = 20). These two cases represent favorable and unfavorable displacements. The viscosity ratio is the mobility ratio for FCM displacements.

Unfavorable viscosity ratio increases solute channeling, as the less viscous solute channels through high permeability regions, while minimizing local mixing. The solute concentration map shows increased spreading through high permeability regions at high viscosity ratio compared to low viscosity ratio (Figure 6.13). The estimated dispersivity

shows a reduction in true mixing as both longitudinal and transverse dispersivity reduces with increasing viscosity ratio (Figures 6.14 and 6.15).

Buoyancy number: The Buoyancy number (N_g) relates the gravity to viscous forces. The terminology buoyancy number is preferred to gravity number because it depends on density difference (Shook *et al.* 1992). A high value of buoyancy number can result in gravity override. Gravity override causes solute to flow through the top section of the model, enhancing longitudinal dispersion. The buoyancy number is defined as,

$$N_g = \frac{k_x \Delta\rho g}{v_x \mu_o} \tag{6.11}$$

where k_x is the mean permeability in the longitudinal direction, $\Delta\rho$ is the difference between the solute density and oil density, g is the gravitational acceleration and μ_o is the oil viscosity. Two cases of buoyancy number were considered (N_g = 0.0001 and N_g = 0.7). High buoyancy number results in gravity override. Gravity override causes solute to flow towards the top section of the model, enhancing longitudinal dispersion (Figure 6.16). The estimated longitudinal dispersivity increased with increased buoyancy number (Figure 6.17). A very slight but insignificant reduction is noticed in estimated transverse dispersivity with increasing buoyancy number.

Density number: The density number (N_ρ) is the ratio of the difference between oil (ρ_o) and solute (ρ_s) density and the oil density. The density number is expressed as,

$$N_\rho = \frac{\Delta\rho}{\rho_o} \tag{6.12}$$

Two simulation cases with density number of 0.5 and 10 were considered. The density number was shown to have insignificant effect on both longitudinal and transverse dispersion (Figures 6.18 and 6.19). The estimated dispersivities for the two density

numbers were identical. This result confirms the result of Gharbi *et al*. (1998), which shows that changing density number (for gravity dominated and viscous dominated flow) does not affect recovery for miscible displacements. The effect of gravity was eliminated by conducting the 2D simulation in I-J orientation with a single layer in the k-direction.

Dip Angle: The dip angle (N_α) is geometrical property of the medium as it does not contain any fluid or reservoir properties (Shook *et al.* 1992). When dip angle is zero the model is horizontal along the x-axis and it tilts upward with increasing dip angle. The dip angle was varied between 0.0^o and 20^o, while keeping other scaling groups constant. The estimated longitudinal and transverse dispersivity were not affected by the changing dip angle (Figures 6.20 and 6.21). The solute concentration map for the simulation models with different dip angle also shows similar solute distribution (Figure 6.22).

Heterogeneity Factors: Heterogeneity is a property of porous media that quantifies the spatial variation of properties. Increasing level of heterogeneity causes a more pronounced spreading of the flood front. Permeability is considered the most significant heterogeneity, because of its higher variation compared to other rock properties and its importance in determining flow characteristics (Lake and Jensen 1989).

Three heterogeneity factors have been included to account for the effect of heterogeneity. The first is the Dykstra-Parsons coefficient (V_{DP}), which is a static measure of heterogeneity and accounts for permeability variation. V_{DP} is estimated using the median permeability ($k_{0.5}$) and the permeability at one standard deviation ($k_{0.84}$) above the median, when the permeability data is plotted on a log-probability plot (Dykstra-Parsons 1950, Lake and Jensen 1989).

$$V_{DP} = \frac{k_{0.5} - k_{0.84}}{k_{0.5}} \tag{6.13}$$

Lake and Jensen (1989) defines autocorrelation as the tendency of two spatially separated quantities to have similar distance. The dimensionless longitudinal and transverse autocorrelation lengths (L_{XD} and L_{YD}) are introduced to account for the spatial variation in permeability. The dimensionless autocorrelation lengths are the correlation lengths in the respective direction normalized by the total length in that direction. Dimensionless autocorrelation lengths of zero indicate random permeability distribution, while a large dimensionless autocorrelation length (> 1) indicates a layered medium.

The stochastic permeability fields used in this research are generated with FFTSIM (Jennings *et al.* 2000). FFTSIM uses the spectral method to generate normally distributed numbers conditioned to the input correlation structures. The normally distributed outputs are converted to a log-normal permeability distribution with specified mean and variance.

The effect of permeability variations (V_{DP}) and spatial distributions (L_{XD} and L_{YD}) have already been considered in chapter 4. Dispersion increases with increasing level of heterogeneity (see Figures 4.19 and 4.20). Lake and Jensen (1989) defined dispersivity, a measure of dispersion, as a dynamic measure of heterogeneity.

The effect of increasing longitudinal autocorrelation is to cause solute to travel through continuous layers increasing longitudinal dispersion while minimizing transverse dispersion (see Figures 4.24 and 4.25). Increasing autocorrelation in the transverse direction causes solute to equilibrate quickly over spatially correlated transverse sections. As solute equilibrates over these transverse sections, dispersion reduces (see Figures 4.28 and 4.29).

6.3 DEVELOPMENT OF RESPONSE SURFACE FOR DISPERSIVITY

Garmeh and Johns (2010) generated response surface for longitudinal dispersion, but did not include the effect of other scaling groups such as gravity. In this section response surface will be generated for both longitudinal and transverse dispersivity while accounting for all significant scaling groups including gravity.

A response surface is a mathematical expression obtained for a process variable in terms of pertinent variables and parameters over a specified range of interest (Myers and Montgomery 1995). Experimental design, which is a method to obtain maximum information using minimal amount of experiments or simulations, is used to generate a response surface (Friedmann *et al.* 2003). Experimental design generates the number and state of each independent parameters used in the simulations to obtain both main and interaction effects of each parameter on the process variable. The Box-Behnken experimental design is used for our analysis.

Box-Behnken experimental design (Box and Behnken 1960) is an independent three level design (high, intermediate and low) that captures quadratic effects. Box-Behnken design is independent because it does not contain an embedded factorial or fractional factorial design (NIST 2006). Box-Behnken can capture the main and the interaction effects of each independent parameter. A quadratic model for a process variable (Y) that depends on two independent parameters (X_1 and X_2) is expressed as (Design Expert 2007),

$$Y = \beta_o + \beta_1 X_1 + \beta_2 X_2 + \beta_{12} X_1 X_2 + \beta_{11} X_1^2 + \beta_{22} X_2^2 + \varepsilon \qquad (6.14)$$

where β_o accounts for the interception constant, $\beta_i X_i$ accounts for the main effects and linear terms, the two factor interactions $\beta_{ij} X_i X_j$ accounts for the interaction between parameters while the quadratic term $\beta_{ii} X_i^2$ accounts for the curvature in the responses.

The experimental error (ε) is the residual between the fitted function and the simulation output.

The high, intermediate and low scaling values used for the experimental design falls within the 5th to 95th percentiles of those values obtained from several databases (Wood *et al.* 2008, Ghomian 2008, Garmeh and Johns 2010). There are seven significant scaling factors that are considered for the experimental design. Density number and dip angle were not included in the experimental design because they have been shown (see section 6.2.2) not to significantly affect dispersion. The effect of Peclet number on estimated dispersion is eliminated by subtracting the inverse of the Peclet number from the estimated longitudinal dispersivities. The values of the parameters used in the experimental design are shown in Table 6.2.

The values used for the experimental design are normalized between -1 and +1 to ensure that the magnitude of the coefficients from the response surface model indicates the significance of each scaling group. This is necessary because of the range of values of the scaling groups can differ by several orders of magnitude. The scaling groups are normalized linearly between -1 and +1 using the expression,

$$\bar{X} = -1 + 2 \cdot \left(X - L \right) / \left(H - L \right) \tag{6.15}$$

where $\bar{X}$ is the normalized value, X is the scaling factor to be normalized, H and L are the high and low value of the scaling factor respectively. The normalized intermediate values are not necessarily zero, because they are determined from the median of databases (Wood *et al.* 2008). The normalized values of the scaling groups, which are used to generate the response surface fits, are shown in Table 6.3.

Sixty-two (62) simulations were required based on three-level Box-Behnken design. Each simulation is repeated with five different permeability realizations with similar V_{DP} and autocorrelation lengths. These five simulations are then averaged to

represent the response for a particular set of V_{DP} and autocorrelation lengths. Therefore 310 simulations were conducted. The values of each simulation used in the experimental design are shown in Appendix F

A response surface function for the normalized longitudinal and transverse dispersivity at dimensionless distances equal to 1.0 and 0.8 were generated and analyzed with Design Expert ™ (Stat-Ease 2010). The response surface function is a second order polynomial of the form,

$$Y = \beta_o + \sum_{i=1}^{n} \beta_i \bar{X}_i + \sum_{i<j}^{n} \sum_{j=2}^{n} \beta_{ij} \bar{X}_i \bar{X}_j + \sum_{i=1}^{n} \beta_{ii} \bar{X}_i^2 \qquad (6.16)$$

where $\bar{X}$ is the normalized value of the dimensionless scaling factor and β_i are the coefficient of the response function. A satisfactory fit was obtained between the response surface and the simulation results (Figures 6.23 and 6.24).

Tables 6.4 and 6.5 shows the coefficients of the response surface function for the normalized longitudinal and transverse dispersivity at $X_D = 1.0$. The coefficients of the response function at $X_D = 0.8$ is shown in Appendix F.

The effect of each scaling group on the estimated longitudinal and transverse dispersivity can be visualized with the aid of a Pareto chart. The Pareto chart is plotted using the absolute value of the linear coefficients of the response surface function. Since the scaling groups used to generate the response surface function are normalized, the magnitude of the coefficients is an indicator of the significance of respective scaling groups. However, the Pareto chart is only qualitative as the cross interactions between variables are not captured by the chart. The V_{DP} and viscosity ratio are the most significant scaling groups affecting longitudinal dispersivity (Figure 6.25a). The transverse dispersivity is most significantly impacted by the dispersion number (N_D), followed by the level of heterogeneity (V_{DP}) and the correlation lengths (Figure 6.25b).

The Pareto chart was also generated using the absolute t-values using Design Expert ™ (Design Expert technical manual 2007) (see Figure 6.26). The Pareto chart confirms that V_{DP} most significantly affects longitudinal dispersivity, while the transverse dispersivity is most significantly impacted by the dispersion number. The arrangement of the significance of other scaling factors is different for the Pareto chart from t-test and from coefficients of the response function. The reason for this difference is that t-test is generated using linear model and thus unaffected by interactions between factors.

Rashid *et al.* (2012) proposed a measure of heterogeneity that uses the shear-strain rate of the single phase velocity field. The measure is called the Homogeneity Index (Hs). Hs is believed by the authors to correlates linearly (better compared to Dykstra Parsons) with breakthrough time and recovery for various realizations of permeability distribution for a waterflood. The details of the formalism to derive Hs and our validation exercise are summarized in Appendix G.

The Homogeneity index is easy to compute and shows some advantages in differentiating permeability realizations for waterfloods. However Hs did not replicate the same advantage in discriminating heterogeneity when considering dispersion. Dispersion is very sensitive to differences in flow structure and Hs may not be as robust as suggested to capture such detailed heterogeneity.

Sensitivity analysis shows that Hs is most significantly affected by the V_{DP}, correlation lengths (L_{XD} and L_{YD}) and effective aspect ratio (R_L) (Figure 6.27). If Hs are robust and can discriminate between permeability realizations, it can successfully replace V_{DP}, L_{XD}, L_{YD} and R_L in the characterization of heterogeneity. Response surface function for Hs in terms of V_{DP}, L_{XD}, L_{YD} and R_L is detailed in Appendix F.

We attempted to use Hs to replace these factors in the development of the response surface function. Hs were computed for each simulation case used for the

experimental design. Figures 6.28 and 6.29 show the accuracy of the response surface when Hs replace the conventional heterogeneity factors. The results clearly shows that Hs cannot replace conventional heterogeneity factors as the match obtained from the response function shows more scatters and pronounced deviation from the unit slope (compare Figures 6.28 and 6.23).

6.3 CONCLUSIONS

In this chapter we presented the complete dimensionless scaling groups that affect FCM simulations. The scaling groups included density number, dip angle and gravity number. We conducted sensitivity analysis of each of these scaling groups on both longitudinal and transverse dispersion.

Peclet number increases longitudinal dispersion but the effect of input Peclet number can be minimized by subtracting the inverse of the Peclet number from the estimated longitudinal dispersivity. The dispersion number causes an increase in dispersion, especially transverse dispersion. At high dispersion number, solute concentration equilibrates almost instantaneously across the model cross-section, eliminating concentration gradients in the transverse direction. Adverse mobility ratio can aid spreading as fluid channels through high permeability regions minimizing true mixing. A large gravity number can result in gravity override causing solute to flow through continuous layers enhancing dispersion. Dip angle and density number were also shown to be insensitive to dispersion.

A response surface function was generated for longitudinal and transverse dispersivity. The longitudinal dispersivity is most affected by the level of heterogeneity, while the transverse dispersivity is mostly impacted by the dispersion number.

The homogeneity index (Hs) was also presented and shown not to be robust enough to replace conventional heterogeneity factors, especially in discriminating permeability realizations for the purpose of estimating dispersion.

Scaling Groups	Case1	Case2	Case3
L_{XD}	0.25	0.25	0.25
L_{YD}	0.10	0.10	0.10
V_{DP}	0.60	0.60	0.60
N_D	1.72	1.72	1.72
V_o	1.50	1.50	1.50
R_L	2.50	2.50	2.50
N_{pe}	130	130	130
N_g	1.00	1.00	1.00
N_ρ	0.50	0.50	0.50
N_α	0.00	0.00	0.00
L/H	3.00	3.00	3.00
Parameters			
Δx (ft)	1.50	2.50	3.50
Δz (ft)	2.00	3.33	4.67
α_L	0.76	1.26	1.77
α_T	0.07	0.12	0.17
$\Delta\rho$ (lb/cu. ft)	23.57	11.99	18.58
ρ_o (lb/cu. ft)	47.14	23.99	37.15
ρ_s (lb/ cu. ft)	23.57	11.99	18.58
μ_s (cp)	0.10	0.06	0.07
μ_o (cp)	0.15	0.09	0.10
q (bbl/day)	57.07	80.00	150.00

Table 6.1: Scaling groups and their constituent parameters used for validation

Group	Low	Intermediate	High
L_{XD}	0.1	0.25	2
L_{YD}	0.02	0.1	0.5
V_{DP}	0.4	0.6	0.8
N_D	1	3.3	10
V_o	1	5	25
R_L	0.1	6	10
N_g	0.001	0.02	0.1

Table 6.2: Scaling groups for experimental design and their values

Group	Low	Intermediate	High
L_{XD}	-1	-0.84	1
L_{ZD}	-1	-0.67	1
V_{DP}	-1	0.00	1
N_D	-1	-0.49	1
V_o	-1	-0.67	1
R_L	-1	0.19	1
N_g	-1	-0.62	1

Table 6.3: Scaling groups for experimental design and their normalized values

0.020194	*β_o		0.001252	* L_{YD} * N_G
0.001478	* L_{XD}		0.003271	* V_{DP} * N_D
-0.00026	* L_{YD}		0.002805	* V_{DP} * V_o
0.016842	* V_{DP}		-0.00141	* V_{DP} * R_L
0.001526	* N_D		-0.00221	* V_{DP} * N_G
-0.00563	* V_o		-0.00085	* N_D * V_o
-0.00102	* R_L		0.006214	* N_D * R_L
4.2E-06	* N_G		0.002201	* N_D * N_G
-0.00063	* L_{XD} * L_{YD}		-0.00205	* V_o * R_L
6.77E-05	* L_{XD} * V_{DP}		-0.00174	* V_o * N_G
-0.00085	* L_{XD} * N_D		0.00081	* R_L * N_G
-0.00246	* L_{XD} * V_o		-0.00287	* L_{XD}^2
-0.00363	* L_{XD} * R_L		-0.01035	* L_{YD}^2
0.000199	* L_{XD} * N_G		0.005904	* V_{DP}^2
-0.00266	* L_{YD} * V_{DP}		-0.00075	* N_D^2
0.003454	* L_{YD} * N_D		0.011195	* V_o^2
0.000218	* L_{YD} * V_o		-0.00189	* R_L^2
0.001804	* L_{YD} * R_L		-0.0033	* N_G^2

Table 6.4: Response surface function coefficients for normalized longitudinal dispersivity $x_D = 1.0$. The coefficients are multiplied by appropriate normalized scaling factors.

0.025491	*β_o		0.000403	* L_{YD} * N_G
-0.00401	* L_{XD}		-0.00436	* V_{DP} * N_D
0.002595	* L_{YD}		0.002122	* V_{DP} * V_o
0.00392	* V_{DP}		0.003569	* V_{DP} * R_L
0.012022	* N_D		-0.00024	* V_{DP} * N_G
-0.00186	* V_o		0.000846	* N_D * V_o
0.002461	* R_L		-0.00389	* N_D * R_L
-0.0003	* N_G		-0.00107	* N_D * N_G
-0.00063	* L_{XD} * L_{YD}		0.000292	* V_o * R_L
-0.00155	* L_{XD} * V_{DP}		-0.00044	* V_o * N_G
-0.00069	* L_{XD} * N_D		0.000346	* R_L * N_G
-0.00181	* L_{XD} * V_o		0.006235	* L_{XD}^2
2.88E-05	* L_{XD} * R_L		-0.00939	* L_{YD}^2
8.86E-05	* L_{XD} * N_G		0.002443	* V_{DP}^2
0.001106	* L_{YD} * V_{DP}		-0.01101	* N_D^2
0.00154	* L_{YD} * N_D		0.004353	* V_o^2
0.00045	* L_{YD} * V_o		-0.00459	* R_L^2
0.002414	* L_{YD} * R_L		-0.00558	* N_G^2

Table 6.5: Response surface function coefficients for normalized transverse dispersivity at $x_D = 1.0$. The coefficients are multiplied by appropriate normalized scaling factors.

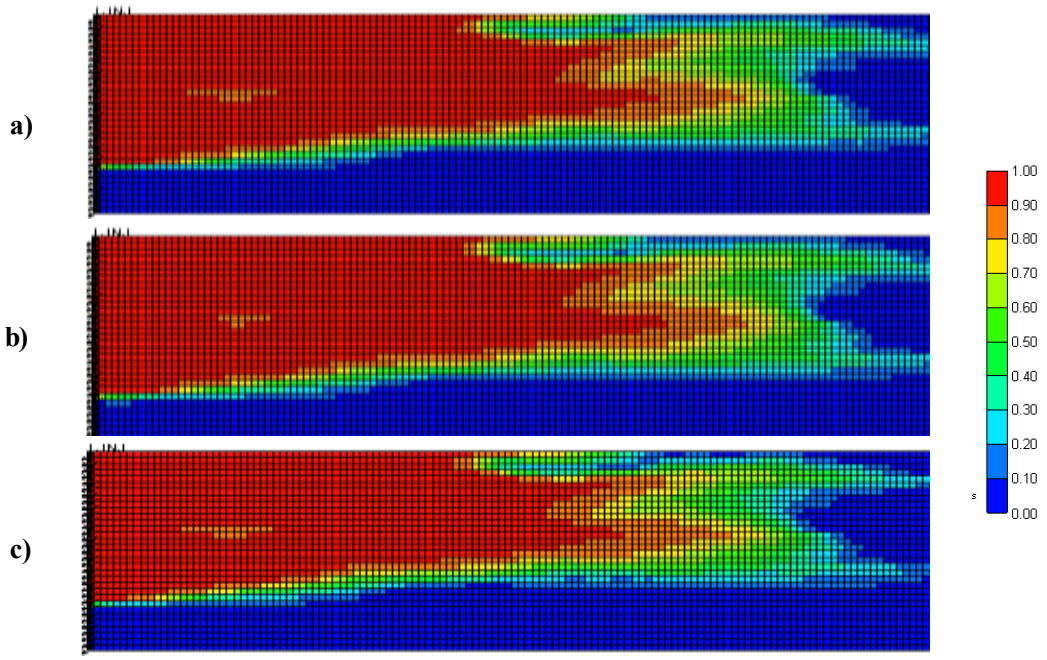

Figure 6.1: Solute concentration map at 0.5 PVI for the simulation models used for validation (a) case 1 (b) case 2 and (c) case 3.

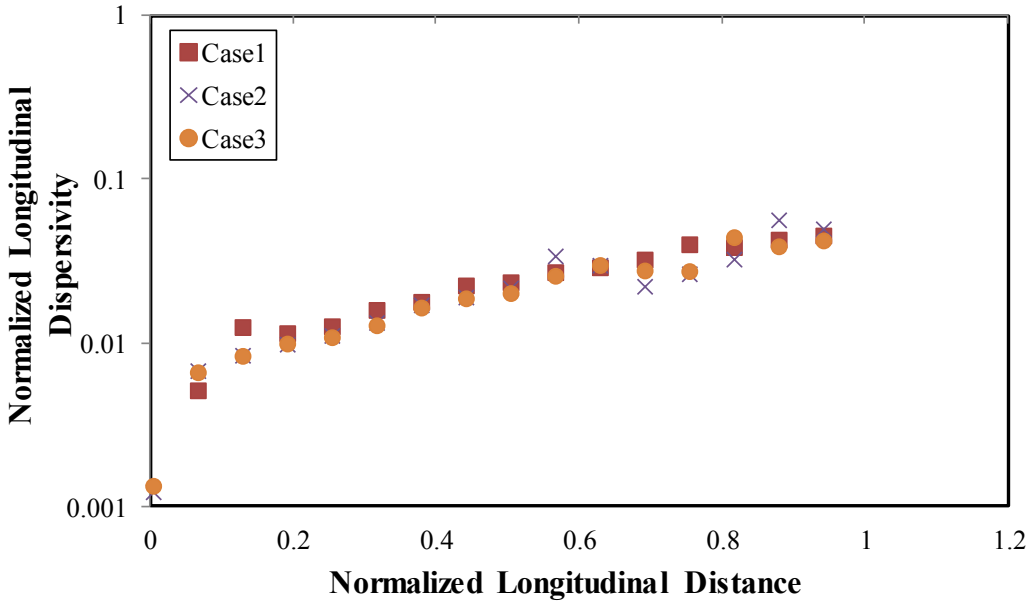

Figure 6.2: Estimated normalized longitudinal dispersivity for simulation models with similar dimensionless scaling groups.

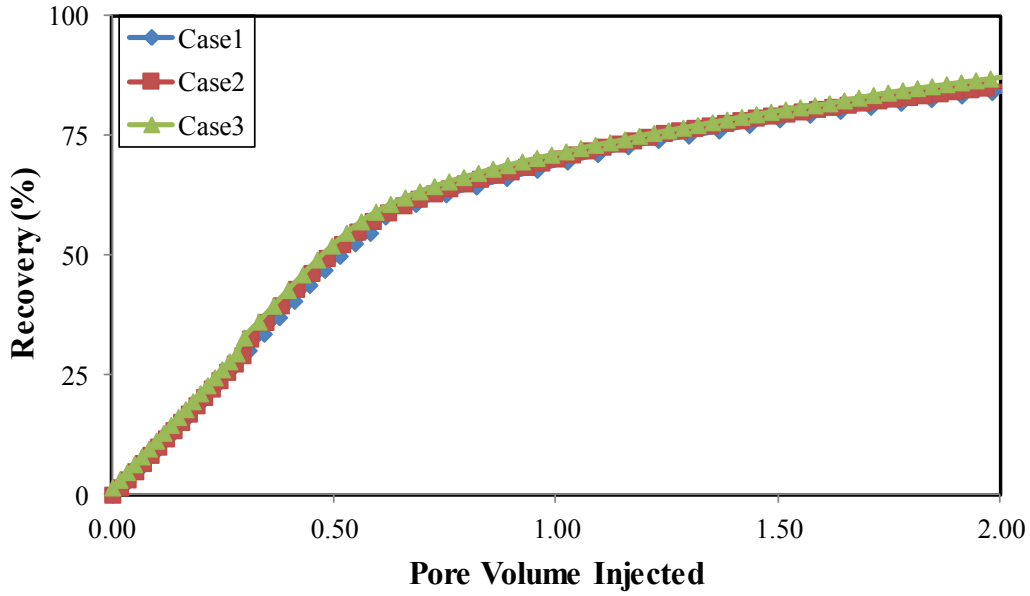

Figure 6.3: Hydrocarbon recovery for simulation models with similar dimensionless scaling groups.

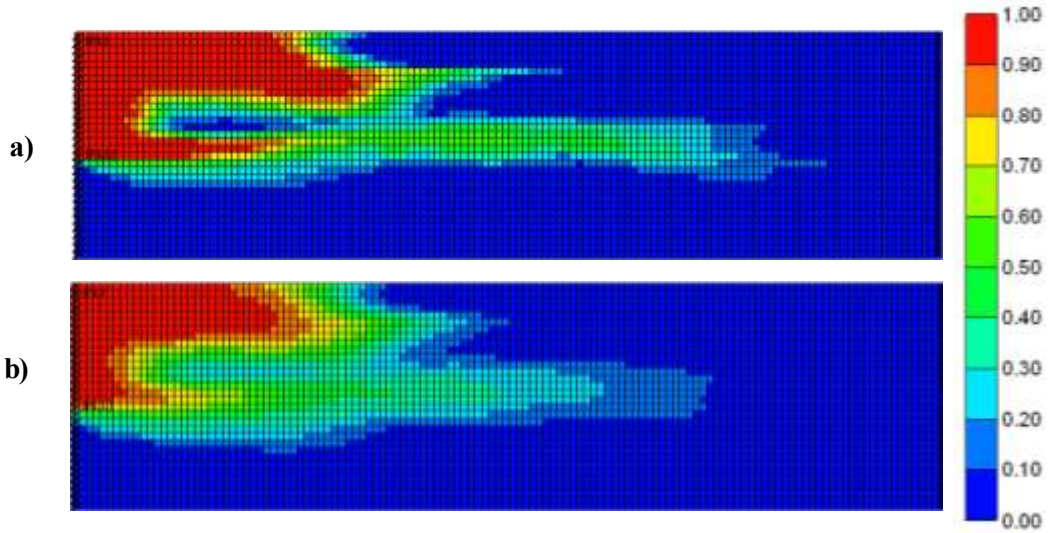

Figure 6.4: Solute concentration map at 0.2 pore volume injected for models with different Peclet number (a) $N_{pe} = 256$ and (b) $N_{pe} = 64$. Other scaling groups are constant $L_{XD} = 0.25$, $L_{YD} = 0.1$, $V_{DP} = 0.6$, $N_D = 1.0$, $V_o = 1.0$, $R_L = 2.5$, $N_\rho = 0.0$, $N_g = 0.0$, $N_\alpha = 0.0^O$.

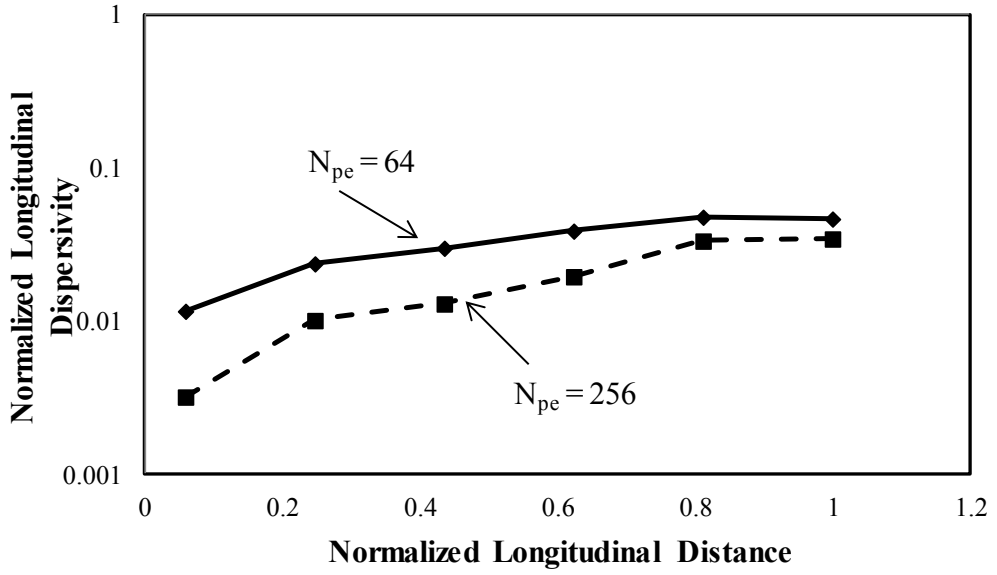

Figure 6.5: Normalized longitudinal dispersivity from FCM simulation of simulation models with different Peclet number (N_{pe}). Other scaling groups are constant $L_{XD} = 0.25$, $L_{YD} = 0.1$, $V_{DP} = 0.6$, $N_D = 1.0$, $V_o = 1.0$, $R_L = 2.5$, $N_\rho = 0.0$, $N_g = 0.0$, $N_\alpha = 0.0^O$.

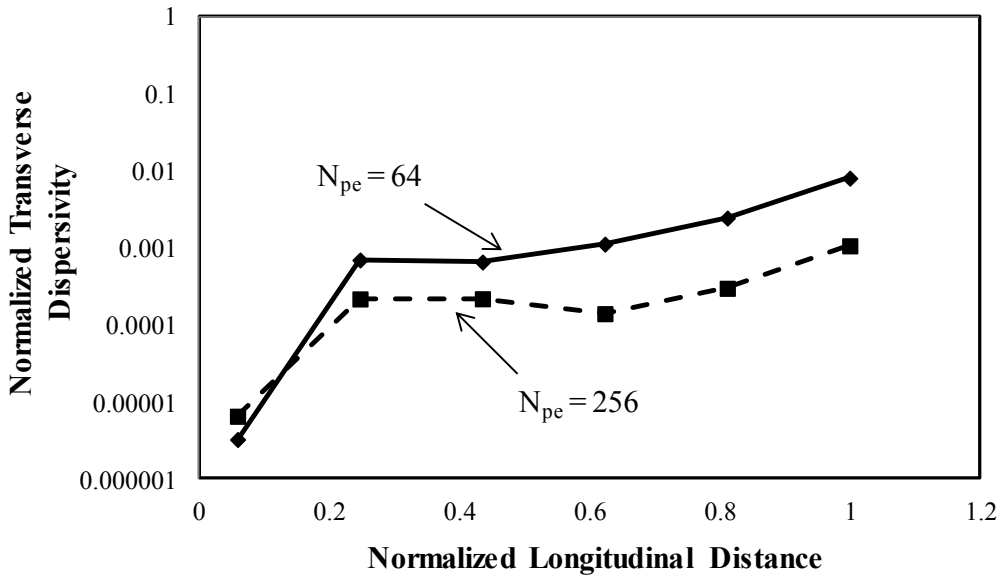

Figure 6.6: Normalized transverse dispersivity from FCM simulation of simulation models with different Peclet number (N_{pe}). Other scaling groups are constant $L_{XD} = 0.25$, $L_{YD} = 0.1$, $V_{DP} = 0.6$, $N_D = 1.0$, $V_o = 1.0$, $R_L = 2.5$, $N_\rho = 0.0$, $N_g = 0.0$, $N_\alpha = 0.0^O$.

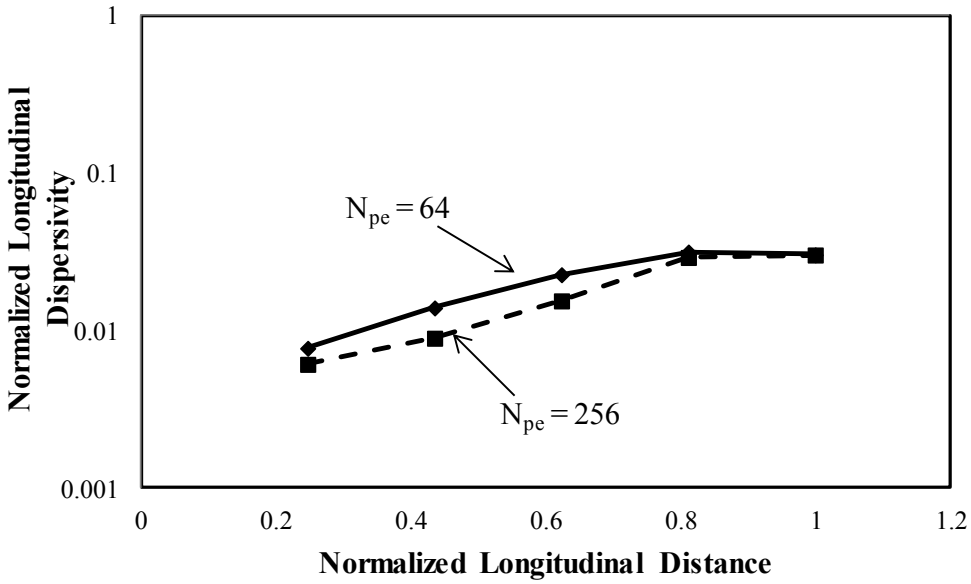

Figure 6.7: Normalized longitudinal dispersivity (minus the inverse of respective Peclet numbers) of simulation models with different Peclet number (N_{pe}). Other scaling groups are constant $L_{XD} = 0.25$, $L_{YD} = 0.1$, $V_{DP} = 0.6$, $N_D = 1.0$, $V_o = 1.0$, $R_L = 2.5$, $N_\rho = 0.0$, $N_g = 0.0$, $N_\alpha = 0.0^O$

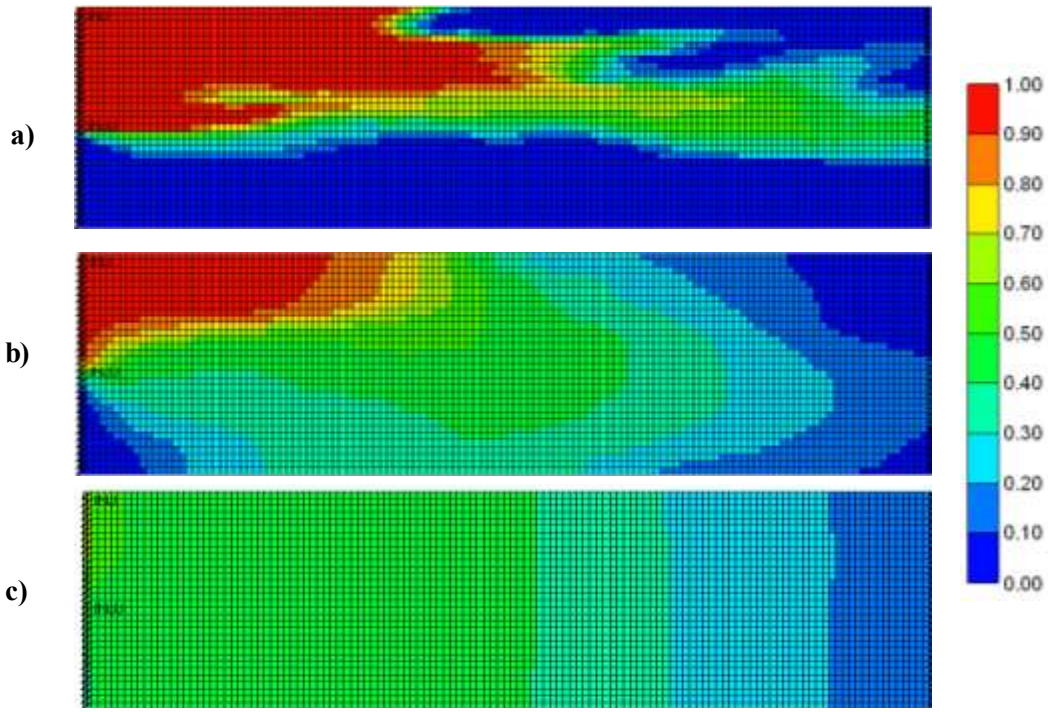

Figure 6.8: Solute concentration map at 0.4 pore volume injecte for models with different dispersion number (a) $N_D = 1$ (b) $N_D = 10$ and (c) $N_D = 100$. Other scaling groups are constant $L_{XD} = 0.25$, $L_{YD} = 0.1$, $V_{DP} = 0.6$, $N_{pe} = 256$, $V_o = 1.0$, $R_L = 2.5$, $N_\rho = 0.0$, $N_g = 0.0$, $N_\alpha = 0.0^O$.

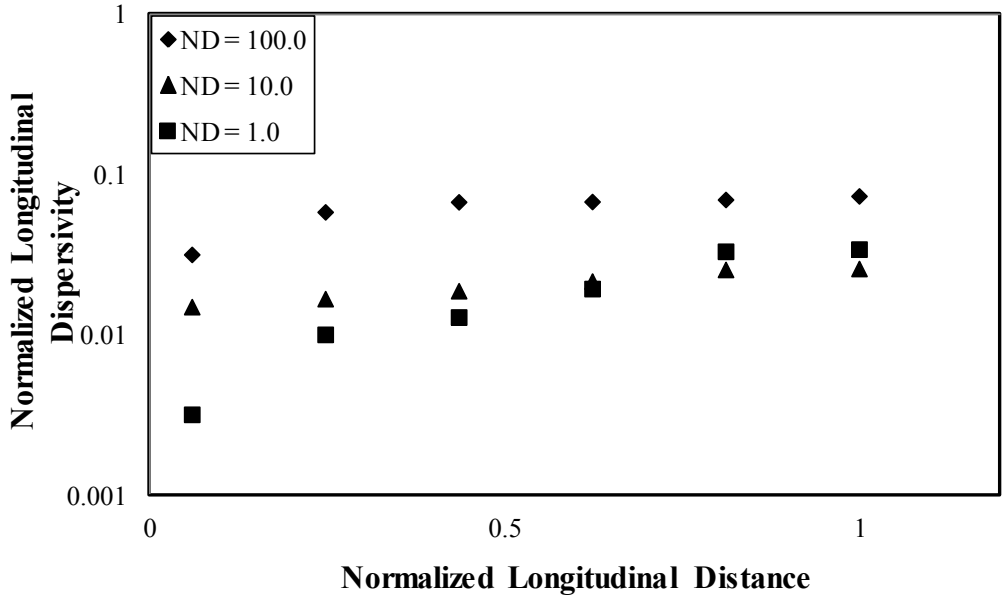

Figure 6.9: Normalized longitudinal dispersivity with different dispersion numbers (N_D). Other scaling groups are constant $L_{XD} = 0.25$, $L_{YD} = 0.1$, $V_{DP} = 0.6$, $N_{pe} = 256$, $V_o = 1.0$, $R_L = 2.5$, $N_\rho = 0.0$, $N_g = 0.0$, $N_\alpha = 0.0^O$.

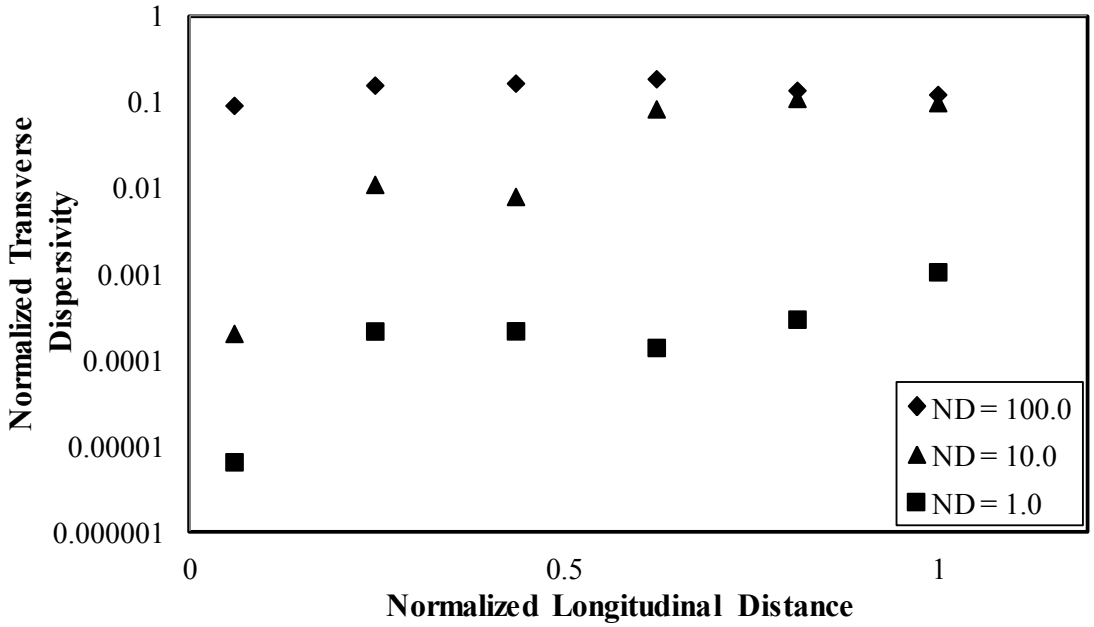

Figure 6.10: Normalized transverse dispersivity with different dispersion numbers (N_D). Other scaling groups are constant $L_{XD} = 0.25$, $L_{YD} = 0.1$, $V_{DP} = 0.6$, $N_{pe} = 256$, $V_o = 1.0$, $R_L = 2.5$, $N_\rho = 0.0$, $N_g = 0.0$, $N_\alpha = 0.0^O$.

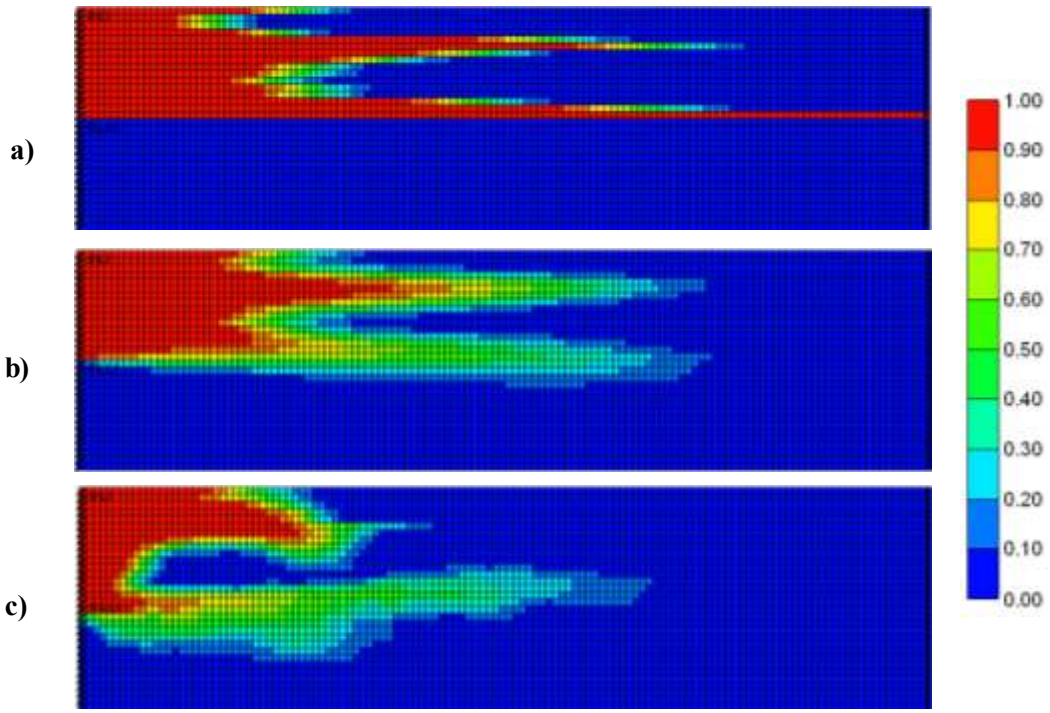

Figure 6.11: Solute concentration at 0.2 pore volume injected for models with different effective aspect ratio (a) $R_L = 0.0$ (b) $R_L = 0.1$ and (c) $R_L = 10$. Other scaling groups are constant $L_{XD} = 0.25$, $L_{YD} = 0.1$, $V_{DP} = 0.6$, $N_{pe} = 256$, $N_D = 1.3$, $V_o = 1.0$, $N_\rho = 0.0$, $N_g = 0.0$, $N_\alpha = 0.0^O$.

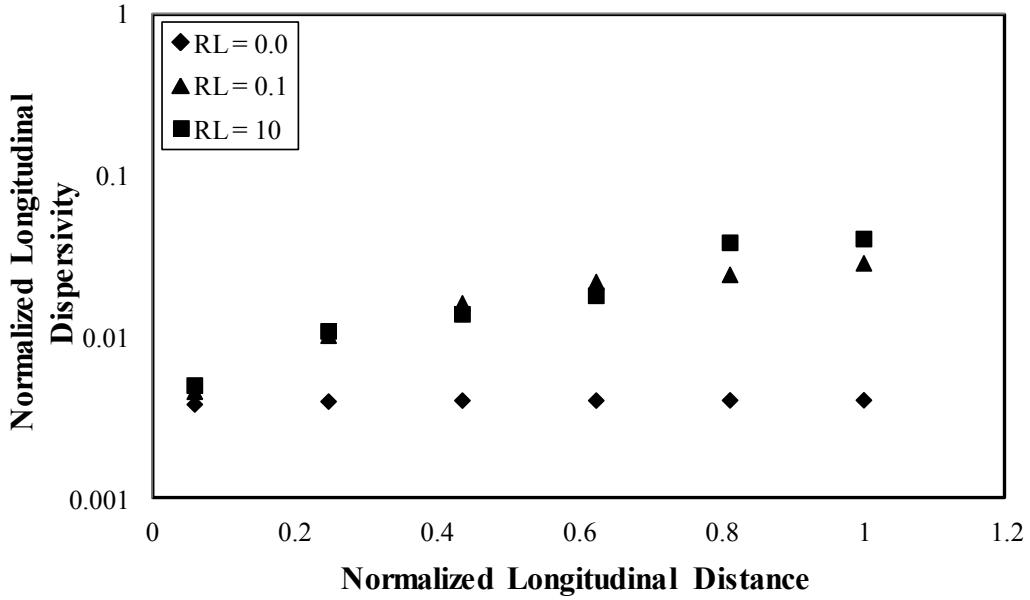

Figure 6.12: Normalized longitudinal dispersivity for different effective aspect ratio. Other scaling groups are constant $L_{XD} = 0.25$, $L_{YD} = 0.1$, $V_{DP} = 0.6$, $N_{pe} = 256$, $N_D = 1.3$, $V_o = 1.0$, $N_\rho = 0.0$, $N_g = 0.0$, $N_\alpha = 0.0^O$.

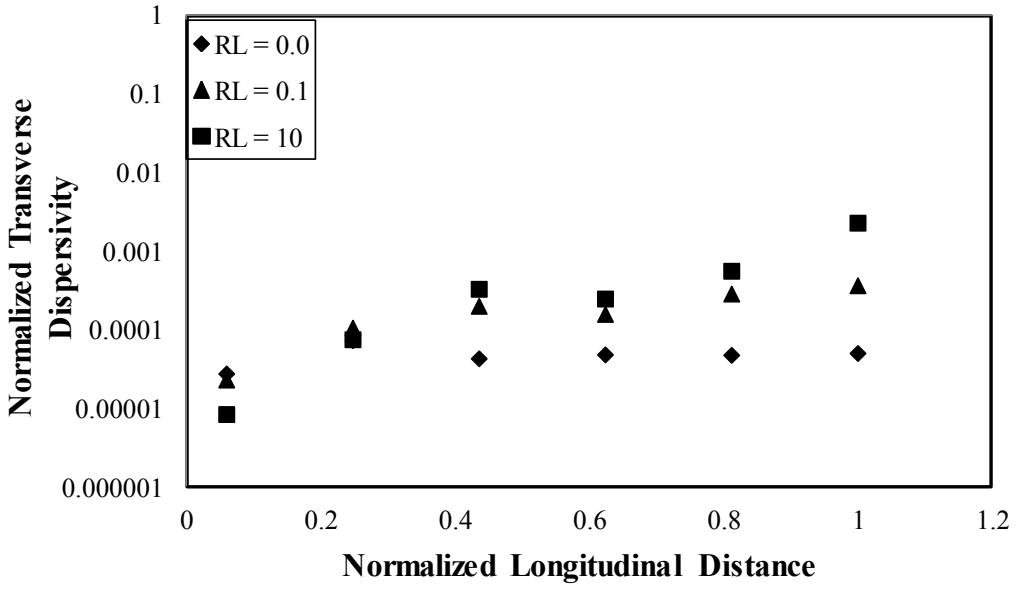

Figure 6.12: Normalized transverse dispersivity for different effective aspect ratio. Other scaling groups are constant $L_{XD} = 0.25$, $L_{YD} = 0.1$, $V_{DP} = 0.6$, $N_{pe} = 256$, $N_D = 1.3$, $V_o = 1.0$, $N_\rho = 0.0$, $N_g = 0.0$, $N_\alpha = 0.0^O$.

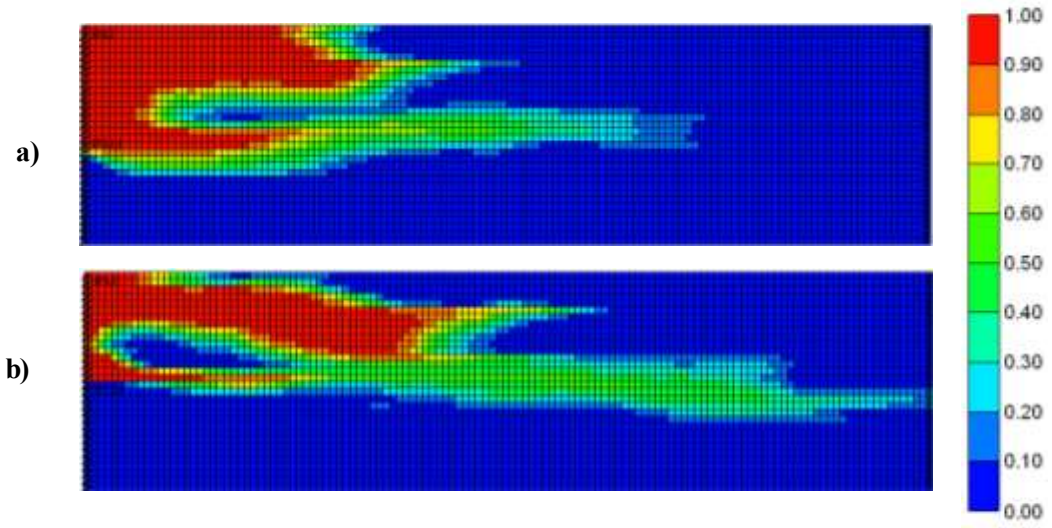

Figure 6.13: Solute concentration at 0.2 PVI for models with different viscosity ratio (a) $V_o = 0.6$ and (b) $V_o = 20$. Other scaling groups are constant $L_{XD} = 0.25$, $L_{YD} = 0.1$, $V_{DP} = 0.6$, $N_{pe} = 256$, $N_D = 1.0$, $R_L = 2.5$, $N_\rho = 0.0$, $N_g = 0.0$, $N_\alpha = 0.0^O$.

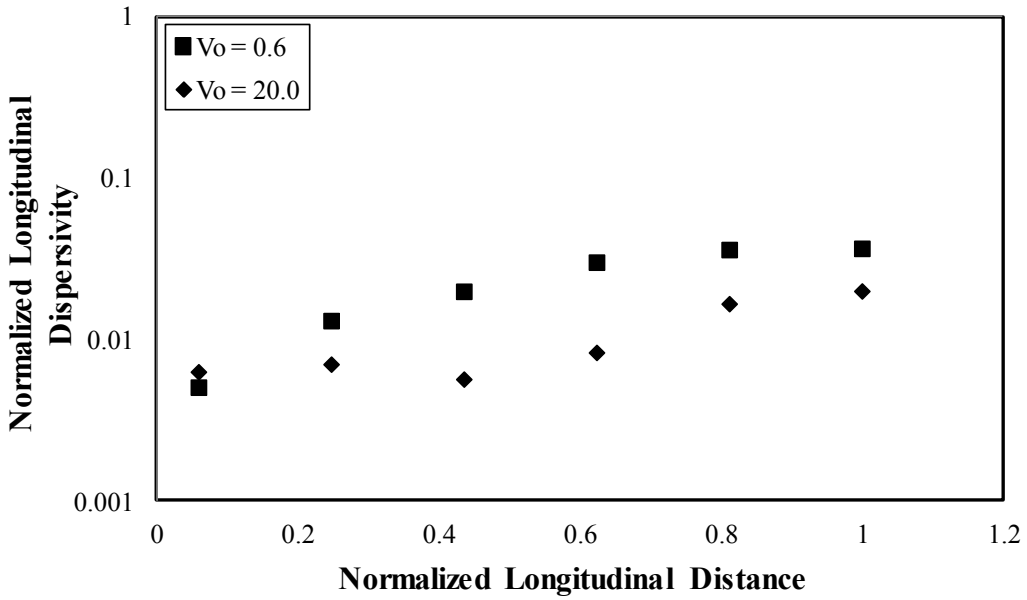

Figure 6.14: Normalized longitudinal dispersivity for different viscosity ratios. Other scaling groups are constant $L_{XD} = 0.25$, $L_{YD} = 0.1$, $V_{DP} = 0.6$, $N_{pe} = 256$, $N_D = 1.0$, $R_L = 2.5$, $N_\rho = 0.0$, $N_g = 0.0$, $N_\alpha = 0.0^O$.

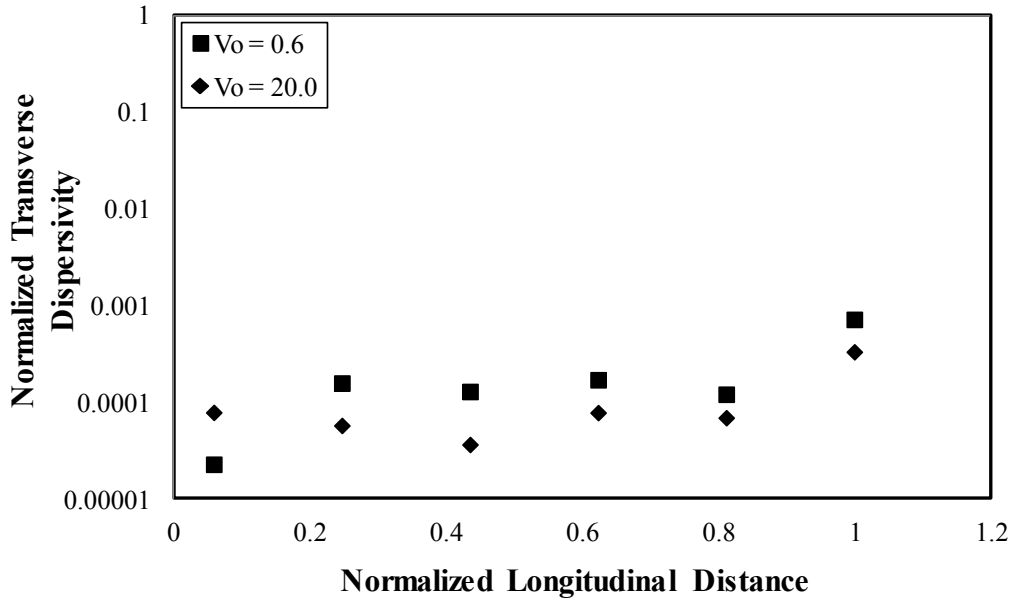

Figure 6.15: Normalized transverse dispersivity for different viscosity ratios. Other scaling groups are constant $L_{XD} = 0.25$, $L_{YD} = 0.1$, $V_{DP} = 0.6$, $N_{pe} = 256$, $N_D = 1.0$, $R_L = 2.5$, $N_\rho = 0.0$, $N_g = 0.0$, $N_\alpha = 0.0^O$.

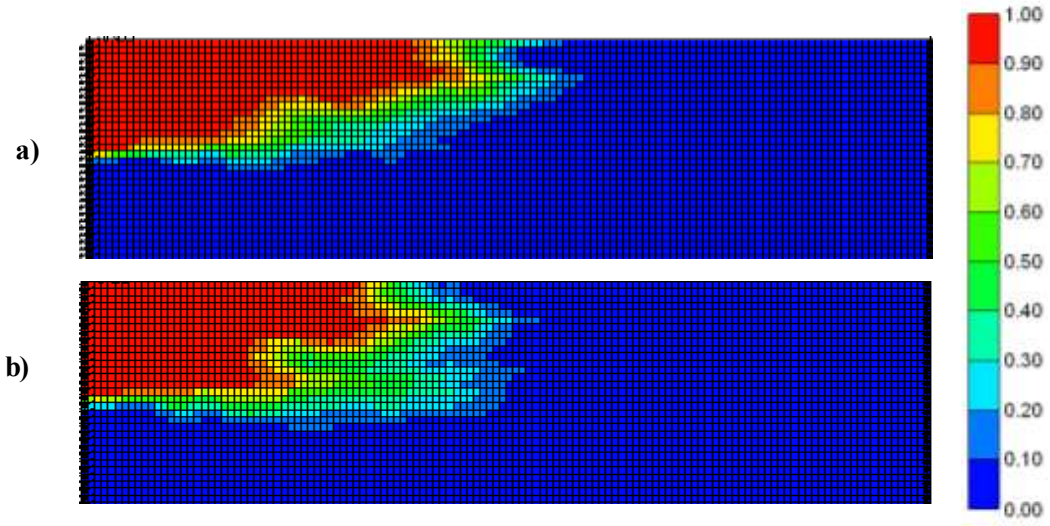

Figure 6.16: Solute concentration map at 0.2 pore volume injected for models with different buoyancy number (a) $N_g = 0.7$ and (b) $N_g = 0.0001$. Other scaling groups are constant $L_{XD} = 0.0$, $L_{YD} = 0.0$, $V_{DP} = 0.6$, $N_{pe} = 256$, $N_D = 1.0$, $R_L = 2.5$, $N_\rho = 0.0$, $V_o = 1.0$, $N_\alpha = 0.0^O$.

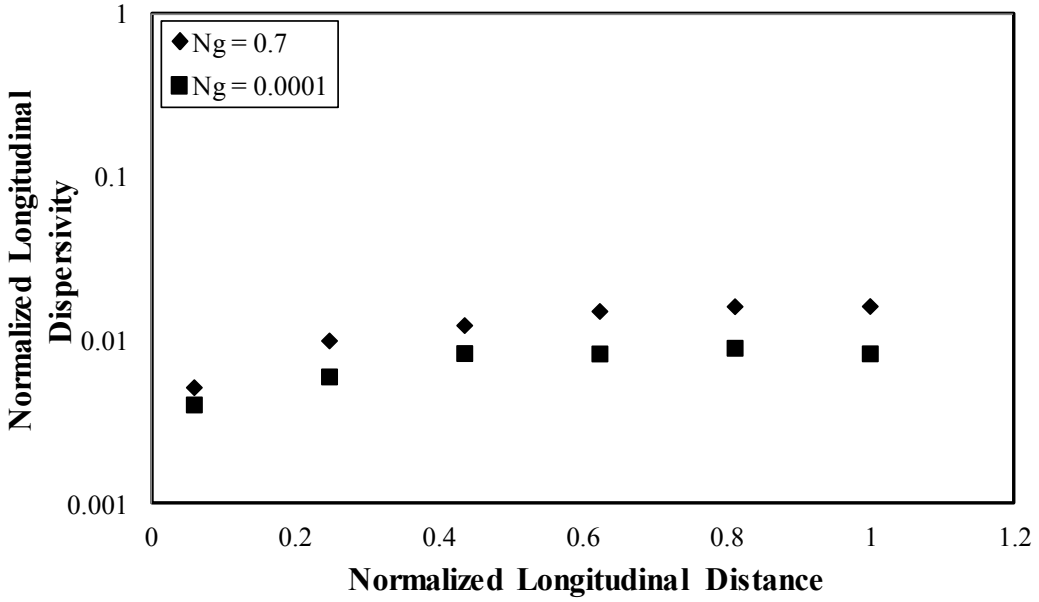

Figure 6.17a: Normalized longitudinal dispersivity for different buoyancy numbers. Other scaling groups are constant $L_{XD} = 0.0$, $L_{YD} = 0.0$, $V_{DP} = 0.6$, $N_{pe} = 256$, $N_D = 1.0$, $R_L = 2.5$, $N_\rho = 0.0$, $V_o = 1.0$, $N_\alpha = 0.0^O$.

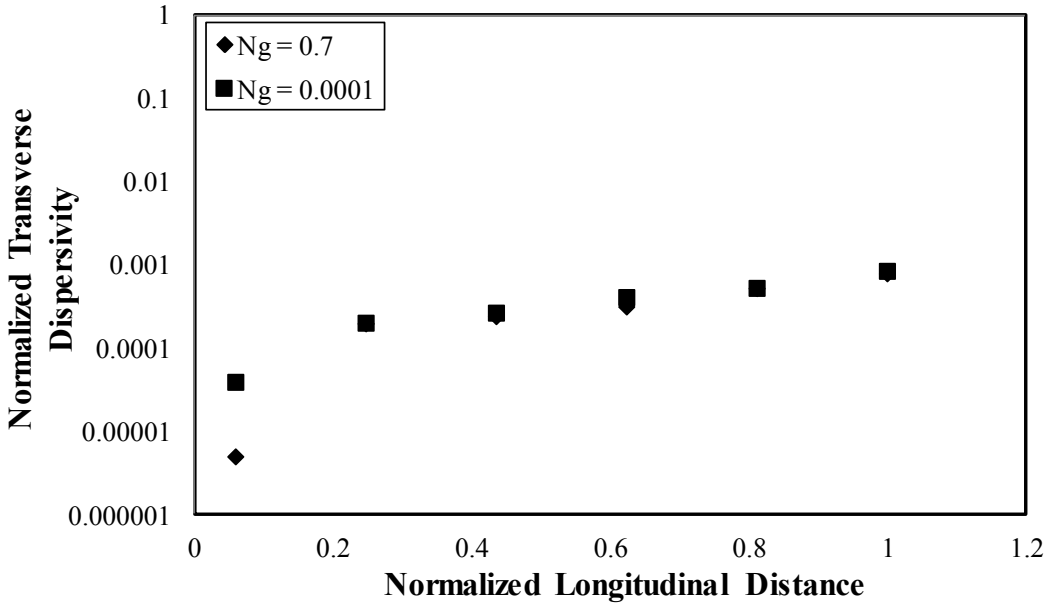

Figure 6.17b: Normalized transverse dispersivity for different buoyancy numbers. Other scaling groups are constant $L_{XD} = 0.0$, $L_{YD} = 0.0$, $V_{DP} = 0.6$, $N_{pe} = 256$, $N_D = 1.0$, $R_L = 2.5$, $N_\rho = 0.0$, $V_o = 1.0$, $N_\alpha = 0.0^O$.

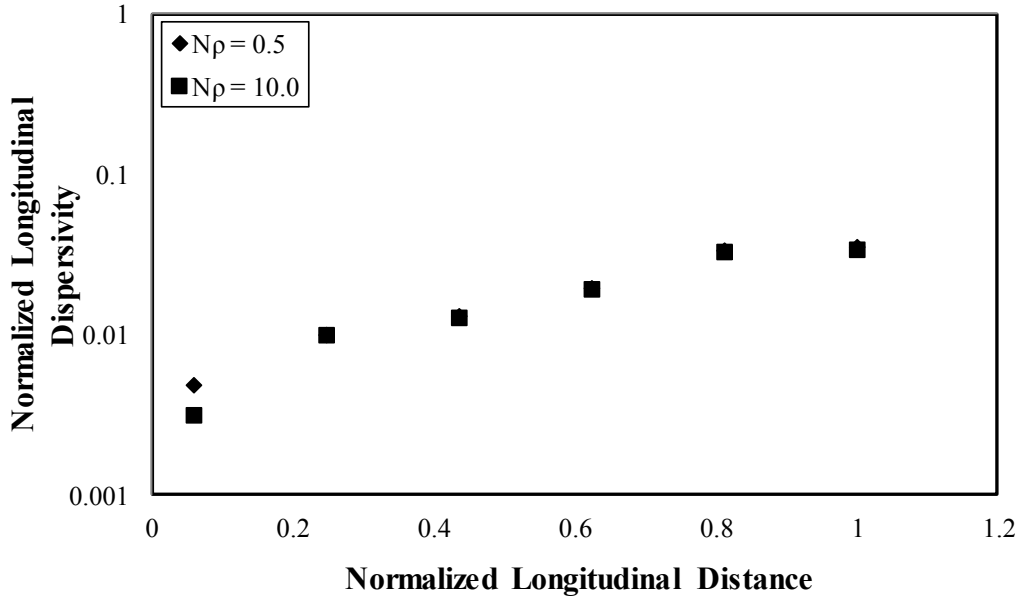

Figure 6.18: Normalized longitudinal dispersivity for different density numbers. Other scaling groups are constant $L_{XD} = 0.25$, $L_{YD} = 0.1$, $V_{DP} = 0.6$, $N_{pe} = 256$, $N_D = 1.0$, $R_L = 2.5$, $N_g \sim 0.0$, $V_o = 1.0$, $N_\alpha = 0.0^O$.

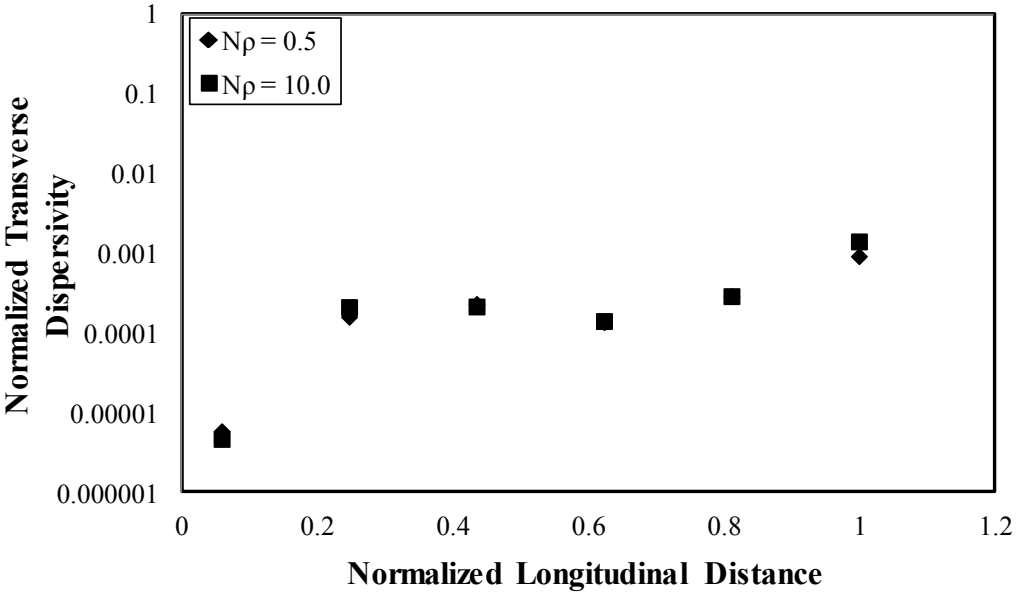

Figure 6.19: Normalized transverse dispersivity for different density numbers. Other scaling groups are constant $L_{XD} = 0.25$, $L_{YD} = 0.1$, $V_{DP} = 0.6$, $N_{pe} = 256$, $N_D = 1.0$, $R_L = 2.5$, $N_g \sim 0.0$, $V_o = 1.0$, $N_\alpha = 0.0^O$.

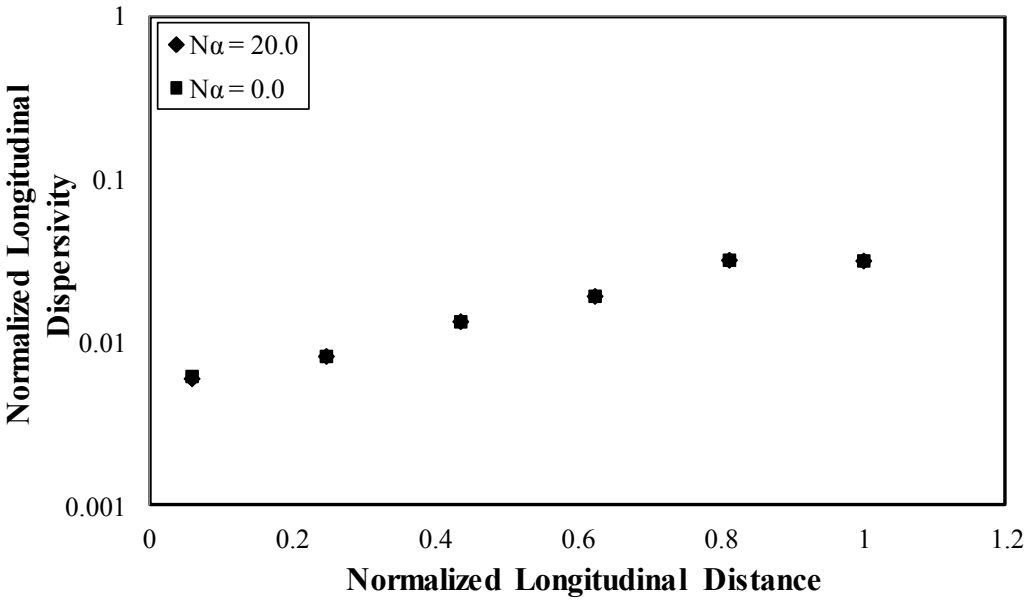

Figure 6.20: Normalized longitudinal dispersivity for different dip angles. Other scaling groups are constant $L_{XD} = 0.25$, $L_{YD} = 0.1$, $V_{DP} = 0.6$, $N_{pe} = 256$, $N_D = 1.0$, $R_L = 2.5$, $N_g = 0.0$, $V_o = 1.0$, $N_\rho = 0.0$.

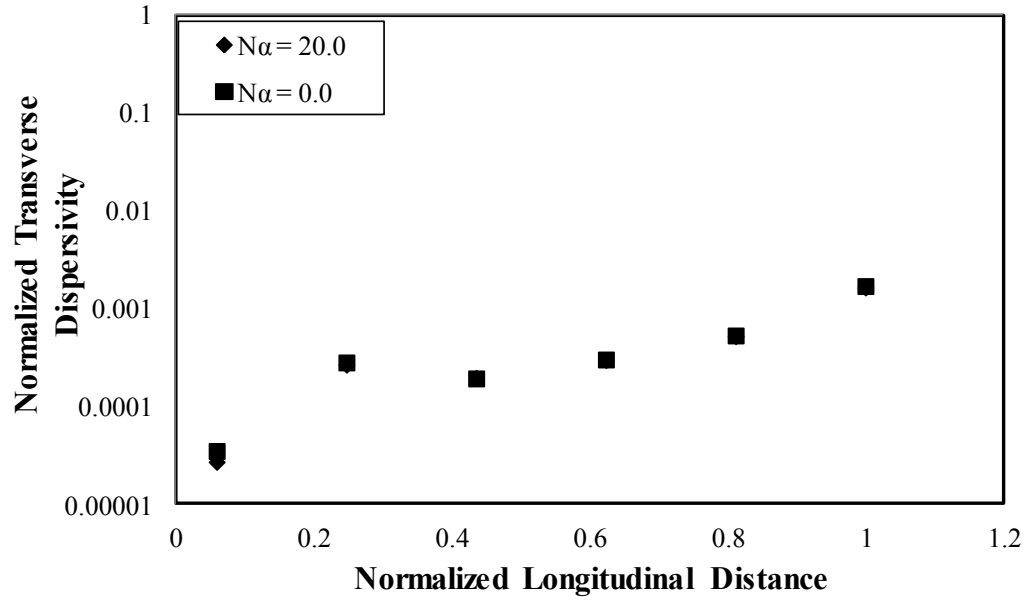

Figure 6.21: Normalized transverse dispersivity for different dip angles. Other scaling groups are constant $L_{XD} = 0.25$, $L_{YD} = 0.1$, $V_{DP} = 0.6$, $N_{pe} = 256$, $N_D = 1.0$, $R_L = 2.5$, $N_g = 0.0$, $V_o = 1.0$, $N_\rho = 0.0$.

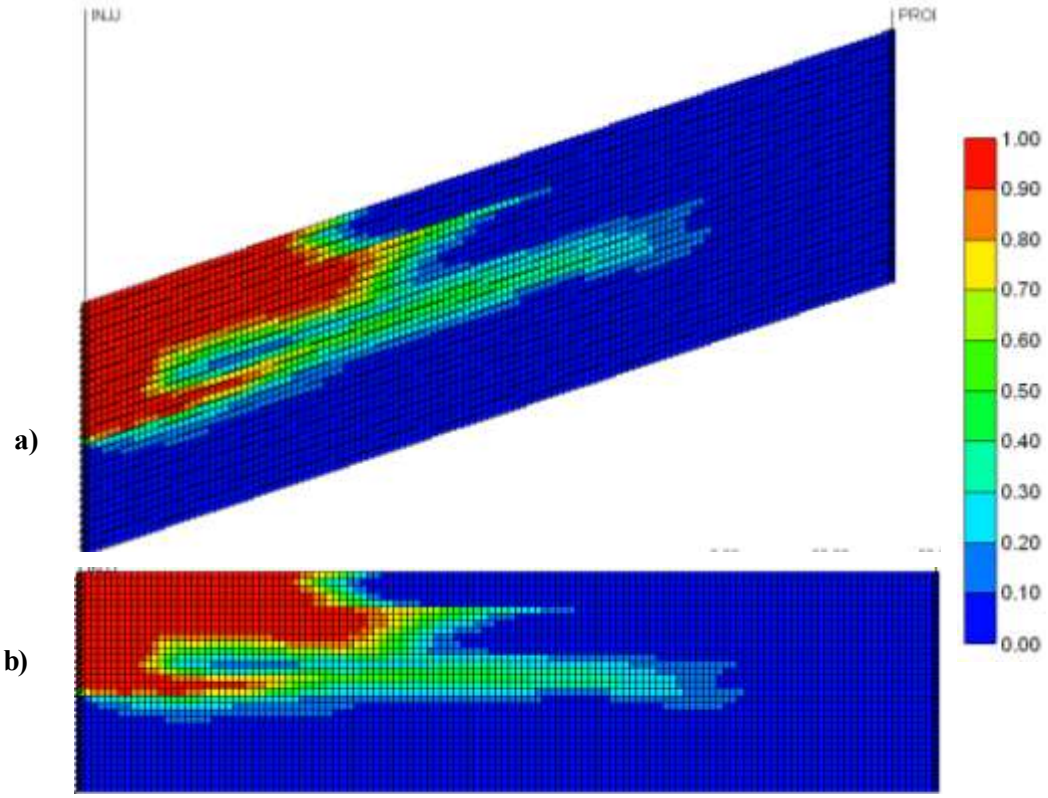

Figure 6.22: Solute concentration at 0.2 pore volume injected for models with different dip angles (a) $N_\alpha = 20^o$ and (b) $N_\alpha = 0^o$. Other scaling groups are constant $L_{XD} = 0.25$, $L_{YD} = 0.1$, $V_{DP} = 0.6$, $N_{pe} = 256$, $N_D = 1.0$, $R_L = 2.5$, $N_g = 0.0$, $V_o = 1.0$, $N_\rho = 0.0$.

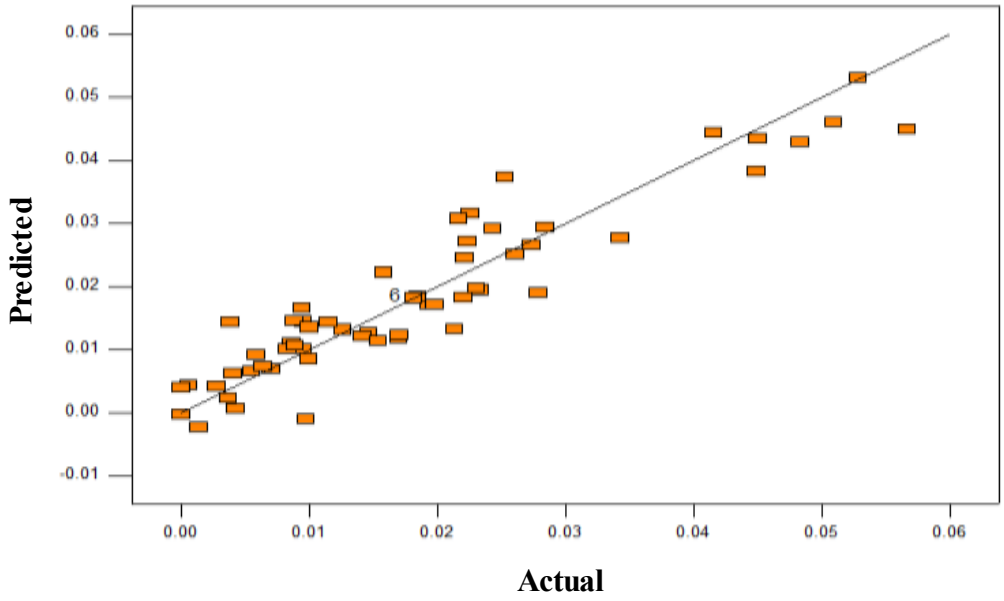

Figure 6.23: Comparison of the actual normalized longitudinal dispersivity and the predicted value from the response surface function.

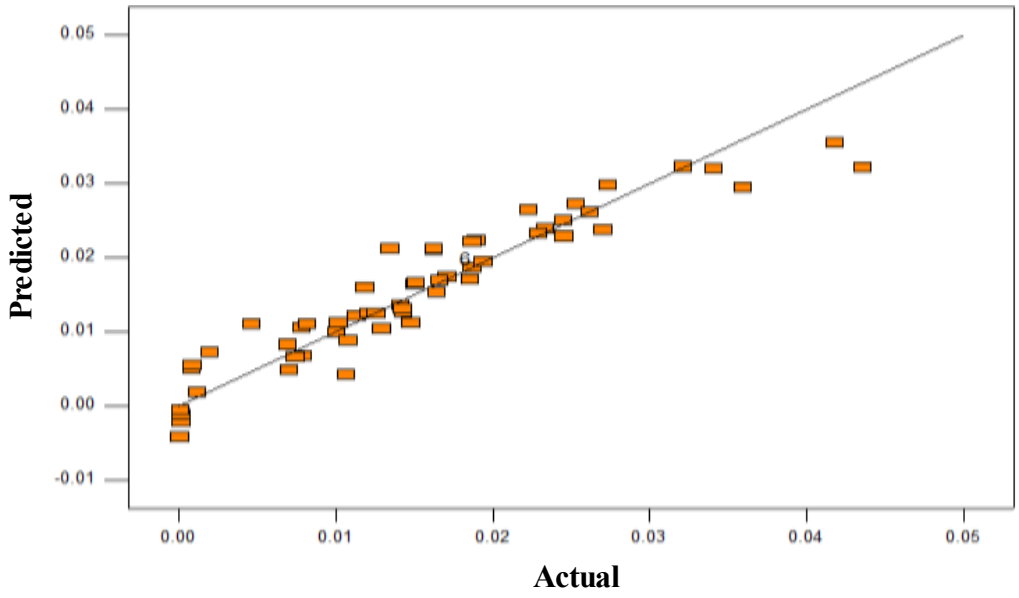

Figure 6.24: Comparison of the actual normalized transverse dispersivity and the predicted value from the response surface function.

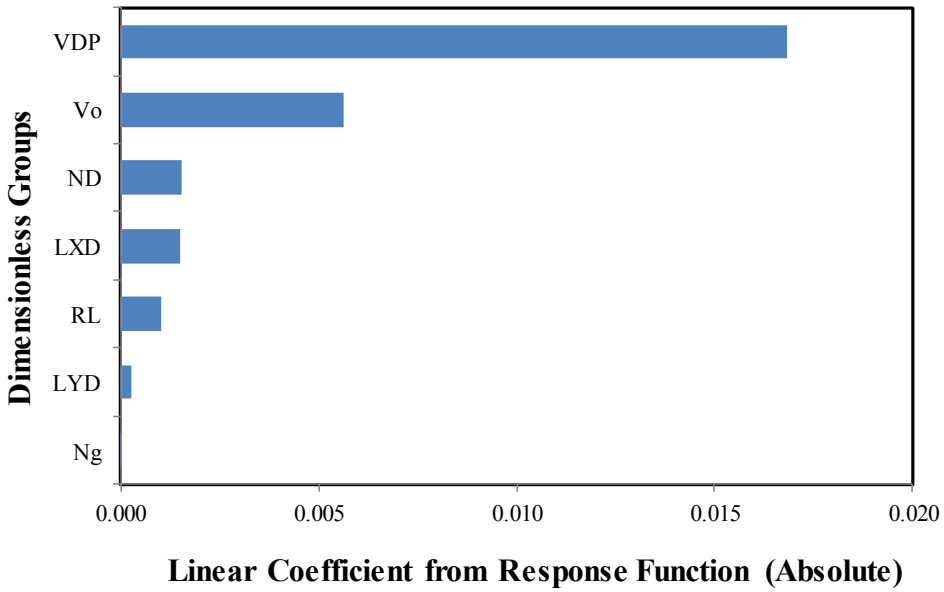

Figure 6.25a: Pareto chart showing the significance of each scaling group on longitudinal dispersivity at $X_D = 1.0$ based on linear coefficient of response function.

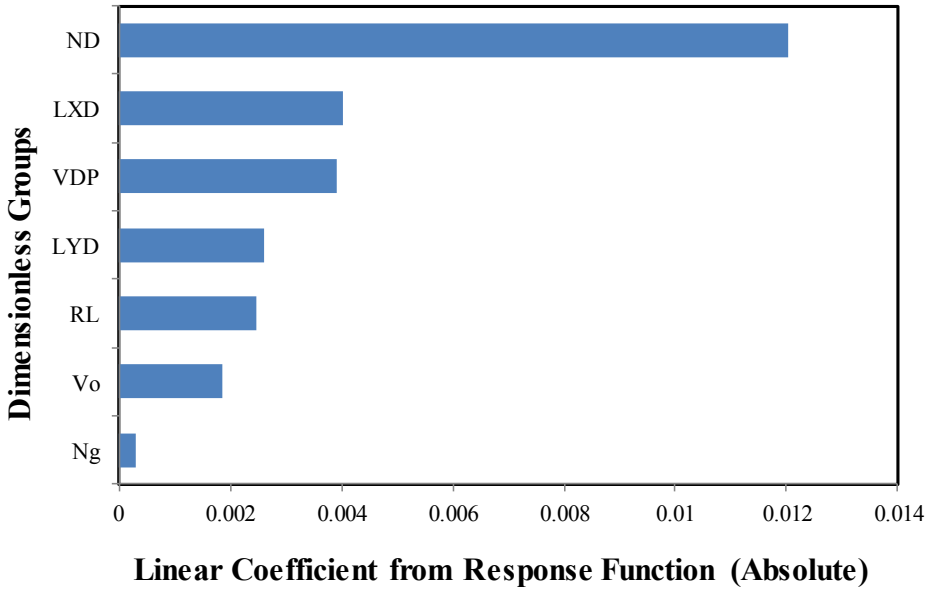

Figure 6.25b: Pareto chart showing the significance of each scaling group on transverse dispersivity at $X_D = 1.0$ based on linear coefficient of response function.

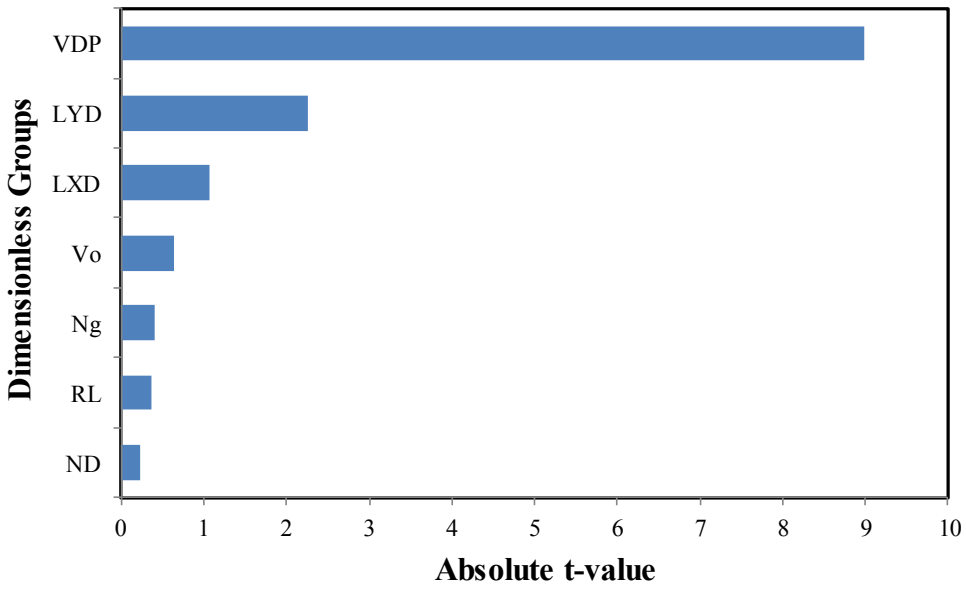

Figure 6.26a: Pareto chart showing the significance of each scaling group on longitudinal dispersivity at $X_D = 1.0$ based on absolute t-value.

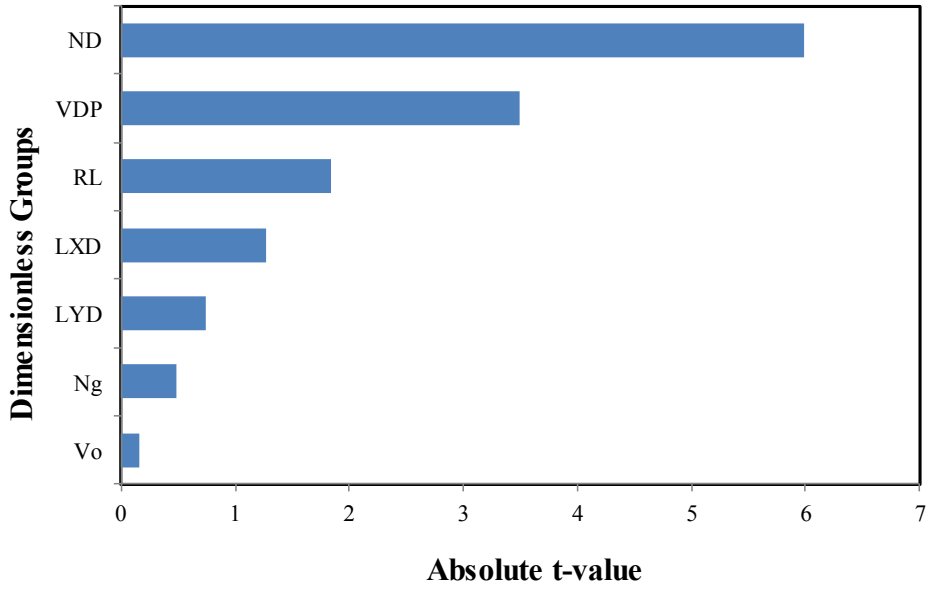

Figure 6.26b: Pareto chart showing the significance of each scaling group on transverse dispersivity at $X_D = 1.0$ based on absolute t-value.

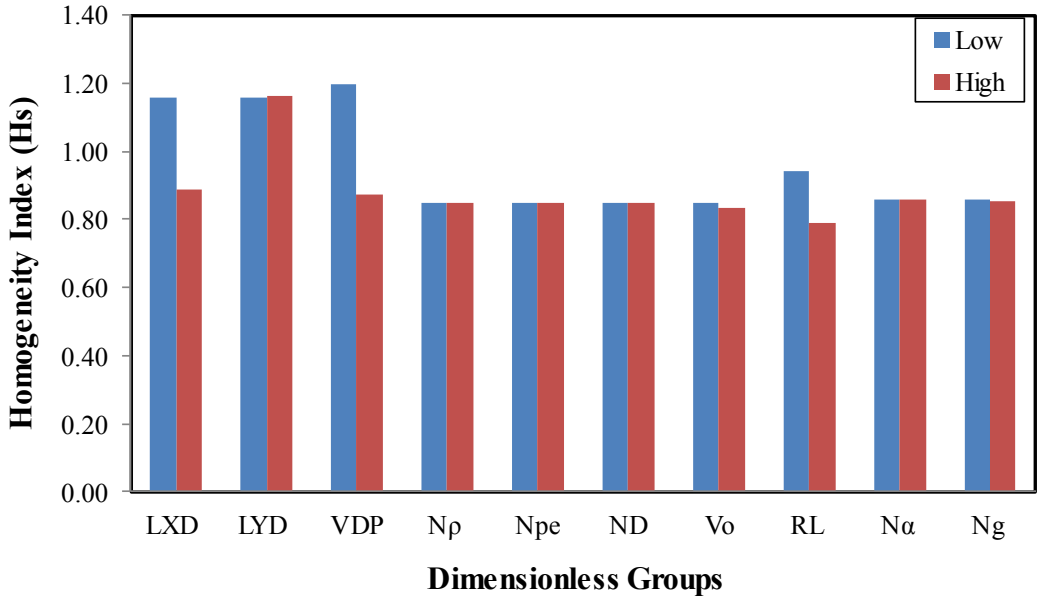

Figure 6.27: Sensitivity of Homogeneity index (Hs) to dimensionless scaling factors

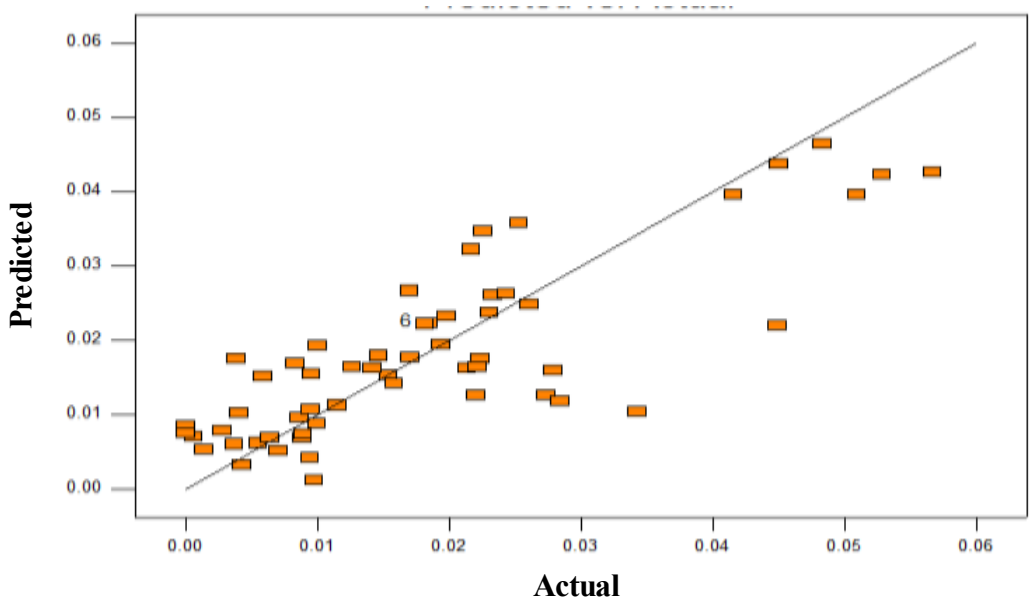

Figure 6.28: Comparison of the actual normalized longitudinal dispersivity and the predicted value from the response surface function when Hs replace V_{DP}, L_{XD}, L_{YD} and R_L in the characterization of heterogeneity.

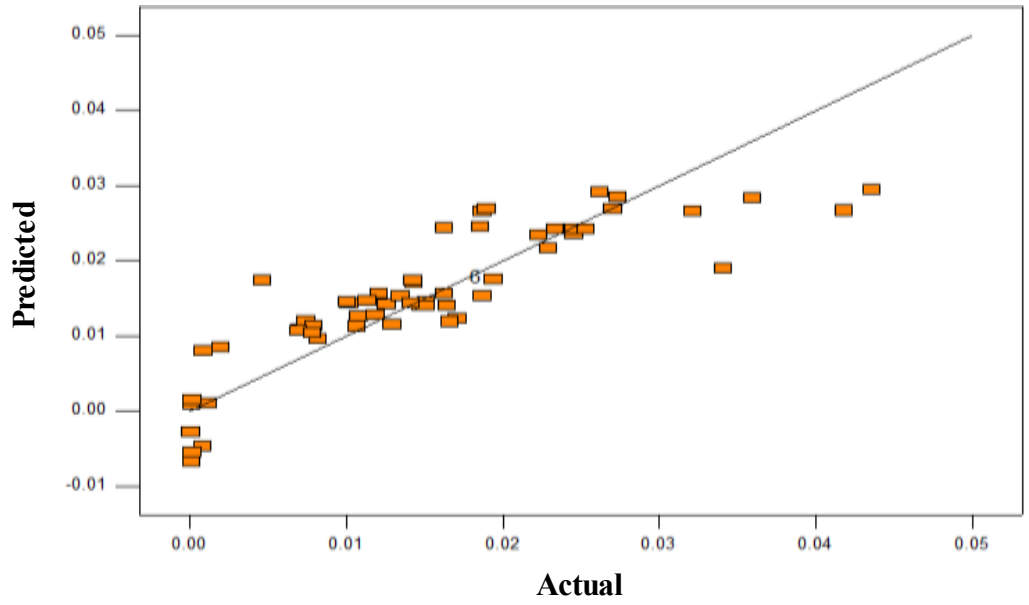

Figure 6.29: Comparison of the actual normalized transverse dispersivity and the predicted value from the response surface function when Hs replaces V_{DP}, L_{XD}, L_{YD} and R_L in the characterization of heterogeneity.

Chapter 7: Conclusions and Recommendations

7.1 Summary and Conclusions

Dispersion affects the recovery of miscible displacements by either reducing local displacement efficiency as the strength of the injected solute weakens or increasing sweep efficiency as the solute spreads to formerly uncontacted areas of the reservoir. This dissertation investigates anisotropic mixing in large scale media and how that knowledge can be used in upscaling for miscible displacements.

The main objectives of this research as stated earlier in chapter 1 is,

1. Estimate longitudinal and transverse dispersivity in large-scale media.
2. Investigate the effect of permeability distribution on anisotropic mixing in miscible displacements.
3. Determine the effect and significance of dimensionless scaling groups for first contact miscible (FCM) displacements on longitudinal and transverse dispersivity and use experimental design to develop a response surface function for both longitudinal and transverse dispersivity based on these scaling groups.
4. Determine the maximum grid-block size in both x- and y-directions that will ensure equivalent mixing during upscaling for miscible floods.
5. Employ use of non-uniform coarsening schemes to account for different mixing levels in reservoir models with different sets of permeability distributions.

These objectives were achieved by developing a procedure that uses the analytical solution of the 2-D CDE to determine simultaneously both longitudinal and transverse dispersivity for large scale media. This is a significant improvement from the

conventional 1-D CDE solution that can only estimate longitudinal dispersivity. We also showed how the local solute concentration profile can be used to determine the average particle velocity for the estimation of dispersion. The average arrival time of the center of mass of the solute gives a better estimate of the velocity than using the injected velocity or the grid-block velocity. This procedure was validated with a series of FCM simulations.

The effects of different permeability distributions and realizations on dispersion were investigated. The flow structure of different realizations of permeability distributions are shown to be different and affect the development of dispersion differently. Dispersion was confirmed to be scale-dependent and proportional to the level of heterogeneity. We concluded that transverse mixing can become significant when there is a concentration gradient in the transverse direction and when there is significant local variation in flow directions due to heterogeneity.

We showed that the effect of increasing autocorrelation in the longitudinal direction is to increase longitudinal dispersion as solute travels through more continuous layers, while reducing transverse dispersion. The effect of increasing autocorrelation in the transverse direction is to reduce dispersion in both longitudinal and transverse directions. This reduction is because of solute concentration equilibrating in continuous sections resulting in stable mixing zone and reduced fingering. Viscous cross-flow modeled as the permeability anisotropy ratio (kv/kh) significantly affects dispersion. As cross-flow increases, dispersion increases. Dispersion is also not an intrinsic property of the porous media and it can be affected by the nature of the solute source (instantaneous or continuous) and imposed boundary conditions.

We presented mathematical formalism and a procedure to use estimated longitudinal and transverse dispersivities to determine the maximum upscaled grid block

sizes in both x- and y-directions. The procedure was validated with several cases of FCM simulations showing that the suggested upscaled models compares favorably with the fine scale models. The procedure was extended to a MCM displacement. Comparable sweep and recovery were obtained between the fine and upscaled model of FCM simulations. The upscaling procedure was extended to reservoir models with different sets of permeability distributions. Non-uniform and uniform coarsening schemes were presented and shown to replicate the behavior of the fine scale model.

Finally, we determined the impact of the scaling groups affecting miscible displacements on dispersion. The effect of each scaling group on longitudinal and transverse dispersion was presented. Dip angle and density number were shown not to significantly affect dispersion. Response surface functions for longitudinal and transverse dispersivities were generated as a function of the significant scaling groups using experimental design. Longitudinal dispersion is most significantly impacted by the level of heterogeneity (V_{DP}) while transverse dispersion is mostly impacted by the transverse dispersion number.

7.2 Recommendation and Future Research

This dissertation presents a procedure to estimate dispersion in 2D models; additional effort is required to extend the procedure to 3D model. We present a mathematical formalism for using estimated longitudinal and transverse dispersivity to determine the maximum grid-block size for upscaling. However, there could be instances where the recommended maximum grid-block size may be too small for routine reservoir simulations. Therefore the use of negative input dispersivities could be investigated. This may compensate for using large grid-block sizes. Also the use of pseudo-relative

permeability could be explored to minimize the effect of excessive numerical dispersion from coarse simulation model. Lastly, testing the proposed upscaling procedure with field data will be beneficial and validate its utility.

Appendix A: Analytical Solution for Two-Dimensional CDE for a Finite Volume Source

The derivation for a two-dimensional CDE solution for a finite volume source is presented. The derived analytical solution will be used to model the flow of solute in a finite-difference simulator. The model is semi-infinite in length and has an infinite height.

The two dimensional CDE is given as,

$$\frac{\partial C}{\partial t} = D_x \frac{\partial^2 C}{\partial x^2} + D_y \frac{\partial^2 C}{\partial y^2} - v_x \frac{\partial C}{\partial x} - v_y \frac{\partial C}{\partial y} \tag{A.1}$$

where C is the concentration of the solute (mass of solute per unit volume of the fluid) [M/L^3], D_x is the longitudinal dispersion coefficient [L^2/T], D_y is the transverse dispersion coefficient [L^2/T], v_x is the average pore velocity in the longitudinal direction [L/T], v_y is the average pore velocity in the transverse direction [L/T].

Equation (A.1) is subject to the following assumptions; constant average velocity in both directions, constant porosity, constant longitudinal and transverse dispersion coefficient, negligible off-diagonal dispersion coefficient since flow is assumed to be dominant in the longitudinal direction and incompressible fluids.

The boundary conditions for this case are given as;

$$C(\infty, y, t) = 0 \tag{A.2a}$$

$$C(x, \pm\infty, t) = 0 \tag{A.2b}$$

$$C(0, y, t) = C_0 \delta(y - y') \delta(t - t') \tag{A.2c}$$

where $\delta(\ )$ is the Dirac delta function, y' and t' are the coordinate of the center of the point source and the time the instantaneous volume source commences respectively. The initial condition is,

$$C(x, y, 0) = 0. \tag{A.2d}$$

A variable transformation is used to remove the convective terms in equation (A.1), to make it easily solvable. Ozsik (1980) gave a generalized variable transformation of the dependent variable "T" into a new dependent variable "W". Consider a partial differential equation (PDE) with a dependent variable T,

$$\frac{\partial T}{\partial t} = \alpha_1 \frac{\partial^2 T}{\partial x^2} + \alpha_2 \frac{\partial^2 T}{\partial y^2} - \beta_1 \frac{\partial T}{\partial x} - \beta_2 \frac{\partial T}{\partial y} \tag{A.3}$$

where α and β in equation (A.3) are constants. A new dependent variable *"W"* can be defined from *"T"* by multiplying "T" by an appropriate transformation parameter.

$$W(x,y,t) = T(x,y,t)\exp\left[-\frac{\beta_1 x}{2\alpha_1} + \frac{\beta_1^2 t}{4\alpha_1}\right]\exp\left[-\frac{\beta_2 y}{2\alpha_2} + \frac{\beta_2^2 t}{4\alpha_2}\right]. \tag{A.4}$$

Multiplying equation (A.3) by the defined transformation parameter from equation (A.4) results in;

$$\frac{\partial W}{\partial t} = \alpha_1 \frac{\partial^2 W}{\partial x^2} + \alpha_2 \frac{\partial^2 W}{\partial y^2}. \tag{A.5}$$

Equation (A.5), which does not have a convective term, is a result of a variable transformation of equation (A.3). The dependent variable of the CDE equation "C" can be transformed to a new dependent variable "c" by multiplying by the transformation parameter defined below,

$$c(x,y,t) = C(x,y,t)\exp\left[-\frac{v_x x}{2D_x} + \frac{v_x^2 t}{4D_x}\right]\exp\left[-\frac{v_y y}{2D_y} + \frac{v_y^2 t}{4D_y}\right] \tag{A.6}$$

The resulting PDE after the variable transformation is given as,

$$\frac{\partial c}{\partial t} = D_x \frac{\partial^2 c}{\partial x^2} + D_y \frac{\partial^2 c}{\partial y^2} \tag{A.7}$$

subject to the following boundary and initial conditions;

$$c(\infty, y, t) = 0 \tag{A.8a}$$

$$c(x, \pm\infty, t) = 0 \tag{A.8b}$$

$$c(0,y,t) = C_0 \exp\left[\frac{v_x^2 t}{4D_x}\right] \exp\left[-\frac{v_y y}{2D_y} + \frac{v_y^2 t}{4D_y}\right] \delta\left(y - y'\right) \delta\left(t - t'\right) \tag{A.8c}$$

$$c(x,y,0) = 0 \tag{A.8d}$$

The above transformation is validated by appropriately differentiating the dependent variable "C" in equation (A.6) and substituting in equation (A.1) to obtain equation (A.7).

The partial derivative of x in equation (A.7) is removed by applying a Fourier sine transform defined by Churchill (1972, p 401-402) as,

$$S_\alpha \left\{F(x)\right\} = \int_0^\infty F(x) \sin(\alpha x)\, dx = f_s(\alpha) \quad (\alpha > 0) \tag{A.9}$$

whose basic operation property can be expressed as,

$$S_\alpha \left\{\frac{d^2 F(x)}{dx^2}\right\} = -\alpha^2 f_s(\alpha) + \alpha F(0) \tag{A.10}$$

where F(0) is the function evaluated at x=0. The inverse of the finite sine transformation is given as,

$$S_\alpha^{-1} \left\{f_s(\alpha)\right\} = F(x) = \frac{2}{\pi} \int_0^\infty f_s(\alpha) \sin(\alpha x) d\alpha \quad (x > 0). \tag{A.11}$$

The transformed equation, with its boundary and initial conditions is expressed as,

$$\frac{\partial \bar{c}}{\partial t} + \alpha^2 D_x \bar{c} - D_y \frac{\partial^2 \bar{c}}{\partial y^2} = \alpha D_x C_0 \exp\left[\frac{v_x^2 t}{4D_x} + \frac{v_y^2 t}{4D_y}\right] \exp\left[-\frac{v_y y}{2D_y}\right] \delta\left(y - y'\right) \delta\left(t - t'\right) \tag{A.12}$$

where $\bar{c}(y,t)$ is the transformed dependent variable.

An exponential Fourier transform is applied to remove the y-derivative. The exponential Fourier transform is defined by Churchill (1972, pp 384) as,

$$E_\beta \left\{F(y)\right\} = \int_{-\infty}^{+\infty} F(y) \exp\left[-i\beta y\right] dy = f_e(\beta) \tag{A.13}$$

where $i = \sqrt{-1}$ and the operational property is given as,

$$E_\beta\left\{\frac{d^2F(y)}{dy^2}\right\}=-\beta^2 f_e(\beta) \tag{A.14}$$

The inverse of the exponential Fourier transform is given as,

$$E_\beta^{-1}\left\{f_e(\beta)\right\}=\frac{1}{2\pi}\int_{-\infty}^{+\infty} f_e(\beta)\exp[-i\beta y]d\beta\,. \tag{A.15}$$

The required exponential Fourier integral in equation (A.12) is resolved as,

$$E_\beta^{-1}\left\{\exp\left[\frac{-v_y y}{2D_y}\right]\partial(y-y')\right\}=\exp\left[\frac{-v_y y'}{2D_y}-i\beta y'\right] \tag{A.16}$$

The transformed equation, with its boundary and initial conditions is expressed as,

$$\frac{d\overline{c}}{dt}+\left(\alpha^2D_x+\beta^2D_y\right)\overline{c}=\alpha D_x C_0\exp\left[\frac{v_x^2 t}{4D_x}+\frac{v_y^2 t}{4D_y}-\frac{v_y y'}{2D_y}-i\beta y'\right]\delta\left(t-t'\right). \tag{A.17}$$

where $\overline{c}(t)$ is the transformed dependent variable. Equation (A.17) is the transformed ordinary differential equation (ODE). It is solved by using an integrating factor. Given an ODE of the form,

$$\frac{dw}{dt}+gw=h(t) \tag{A.18a}$$

the solution is given as (Wexler, 1989),

$$w=\frac{1}{p(t)}\int_{t_0}^{t} p(\tau)h(\tau)d\tau+w_0\frac{p(t)}{p(t_0)} \tag{A.18b}$$

where p(t) is the integrating factor expressed as,

$$p(t)=\exp\left[\int g(\tau)d\tau\right] \tag{A.18c}$$

Applying equation (A.18) to the transformed ODE gives,

$$p(t)=\exp\left[\int_0^t\left(\alpha^2D_x+\beta^2D_y\right)d\tau\right]=\exp\left[\alpha^2D_x t+\beta^2D_y t\right] \tag{A.19}$$

$$\overline{c}=\frac{\alpha D_x C_0\exp\left[-\frac{v_y y'}{2D_y}-i\beta y'\right]}{\exp\left[\alpha^2D_x t+\beta^2D_y t\right]}\int_{t=0}^{t}\exp\left[\alpha^2D_x\tau+\beta^2D_y\tau+\frac{v_x^2\tau}{4D_x}+\frac{v_y^2\tau}{4D_y}\right]\delta\left(\tau-t'\right)d\tau\,. \tag{A.20}$$

Integrating equation (A.20),

$$\bar{\bar{c}} = \alpha D_x \left(t - t'\right) C_0 \exp\left[-\frac{v_y y'}{2D_y} - i\beta y' - \alpha^2 D_x \left(t - t'\right) - \beta^2 D_y \left(t - t'\right) + \frac{v_x^2 t'}{4D_x} + \frac{v_y^2 t'}{4D_y} \right].$$

(A.21)

The α term is transformed back into x by applying the inverse Fourier sine transform, using table of inverse Fourier sine transform by Churchill (1972, pp 474).

$$S_\alpha^{-1}\left\{ \alpha \exp\left[-\alpha^2 D_x \left(t - t'\right) \right] \right\} = \frac{x}{2D_x \left(t - t'\right) \sqrt{\pi D_x \left(t - t'\right)}} \exp\left[\frac{-x^2}{4D_x \left(t - t'\right)} \right]. \quad \text{(A.22)}$$

Substitution of the transformation in equation (A.22) into equation (A.21) gives,

$$\bar{\bar{c}} = \frac{C_0 x}{2\sqrt{\pi D_x \left(t - t'\right)}} \exp\left[-\frac{v_y y'}{2D_y} - i\beta y' - \frac{x^2}{4D_x \left(t - t'\right)} - \beta^2 D_y \left(t - t'\right) + \frac{v_x^2 t'}{4D_x} + \frac{v_y^2 t'}{4D_y} \right]$$

(A.23)

The β term is transformed back to y by applying the inverse exponential Fourier transform. The inverse exponential Fourier transform is given as,

$$E_\beta^{-1}\left\{ \exp\left[-i\beta y' - \beta^2 D_y \left(t - t'\right) \right] \right\} = \frac{\exp\left[-i\beta y' \right]}{2\sqrt{\pi D_y \left(t - t'\right)}} \exp\left[\frac{-y^2}{4D_y \left(t - t'\right)} \right]. \quad \text{(A.24)}$$

Using the shift theorem (Churchill, 1972, p 471),

$$E_\beta^{-1}\left\{ \exp\left[i\beta y' f\left(\beta\right) \right] \right\} = F\left(y + y'\right). \quad \text{(A.25)}$$

The inverse exponential transform is given as,

$$E_\beta^{-1}\left\{ \exp\left[-i\beta y' - \beta^2 D_y \left(t - t'\right) \right] \right\} = \frac{1}{2\sqrt{\pi D_y \left(t - t'\right)}} \exp\left[\frac{-\left(y - y'\right)^2}{4D_y \left(t - t'\right)} \right]. \quad \text{(A.26)}$$

Substituting the transformation in equation (A.26) into equation (A.23) gives,

$$c = \frac{C_0 x}{4\pi \left(t - t'\right) \sqrt{D_x D_y}} \exp\left[-\frac{v_y y'}{2D_y} - \frac{x^2}{4D_x \left(t - t'\right)} - \frac{\left(y - y'\right)^2}{4D_y \left(t - t'\right)} + \frac{v_x^2 t'}{4D_x} + \frac{v_y^2 t'}{4D_y} \right]. \quad \text{(A.27)}$$

The dependent variable *"c"* is transformed back to *"C"* by multiplying by the transformation parameter given by equation (A.6).

$$C = \frac{C_0 x}{4\pi\left(t-t'\right)\sqrt{D_x D_y}} \cdot \exp\left[\frac{v_x x}{2D_x} - \frac{x^2}{4D_x\left(t-t'\right)} - \frac{v_x^2\left(t-t'\right)}{4D_x} + \frac{v_y\left(y-y'\right)}{2D_y} - \frac{\left(y-y'\right)^2}{4D_y\left(t-t'\right)} - \frac{v_y^2\left(t-t'\right)}{4D_y}\right] \cdot \tag{A.28}$$

The analytical solution for the instantaneous line source of finite height along the y-axis is obtained by integrating equation (A.28) from y'=Y_1 to y'=Y_2.

$$C = \frac{C_0 x}{4\pi\left(t-t'\right)\sqrt{D_x D_y}} \exp\left[\frac{v_x x}{2D_x} - \frac{x^2}{4D_x\left(t-t'\right)} - \frac{v_x^2\left(t-t'\right)}{4D_x} + -\frac{v_y^2\left(t-t'\right)}{4D_y}\right] \cdot \int_{Y_1}^{Y_2} \exp\left[\frac{v_y\left(y-y'\right)}{2D_y} - \frac{\left(y-y'\right)^2}{4D_y\left(t-t'\right)}\right] dy' \tag{A.29}$$

After integration and simplification,

$$C = \frac{C_0 x}{4\sqrt{D_x \pi\left(t-t'\right)}} \exp\left[\frac{v_x x}{2D_x} - \frac{x^2}{4D_x\left(t-t'\right)} - \frac{v_x^2\left(t-t'\right)}{4D_x}\right] \cdot \left\{erf\left[\frac{Y_2 - y}{2\sqrt{D_y\left(t-t'\right)}} + \frac{v_y}{2}\sqrt{\frac{\left(t-t'\right)}{D_y}}\right] - erf\left[\frac{Y_1 - y}{2\sqrt{D_y\left(t-t'\right)}} - \frac{v_y}{2}\sqrt{\frac{\left(t-t'\right)}{D_y}}\right]\right\} \cdot \tag{A.30}$$

Simplifying,

$$C = \frac{C_0 x}{4\sqrt{D_x \pi\left(t-t'\right)}} \exp\left[-\frac{\left(x - v_x\left(t-t'\right)\right)^2}{4D_x\left(t-t'\right)}\right] \cdot \left\{erf\left[\frac{Y_2 - y}{2\sqrt{D_y\left(t-t'\right)}} + \frac{v_y}{2}\sqrt{\frac{\left(t-t'\right)}{D_y}}\right] - erf\left[\frac{Y_1 - y}{2\sqrt{D_y\left(t-t'\right)}} - \frac{v_y}{2}\sqrt{\frac{\left(t-t'\right)}{D_y}}\right]\right\} \cdot \tag{A.31}$$

The solution can be extended to a finite length in the x-direction by integrating along the x-axis to obtain,

$$C = \frac{C_0}{4\sqrt{D_x \pi \left(t - t^{'}\right)}} \int_{X_1}^{X_2} \exp\left[-\frac{\left(x - v_x\left(t - t^{'}\right)\right)^2}{4D_x\left(t - t^{'}\right)} \right] dx \cdot$$
$$\left\{ erf\left[\frac{Y_2 - y}{2\sqrt{D_y\left(t - t^{'}\right)}} + \frac{v_y}{2}\sqrt{\frac{\left(t - t^{'}\right)}{D_y}} \right] - erf\left[\frac{Y_1 - y}{2\sqrt{D_y\left(t - t^{'}\right)}} - \frac{v_y}{2}\sqrt{\frac{\left(t - t^{'}\right)}{D_y}} \right] \right\}. \quad \text{(A.32)}$$

Integrating and simplifying,

$$C\left(x, y, t\right) = \frac{C_0}{4}\left\{ erf\left(\frac{X_1 - v_x\left(t - t^{'}\right)}{\sqrt{4D_x\left(t - t^{'}\right)}} \right) - erf\left(\frac{X_2 - v_x\left(t - t^{'}\right)}{\sqrt{4D_x t}} \right) \right\} \cdot$$
$$\left\{ erf\left[\frac{Y_2 - y}{2\sqrt{D_y\left(t - t^{'}\right)}} + \frac{v_y}{2}\sqrt{\frac{\left(t - t^{'}\right)}{D_y}} \right] - erf\left[\frac{Y_1 - y}{2\sqrt{D_y\left(t - t^{'}\right)}} - \frac{v_y}{2}\sqrt{\frac{\left(t - t^{'}\right)}{D_y}} \right] \right\}. \quad \text{(A.33)}$$

Generally, the time the instantaneous volume source commences and finishes is zero, therefore t' is zero. Also X_i (i =1, 2) can be better expressed in terms of the coordinate of the point source in the x-direction as "$x_i - x$" and erf(-x) = -erf(x) . Equation (A.33) can thus be expressed as,

$$C\left(x, y, t\right) = \frac{C_0}{4}\left\{ erf\left(\frac{x_2 - x + v_x\left(t - t^{'}\right)}{\sqrt{4D_L t}} \right) - erf\left(\frac{x_1 - x + v_x\left(t - t^{'}\right)}{\sqrt{4D_L t}} \right) \right\} \cdot$$
$$\left\{ erf\left[\frac{Y_2 - y}{2\sqrt{D_y\left(t - t^{'}\right)}} + \frac{v_y}{2}\sqrt{\frac{\left(t - t^{'}\right)}{D_y}} \right] - erf\left[\frac{Y_1 - y}{2\sqrt{D_y\left(t - t^{'}\right)}} - \frac{v_y}{2}\sqrt{\frac{\left(t - t^{'}\right)}{D_y}} \right] \right\}. \quad \text{(A.34)}$$

Appendix B: Analytical Solution for Two-Dimensional CDE for a Continuous Injection Source and Finite Height Medium

The derivation for a two-dimensional CDE solution for a finite volume source is presented. The model is semi-infinite in length and has an infinite height.

The two dimensional CDE is given as,

$$\frac{\partial C}{\partial t} = D_x \frac{\partial^2 C}{\partial x^2} + D_y \frac{\partial^2 C}{\partial y^2} - v_x \frac{\partial C}{\partial x} - v_y \frac{\partial C}{\partial y} \tag{B.1}$$

where C is the concentration of the solute (mass of solute per unit volume of the fluid) [M/L^3], D_x is the longitudinal dispersion coefficient [L^2/T], D_y is the transverse dispersion coefficient [L^2/T], v_x is the average pore velocity in the longitudinal direction [L/T], v_y is the average pore velocity in the transverse direction [L/T].

Equation (B.1) is subject to the following assumptions; constant average velocity in both directions, constant porosity, constant longitudinal and transverse dispersion coefficient, negligible off-diagonal dispersion coefficient since flow is assumed to be dominant in the longitudinal direction and incompressible fluid

The boundary and initial conditions for this case is given as;

$$C = 0, \qquad y = 0, y = W \tag{B.2a}$$

$$C = 0, \qquad x = \infty \tag{B.2b}$$

$$C(0, y, t) = C_0 \quad at \quad Y_1 < y < Y_2 \tag{B.2c}$$

where W is the height of the medium

$$C(x, y, 0) = 0 \tag{B.2d}$$

The dependent variable of the CDE equation "C" can be transformed to a new dependent variable "c" by multiplying by the transformation parameter defined below,

$$c(x, y, t) = C(x, y, t) \exp\left[-\frac{v_x x}{2D_x} + \frac{v_x^2 t}{4D_x} \right] \exp\left[-\frac{v_y y}{2D_y} + \frac{v_y^2 t}{4D_y} \right]. \tag{B.3}$$

The resulting PDE after the variable transformation is given as,

$$\frac{\partial c}{\partial t} = D_x \frac{\partial^2 c}{\partial x^2} + D_y \frac{\partial^2 c}{\partial y^2} \tag{B.4}$$

subject to the following boundary condition,

$$c(0, y, t) = C_0 \exp\left[\frac{v_x^2 t}{4D_x}\right] \exp\left[-\frac{v_y y}{2D_y} + \frac{v_y^2 t}{4D_y}\right] \qquad at \quad Y_1 < y < Y_2 \tag{B.5a}$$

$$c = 0, \qquad y = 0, y = W \tag{B.5b}$$

$$c = 0, \qquad x = \infty \tag{B.5c}$$

$$c(x, y, 0) = 0. \tag{B.5d}$$

The partial derivative of x in equation (B.1) is removed by applying the Fourier sine transform defined by Churchill (1972, p 401-402) as

$$S_\alpha \{F(x)\} = \int_0^\infty F(x) \sin(\alpha x) dx = f_s(\alpha) \quad (\alpha > 0) \tag{B.6}$$

whose basic operation property can be expressed as,

$$S_\alpha \left\{\frac{d^2 F(x)}{dx^2}\right\} = -\alpha^2 f_s(\alpha) + \alpha F(0). \tag{B.7}$$

The inverse of the finite sine transformation is given as,

$$S_\alpha^{-1} \{f_s(\alpha)\} = F(x) = \frac{2}{\pi} \int_0^\infty f_s(\alpha) \sin(\alpha x) d\alpha \quad (x > 0). \tag{B.8}$$

The transformed equation, with its boundary and initial conditions is expressed as,

$$\frac{\partial \bar{c}}{\partial t} + \alpha^2 D_x \bar{c} - D_y \frac{\partial^2 \bar{c}}{\partial y^2} = \alpha D_x C_0 \exp\left[\frac{v_x^2 t}{4D_x} + \frac{v_y^2 t}{4D_y}\right] \exp\left[-\frac{v_y y}{2D_y}\right] \tag{B.9}$$

subject to the boundary and initial conditions,

$$\bar{c} = 0, \qquad y = 0, y = W \tag{B.10a}$$

$$\bar{c}(x, y, 0) = 0. \tag{B.10b}$$

The partial derivative of y in equation (B.9) is removed by applying the finite Fourier cosine transform defined by Churchill (1972, p 354-355) as

$$C\{F(y)\} = \int_0^W F(y) \cos\left(\frac{n\pi y}{W}\right) dy = f_c \qquad (0 < y < W) \tag{B.11}$$

whose basic operation property can be expressed as,

$$C\left\{\frac{d^2F(y)}{dy^2}\right\} = (-1)^n \frac{dG}{dy}_{y=W} - \frac{dG}{dy}_{y=0} - \left(\frac{n\pi}{W}\right)^2 f_c . \tag{B.12}$$

The inverse of the Finite cosine transformation is given as,

$$C^{-1}\{f_c\} = \frac{f_c(0)}{W}_{n=0} + \frac{2}{W}\sum_{n=1}^{\infty} f_c(n)\cos\left(\frac{n\pi y}{W}\right). \tag{B.13}$$

Let $\eta = \frac{n\pi}{W}$ and applying the finite Fourier cosine transform,

$$\frac{d\bar{\bar{c}}}{dt} + \left(\alpha^2 D_x + \eta^2 D_y\right)\bar{\bar{c}} = \alpha D_x C_0 \exp\left[\frac{v_x^2 t}{4D_x} + \frac{v_y^2 t}{4D_y}\right] I_y \tag{B.14}$$

where,

$$I_y = \int_{Y_1}^{Y_2} \exp\left[\frac{-v_y y}{2D_y}\right]\cos(\eta y)\, dy . \tag{B.15}$$

The above integral is over Y_2 to Y_1 rather than from 0 to W because C_0 only has nonzero values between Y_2 to Y_1.

Equation (B.14), which is the transformed ordinary differential equation (ODE), is solved by an integrating factor. Given an ODE of the form below,

$$\frac{dw}{dt} + gw = h(t) \tag{B.16a}$$

the solution is given as (Wexler, 1989),

$$w = \frac{1}{p(t)}\int_{t_0}^{t} p(\tau)h(\tau)\, d\tau + w_0 \frac{p(t)}{p(t_0)} \tag{B.16b}$$

where p(t) is the integrating factor and it is expressed as,

$$p(t) = \exp\left[\int g(\tau)\, d\tau\right]. \tag{B.16c}$$

Applying equation (B.16) to the transformed ODE gives,

$$p(t) = \exp\left[\int_0^t \left(\alpha^2 D_x + \eta^2 D_y\right) d\tau\right] = \exp\left[\alpha^2 D_x t + \eta^2 D_y t\right] \tag{B.17}$$

$$\bar{\bar{c}} = \frac{\alpha D_x C_0 I_y}{\exp\left[\alpha^2 D_x t + \eta^2 D_y t\right]}\int_{t=0}^{t} \exp\left[\alpha^2 D_x \tau + \eta^2 D_y \tau + \frac{v_x^2 \tau}{4D_x} + \frac{v_y^2 \tau}{4D_y}\right] d\tau . \tag{B.18}$$

Integrating equation (B.18) ,

$$\overline{\overline{c}} = \frac{\alpha D_x C_0 I_y}{\alpha^2 D_x + \eta^2 D_y + \frac{v_x^2}{4D_x} + \frac{v_y^2}{4D_y}} \left\{ \exp\left[\frac{v_x^2 t}{4D_x} + \frac{v_y^2 t}{4D_y} \right] - \exp\left[-\alpha^2 D_x t - \eta^2 D_y t \right] \right\}. \qquad \text{(B.19)}$$

The inverse Fourier sine transform is applied to remove the "α" term.

$$\overline{\overline{c}} = C_0 I_y \left\{ \exp\left[\frac{v_x^2 t}{4D_x} + \frac{v_y^2 t}{4D_y} \right] S_\alpha^{-1} \left\{ \frac{\alpha}{\alpha^2 + \eta^2 \frac{D_y}{D_x} + \frac{v_x^2}{4D_x^2} + \frac{v_y^2}{4D_x D_y}} \right\} - \exp\left[-\eta^2 D_y t \right] \times S_\alpha^{-1} \left\{ \frac{\alpha \exp\left[-\alpha^2 D_x t \right]}{\alpha^2 + \eta^2 \frac{D_y}{D_x} + \frac{v_x^2}{4D_x^2} + \frac{v_y^2}{4D_x D_y}} \right\} \right\}. \qquad \text{(B.20)}$$

The table of inverse Fourier sine transform in Churchill (1972, pp. 474) is used to resolve the first inverse.

$$S_\alpha^{-1} \left\{ \frac{\alpha}{\alpha^2 + \eta^2 \frac{D_y}{D_x} + \frac{v_x^2}{4D_x^2} + \frac{v_y^2}{4D_x D_y}} \right\} = \exp\left[-x \left(\alpha^2 + \eta^2 \frac{D_y}{D_x} + \frac{v_x^2}{4D_x^2} + \frac{v_y^2}{4D_x D_y} \right)^{1/2} \right]. \qquad \text{(B.21)}$$

There is no match for the second inverse transform in the inverse table. Therefore an integration of the form below is performed,

$$S_\alpha^{-1} \left\{ \frac{\alpha \exp\left[-a\alpha^2 \right]}{\alpha^2 + b^2} \right\} = \frac{2}{\pi} \int_0^\infty \frac{\alpha \exp\left[-a\alpha^2 \right]}{\alpha^2 + b^2} \sin(\alpha x) \, d\alpha \qquad \text{(B.22a)}$$

where,

$$a = D_x t \qquad \text{(B.22b)}$$

$$\gamma = b = \left(\eta^2 \frac{D_y}{D_x} + \frac{v_x^2}{4D_x^2} + \frac{v_y^2}{4D_x D_y} \right)^{1/2}. \tag{B.22c}$$

The solution of this integral is given by Gradshteyn and Ryzhik (2007, pp. 504, eq. 3.954),

$$S_\alpha^{-1}\left\{ \frac{\alpha \exp\left[-a\alpha^2\right]}{\alpha^2 + b^2} \right\} = \frac{2}{\pi}\left\{ -\frac{\pi}{4}\exp\left[ab^2\right]\left[\begin{array}{l} 2\sinh(xb) + \exp\left[-xb\right] erf\left[b\sqrt{a} - \frac{x}{2\sqrt{a}} \right] \\ -\exp\left[xb\right] erf\left[b\sqrt{a} + \frac{x}{2\sqrt{a}} \right] \end{array} \right] \right\}. \tag{B.23}$$

where sinh(xb) is the hyperbolic sine. Substituting $\sinh(xb) = 0.5\left(\exp\left[xb\right] - \exp\left[-xb\right]\right)$ and re-arranging equation (B.23) gives,

$$S_\alpha^{-1}\left\{ \frac{\alpha \exp\left[-a\alpha^2\right]}{\alpha^2 + b^2} \right\} = \frac{1}{2}\exp\left[ab^2\right] \cdot \left[\exp\left[-xb\right] erfc\left[b\sqrt{a} - \frac{x}{2\sqrt{a}} \right] - \exp\left[xb\right] erfc\left[b\sqrt{a} + \frac{x}{2\sqrt{a}} \right] \right]. \tag{B.24}$$

where $1 - erf(x) = erfc(x)$.

Substituting the inverse transform into the solution,

$$\bar{c} = C_0 I_y \left\{ \exp\left[\frac{v_x^2 t}{4D_x} + \frac{v_y^2 t}{4D_y} - x\gamma \right] - \frac{1}{2}\exp\left[\frac{v_x^2 t}{4D_x} + \frac{v_y^2 t}{4D_y} \right] \left\{ \begin{array}{l} \exp\left[-x\gamma\right] erfc\left[\gamma\sqrt{D_x t} - \frac{x}{2\sqrt{D_x t}} \right] \\ -\exp\left[x\gamma\right] erfc\left[\gamma\sqrt{D_x t} + \frac{x}{2\sqrt{D_x t}} \right] \end{array} \right\} \right\}$$

. (B.25)

Using the identity $erfc(-x) = 2 - erfc(x)$, equation (B.25) can be simplified,

$$\bar{c} = C_0 I_y \left\{ \frac{1}{2} \exp\left[\frac{v_x^2 t}{4D_x} + \frac{v_y^2 t}{4D_y} \right] \left\{ \begin{array}{l} \exp\left[-x\gamma\right] erfc\left[\frac{x - 2D_x t\gamma}{2\sqrt{D_x t}} \right] \\ + \exp\left[x\gamma\right] erfc\left[\frac{x + 2D_x t\gamma}{2\sqrt{D_x t}} \right] \end{array} \right\} \right\}. \quad \text{(B.26)}$$

The integral I_y can be simplified with the following conditions. When v_y=0 and n=0

$$I_{y, v_y = 0, n=0} = \int_{Y_1}^{Y_2} dy = Y_2 - Y_1. \quad \text{(B.27)}$$

If $v_y \neq 0$ and n = 0

$$I_{y,n=0} = \int_{Y_1}^{Y_2} \exp\left[\frac{-v_y y}{2D_y} \right] dy = \frac{2D_y}{v_y} \left\{ \exp\left[\frac{-v_y Y_1}{2D_y} \right] - \exp\left[\frac{-v_y Y_2}{2D_y} \right] \right\}. \quad \text{(B.28)}$$

When n>0

$$I_{y,n>0} = \int_{Y_1}^{Y_2} \exp\left[\frac{-v_y y}{2D_y} \right] \cos(\eta y)\, dy = \frac{1}{\left(\frac{v_y}{2D_y} \right)^2 + \eta^2} \left\{ \begin{array}{l} \exp\left[\frac{-v_y Y_2}{2D_y} \right] \left(\eta \sin(\eta Y_2) - \frac{v_y \cos(\eta Y_2)}{2D_y} \right) \\ - \exp\left[\frac{-v_y Y_1}{2D_y} \right] \left(\eta \sin(\eta Y_1) - \frac{v_y \cos(\eta Y_1)}{2D_y} \right) \end{array} \right\}$$

. (B.29)

Applying the inverse finite Fourier cosine transform and simplifying,

$$c = \frac{C_0}{W} \sum_{n=0}^{\infty} L_n P_n \cos(\eta y) \exp\left[\frac{v_x^2 t}{4D_x} + \frac{v_y^2 t}{4D_y} \right] \left\{ \begin{array}{l} \exp\left[-x\gamma\right] erfc\left[\frac{x - 2D_x t\gamma}{2\sqrt{D_x t}} \right] \\ + \exp\left[x\gamma\right] erfc\left[\frac{x + 2D_x t\gamma}{2\sqrt{D_x t}} \right] \end{array} \right\} \quad \text{(B.30)}$$

where,

$$L_n = \begin{cases} \frac{1}{2} & n = 0 \\ 1 & n > 0 \end{cases}$$

$$P_n = \begin{cases} I_{y,v_y=0,n=0} & v_y = 0, n = 0 \\ I_{y,v_y\neq 0,n=0} & v_y \neq 0, n = 0 \\ I_{y,n>0} & n > 0 \end{cases}.$$

The dependent variable "c" is transformed back to "C" by multiplying by the transformation parameter given by equation (B.3).

$$C(x,y,t) = c(x,y,t)\exp\left[\frac{v_x x}{2D_x} - \frac{v_x^2 t}{4D_x}\right]\exp\left[\frac{v_y y}{2D_y} - \frac{v_y^2 t}{4D_y}\right]. \tag{B.31}$$

The final solution for the 2-D CDE with finite height, semi-infinite medium is given by,

$$C(x,y,t) = \frac{C_0}{W}\sum_{n=0}^{\infty} L_n P_n \cos(\eta y)\exp\left[\frac{v_x x}{2D_x} + \frac{v_y y}{2D_y}\right]\left\{\begin{array}{l} \exp[-x\gamma]\,erfc\left[\dfrac{x - 2D_x t\gamma}{2\sqrt{D_x t}}\right] \\ +\exp[x\gamma]\,erfc\left[\dfrac{x + 2D_x t\gamma}{2\sqrt{D_x t}}\right] \end{array}\right\} \tag{B.32}$$

where,

$$L_n = \begin{cases} \frac{1}{2} & n = 0 \\ 1 & n > 0 \end{cases}$$

$$P_n = \begin{cases} I_{y,v_y=0,n=0} & v_y = 0, n = 0 \\ I_{y,v_y\neq 0,n=0} & v_y \neq 0, n = 0 \\ I_{y,n>0} & n > 0 \end{cases}$$

$$\gamma = \left(\eta^2\frac{D_y}{D_x} + \frac{v_x^2}{4D_x^2} + \frac{v_y^2}{4D_x D_y}\right)^{1/2}$$

$$\eta = \frac{n\pi}{W}$$

$$I_{y,v_y=0,n=0} = Y_2 - Y_1$$

$$I_{y,v_y\neq 0,n=0} = \frac{2D_y}{v_y}\left\{\exp\left[\frac{-v_y Y_1}{2D_y}\right] - \exp\left[\frac{-v_y Y_2}{2D_y}\right]\right\}$$

$$I_{y,n>0} = \frac{1}{\left(\frac{v_y}{2D_y}\right)^2 + \eta^2} \left\{ \begin{array}{l} \exp\left[\frac{-v_y Y_2}{2D_y}\right]\left(\eta \sin\left(\eta Y_2\right) - \frac{v_y \cos\left(\eta Y_2\right)}{2D_y}\right) \\ -\exp\left[\frac{-v_y Y_1}{2D_y}\right]\left(\eta \sin\left(\eta Y_1\right) - \frac{v_y \cos\left(\eta Y_1\right)}{2D_y}\right) \end{array} \right\}.$$

Appendix C: Derivation of Scaling Groups for Miscible Fluid Displacements

Inspectional analysis has been used by several authors to derive the scaling groups for miscible displacements. The derivations are repeated here for completeness. The effect of off-diagonal dispersion coefficient is also investigated.

Consider a FCM displacement of incompressible fluids in a two-dimensional medium. The reservoir is homogenous, but anisotropic with a dip angle α (see Figure C.1). The principle flow direction is the x-axis with no flow across the top and bottom of the medium. There are no chemical reactions and negligible adsorption in this medium. The injection rate at the left hand side is constant and the production well is at constant pressure. The porosity for this medium is assumed uniform and constant.

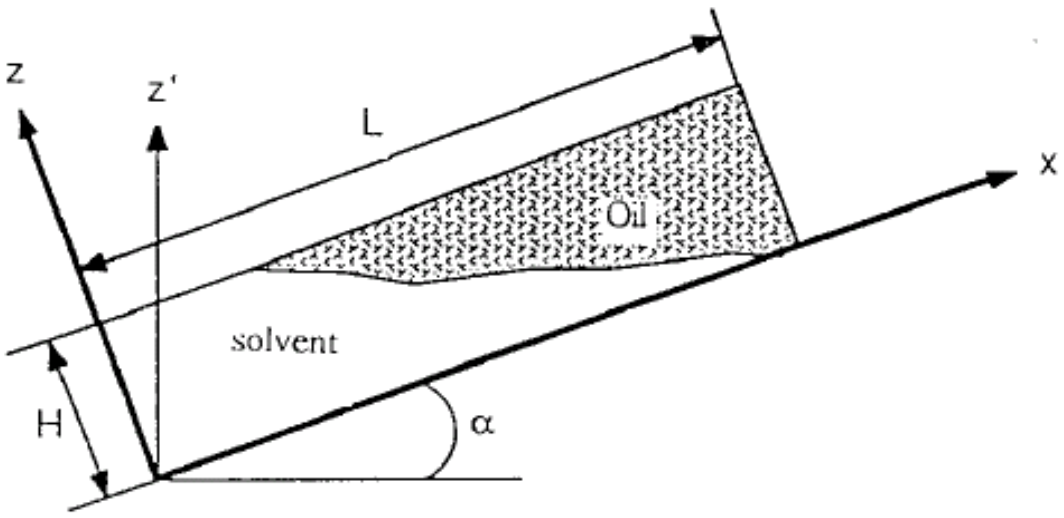

Figure C.1: Oil displacement in a two-dimensional porous medium (from Shook *et al.* 1992, Gharbi *et al.* 1998)

This displacement can be modeled with the conservation equation, continuity equation and other auxiliary equations such as Darcy's equation and mixing rules for

viscosity and density. The conservation equation for FCM displacement for a 2D reservoir is,

$$\frac{\partial}{\partial t}(\phi c_i)+\frac{\partial}{\partial x}(c_i u_x)+\frac{\partial}{\partial z}(c_i u_z)-\phi D_{ixx}\frac{\partial^2 c_i}{\partial x^2}-\phi D_{izz}\frac{\partial^2 c_i}{\partial z^2}=0 \quad i=1..n_c \tag{C.1}$$

where D_{ixx} and D_{izz} are the longitudinal and transverse dispersion coefficients respectively. We assume that flow is dominant in the principal flow directions and therefore the off-diagonal terms of the dispersion tensor are negligible.

The continuity equation for steady-state flow is given by,

$$\nabla\cdot\vec{u}=0 \tag{C.2}$$

where the volumetric flux is expressed by Darcy's law as;

$$u_x=-\frac{k_x}{\mu_m}\left(\frac{\partial P}{\partial x}+\rho_m g\sin(\alpha)\right) \tag{C.3a}$$

$$u_z=-\frac{k_z}{\mu_m}\left(\frac{\partial P}{\partial z}+\rho_m g\cos(\alpha)\right). \tag{C.3b}$$

The viscosity and density of the single-phase mixture (μ_m, ρ_m) is given by mixing rules. A quarter mixing rule is used for the viscosity while a linear mixing rule is used for the density.

$$\mu_m=\left[\mu_o^{-1/4}+\beta\left(\mu_s^{-1/4}-\mu_o^{-1/4}\right)\right]^{-4} \tag{C.4a}$$

$$\rho_m=\rho_o+\beta\Delta\rho\,. \tag{C.4b}$$

The mixing rules are a function of the concentration of the invading solvent (β), which is expressed as;

$$\beta=\frac{c_1-c_1^I}{c_1^J-c_1^I} \tag{C.5}$$

where c_1 is the injection component. The imposed initial and boundary conditions for this system are listed below,

$$c=c_i^I \quad @t=t_o \quad \forall x,z \quad i=1,..n_c \tag{C.6}$$

$$P=P_o \quad @t=t_o \quad \forall x,z \tag{C.7}$$

$$c = c_i^J \quad @\, x = x_o \quad \forall x, z \quad i = 1,..n_c \tag{C.8}$$

$$u_x = u_{inj} \,@\, x = x_o \quad \forall x, z \tag{C.9}$$

$$u_z = 0 \quad @\, z = z_o \quad \forall t, x \tag{C.10}$$

$$u_z = 0 \quad @\, z = H \quad \forall t, x \tag{C.11}$$

$$P = P_{wf} + \overline{\rho} g \cos(\alpha)(H - z) \quad @\, x = L \quad \forall t, z\,. \tag{C.12}$$

The average density in the pressure boundary condition at the outlet of the medium is the volumetric flux averaged density at the outlet or the production well. Shook *et al.* (1992) defined this average density as;

$$\overline{\rho} = \rho_o + \Delta\rho \frac{\int_0^H u_x dz}{H u_T} \tag{C.13}$$

where $0 \le z \le H$.

Arbitrary scaling factors are now introduced in order to define dimensionless variables.

$$\begin{aligned} c_i &= c_i^{2^*} c_{iD} + c_i^{1^*} \\ x &= x^{2^*} x_D + x^{1^*} \\ z &= z^{2^*} z_D + z^{1^*} \\ P &= P^{2^*} P_D + P^{1^*} \\ t &= t^{2^*} t_D + t^{1^*} \\ u_x &= u_x^{2^*} u_{xD} + u_x^{1^*} \\ u_z &= u_z^{2^*} u_{zD} + u_z^{1^*} \end{aligned} \quad . \tag{C.14}$$

The scaling factors and dimensionless variable are substituted into the governing equations. Substitution into the accumulation term of the conservation equation gives,

$$\frac{\partial}{\partial t}(\phi c_i) = \phi \frac{\partial\left(c_i^{2^*} c_{iD} + c_i^{1^*}\right)}{\partial\left(t^{2^*} t_D + t^{1^*}\right)} = \left[\frac{\phi c_i^{2^*}}{t^{2^*}}\right] \frac{\partial}{\partial t_D}(c_{iD}) \quad i = 1,..,n_c\,. \tag{C.15}$$

The flux term in the x-direction gives;

$$\frac{\partial}{\partial x}\left(c_i u_x\right)=\left(u_x^{2^*}u_{xD}+u_x^{1^*}\right)\frac{\partial\left(c_i^{2^*}c_{iD}+c_i^{1^*}\right)}{\partial\left(x^{2^*}x_D+x^{1^*}\right)}=\left[\frac{u_x^{2^*}c_i^{2^*}}{x^{2^*}}\right]u_{xD}\frac{\partial c_{iD}}{\partial x_D}+\left[\frac{u_x^{1^*}c_i^{2^*}}{x^{2^*}}\right]\frac{\partial c_{iD}}{\partial x_D}. \quad \text{(C.16)}$$

Because we do not want to change the original form of the equation the term $u_x^{1^*}$ on the right side of equation (C.16) is set to zero. This is permissible since the scaling groups are arbitrary. Therefore the above equation is reduced to;

$$\frac{\partial}{\partial x}\left(c_i u_x\right)=\left[\frac{u_x^{2^*}c_i^{2^*}}{x^{2^*}}\right]u_{xD}\frac{\partial c_{iD}}{\partial x_D}. \quad \text{(C.17)}$$

Similarly, the flux term of the conservation equation in z-direction is reduced to;

$$\frac{\partial}{\partial z}\left(c_i u_z\right)=\left[\frac{u_z^{2^*}c_i^{2^*}}{z^{2^*}}\right]u_{zD}\frac{\partial c_{iD}}{\partial z_D}. \quad \text{(C.18)}$$

The dispersion terms in the conservation equation in the x-direction is expanded as;

$$\phi D_{ixx}\frac{\partial^2 c_i}{\partial x^2}=\phi D_{ixx}\frac{\partial}{\partial x}\left(\frac{\partial c_i}{\partial x}\right)=\phi D_{ixx}\frac{\partial}{\partial\left(x^{2^*}x_D+x^{1^*}\right)}\left(\frac{\partial\left(c_i^{2^*}c_{iD}+c_i^{1^*}\right)}{\partial\left(x^{2^*}x_D+x^{1^*}\right)}\right) \quad \text{(C.19a)}$$

$$\phi D_{ixx}\frac{\partial^2 c_i}{\partial x^2}=\left[\frac{\phi D_{ixx}c_i^{2^*}}{\left(x^{2^*}\right)^2}\right]\frac{\partial^2 c_{iD}}{\partial x_D^2}. \quad \text{(C.19b)}$$

Similarly the dispersion term in the z-direction is expressed as;

$$\phi D_{izz}\frac{\partial^2 c_i}{\partial z^2}=\left[\frac{\phi D_{izz}c_i^{2^*}}{\left(z^{2^*}\right)^2}\right]\frac{\partial^2 c_{iD}}{\partial z_D^2}. \quad \text{(C.20)}$$

Combining the terms in the conservation equations in dimensionless form and simplifying gives,

$$\begin{aligned}&\left[\frac{\phi c_i^{2^*}}{t^{2^*}}\right]\frac{\partial}{\partial t_D}\left(c_{iD}\right)+\left[\frac{u_x^{2^*}c_i^{2^*}}{x^{2^*}}\right]u_{xD}\frac{\partial c_{iD}}{\partial x_D}+\left[\frac{u_z^{2^*}c_i^{2^*}}{z^{2^*}}\right]u_{zD}\frac{\partial c_{iD}}{\partial z_D}\\&-\left[\frac{\phi D_{ixx}c_i^{2^*}}{\left(x^{2^*}\right)^2}\right]\frac{\partial^2 c_{iD}}{\partial x_D^2}-\left[\frac{\phi D_{izz}c_i^{2^*}}{\left(z^{2^*}\right)^2}\right]\frac{\partial^2 c_{iD}}{\partial z_D^2}=0\end{aligned} \quad \text{(C.21)}$$

which yields,

$$\frac{\partial}{\partial t_D}\left(c_{iD}\right)+\underbrace{\left[\frac{t^{2^*}u_x^{2^*}}{\phi x^{2^*}}\right]}_{1}u_{xD}\frac{\partial c_{iD}}{\partial x_D}+\underbrace{\left[\frac{t^{2^*}u_z^{2^*}}{\phi z^{2^*}}\right]}_{2}u_{zD}\frac{\partial c_{iD}}{\partial z_D}-\underbrace{\left[\frac{t^{2^*}D_{ixx}}{\left(x^{2^*}\right)^2}\right]}_{3}\frac{\partial^2 c_{iD}}{\partial x_D^2}-\underbrace{\left[\frac{t^{2^*}D_{izz}}{\left(z^{2^*}\right)^2}\right]}_{4}\frac{\partial^2 c_{iD}}{\partial z_D^2}=0. \tag{C.22}$$

Substitution of the scaling factors into the continuity equation and simplifying results in

$$\frac{\partial u_x}{\partial x}+\frac{\partial u_z}{\partial z}=\frac{\partial\left(u_x^{2^*}u_{xD}+u_x^{1^*}\right)}{\partial\left(x^{2^*}x_D+x^{1^*}\right)}+\frac{\partial\left(u_z^{2^*}u_{zD}+u_z^{1^*}\right)}{\partial\left(z^{2^*}z_D+z^{1^*}\right)}=\frac{u_x^{2^*}}{x^{2^*}}\frac{\partial u_{xD}}{\partial x_D}+\frac{u_z^{2^*}}{z^{2^*}}\frac{\partial u_{zD}}{\partial z_D}=0 \tag{C.23a}$$

which yields,

$$\frac{\partial u_{xD}}{\partial x_D}+\underbrace{\left[\frac{x^{2^*}u_z^{2^*}}{z^{2^*}u_x^{2^*}}\right]}_{5}\frac{\partial u_{zD}}{\partial z_D}=0. \tag{C.23b}$$

Expanding the Darcy equation in the x-direction with the scaling factors;

$$u_x^{2^*}u_{xD}+u_x^{1^*}=-\frac{k_x}{\left[\mu_o^{-1/4}+\beta\left(\mu_s^{-1/4}-\mu_o^{-1/4}\right)\right]^{-4}}\left(\frac{\partial\left(P^{2^*}P_D+P^{1^*}\right)}{\partial\left(x^{2^*}x_D+x^{1^*}\right)}+\left(\rho_o+\beta\Delta\rho\right)g\sin\left(\alpha\right)\right). \tag{C.24}$$

Recall that we had set $u_x^{1^*}$ to zero and simplifying;

$$u_{xD}=-\frac{1}{\left[\mu_o^{-1/4}+\beta\left(\mu_s^{-1/4}-\mu_o^{-1/4}\right)\right]^{-4}}\frac{k_x}{u_x^{2^*}}\left(\frac{P^{2^*}}{x^{2^*}}\frac{\partial P_D}{\partial x_D}+\left(\rho_o+\beta\Delta\rho\right)g\sin\left(\alpha\right)\right) \tag{C.25}$$

$$u_{xD} = -\frac{1}{\left[\underbrace{\left(\frac{u_x^{2^*} x^{2^*} \mu_o}{k_x P^{2^*}}\right)^{-1/4}}_{6} + \underbrace{\left(\frac{u_x^{2^*} x^{2^*} [\beta]^{-4} \mu_s}{k_x P^{2^*}}\right)^{-1/4}}_{7} - \underbrace{\left(\frac{u_x^{2^*} x^{2^*} [\beta]^{-4} \mu_0}{k_x P^{2^*}}\right)^{-1/4}}_{8}\right]^{-4}} \frac{\partial P_D}{\partial x_D}$$

$$-\sin(\alpha)\left\{\frac{1}{\left[\underbrace{\left(\frac{u_x^{2^*} \mu_o}{k_x \rho_o g}\right)^{-1/4}}_{9} + \underbrace{\left(\frac{u_x^{2^*} [\beta]^{-4} \mu_s}{k_x \rho_o g}\right)^{-1/4}}_{10} - \underbrace{\left(\frac{u_x^{2^*} [\beta]^{-4} \mu_0}{k_x \rho_o g}\right)^{-1/4}}_{11}\right]^{-4}}\right\}$$

$$-\sin(\alpha)\left\{\frac{1}{\left[\underbrace{\left(\frac{u_x^{2^*} \mu_o}{k_x \beta \Delta \rho g}\right)^{-1/4}}_{12} + \underbrace{\left(\frac{u_x^{2^*} [\beta]^{-4} \mu_s}{k_x \beta \Delta \rho g}\right)^{-1/4}}_{13} - \underbrace{\left(\frac{u_x^{2^*} [\beta]^{-4} \mu_0}{k_x \beta \Delta \rho g}\right)^{-1/4}}_{14}\right]^{-4}}\right\} \quad . \qquad \text{(C.26)}$$

Similarly the Darcy equation in z-direction is expressed as;

$$u_{zD} = -\frac{1}{\left[\underbrace{\left(\frac{u_z^{2^*} z^{2^*} \mu_o}{k_z P^{2^*}}\right)^{-1/4}}_{15} + \underbrace{\left(\frac{u_z^{2^*} z^{2^*} [\beta]^{-4} \mu_s}{k_z P^{2^*}}\right)^{-1/4}}_{16} - \underbrace{\left(\frac{u_z^{2^*} z^{2^*} [\beta]^{-4} \mu_0}{k_z P^{2^*}}\right)^{-1/4}}_{17}\right]^{-4}} \frac{\partial P_D}{\partial z_D}$$

$$-\cos(\alpha)\left\{\frac{1}{\left[\underbrace{\left(\frac{u_z^{2^*} \mu_o}{k_z \rho_o g}\right)^{-1/4}}_{18} + \underbrace{\left(\frac{u_z^{2^*} [\beta]^{-4} \mu_s}{k_z \rho_o g}\right)^{-1/4}}_{19} - \underbrace{\left(\frac{u_z^{2^*} [\beta]^{-4} \mu_0}{k_z \rho_o g}\right)^{-1/4}}_{20}\right]^{-4}}\right\}$$

$$-\cos(\alpha)\left\{\frac{1}{\left[\underbrace{\left(\frac{u_z^{2^*} \mu_o}{k_z \beta \Delta \rho g}\right)^{-1/4}}_{21} + \underbrace{\left(\frac{u_z^{2^*} [\beta]^{-4} \mu_s}{k_z \beta \Delta \rho g}\right)^{-1/4}}_{22} - \underbrace{\left(\frac{u_z^{2^*} [\beta]^{-4} \mu_0}{k_z \beta \Delta \rho g}\right)^{-1/4}}_{23}\right]^{-4}}\right\} \quad . \qquad \text{(C.27)}$$

Substitution of the scaling factors into the initial and boundary conditions gives;

$$c_i^{2^*} c_{iD} + c_i^{1^*} = c_i^I \quad @t^{2^*} t_D + t^{1^*} = t_o \quad \forall x_D, z_D \quad i = 1,..,n_c \quad . \tag{C.28a}$$

Let $c_{iD} = 0$, at $t_D = 0$, therefore $c_i^{1^*} = c_i^I$ and $t^{1^*} = t_o$

$$P^{2^*} P_D + P^{1^*} = P_o \quad @t^{2^*} t_D = 0 \quad \forall x_D, z_D \tag{C.28b}$$

Let $P_D = 0$ at $t_D = 0$, therefore $P^{1^*} = P_o$

$$c_1^{2^*} c_{1D} + c_1^{1^*} = c_1^J \quad @x^{2^*} x_D + x^{1^*} = x_o \quad \forall t_D, z_D \tag{C.29}$$

Let $c_{1D} = 1$, at $x_D = 0$, therefore $c_1^{2^*} = c_1^J - c_i^I$ and $x^{1^*} = x_o$

$$u_x^{2^*} u_{xD} + u_x^{1^*} = u_{inj} \quad @x^{2^*} x_D + x^{1^*} = x_o \quad \forall t_D, z_D \tag{C.30}$$

Let $u_{xD} = 1$, at $x_D = 0$, therefore $u_x^{2^*} = u_{inj}$

$$u_z^{2^*} u_{zD} + u_z^{1^*} = 0 \quad @z^{2^*} z_D + z^{1^*} = z_o \quad \forall t_D, x_D \tag{C.31}$$

Let $u_{zD} = 0$, at $z_D = 0$, therefore $z^{1^*} = z_o$

$$u_z^{2^*} u_{zD} + u_z^{1^*} = 0 \quad @z^{2^*} z_D + z^{1^*} = H \tag{C.32}$$

Let $u_{zD} = 0$, at $z_D = 1$, therefore $z^{2^*} = H - z_o = H_{Z_0 = 0}$

$$P^{2^*} P_D + P^{1^*} = P_{wf} + \frac{g\cos(\alpha)\left(H - z^{2^*} z_D - z^{1^*}\right)}{H u_T} \left\{ \rho_o + \Delta\rho \int_0^{H - z^{1^*} / z^{2^*}} \left(u_x^{2^*} u_{xD} + u_x^{1^*}\right) d\left(z^{2^*} z_D + z^{1^*}\right) \right\} \tag{C.33}$$

at $x^{2^*} x_D + x^{1^*} = L$, where $0 \le z^{2^*} z_D + z^{1^*} \le H \quad \forall t_D, x_D$

Simplifying equation (C.33);

$$P_D = \underbrace{\frac{P_{wf} - P^{1^*}}{P^{2^*}}}_{24} + \underbrace{\frac{\rho_o g\cos(\alpha)\left(H - z^{2^*} z_D - z^{1^*}\right)}{P^{2^*}}}_{25} + \underbrace{\frac{\Delta\rho g\cos(\alpha)\left(H - z^{2^*} z_D - z^{1^*}\right) u_x^{2^*} z^{2^*}}{H u_T P^{2^*}}}_{26} \int_0^{H - z^{1^*} / z^{2^*}} \underbrace{u_{xD} dz_D}_{27} \tag{C.34}$$

at $x_D = \underbrace{\frac{L - x^{1^*}}{x^{2^*}}}_{28}$, where $\underbrace{\frac{-z^{1^*}}{z^{2^*}}}_{29} \le z_D \le \underbrace{\frac{H - z^{1^*}}{z^{2^*}}}_{30} \quad \forall t_D, x_D$

Let $x_D = 1$ and $0 \le z_D \le 1$, therefore, $x^{2*} = L - x_o = L_{x_o=0}$, $z^{1*} = 0$ and $z^{2*} = H$

Setting dimensionless group 24, $\frac{P_{wf} - P^{1*}}{P^{2*}}$ to 1, gives,

$$P^{2*} = P_{wf} - P^{1*} = P_{wf} - P_o = \Delta P \tag{C.35}$$

Setting dimensionless group 6, $\frac{u_x^{2*} x^{2*} \mu_o}{k_x P^{2*}}$ to 1, gives,

$$P^{2*} = \frac{u_x^{2*} x^{2*} \mu_o}{k_x} \tag{C.36}$$

P^{2*} can be expressed as equation (C.35) or (C.36).

Since scaling factors are arbitrary, they can be eliminated or defined by setting the derived dimensionless groups to zero or one. However, the process of elimination or definition should not change the original form of the governing equations. Also the scale factors that multiply the dimensionless variables should not be set to zero, else the dimensionless variable will be lost.

Setting dimensionless group 1, $\frac{t^{2*} u_x^{2*}}{\phi x^{2*}}$ to 1, gives,

$$u_x^{2*} = \frac{\phi x^{2*}}{t^{2*}} \tag{C.37}$$

Setting dimensionless group 2, $\frac{t^{2*} u_z^{2*}}{\phi z^{2*}}$ to 1, and simplifying by substituting equation 37 gives,

$$u_z^{2*} = \frac{\phi z^{2*}}{t^{2*}} = \frac{u_x^{2*} z^{2*}}{x^{2*}} \tag{C.38}$$

Substitution of t^{2*} into dimensionless group 3, $\frac{t^{2*} D_{ixx}}{\left(x^{2*}\right)^2}$ using equation (C.37), gives,

$$\frac{t^{2*} D_{ixx}}{\left(x^{2*}\right)^2} = \frac{\phi x^{2*}}{u_x^{2*}} \frac{D_{ixx}}{\left(x^{2*}\right)^2} = \frac{\phi D_{ixx}}{u_x^{2*} x^{2*}} \tag{C.39}$$

Therefore the first dimensionless group is,

$$G1 = \frac{\phi D_{ixx}}{u_{inj} L} = \frac{1}{N_{pe}} \tag{C.40}$$

Simplifying dimensionless group 4, $\left[\frac{t^{2*} D_{izz}}{\left(z^{2*}\right)^2}\right]$, gives,

$$\frac{t^{2*} D_{izz}}{\left(z^{2*}\right)^2} = \frac{\phi x^{2*} D_{izz}}{u_x^{2*}\left(z^{2*}\right)^2} \tag{C.41}$$

Therefore,

$$G2 = \frac{\phi D_{izz} L}{u_{inj} H^2} \tag{C.42}$$

Dimensionless group 5 is unity after substituting the scaling factors. Setting dimensionless group 6, $\frac{u_x^{2*} x^{2*} \mu_o}{k_x P^{2*}}$ to 1, gives,

$$\mu_o = \frac{k_x P^{2*}}{u_x^{2*} x^{2*}} \tag{C.43}$$

$$u_x^{2*} = \frac{k_x P^{2*}}{\mu_o x^{2*}} \tag{C.44}$$

Substitute equation (C.43) into dimensionless group 7, $\left(\frac{u_x^{2*} x^{2*} [\beta]^{-4} \mu_s}{k_x P^{2*}}\right)$ and 8, $\left(\frac{u_x^{2*} x^{2*} [\beta]^{-4} \mu_0}{k_x P^{2*}}\right)$

$$\left(\frac{u_x^{2*} x^{2*} \mu_o}{k_x P^{2*}}\right)^{-1/4} + \left(\frac{u_x^{2*} x^{2*} [\beta]^{-4} \mu_s}{k_x P^{2*}}\right)^{-1/4} - \left(\frac{u_x^{2*} x^{2*} [\beta]^{-4} \mu_0}{k_x P^{2*}}\right)^{-1/4} = 1 + \left(\frac{[\beta]^{-4} \mu_s}{\mu_o}\right)^{-1/4} - \left([\beta]^{-4}\right)^{-1/4} \tag{C.45}$$

Hence,

$$G3 = \frac{\mu_o}{\mu_s} \tag{C.46}$$

Substitute for μ_o and u_x^{2*} in dimensionless groups 9, 10 and 11 and simplifying.

$$\sin(\alpha)\left\{\frac{1}{\left[\left(\frac{u_x^{2*}\mu_o}{k_x\rho_o g}\right)^{-1/4}+\left(\frac{u_x^{2*}[\beta]^{-4}\mu_s}{k_x\rho_o g}\right)^{-1/4}-\left(\frac{u_x^{2*}[\beta]^{-4}\mu_0}{k_x\rho_o g}\right)^{-1/4}\right]^{-4}}\right\}=$$

$$\sin(\alpha)\left\{\frac{1}{\left[\left(\frac{P^{2*}}{\rho_o g x^{2*}}\right)^{-1/4}+\left([\beta]^{-4}\frac{P^{2*}}{\rho_o g x^{2*}}\frac{\mu_s}{\mu_o}\right)^{-1/4}-\left([\beta]^{-4}\frac{P^{2*}}{\rho_o g x^{2*}}\right)^{-1/4}\right]^{-4}}\right\} \tag{C.47}$$

Therefore,

$$G4=\alpha \tag{C.48}$$

$$G5=\frac{\rho_o g x^{2*}}{P^{2*}}=\frac{\rho_o g L}{\Delta P} \tag{C.49}$$

Substitute for μ_o and u_x^{2*} in dimensionless groups 12, 13 and 14.

$$\sin(\alpha)\left\{\frac{1}{\left[\left(\frac{u_x^{2*}\mu_o}{k_x\beta\Delta\rho g}\right)^{-1/4}+\left(\frac{u_x^{2*}[\beta]^{-4}\mu_s}{k_x\beta\Delta\rho g}\right)^{-1/4}-\left(\frac{u_x^{2*}[\beta]^{-4}\mu_0}{k_x\beta\Delta\rho g}\right)^{-1/4}\right]^{-4}}\right\}=$$

$$\sin(\alpha)\left\{\frac{1}{\left[\left(\frac{P^{2*}}{\Delta\rho g x^{2*}}\frac{1}{\beta}\right)^{-1/4}+\left(\frac{P^{2*}}{\Delta\rho g x^{2*}}\frac{\mu_s}{\mu_0}[\beta]^{-5}\right)^{-1/4}-\left(\frac{P^{2*}}{\Delta\rho g x^{2*}}[\beta]^{-5}\right)^{-1/4}\right]^{-4}}\right\} \tag{C.50}$$

Therefore,

$$G6=\frac{\Delta\rho g x^{2*}}{P^{2*}}=\frac{\Delta\rho g L}{\Delta P} \tag{C.51}$$

Similarly, substituting for μ_o (equation (C.43)), u_x^{2*} (equation (C.44)) and u_z^{2*} (equation (C.38)) into dimensionless groups 15 through 23, gives,

$$u_{zD} = -\frac{1}{\left[\left(\left(\frac{z^{2*}}{x^{2*}}\right)^2 \frac{k_x}{k_z}\right)^{-1/4} + \left(\left(\frac{z^{2*}}{x^{2*}}\right)^2 \frac{k_x}{k_z}\frac{\mu_s}{\mu_0}[\beta]^{-4}\right)^{-1/4} - \left(\left(\frac{z^{2*}}{x^{2*}}\right)^2 \frac{k_x}{k_z}[\beta]^{-4}\right)^{-1/4}\right]^{-4}} \frac{\partial P_D}{\partial z_D}$$

$$-\cos(\alpha)\left\{\frac{1}{\left[\left(\frac{z^{2*}}{x^{2*}}\frac{k_x}{k_z}\frac{P^{2*}}{\rho_o g x^{2*}}\right)^{-1/4} + \left(\frac{z^{2*}}{x^{2*}}\frac{k_x}{k_z}\frac{P^{2*}}{\rho_o g x^{2*}}\frac{\mu_s}{\mu_0}[\beta]^{-4}\right)^{-1/4} - \left(\frac{z^{2*}}{x^{2*}}\frac{k_x}{k_z}\frac{P^{2*}}{\rho_o g x^{2*}}[\beta]^{-4}\right)^{-1/4}\right]^{-4}}\right\}$$

$$-\cos(\alpha)\left\{\frac{1}{\left[\left(\frac{z^{2*}}{x^{2*}}\frac{k_x}{k_z}\frac{P^{2*}}{\Delta\rho g x^{2*}}\frac{1}{\beta}\right)^{-1/4} + \left(\frac{z^{2*}}{x^{2*}}\frac{k_x}{k_z}\frac{P^{2*}}{\Delta\rho g x^{2*}}\frac{\mu_s}{\mu_0}[\beta]^{-5}\right)^{-1/4} - \left(\frac{z^{2*}}{x^{2*}}\frac{k_x}{k_z}\frac{P^{2*}}{\Delta\rho g x^{2*}}[\beta]^{-5}\right)^{-1/4}\right]^{-4}}\right\} \tag{C.52}$$

The following dimensionless groups are obtained from equation (C.52),

$$G7 = \left(\frac{x^{2*}}{z^{2*}}\right)^2 \frac{k_z}{k_x} = \frac{k_z}{k_x}\frac{L^2}{H^2} \tag{C.53}$$

$$G8 = \left(\frac{x^{2*}}{z^{2*}}\right)\frac{k_z}{k_x} = \frac{k_z}{k_x}\frac{L}{H} \tag{C.54}$$

Using the scaling factors, the final form of the dimensionless variables is given by;

$$c_i = c_i^{2*} c_{iD} + c_i^{1*} \rightarrow c_{iD} = \frac{c_i - c_i^I}{c_i^J - c_i^I}$$

$$x = x^{2*} x_D + x^{1*} \rightarrow x_D = \frac{x - x_o}{L}$$

$$z = z^{2*} z_D + z^{1*} \rightarrow z_D = \frac{z - z_o}{H}$$

$$P = P^{2^*}P_D + P^{1^*} \rightarrow P_D = \frac{P - P_o}{P_{wf} - P_o}$$

$$t = t^{2^*}t_D + t^{1^*} \rightarrow t_D = \frac{t - t_o}{t^{2^*}} = \frac{(t - t_o)u_x^{2^*}}{\phi x^{2^*}} = \frac{u_{inj}t}{\phi L}$$

$$u_x = u_x^{2^*}u_{xD} + u_x^{1^*} \rightarrow u_{xD} = \frac{u_x}{u_x^{2^*}} = \frac{u_x}{u_{inj}}$$

$$u_z = u_z^{2^*}u_{zD} + u_z^{1^*} \rightarrow u_{zD} = \frac{u_z}{u_z^{2^*}} = \frac{u_z}{u_{inj}}\frac{L}{H}$$

To minimize the number of dimensionless groups we take the logarithm of both sides of the dimensionless groups to convert them to a linear combination of parameters.

$$\begin{vmatrix} \ln G1 \\ \ln G2 \\ \ln G3 \\ \ln G4 \\ \ln G5 \\ \ln G6 \\ \ln G7 \\ \ln G8 \end{vmatrix} = \begin{pmatrix} 1 & 0 & 0 & 0 & 0 & 0 & 1 & -1 & -1 & 0 & 0 & 0 & 0 & 0 & 0 \\ -1 & 2 & 0 & 0 & 0 & 0 & 1 & -1 & 0 & -1 & 0 & 0 & 0 & 0 & 0 \\ 0 & 0 & 0 & 0 & -1 & 1 & 0 & 0 & 0 & 0 & 0 & 0 & 0 & 0 & 0 \\ 0 & 0 & 0 & 0 & 0 & 0 & 0 & 0 & 0 & 0 & 1 & 0 & 0 & 0 & 0 \\ 1 & 0 & 0 & 0 & 0 & 0 & 0 & 0 & 0 & 0 & 0 & 1 & 0 & 1 & -1 \\ 1 & 0 & 0 & 0 & 0 & 0 & 0 & 0 & 0 & 0 & 0 & 0 & 1 & 1 & -1 \\ 2 & -2 & -1 & 1 & 0 & 0 & 0 & 0 & 0 & 0 & 0 & 0 & 0 & 0 & 0 \\ 1 & -1 & -1 & 1 & 0 & 0 & 0 & 0 & 0 & 0 & 0 & 0 & 0 & 0 & 0 \end{pmatrix} \begin{vmatrix} \ln L \\ \ln H \\ \ln k_x \\ \ln k_z \\ \ln \mu_s \\ \ln \mu_o \\ \ln u_{inj} \\ \ln \phi \\ \ln D_{xx} \\ \ln D_{zz} \\ \ln \alpha \\ \ln \rho_o \\ \ln \Delta\rho \\ \ln g \\ \ln \Delta P \end{vmatrix}$$

The rank of the matrix is evaluated to be eight. Therefore the number of independent scaling groups is eight. The reduced coefficient matrix is obtained from elementary row elimination method is,

$$\begin{vmatrix} \ln G1 \\ \ln G2 \\ \ln G3 \\ \ln G4 \\ \ln G5 \\ \ln G6 \\ \ln G7 \\ \ln G8 \end{vmatrix} = \begin{pmatrix} 1 & 0 & 0 & 0 & 0 & 0 & 1 & -1 & -1 & 0 & 0 & 0 & 0 & 0 & 0 \\ 2 & -2 & 0 & 0 & 0 & 0 & 0 & 0 & -1 & 1 & 0 & 0 & 0 & 0 & 0 \\ 0 & 0 & 0 & 0 & -1 & 1 & 0 & 0 & 0 & 0 & 0 & 0 & 0 & 0 & 0 \\ 0 & 0 & 0 & 0 & 0 & 0 & 0 & 0 & 0 & 0 & 1 & 0 & 0 & 0 & 0 \\ 0 & 0 & 0 & 0 & 0 & 0 & 0 & 0 & 0 & 0 & 0 & -1 & 1 & 0 & 0 \\ 1 & 0 & 0 & 0 & 0 & 0 & 0 & 0 & 0 & 0 & 0 & 0 & 1 & 1 & -1 \\ 2 & -2 & -1 & 1 & 0 & 0 & 0 & 0 & 0 & 0 & 0 & 0 & 0 & 0 & 0 \\ 1 & -1 & 0 & 0 & 0 & 0 & 0 & 0 & 0 & 0 & 0 & 0 & 0 & 0 & 0 \end{pmatrix} \begin{vmatrix} \ln L \\ \ln H \\ \ln k_x \\ \ln k_z \\ \ln \mu_s \\ \ln \mu_o \\ \ln u_{inj} \\ \ln \phi \\ \ln D_{xx} \\ \ln D_{zz} \\ \ln \alpha \\ \ln \rho_o \\ \ln \Delta\rho \\ \ln g \\ \ln \Delta P \end{vmatrix}$$

After exponentiation, the eight dimensionless groups are;

$$G1^* = \frac{u_{inj} L}{\phi D_{ixx}} \tag{C.56}$$

$$G2^* = \frac{D_{zz} L^2}{D_{xx} H^2} \tag{C.57}$$

$$G3^* = \frac{\mu_o}{\mu_s} \tag{C.58}$$

$$G4^* = \alpha \tag{C.59}$$

$$G5^* = \frac{\Delta\rho}{\rho_o} \tag{C.60}$$

$$G6^* = \frac{\Delta\rho g L}{\Delta P} \tag{C.61a}$$

From equations (C.35) and (C.36), $\Delta P = \frac{u_{inj} \mu_o L}{k_x}$, therefore dimensionless group G6* can also be written as,

$$G6^* = \frac{k_x \Delta\rho g}{u_{inj}\mu_o} \tag{C.61b}$$

$$G7^* = \frac{k_z L^2}{k_x H^2} \tag{C.62}$$

$$G8^* = \frac{L}{H} \quad . \tag{C.63}$$

Based on a traditional definition of dimensionless groups (Garmeh and Johns 2010, Gharbi *et. al.* 1998), these groups are defined as,

Longitudinal Peclet number (N_{pe}) = $\frac{u_{inj} L}{\phi D_{ixx}}$

Dispersion number (N_D) = $\sqrt{G2^*} = \frac{L}{H}\sqrt{\frac{D_{zz}}{D_{xx}}}$

Viscosity ratio (Vo) = $G3^* = \frac{\mu_o}{\mu_s}$

Dip angle group (N_α) = $G4^* = \alpha$

Density number (N_ρ) = $G5^* = \frac{\Delta\rho}{\rho_o}$

Gravity number (N_g) = $G6^* = \frac{k_x \Delta\rho g}{u_{inj}\mu_o}$

Effective aspect ratio (R_L) = $\sqrt{G7^*} = \frac{L}{H}\sqrt{\frac{k_z}{k_x}}$

Aspect ratio (A_r) = $G8^* = \frac{L}{H}$

Not all these scaling groups impact miscible displacement significantly (e.g. density number) over their practical ranges. Sensitivity analysis will be conducted to test their significance. The aspect ratio is not independent as it is clearly embedded in the effective aspect ratio and the dispersion number. Therefore the aspect ratio is not used as an independent scaling factor.

The off-diagonal term of the dispersion tensor was ignored in our analysis because the flow is dominant in the direction of the principal axis. We attempted to

identify the effect of the off-diagonal term on the scaling factors using the formalism of inspectional analysis.

Derivation of Scaling Groups for FCM Displacement including the off-diagonal terms

The single-phase incompressible flow, the component material balances are given by,

$$\frac{\partial}{\partial t}\phi\sum_{i=1}^{n_c} c_i + \nabla\cdot\sum_{i=1}^{n_c} c_i\vec{u} - \nabla\cdot\phi\sum_{i=1}^{n_c}\vec{D}_i\cdot\nabla c_i = 0 \qquad i = 1,...,n_c \qquad \text{(C.64)}$$

For a two-dimensional medium with constant rock properties, negligible adsorption and no reaction, the conservation equation is given by,

$$\frac{\partial}{\partial t}(\phi c_i) + \frac{\partial}{\partial x}(c_i u_x) + \frac{\partial}{\partial z}(c_i u_z) - \phi D_{ixx}\frac{\partial^2 c_i}{\partial x^2} - \phi D_{izz}\frac{\partial^2 c_i}{\partial z^2} - 2\phi D_{ixz}\frac{\partial^2 c_i}{\partial x\partial z} = 0 \qquad i = 1,...,n_c \qquad \text{(C.65)}$$

The scaling factors and dimensionless variable are substituted into the governing equations. Substitution into the accumulation term of the conservation equation gives,

$$\frac{\partial}{\partial t}(\phi c_i) = \phi\frac{\partial\left(c_i^{2^*}c_{iD} + c_i^{1^*}\right)}{\partial\left(t^{2^*}t_D + t^{1^*}\right)} = \left[\frac{\phi c_i^{2^*}}{t^{2^*}}\right]\frac{\partial}{\partial t_D}(c_{iD}) \qquad i = 1,...,n_c, \qquad \text{(C.66)}$$

The flux term in the x-direction gives;

$$\frac{\partial}{\partial x}(c_i u_x) = \left(u_x^{2^*}u_{xD} + u_x^{1^*}\right)\frac{\partial\left(c_i^{2^*}c_{iD} + c_i^{1^*}\right)}{\partial\left(x^{2^*}x_D + x^{1^*}\right)} = \left[\frac{u_x^{2^*}c_i^{2^*}}{x^{2^*}}\right]u_{xD}\frac{\partial c_{iD}}{\partial x_D} + \left[\frac{u_x^{1^*}c_i^{2^*}}{x^{2^*}}\right]\frac{\partial c_{iD}}{\partial x_D} \qquad \text{(C.67)}$$

Because we do not want to change the original form of the equation the term $u_x^{1^*}$ on the right side of equation (C.67) is set to zero. This is permissible since the scaling groups are arbitrary. Therefore the above equation is reduced to;

$$\frac{\partial}{\partial x}(c_i u_x) = \left[\frac{u_x^{2^*}c_i^{2^*}}{x^{2^*}}\right]u_{xD}\frac{\partial c_{iD}}{\partial x_D} \qquad \text{(C.68)}$$

Similarly, the flux term of the conservation equation in z-direction is reduced to;

$$\frac{\partial}{\partial z}\left(c_i u_z\right)=\left[\frac{u_z^{2^*} c_i^{2^*}}{z^{2^*}}\right] u_{zD}\,\frac{\partial c_{iD}}{\partial z_D} \tag{C.69}$$

The dispersion terms in the conservation equation in the x-direction is expanded as;

$$\phi D_{ixx}\,\frac{\partial^2 c_i}{\partial x^2}=\phi D_{ixx}\,\frac{\partial}{\partial x}\left(\frac{\partial c_i}{\partial x}\right)=\phi D_{ixx}\,\frac{\partial}{\partial\left(x^{2^*}x_D+x^{1^*}\right)}\left(\frac{\partial\left(c_i^{2^*}c_{iD}+c_i^{1^*}\right)}{\partial\left(x^{2^*}x_D+x^{1^*}\right)}\right) \tag{C.70}$$

$$\phi D_{ixx}\,\frac{\partial^2 c_i}{\partial x^2}=\left[\frac{\phi D_{ixx} c_i^{2^*}}{\left(x^{2^*}\right)^2}\right]\frac{\partial^2 c_{iD}}{\partial x_D^2} \tag{C.71}$$

Similarly the dispersion term in the z-direction is expressed as;

$$\phi D_{izz}\,\frac{\partial^2 c_i}{\partial z^2}=\left[\frac{\phi D_{izz} c_i^{2^*}}{\left(z^{2^*}\right)^2}\right]\frac{\partial^2 c_{iD}}{\partial z_D^2} \tag{C.72}$$

The off-diagonal dispersion term is expressed as;

$$\phi D_{ixz}\,\frac{\partial^2 c_i}{\partial x\partial z}=\phi D_{ixz}\,\frac{\partial}{\partial z}\left(\frac{\partial c_i}{\partial x}\right)=\phi D_{ixz}\,\frac{\partial}{\partial\left(z^{2^*}z_D+z^{1^*}\right)}\left(\frac{\partial\left(c_i^{2^*}c_{iD}+c_i^{1^*}\right)}{\partial\left(x^{2^*}x_D+x^{1^*}\right)}\right) \tag{C.73}$$

which yields,

$$\phi D_{ixz}\,\frac{\partial^2 c_i}{\partial x\partial z}=\left[\frac{\phi D_{ixz} c_i^{2^*}}{\left(z^{2^*}x^{2^*}\right)}\right]\frac{\partial^2 c_{iD}}{\partial z_D\partial x_D}\qquad . \tag{C.74}$$

Combining the terms in the conservation equations in dimensionless form and simplifying gives,

$$\begin{aligned}&\left[\frac{\phi c_i^{2^*}}{t^{2^*}}\right]\frac{\partial}{\partial t_D}\left(c_{iD}\right)+\left[\frac{u_x^{2^*}c_i^{2^*}}{x^{2^*}}\right]u_{xD}\,\frac{\partial c_{iD}}{\partial x_D}+\left[\frac{u_z^{2^*}c_i^{2^*}}{z^{2^*}}\right]u_{zD}\,\frac{\partial c_{iD}}{\partial z_D}-\left[\frac{\phi D_{ixx}c_i^{2^*}}{\left(x^{2^*}\right)^2}\right]\frac{\partial^2 c_{iD}}{\partial x_D^2}\\&-\left[\frac{\phi D_{izz}c_i^{2^*}}{\left(z^{2^*}\right)^2}\right]\frac{\partial^2 c_{iD}}{\partial z_D^2}-\left[\frac{2\phi D_{ixz}c_i^{2^*}}{\left(z^{2^*}x^{2^*}\right)}\right]\frac{\partial^2 c_{iD}}{\partial z_D\partial x_D}=0\end{aligned} \tag{C.75}$$

which yields,

$$\frac{\partial}{\partial t_D}\left(c_{iD}\right)+\underbrace{\left[\frac{t^{2^*}u_x^{2^*}}{\phi x^{2^*}}\right]}_{1}u_{xD}\frac{\partial c_{iD}}{\partial x_D}+\underbrace{\left[\frac{t^{2^*}u_z^{2^*}}{\phi z^{2^*}}\right]}_{2}u_{zD}\frac{\partial c_{iD}}{\partial z_D}-\underbrace{\left[\frac{t^{2^*}D_{ixx}}{\left(x^{2^*}\right)^2}\right]}_{3}\frac{\partial^2 c_{iD}}{\partial x_D^2}-\underbrace{\left[\frac{t^{2^*}D_{izz}}{\left(z^{2^*}\right)^2}\right]}_{4}\frac{\partial^2 c_{iD}}{\partial z_D^2}$$
$$-\underbrace{\left[\frac{t^{2^*}D_{ixz}}{\left(z^{2^*}x^{2^*}\right)}\right]}_{5}\frac{\partial^2 c_{iD}}{\partial z_D\partial x_D}=0 \qquad \text{(C.76)}$$

The off-diagonal term introduces a new scaling group $\left[\frac{t^{2^*}D_{ixz}}{\left(z^{2^*}x^{2^*}\right)}\right]$. Using earlier definition of the scaling parameters, this scaling group can be expressed as,

$$G9^* = \frac{\phi D_{xz}}{u_{inj}H} \quad . \qquad \text{(C.77)}$$

The dimensionless scaling groups (including the new group from the off-diagonal term) are minimized by taking the logarithm of both sides in-order to find the linearly independent scaling groups. A new scaling group emerged. The new scaling group, "diagonal dispersion number" is given by,

$$G9 = \frac{LD_{zz}}{HD_{xz}} \quad . \qquad \text{(C.78)}$$

Another form of the dispersion number that could be obtained from the minimization process is,

$$G9 = \frac{HD_{xx}}{LD_{xz}} \quad . \qquad \text{(C.79)}$$

The diagonal dispersion number relates the ratio of the time scale a particle will be transported by directional dispersion to the time it will be transported in the diagonal direction by diagonal dispersion. However, the diagonal dispersion is not independent of other factors. As the Peclet number and dispersion number changes, diagonal dispersion number changes. Therefore it is not carried forward in our analysis.

Appendix D: Effect of Non-Uniform Grids on Numerical Dispersion

The premise for this derivation is that in order to compute the change in concentration or saturation for a single phase fluid, pressure or potential is first estimated using the diffusivity equation. The computed pressure or potential is then used to calculate the Darcy velocity using Darcy's law. The velocity is then used in the convection equation to solve for the change in concentration with time.

For a single-phase fluid with no source/sink term, the continuity equation is expressed as;

$$\frac{\partial}{\partial t}(\rho\phi) + \nabla.(\rho\vec{u}) = 0 \qquad \text{(D.1)}$$

Fluid density is ρ, ϕ is the porosity and $\vec{u}$ is the Darcy velocity vector. The single phase Darcy's law is expressed as;

$$\vec{u} = -\frac{k}{\mu}\left(\vec{\nabla}p - \rho g \Delta D\right) = -\frac{k}{\mu}\vec{\nabla}\Phi \qquad \text{(D.2)}$$

Substituting equation (D.2) into (D.1) gives the diffusivity equation, which is given as,

$$\frac{\partial}{\partial t}(\rho\phi) = \nabla.\left(\rho\frac{k}{\mu}\Delta\Phi\right) \quad . \qquad \text{(D.3)}$$

The diffusivity equation introduces a second-order differential in potential (Φ) which introduces different discretization errors when considering uniform and unequally spaced grid-block sizes.

Consider a one-dimensional, incompressible fluid with constant fluid and rock properties, the diffusivity equation can be expressed with an operator π as;

$$\pi = \frac{d}{dx}\left(k\frac{d\Phi}{dx}\right) = 0 \qquad \text{(D.4)}$$

The finite difference approximation for equation (D.4) to consist of a difference operator L(Φ) and a local discretization error e(Φ).

$$\pi(\Phi) = L(\Phi) + e(\Phi) \quad . \tag{D.5}$$

Various finite difference schemes have been proposed to approximate second order operators. Consider a second-order operator expressed as $\frac{d}{dx}\left(k\frac{dU}{dx}\right)$, Settari and Aziz (1972) gave three of these schemes, which are expressed below;

Scheme 1;

$$L_1(U) = \frac{1}{\Delta x_i}\left[k_{i+1/2}\left(\frac{u_{i+1}-u_i}{\Delta x_{i+1/2}}\right) + k_{1-1/2}\left(\frac{u_{i-1}-u_i}{\Delta x_{i-1/2}}\right)\right] \tag{D.6}$$

where;

$$k_{i\pm 1/2} = \tfrac{1}{2}\left(k_i + k_{i\pm 1}\right) \quad . \tag{D.7}$$

Scheme 2;

$$L_2(U) = \frac{2}{\Delta x_+ + \Delta x_-}\left[k_{i+1/2}\left(\frac{u_{i+1}-u_i}{\Delta x_+}\right) + k_{1-1/2}\left(\frac{u_{i-1}-u_i}{\Delta x_-}\right)\right] \tag{D.8}$$

$$\Delta x_+ = x_{i+1} - x_i \tag{D.9}$$

$$\Delta x_- = x_i - x_{i-1} \quad . \tag{D.10}$$

Scheme 3;

Scheme 3 is based on the approximation of the expanded form of the second-order operator.

$$\frac{d}{dx}\left(k\frac{dU}{dx}\right) = k\frac{d^2U}{dx^2} + \frac{dK}{dx}\frac{dU}{dx} \quad . \tag{D.11}$$

The difference operator for Scheme 3 is given as;

$$L_3(U) = \frac{2k_i}{\Delta x_+ + \Delta x_-}\left[\left(\frac{u_{i+1}-u_i}{\Delta x_+}\right) + \left(\frac{u_{i-1}-u_i}{\Delta x_-}\right)\right] + \frac{k_{i+1}-k_{i-1}}{\Delta x_+ + \Delta x_-}\cdot\frac{u_{i+1}-u_{i-1}}{\Delta x_+ + \Delta x_-} \quad . \tag{D.12}$$

For the purpose of illustrating the effect of unequally spaced grid-block sizes on local truncation error, we will use Scheme 3.

$$L_3(\Phi) = \frac{2k_i}{\Delta x_+ + \Delta x_-}\left[\left(\frac{\Phi_{i+1}-\Phi_i}{\Delta x_+}\right) + \left(\frac{\Phi_{i-1}-\Phi_i}{\Delta x_-}\right)\right] + \frac{k_{i+1}-k_{i-1}}{\Delta x_+ + \Delta x_-}\cdot\frac{\Phi_{i+1}-\Phi_{i-1}}{\Delta x_+ + \Delta x_-} \tag{D.13}$$

Uniform Grid Spacing

For uniform grid spacing $\Delta x_+ = \Delta x_-$, therefore the difference operator in equation (D.13) can be simplified to;

$$L(\Phi) = k_i\left(\frac{\Phi_{i+1} - 2\Phi_i + \Phi_{i-1}}{\Delta x^2}\right) + \frac{k_{i+1} - k_{i-1}}{2\Delta x^2}.\frac{\Phi_{i+1} - \Phi_{i-1}}{2\Delta x^2} \quad . \tag{D.14}$$

Expansion of the terms in equation (D.14) using Taylor's series expansion;

$$\Phi_{i+1} = \Phi_i + \Delta x\frac{\partial \Phi}{\partial x} + \frac{\Delta x^2}{2}\frac{\partial^2 \Phi}{\partial x^2} + \frac{\Delta x^3}{3!}\frac{\partial^3 \Phi}{\partial x^3} + \frac{\Delta x^4}{4!}\frac{\partial^4 \Phi}{\partial x^4} \pm HOT \tag{D.15}$$

$$\Phi_{i-1} = \Phi_i - \Delta x\frac{\partial \Phi}{\partial x} + \frac{\Delta x^2}{2}\frac{\partial^2 \Phi}{\partial x^2} - \frac{\Delta x^3}{3!}\frac{\partial^3 \Phi}{\partial x^3} + \frac{\Delta x^4}{4!}\frac{\partial^4 \Phi}{\partial x^4} \pm HOT \tag{D.16}$$

Addition of equations (D.15) and (D.16), neglecting HOT and simplifying;

$$\left(\frac{\Phi_{i+1} - 2\Phi_i + \Phi_{i-1}}{\Delta x^2}\right) = \frac{\partial^2 \Phi}{\partial x^2} + \frac{\Delta x^2}{12}\frac{\partial^4 \Phi}{\partial x^4} \tag{D.17}$$

$$k_{i+1} = k_i + \Delta x\frac{\partial k}{\partial x} + \frac{\Delta x^2}{2}\frac{\partial^2 k}{\partial x^2} + \frac{\Delta x^3}{3!}\frac{\partial^3 k}{\partial x^3} \pm HOT \tag{D.18}$$

$$k_{i-1} = k_i - \Delta x\frac{\partial k}{\partial x} + \frac{\Delta x^2}{2}\frac{\partial^2 k}{\partial x^2} - \frac{\Delta x^3}{3!}\frac{\partial^3 k}{\partial x^3} \pm HOT \quad . \tag{D.19}$$

Subtraction of equation (D.19) from equation (D.18), neglecting HOT and simplifying;

$$\frac{k_{i+1} - k_{i-1}}{2\Delta x} = \frac{\partial k}{\partial x} + \frac{\Delta x^2}{6}\frac{\partial^3 k}{\partial x^3} \tag{D.20}$$

Similarly, it can be shown that;

$$\frac{\Phi_{i+1} - \Phi_{i-1}}{2\Delta x} = \frac{\partial \Phi}{\partial x} + \frac{\Delta x^2}{6}\frac{\partial^3 \Phi}{\partial x^3} \tag{D.21}$$

Substituting equations (D.17, D.20 and D.21) into equation (D.14)

$$L(\Phi) = k_i\left(\frac{\partial^2 \Phi}{\partial x^2} + \frac{\Delta x^2}{12}\frac{\partial^4 \Phi}{\partial x^4}\right) + \left(\frac{\partial k}{\partial x} + \frac{\Delta x^2}{6}\frac{\partial^3 k}{\partial x^3}\right).\left(\frac{\partial \Phi}{\partial x} + \frac{\Delta x^2}{6}\frac{\partial^3 \Phi}{\partial x^3}\right) \tag{D.22}$$

Simplifying;

$$\begin{aligned}\frac{d}{dx}\left(k\frac{d\Phi}{dx}\right) = k\frac{d^2\Phi}{dx^2} + \frac{dK}{dx}\frac{d\Phi}{dx} + k\frac{\Delta x^2}{12}\frac{\partial^4 \Phi}{\partial x^4} + \frac{\Delta x^2}{6}\frac{\partial^3 \Phi}{\partial x^3}\frac{dK}{dx} \\ + \frac{\Delta x^2}{6}\frac{\partial^3 k}{\partial x^3}\frac{d\Phi}{dx} + \frac{\Delta x^4}{36}\frac{\partial^3 k}{\partial x^3}\frac{\partial^3 \Phi}{\partial x^3}\end{aligned} \tag{D.23a}$$

The local truncation error for second-order operator for uniformly spaced grid-block can be expressed as;

$$e(\Phi) = k\frac{\Delta x^2}{12}\frac{\partial^4\Phi}{\partial x^4} + \frac{\Delta x^2}{6}\left(\frac{\partial^3\Phi}{\partial x^3}\frac{dK}{dx} + \frac{\partial^3 k}{\partial x^3}\frac{d\Phi}{dx}\right) + \frac{\Delta x^4}{36}\frac{\partial^3 k}{\partial x^3}\frac{\partial^3\Phi}{\partial x^3}. \qquad \text{(D.23b)}$$

The scheme is of second order $O(\Delta x^2)$.

Non-Uniform Grid Spacing

For unequally spaced grid-block sizes, the second-order difference operator is given in equation (D.13) as;

$$L(\Phi) = \frac{2k_i}{\Delta x_+ + \Delta x_-}\left[\left(\frac{\Phi_{i+1} - \Phi_i}{\Delta x_+}\right) + \left(\frac{\Phi_{i-1} - \Phi_i}{\Delta x_-}\right)\right] + \frac{k_{i+1} - k_{i-1}}{\Delta x_+ + \Delta x_-}\cdot\frac{\Phi_{i+1} - \Phi_{i-1}}{\Delta x_+ + \Delta x_-} \quad .$$

Using Taylor's series expansion to the terms in equation (D.13)

$$\Phi_{i+1} = \Phi_i + \Delta x_+\frac{\partial\Phi}{\partial x} + \frac{\Delta x_+^2}{2}\frac{\partial^2\Phi}{\partial x^2} + \frac{\Delta x_+^3}{3!}\frac{\partial^3\Phi}{\partial x^3} \pm HOT \qquad \text{(D.24)}$$

$$\frac{\Phi_{i+1} - \Phi_i}{\Delta x_+} = \frac{\partial\Phi}{\partial x} + \frac{\Delta x_+}{2}\frac{\partial^2\Phi}{\partial x^2} + \frac{\Delta x_+^2}{3!}\frac{\partial^3\Phi}{\partial x^3} \pm HOT \qquad \text{(D.25)}$$

$$\Phi_{i-1} = \Phi_i - \Delta x_-\frac{\partial\Phi}{\partial x} + \frac{\Delta x_-^2}{2}\frac{\partial^2\Phi}{\partial x^2} - \frac{\Delta x_-^3}{3!}\frac{\partial^3\Phi}{\partial x^3} \pm HOT \qquad \text{(D.26)}$$

$$\frac{\Phi_{i-1} - \Phi_i}{\Delta x_-} = -\frac{\partial\Phi}{\partial x} + \frac{\Delta x_-}{2}\frac{\partial^2\Phi}{\partial x^2} - \frac{\Delta x_-^2}{3!}\frac{\partial^3\Phi}{\partial x^3} \pm HOT \qquad \text{(D.27)}$$

$$k_{i+1} = k_i + \Delta x_+\frac{\partial k}{\partial x} + \frac{\Delta x_+^2}{2}\frac{\partial^2 k}{\partial x^2} \pm HOT \qquad \text{(D.28)}$$

$$k_{i-1} = k_i - \Delta x_-\frac{\partial k}{\partial x} + \frac{\Delta x_-^2}{2}\frac{\partial^2 k}{\partial x^2} \pm HOT \quad . \qquad \text{(D.29)}$$

Subtraction of equation (D.29) from equation (D.28), neglecting HOT and simplifying;

$$\frac{k_{i+1} - k_{i-1}}{\Delta x_+ + \Delta x_-} = \frac{\partial k}{\partial x} + \frac{(\Delta x_+ - \Delta x_-)}{2}\frac{\partial^2 k}{\partial x^2} \quad . \qquad \text{(D.30)}$$

Similarly, it can be shown that;

$$\frac{\Phi_{i+1} - \Phi_{i-1}}{\Delta x_+ + \Delta x_-} = \frac{\partial\Phi}{\partial x} + \frac{(\Delta x_+ - \Delta x_-)}{2}\frac{\partial^2\Phi}{\partial x^2} \qquad \text{(D.31)}$$

Substitution of equations (D.25, D.27, D.30 and D.31) into equation (D.13), we obtain;

$$L(\Phi)=\frac{2k_i}{\Delta x_+ + \Delta x_-}\left[\frac{\partial\Phi}{\partial x}+\frac{\Delta x_+}{2}\frac{\partial^2\Phi}{\partial x^2}+\frac{\Delta x_+^2}{3!}\frac{\partial^3\Phi}{\partial x^3}-\frac{\partial\Phi}{\partial x}+\frac{\Delta x_-}{2}\frac{\partial^2\Phi}{\partial x^2}-\frac{\Delta x_-^2}{3!}\frac{\partial^3\Phi}{\partial x^3}\right] + \left(\frac{\partial k}{\partial x}+\frac{\left(\Delta x_+ - \Delta x_-\right)}{2}\frac{\partial^2 k}{\partial x^2}\right).\left(\frac{\partial\Phi}{\partial x}+\frac{\left(\Delta x_+ - \Delta x_-\right)}{2}\frac{\partial^2\Phi}{\partial x^2}\right) \tag{D.32}$$

Simplifying

$$L(\Phi)=k_i\frac{\partial^2\Phi}{\partial x^2}+\frac{dK}{dx}\frac{d\Phi}{dx}+\frac{k_i\left(\Delta x_+ - \Delta x_-\right)}{3}\frac{\partial^3\Phi}{\partial x^3} + \frac{\left(\Delta x_+ - \Delta x_-\right)}{2}\left(\frac{\partial^2 k}{\partial x^2}\frac{d\Phi}{dx}+\frac{\partial^2\Phi}{\partial x^2}\frac{dK}{dx}\right)+\frac{\left(\Delta x_+ - \Delta x_-\right)^2}{4}\frac{\partial^2 k}{\partial x^2}\frac{\partial^2\Phi}{\partial x^2}. \tag{D.33}$$

The local truncation error for a second-order operator for unequally spaced grid-block sizes can be expressed as;

$$e(\Phi)=\frac{k_i\left(\Delta x_+ - \Delta x_-\right)}{3}\frac{\partial^3\Phi}{\partial x^3}+\frac{\left(\Delta x_+ - \Delta x_-\right)}{2}\left(\frac{\partial^2 k}{\partial x^2}\frac{d\Phi}{dx}+\frac{\partial^2\Phi}{\partial x^2}\frac{dk}{dx}\right) + \frac{\left(\Delta x_+ - \Delta x_-\right)^2}{4}\frac{\partial^2 k}{\partial x^2}\frac{\partial^2\Phi}{\partial x^2} \tag{D.34}$$

The order of the local truncation error has reduced from second order to first order. This reduction in order will affect the accuracy of the computed potential (or pressure) that will be used to calculate the velocity using the Darcy equation. This is likely the cause of the difference between the numerical dispersion for uniform and unequally spaced grid-block sizes.

Fanchi (1983) derived the expressions for numerical dispersion (Appendix E). Numerical dispersion depends only on the grid-block size and not the relationship between adjacent grid-blocks. We conducted numerical experiments to validate that the numerical dispersion from sets of uniform grid-block sizes behave similarly to physical dispersion.

Numerical Experiments

A series of 1-D FCM simulations were conducted using CMG-GEM® in a homogenous medium. The viscosity and density of the solute and solvent were similar. The simulation has a constant injection and production rate of 0.25 bbl/day. The simulation time step is 0.1 ft/day.

Case 1: The simulation model has 110 grid blocks (NX = 110). The size of the first 100 grid-blocks is 1.0 ft while the size of the remaining 10 grid-blocks is 10 ft. Therefore the total length of the simulation model is 200 ft.

Case 2: The simulation model has 110 grid-blocks. The grid blocks are arranged with alternating sets of 50 grid-blocks with 1.0 ft grid-size and 5 grid-blocks with 10 ft grid-block size. The total length of the model is 200 ft.

Case 3: The simulation model has 200 grid-blocks with size 1.0 ft. This is the control simulation to which the results will be compared. The total length of the simulation model is 200 ft.

Figure D.1 shows the solute concentration map for the different cases at 35 days. The solute concentration maps for the different cases, though they have the same permeability (100 mD) and injection rates, show different levels of spreading. This is due to different level of numerical dispersion for different grid-block sizes.

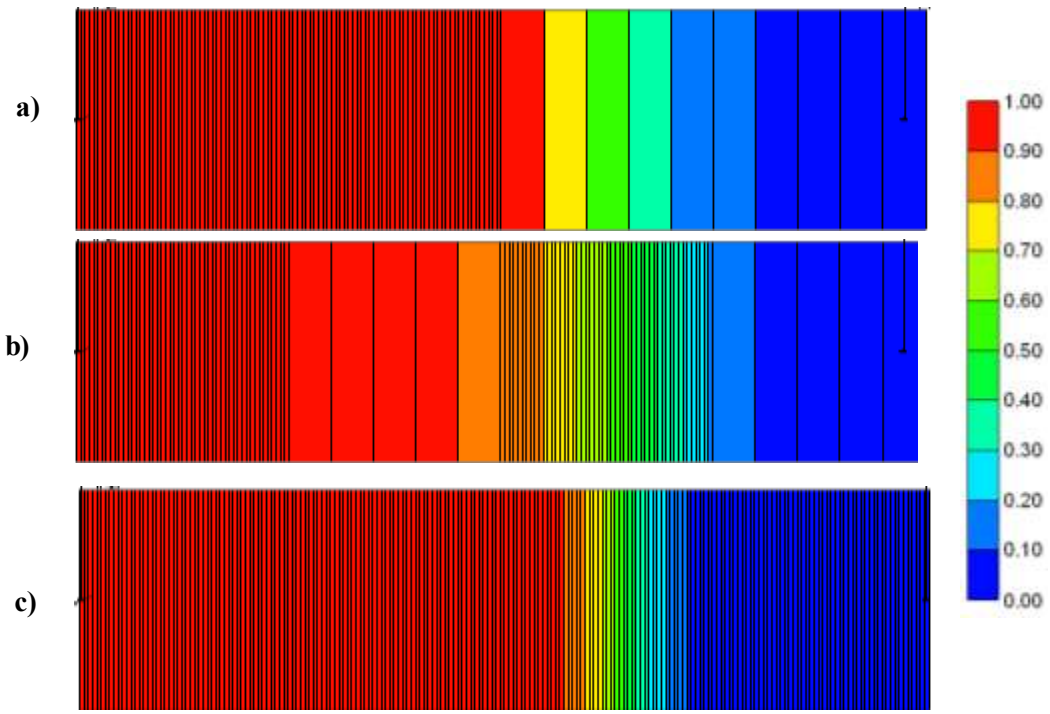

Figure D.1: 1-D Solute concentration map at 35 days for the three simulation models (a) case 1: 100 grids with 1.0 ft grid-block size and 10 grids with 10 ft grid-block size (b) case 2: alternating sets of 50 grids with 1.0 ft grid-block size and 10 grids with 10 ft grid-block size and (c) case 3: 200 grids with uniform grid block size of 1.0 ft.

We compared the velocities from the three models. We expect that the use of variable grid-block sizes should degrade the accuracy of the velocities; hence the models should have different velocity profiles. Figure D.2 confirms that the three cases, though with the same injection and production rates have different velocity profiles.

The velocity all converges at the lateral ends of the model because of the imposed constant rates. The difference in the velocity (from case 3) is attributed to the reduction in accuracy of the discretization due to using non-uniform grid blocks. Different regimes of velocities are noticed with different slopes based on the grid-block sizes in the set.

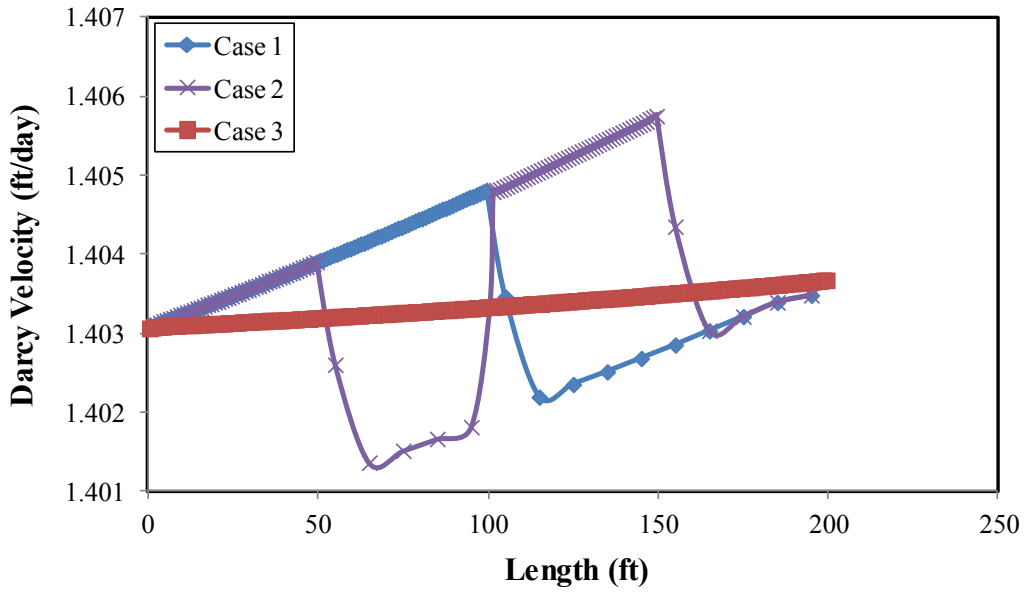

Figure D.2: Velocity profiles at 10 days for simulation models with different sets of grid-block sizes.

The next step is to show that the local (grid-block) concentration profiles is similar to physical dispersion. The first step is to compare the mixing zone growth with the square root of dimensionless time.

$$\Delta x_D = 3.625\sqrt{\frac{t_D}{N_{pe}}} \tag{2.14}$$

where Δx_D is the dimensionless mixing zone, t_D is the dimensionless time and N_{pe} is the Peclet number. The dimensionless mixing zone is expected to scale linearly with the square root of time, with slope showing the level of dispersion.

Figure D.3 shows that for the different simulation cases the mixing zone scales with square root of time. For case 1, two different slopes were observed indicating two regimes of mixing in the model. This confirms that the numerical dispersion from the two sets of grid-block sizes is similar to physical dispersion. For case 2, different sets of

slopes can be observed, showing the different levels of dispersion. There are more oscillations in case 4, showing the effect of the alternating set of grid-blocks.

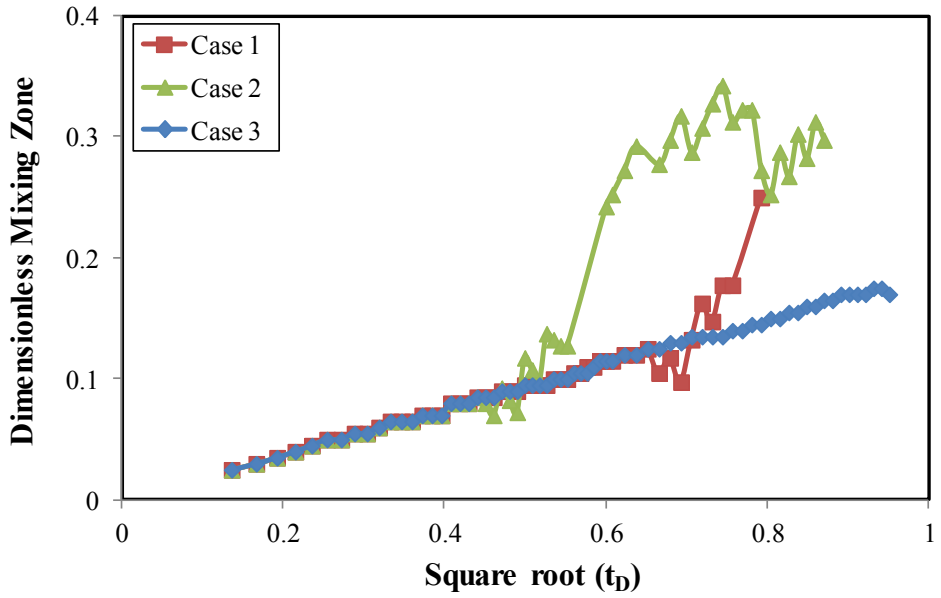

Figure D.3: Dimensionless mixing zone versus square root of dimensionless time for different simulation cases.

The local (grid-block) solute concentration was fitted to the solution of the 1-D CDE. Excellent matches were obtained, even for case 2 that has alternating sets of grid-block sizes. Figure D.4 shows some local concentration profile matches of the 1D CDE analytical solutions and the simulation profiles.

a)

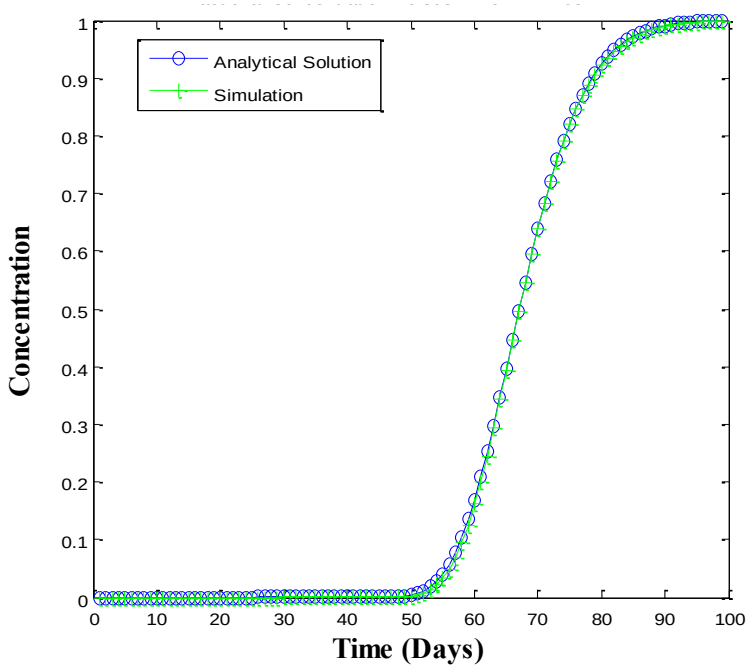

b)

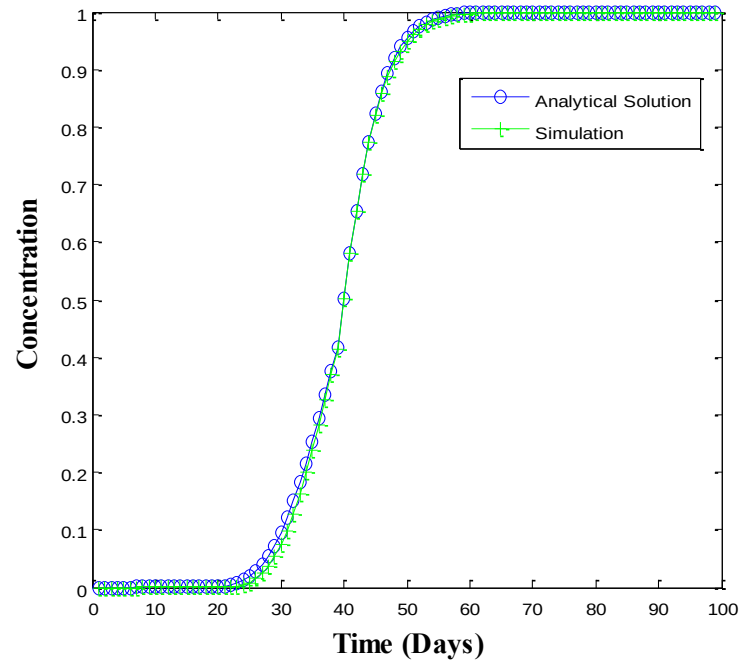

Figure D.4: A plot of dimensionless concentration (y-axis) and time (x-axis) showing a good fit between the 1-D CDE solution and the local concentration histories at different points within the alternating grid-block sizes used in case 2 (a) NX = 103 and (b) NX = 53.

Next we compared the estimated longitudinal dispersivities for the three cases (Figure D.5). The estimated dispersivities for case 1 (100*1 and 10*10) shows that there could be different regimes of dispersion for sets of grid-blocks of different sizes. The first regime has a numerical dispersion of about 0.5 ft (based on the 1.0 ft grid-block) while the second regime shows the dispersion rising from 0.5 ft towards a new asymptotic value (Figure D.5).

Results from case 2 (alternating 50*1 and 5*1) show that the dispersion regime follows the trend in the sizes of the grid-blocks. The dispersivities rises from 0.5 ft towards a new asymptotic value, but due to the next set of 1.0 ft grid blocks it falls towards the new dispersivity of 0.5 ft, but before getting to 0.5 ft it rises again due to next set of 10 ft grid blocks.

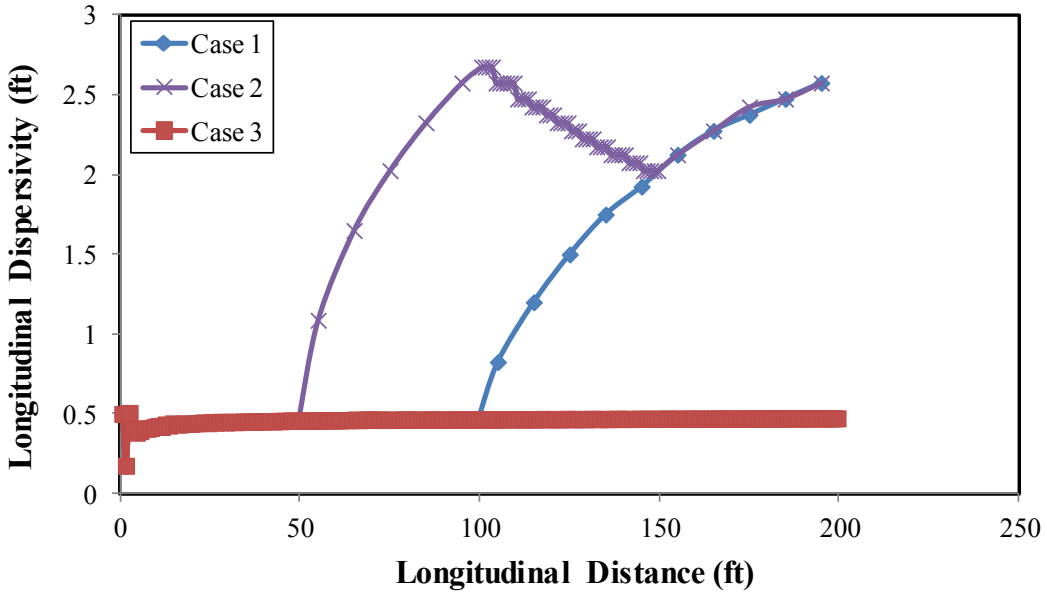

Figure D.5: Estimated longitudinal dispersivity for models with different sets of grid-block sizes.

This is similar to the behavior noticed when we estimated the total dispersivity for the models that have different sets of permeability distribution. The dispersivity of the combined model (256X32) did not jump instantaneously from the asymptotic longitudinal dispersivity of the first set of permeability distribution (1.10 ft) to the dispersivity of the next set of permeability distribution (5.39 ft) but rises towards the new asymptotic value (Figure D.6).

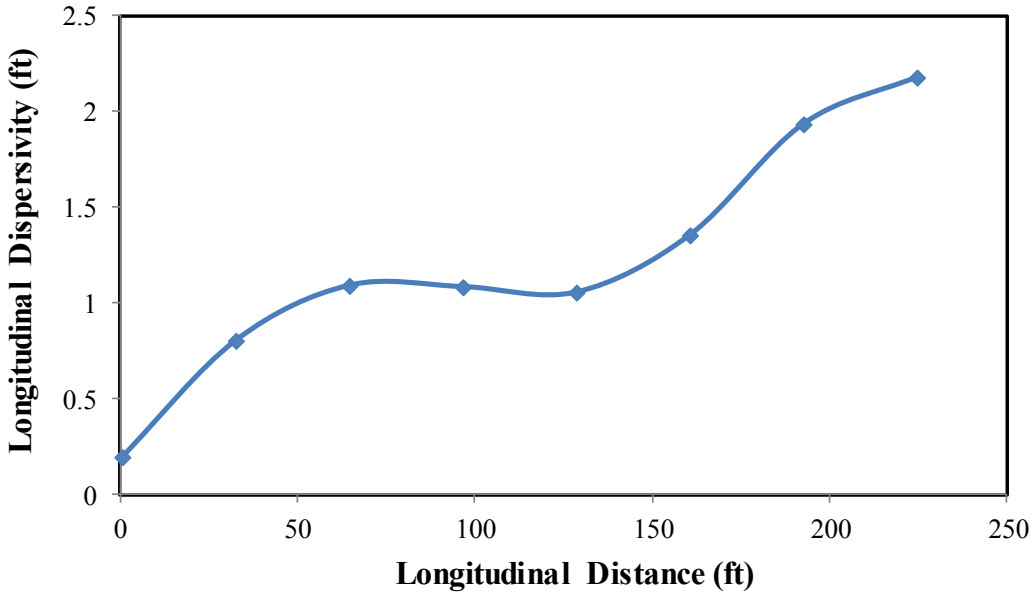

Figure D.6: Estimated longitudinal dispersivity from 2-D simulation model with sets of different permeability distributions. The first set has 128 X 32 grid-blocks that is uncorrelated and the second region has 128 X 32 grid blocks that is 25% correlated in the x-direction and 10% correlation in y-direction.

Finally another case is run to see if the dispersivity will rise to an asymptotic value similar to the expected numerical dispersion for the second set of grid blocks. The simulation model in this case (case 4) has a total of 150 grid-blocks. The first 50 grid-blocks have a grid-block size of 1.0 ft, while the next 100 grid-blocks have a grid-block

size of 10 ft. A 1-D FCM simulation was conducted as discussed above. The estimated longitudinal dispersivity shows that the second regime of dispersivity rises to approach the numerical dispersion of the second set of uniform grid-block sizes (Figure D.7).

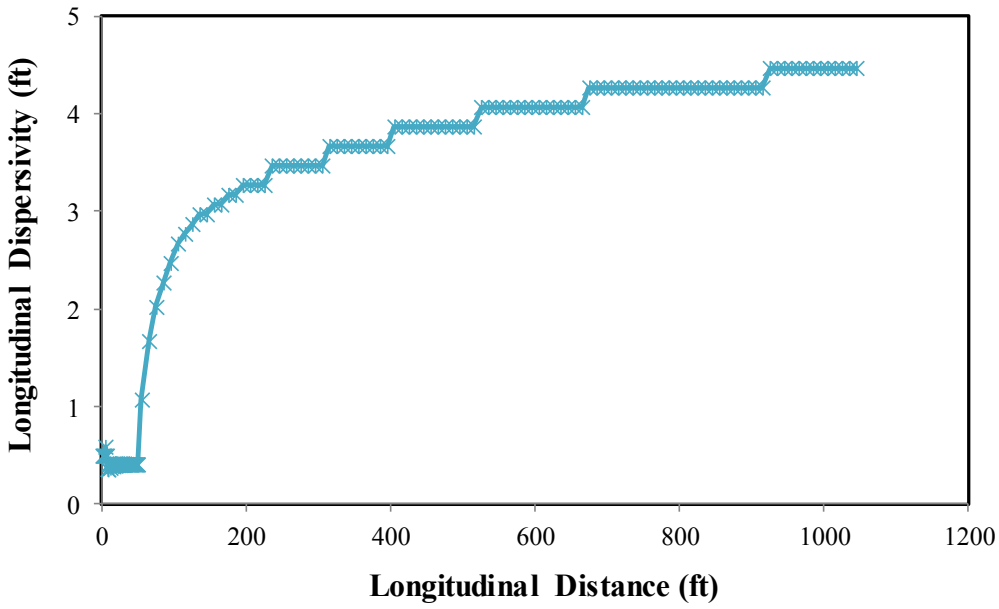

Figure D.7: Estimated longitudinal dispersivity for case 4 showing that the second regime of dispersivity is close to the numerical dispersivity for a grid block size of 10 ft

CONCLUSIONS

1. The form and behavior of numerical dispersion is similar with uniform and variable grid-block sizes.
2. The difference between the numerical dispersion for uniform and variable grid-block sizes is the reduction in the accuracy of the pressure equation and hence the velocity.
3. Sets of uniform grid-blocks sizes will have regimes of dispersion that vary from the numerical dispersion of the first set of uniform grid-block sizes and

rises/reduces gradually to the dispersion of the second set of grid-block sizes. This is similar to the behavior of estimated physical dispersion for different sets of permeability distributions.

4. Though numerical dispersion may have different regimes based on sets of grid block sizes, caution must be exercised for random combination of grid-block sizes as this may result in increased discretization error and may also affect simulation convergence.

Appendix E: Derivation of Numerical Dispersion

This derivation follows the work of Fanchi (1983). Consider the 3-dimensional convection equation;

$$\frac{\partial C}{\partial t}+v_x\frac{\partial C}{\partial x}+v_y\frac{\partial C}{\partial y}+v_z\frac{\partial C}{\partial z}=0. \tag{E.1}$$

The discretization of equation (E.1) can be expressed as;

$$\begin{aligned}&\frac{C_{i,j,k}^{n+1}-C_{i,j,k}^{n}}{\Delta t}+v_x\left[\frac{C_{i+1/2,j,k}-C_{i-1/2,j,k}}{\Delta x}\right]+v_y\left[\frac{C_{i,j+1/2,k}-C_{i,j-1/2,k}}{\Delta y}\right]\\&+v_z\left[\frac{C_{i,j,k+1/2}-C_{i,j,k-1/2}}{\Delta z}\right]=0\end{aligned}. \tag{E.2}$$

Substituting the space and temporal weighting factors (ω and Θ).

$$\frac{C_{i+1/2,j,k}-C_{i-1/2,j,k}}{\Delta x}=\left[\begin{array}{l}\dfrac{(2\omega-1)\left[\theta C_{i,j,k}^{n+1}+(1-\theta)C_{i,j,k}^{n}\right]}{\Delta x}+\dfrac{(1-\omega)\left[\theta C_{i+1,j,k}^{n+1}+(1-\theta)C_{i+1,j,k}^{n}\right]}{\Delta x}\\-\dfrac{\omega\left[\theta C_{i-1,j,k}^{n+1}+(1-\theta)C_{i-1,j,k}^{n}\right]}{\Delta x}\end{array}\right] \tag{E.3}$$

$$\frac{C_{i,j+1/2,k}-C_{i,j-1/2,k}}{\Delta y}=\left[\begin{array}{l}\dfrac{(2\omega-1)\left[\theta C_{i,j,k}^{n+1}+(1-\theta)C_{i,j,k}^{n}\right]}{\Delta y}+\dfrac{(1-\omega)\left[\theta C_{i,j+1,k}^{n+1}+(1-\theta)C_{i,j+1,k}^{n}\right]}{\Delta y}\\-\dfrac{\omega\left[\theta C_{i,j-1,k}^{n+1}+(1-\theta)C_{i,j-1,k}^{n}\right]}{\Delta y}\dfrac{-}{\Delta y}\end{array}\right] \tag{E.4}$$

$$\frac{C_{i,j,k+1/2}-C_{i,j,k-1/2}}{\Delta z}=\left[\begin{array}{l}\dfrac{(2\omega-1)\left[\theta C_{i,j,k}^{n+1}+(1-\theta)C_{i,j,k}^{n}\right]}{\Delta z}+\dfrac{(1-\omega)\left[\theta C_{i,j,k+1}^{n+1}+(1-\theta)C_{i,j,k+1}^{n}\right]}{\Delta z}\\-\dfrac{\omega\left[\theta C_{i,j,k-1}^{n+1}+(1-\theta)C_{i,j,k-1}^{n}\right]}{\Delta z}\end{array}\right] \tag{E.5}$$

For upstream weighting and explicit in time, i.e ω = 1 and Θ = 0, the discretization of the 3-dimension convection equation is given as;

$$\frac{C_{i,j,k}^{n+1}-C_{i,j,k}^{n}}{\Delta t}+v_x\left[\frac{C_{i,j,k}^{n}-C_{i-1,j,k}^{n}}{\Delta x}\right]+v_y\left[\frac{C_{i,j,k}^{n}-C_{i,j-1,k}^{n}}{\Delta y}\right]+v_z\left[\frac{C_{i,j,k}^{n}-C_{i,j,k-1}^{n}}{\Delta z}\right]=0. \qquad \text{(E.6)}$$

Taylor's series expansion is used to analyze the truncation error in equation (E.6).

$$\frac{C_{i,j,k}^{n}-C_{i-1,j,k}^{n}}{\Delta x}=\frac{\partial C}{\partial x}-\frac{\Delta x}{2}\frac{\partial^2 C}{\partial x^2}\pm HOT \qquad \text{(E.7)}$$

$$\frac{C_{i,j,k}^{n}-C_{i,j-1,k}^{n}}{\Delta y}=\frac{\partial C}{\partial y}-\frac{\Delta y}{2}\frac{\partial^2 C}{\partial y^2}\pm HOT \qquad \text{(E.8)}$$

$$\frac{C_{i,j,k}^{n}-C_{i,j,k-1}^{n}}{\Delta z}=\frac{\partial C}{\partial z}-\frac{\Delta z}{2}\frac{\partial^2 C}{\partial z^2}\pm HOT \qquad \text{(E.9)}$$

$$\frac{C_{i,j,k}^{n+1}-C_{i,j,k}^{n}}{\Delta t}=\frac{\partial C}{\partial t}+\frac{\Delta t}{2}\frac{\partial^2 C}{\partial t^2}\pm HOT \qquad \text{(E.10)}$$

Substituting equations (E.7 to E.10) into equation (E.6), and neglecting HOT we get;

$$\frac{\partial C}{\partial t}+\frac{\Delta t}{2}\frac{\partial^2 C}{\partial t^2}+v_x\left(\frac{\partial C}{\partial x}-\frac{\Delta x}{2}\frac{\partial^2 C}{\partial x^2}\right)+v_y\left(\frac{\partial C}{\partial y}-\frac{\Delta y}{2}\frac{\partial^2 C}{\partial y^2}\right)+v_z\left(\frac{\partial C}{\partial z}-\frac{\Delta z}{2}\frac{\partial^2 C}{\partial z^2}\right)=0. \qquad \text{(E.11)}$$

The second order term, $\frac{\partial^2 C}{\partial t^2}$, can be expressed as a derivative of concentration with respect to the spatial variables.

$$\frac{\partial^2 C}{\partial t^2}=\frac{\partial}{\partial t}\left(\frac{\partial C}{\partial t}\right)=-\frac{\partial}{\partial t}\left(v_x\frac{\partial C}{\partial x}+v_y\frac{\partial C}{\partial y}+v_z\frac{\partial C}{\partial z}\right) \qquad \text{(E.12)}$$

$$\begin{aligned}\frac{\partial^2 C}{\partial t^2}&=-\left(v_x\frac{\partial}{\partial t}\left(\frac{\partial C}{\partial x}\right)+v_y\frac{\partial}{\partial t}\left(\frac{\partial C}{\partial x}\right)+v_z\frac{\partial}{\partial t}\left(\frac{\partial C}{\partial z}\right)\right)\\&=-\left(v_x\frac{\partial}{\partial x}\left(\frac{\partial C}{\partial t}\right)+v_y\frac{\partial}{\partial y}\left(\frac{\partial C}{\partial t}\right)+v_y\frac{\partial}{\partial z}\left(\frac{\partial C}{\partial t}\right)\right)\end{aligned} \qquad \text{(E.11)}$$

$$\frac{\partial^2 C}{\partial t^2}=\left(\begin{array}{c}v_x\frac{\partial}{\partial x}\left(v_x\frac{\partial C}{\partial x}+v_y\frac{\partial C}{\partial y}+v_z\frac{\partial C}{\partial z}\right)+v_y\frac{\partial}{\partial y}\left(v_x\frac{\partial C}{\partial x}+v_y\frac{\partial C}{\partial y}+v_z\frac{\partial C}{\partial z}\right)\\+v_z\frac{\partial}{\partial z}\left(v_x\frac{\partial C}{\partial x}+v_y\frac{\partial C}{\partial y}+v_z\frac{\partial C}{\partial z}\right)\end{array}\right) \qquad \text{(E.12)}$$

$$\frac{\partial^2 C}{\partial t^2}=v_x^2\frac{\partial^2 C}{\partial x^2}+2v_xv_y\frac{\partial^2 C}{\partial x\partial y}+2v_xv_z\frac{\partial^2 C}{\partial x\partial z}+2v_yv_z\frac{\partial^2 C}{\partial y\partial z}+v_y^2\frac{\partial^2 C}{\partial y^2}+v_z^2\frac{\partial^2 C}{\partial z^2}. \qquad \text{(E.13)}$$

Substituting equation (E.13) into equation (E.11) and simplifying;

$$\frac{\partial C}{\partial t}+v_x\frac{\partial C}{\partial x}+v_y\frac{\partial C}{\partial x}+v_z\frac{\partial C}{\partial z}=\left(\frac{v_x\Delta x}{2}-\frac{v_x^2\Delta t}{2}\right)\frac{\partial^2 C}{\partial x^2}+\left(\frac{v_y\Delta y}{2}-\frac{v_y^2\Delta t}{2}\right)\frac{\partial^2 C}{\partial y^2}$$
$$+\left(\frac{v_z\Delta z}{2}-\frac{v_z^2\Delta t}{2}\right)\frac{\partial^2 C}{\partial z^2}-v_xv_y\Delta t\frac{\partial^2 C}{\partial x\partial y}-v_xv_z\Delta t\frac{\partial^2 C}{\partial x\partial z}--v_yv_z\Delta t\frac{\partial^2 C}{\partial y\partial z} \quad . \tag{E.14}$$

Compare equation (E.14) to the three-dimensional convection-dispersion equation, given as;

$$\frac{\partial C}{\partial t}+v_x\frac{\partial C}{\partial x}+v_y\frac{\partial C}{\partial y}+v_z\frac{\partial C}{\partial z}=D_{11}\frac{\partial^2 C}{\partial x^2}+D_{22}\frac{\partial^2 C}{\partial y^2}+D_{33}\frac{\partial^2 C}{\partial z^2}$$
$$+2D_{12}\frac{\partial^2 C}{\partial x\partial y}+2D_{13}\frac{\partial^2 C}{\partial x\partial z}+2D_{23}\frac{\partial^2 C}{\partial y\partial z} \quad . \tag{E.15}$$

The symmetric numerical dispersion tensor in three-dimension using upstream weighting, explicit in time and backward difference can be expressed as;

$$D_{11}=\left(\frac{v_x\Delta x}{2}-\frac{v_x^2\Delta t}{2}\right) \tag{E.16}$$

$$D_{22}=\left(\frac{v_y\Delta y}{2}-\frac{v_y^2\Delta t}{2}\right) \tag{E.17}$$

$$D_{33}=\left(\frac{v_z\Delta z}{2}-\frac{v_z^2\Delta t}{2}\right) \tag{E.18}$$

$$D_{12}=-\frac{1}{2}v_xv_y\Delta t \tag{E.19}$$

$$D_{13}=-\frac{1}{2}v_xv_z\Delta t \tag{E.20}$$

$$D_{23}=-\frac{1}{2}v_yv_z\Delta t \tag{E.21}$$

The 3-D form of the convection dispersion is;

$$\frac{\partial C}{\partial t}=\sum_{i=1}^{3}\left(\sum_{j=1}^{3}D_{ij}\frac{\partial^2 C}{\partial x_i\partial x_j}-v_i\frac{\partial C}{\partial x_i}\right). \tag{E.22}$$

The complete expression for numerical dispersion as derived by Fanchi (1983) is shown in Table E.1.

Difference Technique		Numerical Dispersion Tensor
Space	Time	Ijth Element
Backward-difference	Explicit	$\frac{v_i}{2}\left(\Delta x_i - v_i \Delta t\right)$ $i = j$ $-\frac{1}{2} v_i v_j \Delta t$ $i \neq j$
Centered-difference	Explicit	$-\frac{1}{2} v_i v_j \Delta t$ all i,j
Backward-difference	Implicit	$\frac{v_i}{2}\left(\Delta x_i + v_i \Delta t\right)$ $i = j$ $\frac{1}{2} v_i v_j \Delta t$ $i \neq j$
Centered-difference	Implicit	$\frac{1}{2} v_i v_j \Delta t$ all i, j

Table E.1: Multi-dimensional numerical dispersion, Fanchi (1983).

Appendix F: Experimental Design

The value of each state of the Box-Behnken design used for the experimental design is shown in Table F.1. The center-points are repeated six times to allow for a better estimate of the prediction for the given design. The 62 runs were conducted five times for different permeability realizations. The five realizations were averaged to obtain a representative response for a given permeability distribution and autocorrelation structure.

Runs	L_{XD}	L_{YD}	V_{DP}	N_D	V_o	R_L	N_g
1	-0.842	-0.667	0.000	-1.000	-1.000	-1.000	-0.616
2	-0.842	-0.667	0.000	-1.000	-1.000	1.000	-0.616
3	-0.842	-0.667	0.000	-1.000	1.000	-1.000	-0.616
4	-0.842	-0.667	0.000	-1.000	1.000	1.000	-0.616
5	-0.842	-0.667	0.000	1.000	-1.000	-1.000	-0.616
6	-0.842	-0.667	0.000	1.000	-1.000	1.000	-0.616
7	-0.842	-0.667	0.000	1.000	1.000	-1.000	-0.616
8	-0.842	-0.667	0.000	1.000	1.000	1.000	-0.616
9	-1.000	-0.667	0.000	-0.489	-0.667	-1.000	-1.000
10	-1.000	-0.667	0.000	-0.489	-0.667	-1.000	1.000
11	-1.000	-0.667	0.000	-0.489	-0.667	1.000	-1.000
12	-1.000	-0.667	0.000	-0.489	-0.667	1.000	1.000
13	1.000	-0.667	0.000	-0.489	-0.667	-1.000	-1.000
14	1.000	-0.667	0.000	-0.489	-0.667	-1.000	1.000
15	1.000	-0.667	0.000	-0.489	-0.667	1.000	-1.000
16	1.000	-0.667	0.000	-0.489	-0.667	1.000	1.000
17	-0.842	-1.000	0.000	-0.489	-1.000	0.192	-1.000
18	-0.842	-1.000	0.000	-0.489	-1.000	0.192	1.000
19	-0.842	-1.000	0.000	-0.489	1.000	0.192	-1.000
20	-0.842	-1.000	0.000	-0.489	1.000	0.192	1.000
21	-0.842	1.000	0.000	-0.489	-1.000	0.192	-1.000
22	-0.842	1.000	0.000	-0.489	-1.000	0.192	1.000
23	-0.842	1.000	0.000	-0.489	1.000	0.192	-1.000
24	-0.842	1.000	0.000	-0.489	1.000	0.192	1.000
25	-1.000	-1.000	0.000	-1.000	-0.667	0.192	-0.616

26	-1.000	-1.000	0.000	1.000	-0.667	0.192	-0.616
27	-1.000	1.000	0.000	-1.000	-0.667	0.192	-0.616
28	-1.000	1.000	0.000	1.000	-0.667	0.192	-0.616
29	1.000	-1.000	0.000	-1.000	-0.667	0.192	-0.616
30	1.000	-1.000	0.000	1.000	-0.667	0.192	-0.616
31	1.000	1.000	0.000	-1.000	-0.667	0.192	-0.616
32	1.000	1.000	0.000	1.000	-0.667	0.192	-0.616
33	-0.842	-0.667	-1.000	-1.000	-0.667	0.192	-1.000
34	-0.842	-0.667	-1.000	-1.000	-0.667	0.192	1.000
35	-0.842	-0.667	-1.000	1.000	-0.667	0.192	-1.000
36	-0.842	-0.667	-1.000	1.000	-0.667	0.192	1.000
37	-0.842	-0.667	1.000	-1.000	-0.667	0.192	-1.000
38	-0.842	-0.667	1.000	-1.000	-0.667	0.192	1.000
39	-0.842	-0.667	1.000	1.000	-0.667	0.192	-1.000
40	-0.842	-0.667	1.000	1.000	-0.667	0.192	1.000
41	-1.000	-0.667	-1.000	-0.489	-1.000	0.192	-0.616
42	-1.000	-0.667	-1.000	-0.489	1.000	0.192	-0.616
43	-1.000	-0.667	1.000	-0.489	-1.000	0.192	-0.616
44	-1.000	-0.667	1.000	-0.489	1.000	0.192	-0.616
45	1.000	-0.667	-1.000	-0.489	-1.000	0.192	-0.616
46	1.000	-0.667	-1.000	-0.489	1.000	0.192	-0.616
47	1.000	-0.667	1.000	-0.489	-1.000	0.192	-0.616
48	1.000	-0.667	1.000	-0.489	1.000	0.192	-0.616
49	-0.842	-1.000	-1.000	-0.489	-0.667	-1.000	-0.616
50	-0.842	-1.000	-1.000	-0.489	-0.667	1.000	-0.616
51	-0.842	-1.000	1.000	-0.489	-0.667	-1.000	-0.616
52	-0.842	-1.000	1.000	-0.489	-0.667	1.000	-0.616
53	-0.842	1.000	-1.000	-0.489	-0.667	-1.000	-0.616
54	-0.842	1.000	-1.000	-0.489	-0.667	1.000	-0.616
55	-0.842	1.000	1.000	-0.489	-0.667	-1.000	-0.616
56	-0.842	1.000	1.000	-0.489	-0.667	1.000	-0.616
57	-0.842	-0.667	0.000	-0.489	-0.667	0.192	-0.616
58	-0.842	-0.667	0.000	-0.489	-0.667	0.192	-0.616
59	-0.842	-0.667	0.000	-0.489	-0.667	0.192	-0.616
60	-0.842	-0.667	0.000	-0.489	-0.667	0.192	-0.616
61	-0.842	-0.667	0.000	-0.489	-0.667	0.192	-0.616
62	-0.842	-0.667	0.000	-0.489	-0.667	0.192	-0.616

Table F.1: Box-Behnken experimental design for 7 factors

The coefficients of the response surface function for longitudinal and transverse dispersivity are given for $X_D = 0.8$ in Tables F.2 and F.3 respectively.

0.015478	*β_o		0.001517	* L_{YD} * N_G
0.001644	* L_{XD}		0.000657	* V_{DP} * N_D
-0.00049	* L_{YD}		-0.00145	* V_{DP} * V_o
0.01441	* V_{DP}		0.001801	* V_{DP} * R_L
0.002487	* N_D		-0.00192	* V_{DP} * N_G
-0.00669	* V_o		0.000927	* N_D * V_o
-0.00026	* R_L		0.005521	* N_D * R_L
0.000637	* N_G		0.001155	* N_D * N_G
-0.00099	* L_{XD} * L_{YD}		-0.00274	* V_o * R_L
0.001159	* L_{XD} * V_{DP}		-0.00138	* V_o * N_G
-0.0007	* L_{XD} * N_D		0.000298	* R_L * N_G
-0.00266	* L_{XD} * V_o		-0.0039	* L_{XD}^2
-0.00302	* L_{XD} * R_L		-0.0067	* L_{YD}^2
0.000307	* L_{XD} * N_G		0.007811	* V_{DP}^2
-0.00324	* L_{YD} * V_{DP}		-0.00107	* N_D^2
0.004013	* L_{YD} * N_D		0.01247	* V_o^2
2.83E-05	* L_{YD} * V_o		-0.00144	* R_L^2
0.001202	* L_{YD} * R_L		-0.00354	* N_G^2

Table F.2: Coefficients of the response function for normalized longitudinal dispersivity at $x_D = 0.8$

0.014046	*β_o		-0.00056	* L_{YD} * N_G
-0.00284	* L_{XD}		-0.00361	* V_{DP} * N_D
0.002952	* L_{YD}		0.001429	* V_{DP} * V_o
0.003069	* V_{DP}		0.00066	* V_{DP} * R_L
0.014018	* N_D		-0.00014	* V_{DP} * N_G
-0.00115	* V_o		0.001647	* N_D * V_o
-0.00014	* R_L		-0.00273	* N_D * R_L
-0.00087	* N_G		-0.00095	* N_D * N_G
0.000743	* L_{XD} * L_{YD}		0.000964	* V_o * R_L
-0.0004	* L_{XD} * V_{DP}		-0.00046	* V_o * N_G
-0.00068	* L_{XD} * N_D		0.000617	* R_L * N_G
-0.001	* L_{XD} * V_o		0.011154	* L_{XD}^2
-0.00097	* L_{XD} * R_L		-0.00759	* L_{YD}^2
-0.00022	* L_{XD} * N_G		0.002926	* V_{DP}^2
0.000794	* L_{YD} * V_{DP}		-0.00564	* N_D^2
0.002645	* L_{YD} * N_D		0.007199	* V_o^2
0.000889	* L_{YD} * V_o		-0.00303	* R_L^2
2E-05	* L_{YD} * R_L		-0.00621	* N_G^2

Table F.3: Coefficients of the response function for normalized transverse dispersivity at $x_D = 0.8$

The developed response surface for both longitudinal and transverse dispersion compares well the estimated dispersivities form simulations (Figures F.1 and F.2).

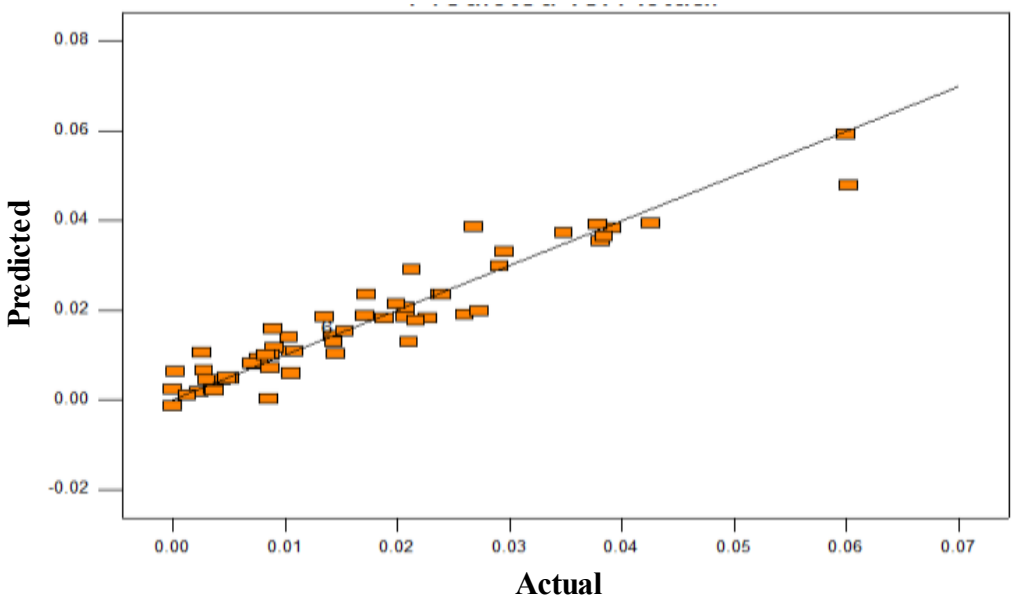

Figure F.1: Comparison of the predicted and actual normalized longitudinal dispersivity at $x_D = 0.8$.

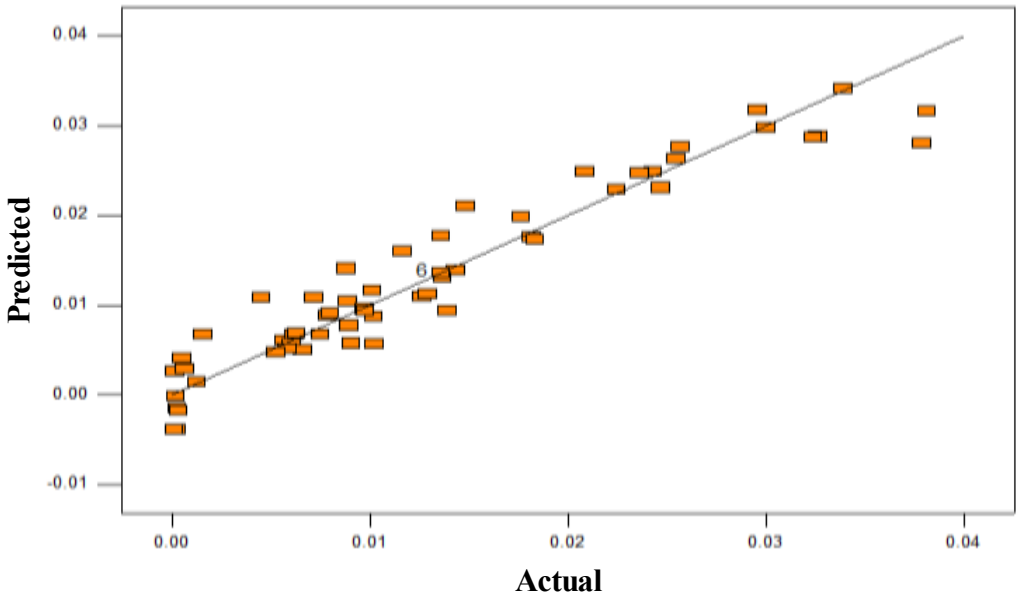

Figure F.2: Comparison of the predicted and actual normalized transverse dispersivity at $x_D = 0.8$

Response Surface for Homogeneity Index

We also designed an experimental design for Homogeneity index (Hs) based on four significant scaling groups. These scaling groups were determined to be significant by sensitivity analyses. The Box-Behnken designs for 4 variables consist of 27 simulation runs. These simulations were conducted for five different realizations of permeability. The total number of simulations conducted was 135 simulations.

The Box-Behnken design table for four variables is shown in Table F.4.

Runs	L_{XD}	L_{YD}	V_{DP}	R_L
1	-1.000	-1.000	0.000	0.192
2	-1.000	1.000	0.000	0.192
3	1.000	-1.000	0.000	0.192
4	1.000	1.000	0.000	0.192
5	-0.842	-0.667	-1.000	-1.000
6	-0.842	-0.667	-1.000	1.000
7	-0.842	-0.667	1.000	-1.000
8	-0.842	-0.667	1.000	1.000
9	-1.000	-0.667	0.000	-1.000
10	-1.000	-0.667	0.000	1.000
11	1.000	-0.667	0.000	-1.000
12	1.000	-0.667	0.000	1.000
13	-0.842	-1.000	-1.000	0.192
14	-0.842	-1.000	1.000	0.192
15	-0.842	1.000	-1.000	0.192
16	-0.842	1.000	1.000	0.192
17	-1.000	-0.667	-1.000	0.192
18	-1.000	-0.667	1.000	0.192
19	1.000	-0.667	-1.000	0.192
20	1.000	-0.667	1.000	0.192
21	-0.842	-1.000	0.000	-1.000
22	-0.842	-1.000	0.000	1.000
23	-0.842	1.000	0.000	-1.000
24	-0.842	1.000	0.000	1.000
25	-0.842	-0.667	0.000	0.192
26	-0.842	-0.667	0.000	0.192
27	-0.842	-0.667	0.000	0.192

Table F.4: Box-Behnken experimental design for four factors

A satisfactory fit was obtained between the generated response surface function and actual values (Figure F.3).

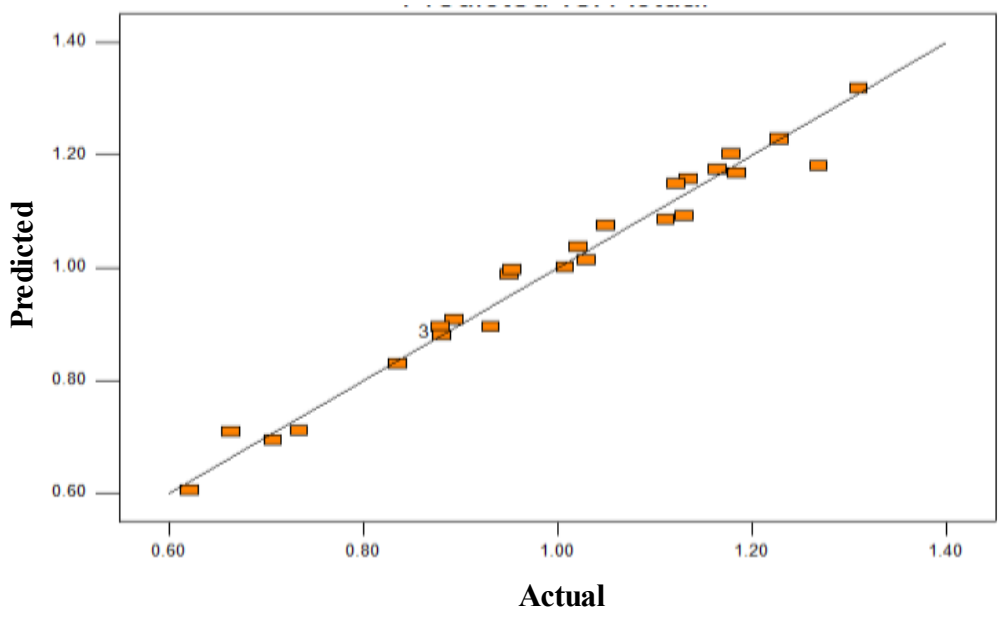

Figure F.3: Comparison of predicted Homogeneity Index from response surface function and actual values

The coefficients for the response function for Hs are given in the Table F.5.

0.70601888	*β_o		0.015734	* L_{YD} * V_{DP}
-0.0302639	* L_{XD}		0.058161	* L_{YD} * R_L
0.00935639	* L_{YD}		-0.01765	* V_{DP} * R_L
-0.2174787	* V_{DP}		0.185836	* L_{XD}^2
-0.0452856	* R_L		0.139569	* L_{YD}^2
-0.026877	* L_{XD} * L_{YD}		-0.00203	* V_{DP}^2
-0.0062975	* L_{XD} * V_{DP}		0.077231	* R_L^2
0.05893297	* L_{XD} * R_L			

Table F.5: Coefficients of the response function for Homogeneity index (Hs)

The Pareto chart for Hs shows that Hs is most significantly impacted by the V_{DP}, correlation in the transverse direction (L_{YD}) and the effective aspect ratio (R_L) (see Figure F.4).

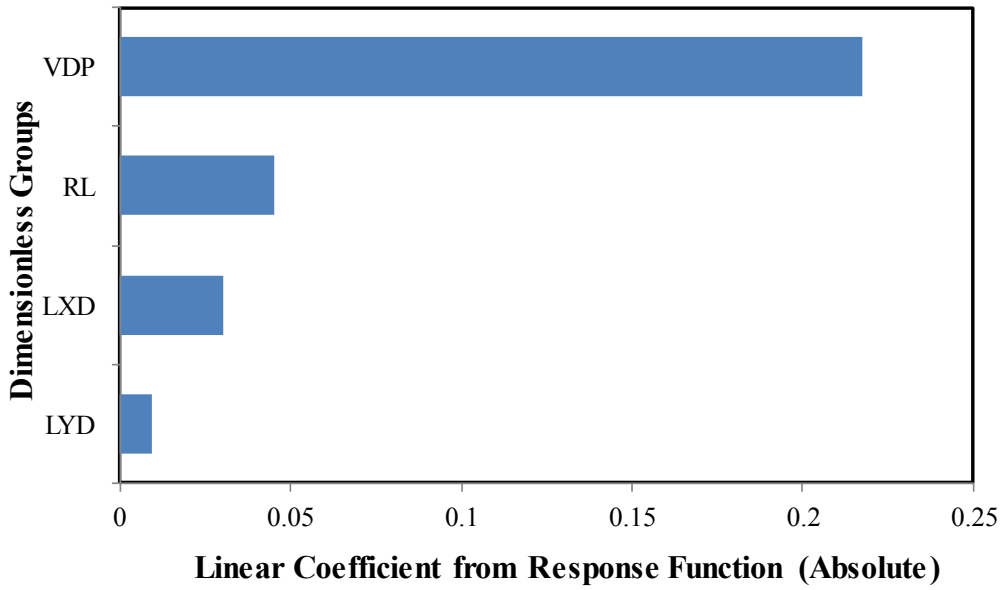

Figure F.4a: Pareto chart for Homogeneity Index (Hs) as a function of significant scaling groups based on linear coefficient from response function.

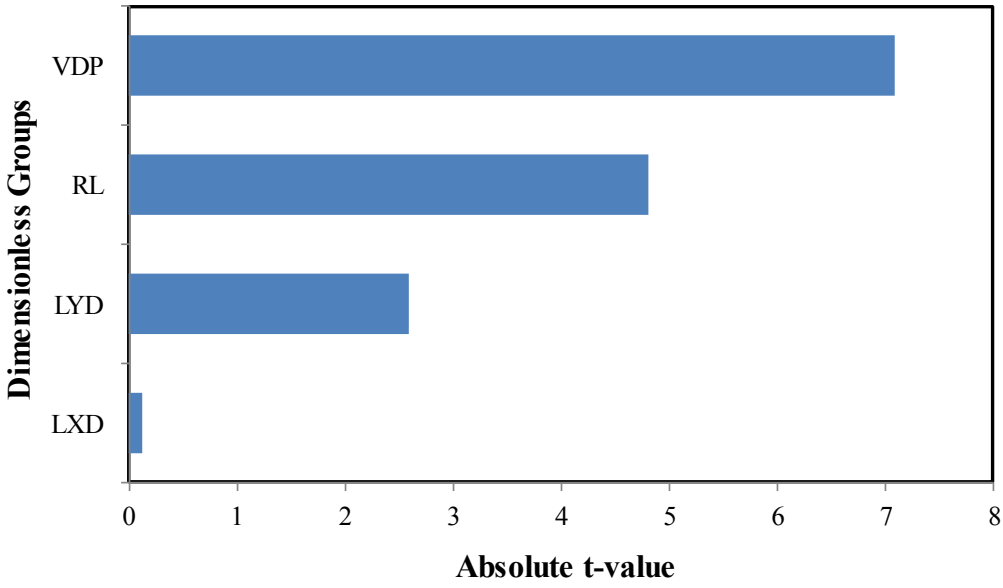

Figure F.4b: Pareto chart for Homogeneity Index (Hs) as a function of significant scaling groups based on absolute t-value.

Appendix G: Homogeneity Index

This section is based on the paper of Rashid et al. 2012. There is on-going research to develop a measure of heterogeneity that can discriminate between different realizations of permeability distributions. As shown in Figures 4.17 and 4.18, different realizations of permeability distributions have different flow structures that can influence dispersion differently.

Rashid *et al.* 2012 proposed a measure of heterogeneity that uses the shear-strain rate of the single phase velocity field. The measure is called Homogeneity Index (Hs). Hs correlates linearly (better compared to the Dykstra Parsons) with breakthrough time and recovery for various realizations of permeability distribution.

The authors considered a change in the velocity field by a small displacement (δr) from point (x_o, y_o) to point (x, y) in a 2D reservoir. The velocity field at the new location can be expressed as,

$$\boldsymbol{v}(x,y) = \boldsymbol{v}_o(x_o,y_o) + \boldsymbol{J}.\delta\boldsymbol{r} \tag{G.1}$$

where $\boldsymbol{J}$ is the velocity-gradient tensor defined as,

$$\boldsymbol{J} = \begin{pmatrix} \frac{\partial u_o}{\partial x} & \frac{\partial u_o}{\partial y} \\ \frac{\partial v_o}{\partial x} & \frac{\partial v_o}{\partial y} \end{pmatrix} \tag{G.2}$$

and u_o and v_o represents the velocity in the x- and y-directions. Changes in the velocity from one location to another for a single phase incompressible flow is caused by permeability heterogeneity and the location of the injectors and producers. The authors further decomposed the velocity gradient into symmetric and asymmetric components,

$$\boldsymbol{v}(x,y)=\boldsymbol{v}_o(x_o,y_o)+\frac{1}{2}\begin{pmatrix} 2\dfrac{\partial u_o}{\partial x} & \dfrac{\partial u_o}{\partial y}+\dfrac{\partial v_o}{\partial x} \\ \dfrac{\partial u_o}{\partial y}+\dfrac{\partial v_o}{\partial x} & 2\dfrac{\partial v_o}{\partial y} \end{pmatrix}\cdot\delta\boldsymbol{r} + \frac{1}{2}\begin{pmatrix} 0 & \dfrac{\partial u_o}{\partial y}-\dfrac{\partial v_o}{\partial x} \\ \dfrac{\partial u_o}{\partial y}-\dfrac{\partial v_o}{\partial x} & 0 \end{pmatrix}\cdot\delta\boldsymbol{r} \quad . \tag{G.3}$$

The three terms on the right of equation (G.3) have different impacts on the motion of a fluid packet. The first term is translational motion, where the fluid packet keeps its shape at it moves along the flow direction. The second term consists of the rate-of-strain tensor, which describes how the velocity field is deformed at it moves away from the initial position. The diagonal elements of the tensor are the normal rate of strain while the off-diagonal elements are proportional to rate of shear deformation. The effect of the off-diagonal element is to change the shape of the fluid, while the diagonal elements only increase or decrease the dimensions of the fluid packet along the x- and y-directions. The effects of the diagonal element are zero as their sum is zero for an incompressible fluid (based on conservation of mass, $\nabla\cdot v=0$). The third and last term is the vorticity ($\boldsymbol{\omega}=\nabla\cdot\boldsymbol{v}$) of the velocity field, which describes the rotation of the fluid packet with respect to its coordinate axis.

The authors focused the rate of shear deformation to characterize heterogeneity. The rate of shear deformation is a measure of the permeability gradient between grid-blocks and thus a measure of heterogeneity. The rate of shear deformation is defined by considering the off-diagonal term,

$$\dot{\gamma}=\frac{\partial u}{\partial y}+\frac{\partial v}{\partial x}. \tag{G.4}$$

The rate of shear deformation can be expanded by substituting Darcy's law. Considering two-phase flow with constant porosity and neglecting capillary pressure, the velocity of fluid 1 can be expressed as,

$$\boldsymbol{v}_1 = -\frac{kk_{r1}}{\mu_1}\left(\nabla p + \rho_1 \boldsymbol{g}\right). \tag{G.5}$$

The relative permeability for fluid 1 in the presence of the second fluid can be better expressed with mobility of fluid 1 as,

$$\lambda_1 = \frac{k_{r1}}{\mu_1}. \tag{G.6}$$

The velocity of fluid 2 can be described similarly to fluid 1. Using the relative mobility of fluid 1 (f_1), which is the mobility of fluid 1 divided by the total mobility (λ_T) and using the relationship ($f_2 = 1 - f_1$), the total velocity ($\boldsymbol{v}_T$) is expressed as,

$$\boldsymbol{v}_T = -k\lambda_T\left[\nabla p + \left(f_1\Delta\rho + \rho_2 g\right)\right]. \tag{G.7}$$

The x- and y-components of the total velocity (u_T, v_T) is then substituted into the equation for the rate of shear deformation (equation G.4) to obtain,

$$\begin{aligned}\frac{\partial u_T}{\partial y} + \frac{\partial v_T}{\partial x} = {} & u_T\frac{1}{k}\frac{\partial k}{\partial y} + v_T\frac{1}{k}\frac{\partial k}{\partial x} + u_T\frac{1}{\lambda_T}\frac{\partial \lambda_T}{\partial y} + v_T\frac{1}{\lambda_T}\frac{\partial \lambda_T}{\partial x} \\ & - k\lambda_T\Delta\rho\left(g_y\frac{\partial f_1}{\partial x} + g_x\frac{\partial f_1}{\partial y}\right)\end{aligned}. \tag{G.8}$$

Equation (G.8) can be further simplified by assuming that the fluid mobility only depends on saturation, to obtain

$$\begin{aligned}\dot{\gamma} = {} & \left(\frac{\partial \ln k}{\partial y}u_T + \frac{\partial \ln k}{\partial x}v_T\right) + \frac{1}{\lambda_T}\frac{\partial \lambda_T}{\partial S_1}\left(\frac{\partial S_1}{\partial y}u_T + \frac{\partial S_1}{\partial x}v_T\right) \\ & - \frac{\partial f_1}{\partial S_1}k\lambda_T\Delta\rho\left(g_y\frac{\partial S_1}{\partial x} + g_x\frac{\partial S_1}{\partial y}\right)\end{aligned}. \tag{G.9}$$

The first term in equation (G.9) shows the effect of permeability changes on the flow field and is maximized by the flow velocity. Neglecting the influence of multiphase flow, the first term can be used to characterize the heterogeneity in porous media. Thus

the rate of shear deformation must be computed for the solution of a single phase flow. Since the rate of shear deformation will vary over the entire reservoir, the authors suggested a measure of heterogeneity, based on the mean and standard deviation of the rate of shear deformation. The heterogeneity measure called Homogeneity index (Gs), is defined as,

$$\mathrm{Hs} = \frac{\text{mean}\left(|\dot{\gamma}|\right)}{\text{standard deviation}\left(|\dot{\gamma}|\right)}. \tag{G.10}$$

The homogeneity index is calculated at the vertex of each grid-block using the single phase velocity field from finite difference type numerical simulator. As the reservoir heterogeneity increases, Hs tends to zero, while Hs tends to infinity as the reservoir becomes more homogenous.

The rate of shear deformation can be expressed for a discrete case as,

$$|\dot{\gamma}| = \left|\frac{\Delta u}{\Delta y} + \frac{\Delta v}{\Delta x}\right|. \tag{G.11}$$

For a finite-difference discretization, the rate of shear deformation is computed at the vertex of each grid-block as

$$\left|\dot{\gamma}\left(i+\frac{1}{2}\right)\right| = abs\left[\frac{u\left(i+1/2, j+1\right)-u\left(i+1/2, j\right)}{\Delta y} + \frac{v\left(i+1, j+1/2\right)-v\left(i, j+1/2\right)}{\Delta x}\right]. \tag{G.12}$$

We validated the effectiveness of the homogeneity index in differentiating between permeability realizations by considering the breakthrough time at 1 PVI and recovery at 1 PVI for a series of waterfloods. The 2-D simulation model consists of 64 grid-blocks in the x-direction and 16 grid-blocks in the y-direction. The grid-block size is 1.0 ft in both directions. The waterflood was conducted with the CMG IMEX®

simulator. Different permeability realizations with different correlation structures were generated with FFTSIM (Jennings *et al.* 2000).

Three levels of heterogeneity were considered (V_{DP} = 0.6, 0.7 and 0.9), with three realizations for each level of heterogeneity. The results show that Hs gave a better linear differentiation compared to V_{DP} for each set of correlation structure, when the PVI at breakthrough time and oil recovery after 1 PVI are considered (Figures G1-4). The coefficient of determination (R^2) for the Hs cases are greater compared to the V_{DP} cases.

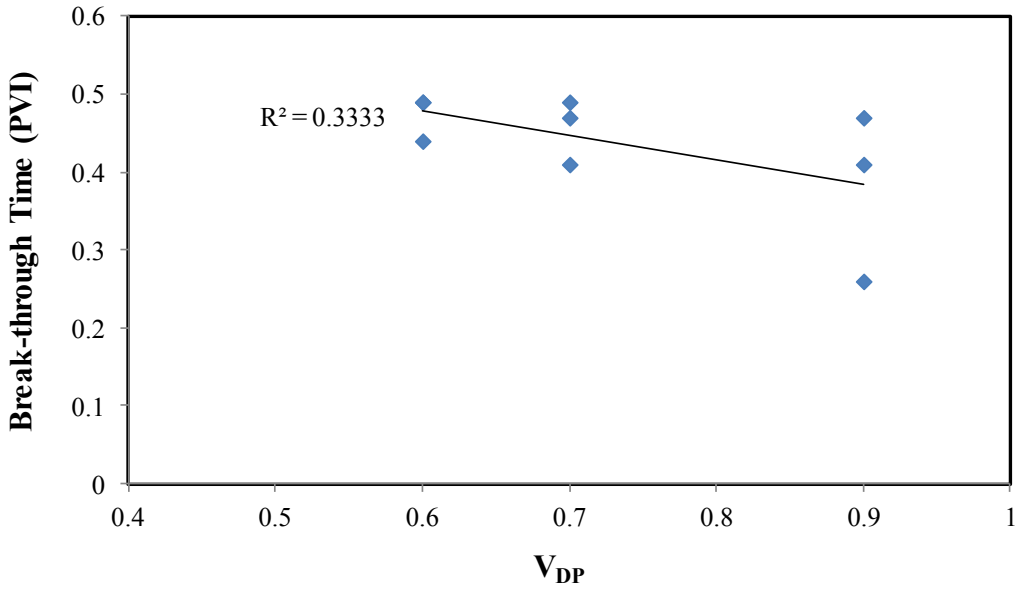

Figure G.1: PVI injected at breakthrough time for different levels of heterogeneity and realizations classified by V_{DP}. The simulation model has a dimensionless longitudinal correlation of 0.25 and transverse correlation of 0.20.

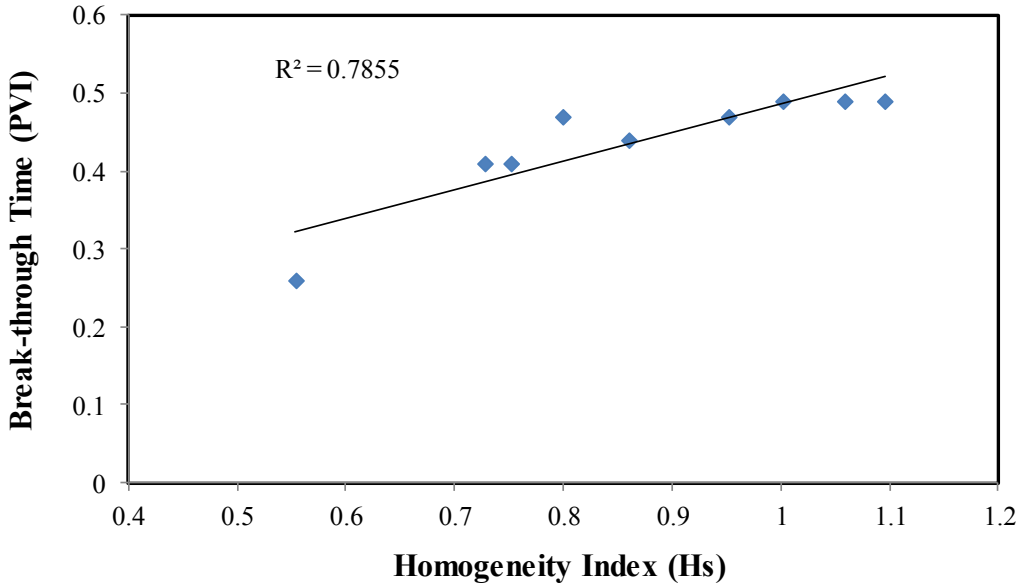

Figure G.2: PVI injected at breakthrough time for different levels of heterogeneity and realizations classified by Hs. The simulation model has a dimensionless longitudinal correlation length of 0.25 and transverse correlation length of 0.20.

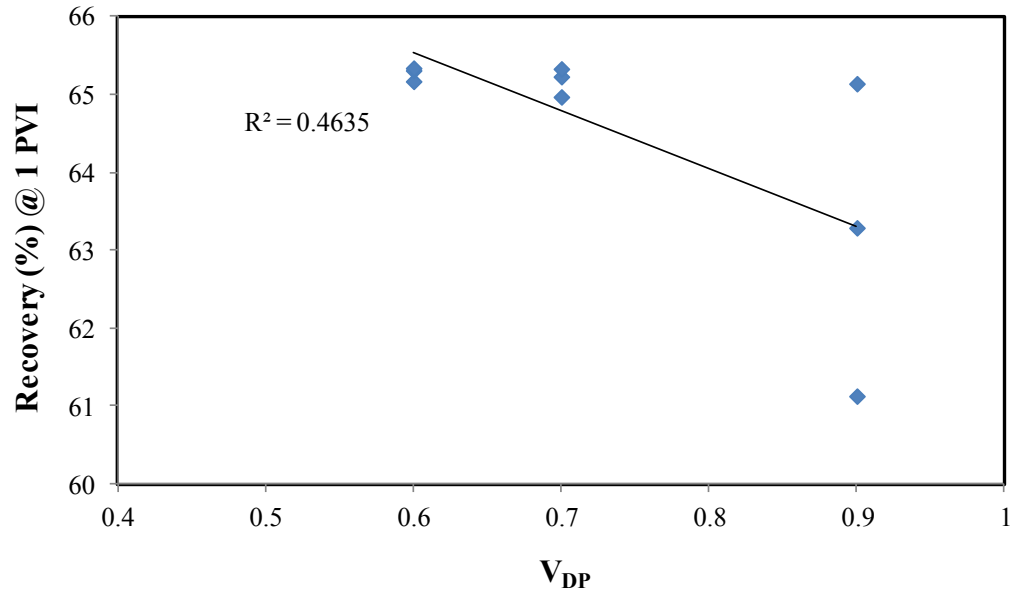

Figure G.3: Recovery (%) at 1 PVI for different levels of heterogeneity and realizations classified by V_{DP}. The simulation model has a dimensionless longitudinal correlation length of 0.25 and transverse correlation length of 0.20.

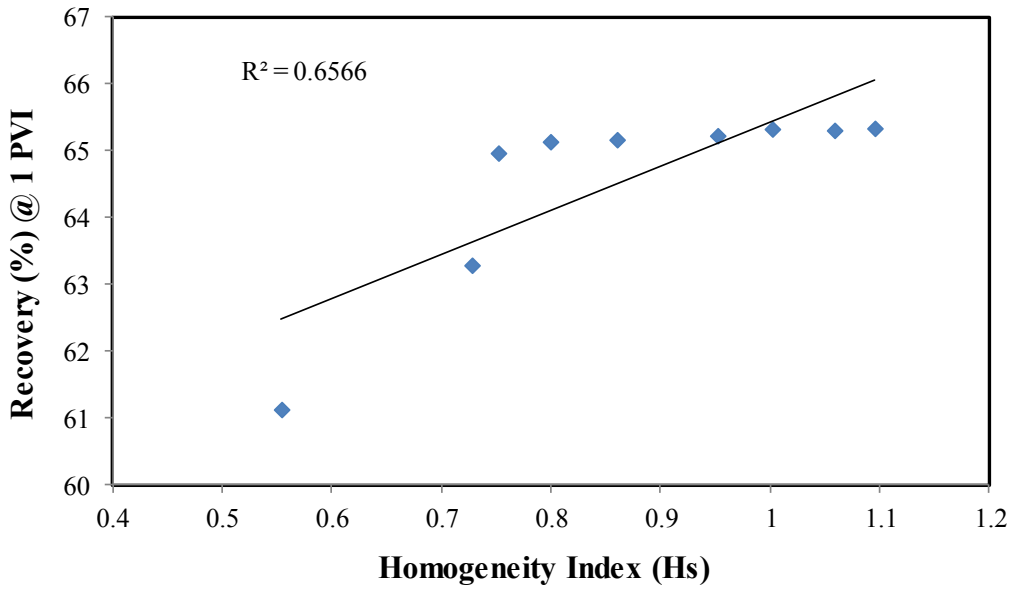

Figure G.4: Recovery (%) at 1 PVI for different levels of heterogeneity and realizations classified by Hs. The simulation model has a dimensionless longitudinal correlation length of 0.25 and transverse correlation length of 0.20.

Similar results were obtained when the dimensionless longitudinal autocorrelation was extended to 5. We also compared the homogeneity index to V_{DP} in discriminating between estimated longitudinal dispersivity for different permeability realizations. FCM simulations were conducted using CMG GEM® for a simulation model with 128 grid-blocks in the x-direction and 32 grid-blocks in the y-direction. The simulation models are randomly correlated. The Homogeneity index was able to differentiate between the different realizations, but not linearly (Figures G.5 and G.6). It is expected that as the levels of heterogeneity increase, dispersion should increase. This shows that Hs may not be as robust as the authors claim; however it has the advantage that it can be easily computed and it better differentiates between permeability realizations than V_{DP} for waterfloods. Hs is also not predictive, as permeability realization of particular Hs cannot be generated.

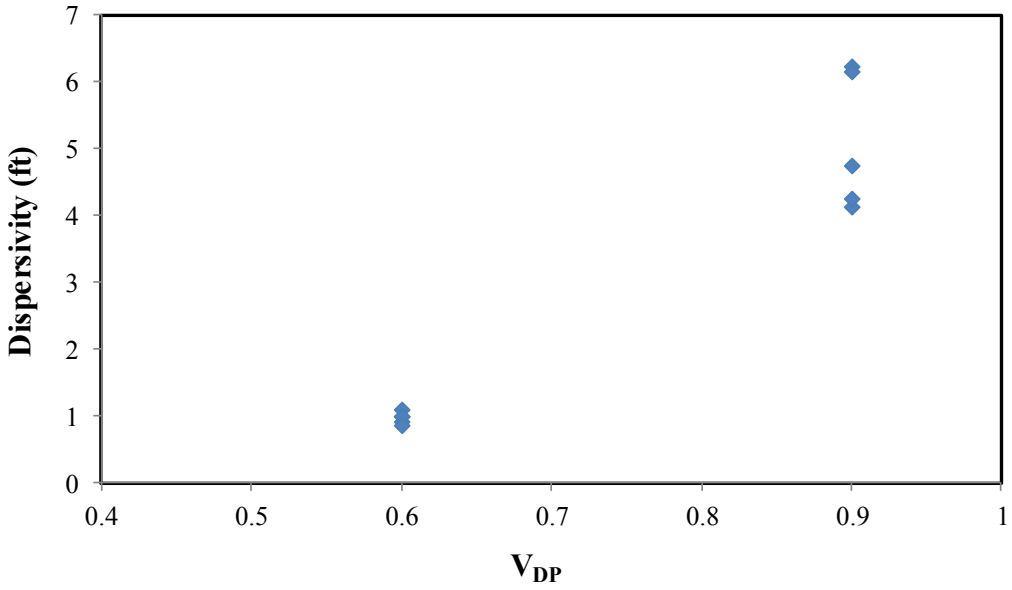

Figure G.5: Longitudinal dispersivity for different levels of heterogeneity and realizations classified by V_{DP}. The simulation model is uncorrelated in longitudinal and transverse direction.

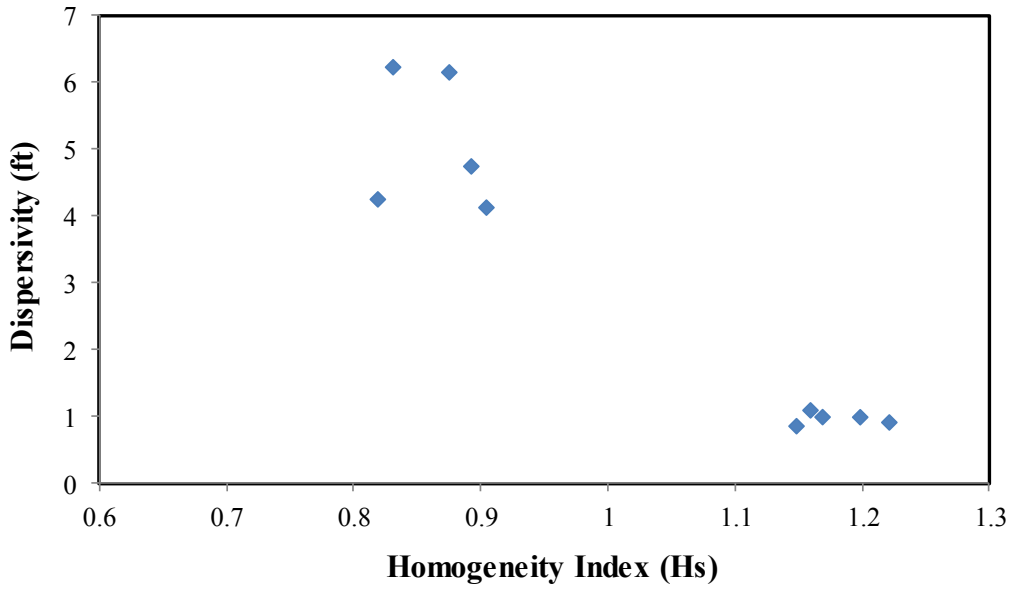

Figure G.6: Longitudinal dispersivity for different levels of heterogeneity and realizations classified by Hs. The simulation model is uncorrelated in longitudinal and transverse direction.

References

Adepoju, O. O., Lake, L. W., and Johns, R. T. 2013. Investigation of Anisotropic Mixing in Miscible Displacements. *SPE Reservoir Evaluation & Engineering*, Feb., 85-96

Alkindi, A., Al-Wahaibi, Y., Bijeljic, B. and Muggeridge, A. 2011. Investigation of Longitudinal and Transverse Dispersion in Stable Displacements with a High Viscosity and Density Contrast between the Fluids. *Journal of Contaminant Hydrology*. 120-121, 170-183

Anderson, M. P. 1984. *Movement of Contaminants in Groundwater: Groundwater Transport – Advection and Dispersion*. Groundwater Contamination. National Academy Press, Washington, DC. 37-45

Aris, R. 1956. On the Dispersion of a Solute in a Fluid Flowing Through a Tube. *Proc. Roy. Soc. A.* 235, 67-77

Aris, R. and Amundson, N. R. 1957. Some Remarks on Longitudinal Mixing or Diffusion in Fixed Beds. *J. Amer. Inst. Chem. Eng*. No. 2,3, 280-282

Arya, A., Hewett, T. A., Larson, R. G. and Lake, L. W. 1988. Dispersion and Reservoir Heterogeneity. *SPE Reservoir Engineering*, Feb., 139-148

Bear, J. 1960. The Transition Zone Between Fresh and Salt Water in Coastal Aquifers. PhD Thesis, University of California, Berkley, California

Bear, J. 1961. On the Tensor Form of Dispersion. J. Geophys. Res. N. 4, 66, 1185-1197

Bear, J. 1972. *Dynamics of Fluids in Porous Media*. American Elsevier Publishing Company, New York, USA.

Begg, S. H. and King, P. R. 1985. Modeling the Effects of Shale on Reservoir Performance: Calculation of Effective Vertical Permeability. Paper SPE 13529 presented at the Reservoir Simulation Symposium, Dallas, TX.

Begg, S. H., Carter, R. R. and Dranfield, P. 1989. Assigning Effective values to Simulator Gridblock Parameters for Heterogeneous Reservoirs. *SPE Reservoir Engineering,* Nov, 455-463

Blackwell, R. J. 1959. Experiments on Mixing by Fluid Flow in Porous Media. *Amer. Inst. Chem. Eng. And Soc. Petrol. Eng*. 52nd Annual Meeting, San Francisco. No 29

Blackwell, R. J. 1962. Laboratory Studies of Microscopic Dispersion Phenomena. *SPE Journal*. 1-8.

Box, G. E. P. and Behnken, D. W. 1960. Some New Three Level Designs for the Study of Quantitative Variables. *Technometrics* 2: 455-475.

Box-Behken designs. 2013. NIST e-Handbook of Statistical Methods, http://www.itl.nist.gov/div898/handbook/pri/section3/pri3362.htm, Downloaded 23 January 2013.

Bruggeman, G. A. 1999. *Analytical Solutions of Geohydrological Problems*. Elsevier, Netherlands.

Carslaw, H. S., and Jaeger, J. C. 1959.*Conduction of Heat in Solids*. 2nd ed., Oxford University Press.

Chen. Y, Durlofsky. L. J., Gerritsen. M. and Wen, X. H. 2003. A Coupled Local-Global Upscaling Approach for Simulating Flow in Highly Heterogeneous Formations. *Adv. In Water Resources*. 26. 1041-1060.

Churchill, R. V. 1972.*Operational Mathematics*. 3rd ed., McGraw-Hill USA.

Cirpka, O. A. and Kitanidis, P. K. 2000. Characterization of Mixing and Dilution in Heterogeneous Aquifers by Means of Local Temporal Moments. *Water Resources Research.* Vol 36, No 5, 1221-1236.

Clearly, R. W., and Ungs, M. J. 1978. Analytical Models for Groundwater Pollution and Hydrology. Report 78-WR-15, *Water Resources Program*, Princeton University, Princeton, New Jersey, USA.

CMG GEM ®, *Computer Modeling Group* Inc, 2010.

Dagan, G. 1982. Stochastic Modeling of Groundwater by Unconditional and Conditional Probabilities, 2. The Solute Transport. *Water Resour. Res*. 18(4), 835-848.

Dagan, G. 1984. Solute Transport in Heterogeneous Porous Formations. *J. Fluid Mech*., Vol. 145, 151-177.

Danel, P. 1952. The Measurement of Groundwater. Ankara Symp. Arid Zone Hydrology, Proc. UNESCO, No. 2, 99-107

Datta-Gupta, A. and King, M. J. 2007. Streamline Simulation: Theory and Practice. *SPE Textbook Series*, Vol. 11.

De Jong, J. 1958. Longitudinal and Transverse Diffusion in Granular Deposits. *Trans. Amer. Geophys. Union*. 39, 67-74.

De Jong, J. 1958a. Discussion on Longitudinal and Transverse Diffusion in Granular Deposits. *Trans. Amer. Geophys. Union*. 39, 1160-1161.

Design-Expert ®, Version 8.0, Stat-ease, Inc, 2010.

Durlofsky, L. J. 1991. Numerical Calculation of Equivalent Grid Block Permeability Tensors for Heterogeneous Porous Media. *Water Resour. Res*., Vol. 27, No. 5 699-708.

Durlofsky, L. J., Behrens, R. A., Jones, R. C., and Bernath, A. 1996.Scale Up of Heterogeneous Three Dimensional Reservoir Descriptions. *SPE Journal*. Vol. 1, No. 3, 313-326.

Dykstra, H. and Parsons, R. L. 1950. *The Prediction of Oil Recovery by Waterflooding in Secondary Recovery of Oil in the United States*. 2nd Ed., Washington DC:API, 160-174.

Factorial designs. 2013. Mathworks Online Help, http://www.mathworks.com/help/stats/fractional-factorial-designs-1.html. Downloaded 23 January 2013

Fanchi, J. R. 1983. Multidimensional Numerical Dispersion. *Society of Petroleum Engineers Journal.* Vol. 23, No. 1, 143-151.

Freeze, R. A. and Cheery, J. A. 1979. *Groundwater*. Prentice Hall, NJ., USA.

Friedmann, F., Chawathe, A. and Larue, D. 2003. Assesing Uncertainty in Channelized Reservoirs Using Experimental Design. *SPE Reservoir Evaluation & Engineering*, Aug., 264-274.

Garmeh, G. and Johns, R. T. 2010. Upscaling Miscible Floods in Heterogenous Reservoirs Considering Reservoir Mixing. *SPE Journal*, Dec., 747-763.

Garmeh, G., Johns, R. T., and Lake, L. W.2009. Pore-Scale Simulation of Dispersion in Porous Media. *SPE Journal*, Dec., 559-567.

Gelhar, L. W. and Axness, C. L. 1981. Stochastic Analysis of Macro-Dispersion in Three Dimensional Heterogeneous Aquifers. Geophysical Research Center, Rep No H8, New Mexico.

Gelhar, L. W. and Axness, C. L. 1983. Three Dimensional Stochastic Analysis of Macrodispersion in Aquifers. *Water Resour. Res*. 19(1), 161-180

Gelhar, L. W. and Collins, M. A. 1971. General Analysis of Longitudinal Dispersion in Non-uniform Flow. *Water Resour. Res*., 7(6), 1511-1521.

Gelhar, L. W., Gutjahr, A. L. and Naff, R. L. 1979. Stochastic Analysis of Macrodispersion in a Stratified Aquifer. *Water Resour. Res*. 15, 1387-1397.

Ghanbarnezhad Moghanlo, R. 2012. Modeling the Fluid Flow of Carbon Dioxide through Permeable Media. PhD Dissertation, University of Texas, Austin, Texas.

Gharbi, R., Peters, E. and Elkamel, A. 1998. Scaling Miscible Fluid Displacements in Porous Media. *Energy & Fuels*, 12, 801-811.

Ghomian, Y. 2008. Reservoir Simulation Studies for Coupled CO2 Sequestration and Enhanced Oil Recovery. PhD Dissertation, University of Texas , Austin, Texas.

Goode, D. J. and Konikow, L. F. 1990. Apparent Dispersion in Transient Groundwater Flow. *Water Resour. Res*. 26(10), 2339-2351.

Gradshteyn, I. S. and Ryzhik, I. M. 2007.*Tables of Integrals, Series, and Products*. 7th ed., Elsevier, Oxford, UK.

Greenkorn, R. A. 1964. Flow Models and Scaling Laws for Flow Through Porous Media. *Ind. Eng. Chem*., Vol. 56, No. 3, 32-37.

Greenkorn, R. A. and Cala, M. A. 1986. Scaling Dispersion in Heterogeneous Porous Media. *Ind. Eng. Chem. Fundam*., 25, 506-510.

Greenkorn, R. A., Johnson, C. R. and Haring, R. E. 1965. Miscible Displacements in a Controlled Natural System. *Journal of Petroleum Tech.,* Nov., 1329-1335.

Haajizadeh, H., Fayers, F. J., and Cockin, A. P. 2000. Effects of Phase Behavior Dispersion and Gridding on Sweep Patterns for Nearly Miscible Displacements. Paper presented at the SPE Annual Technical Conference and Exhibition, Dallas, Texas, 1-4 Oct.

Haajizadeh, H., Fayers, F. J., Cockin, A. P., Roffey, M., and Bond, D. J. 1999. On the Importance of Dispersion and Heterogeneity in the Compositional Simulation of Miscible Gas Processes. Paper presented at the SPE Asia Pacific Improved Oil Recovery Conference, Kuala Lumpur, Malaysia, 25-26 Oct.

Hassinger, R. C. and Dale, U. 1963. A Mathematical and Experimental Examination of Transverse Dispersion Coefficients. *SPE Journal,* Jun. 195-204.

Hulin, J. P. and Plona, T. J. 1989. Echo Tracer Dispersion in Porous Media. *Physics of Fluids*. Vol. 1, No 8, 1341-1347.

Jennings, J. W., S. C. Ruppel, and W. B. Ward. 2000. Geostatistical Analysis of Permeability Data and Modeling of Fluid Flow Effects in Carbonate Outcrops. *SPE Reservoir Evaluation and Engineering*, 3(4), 292-303.

Jha, R. K., Brynat, S. L., Lake, L. W. and John, A. 2006. Investigation of Pore-Scale (Local) Mixing. Paper SPE 99782 presented at the SPE/DOE Symposium on Improved Oil Recovery, Tulsa, Oklahoma, Apr. 22-26.

Jha, R. K., John, A. K., Bryant, S. L., and Lake, L. W. 2009. Flow Reversal and Mixing. *SPE Journal*. Vol. 14, No. 1, 41-49.

John, A. K., Lake, L. W., Bryant, S. L., and Jennings, J. W. 2010. Investigation of Mixing in Field-Scale Miscible Displacements Using Particle-Tracking Simulations of Tracer Floods with Flow Reversal. *SPE Journal*, Vol. 15, No. 3, 598-609.

Johns, R. T., Fayers, F. J., and F. M. Orr, Jr. 1994. Effect of Gas Enrichment and Dispersion on Nearly Miscible Displacements in Condensing/Vaporizing Drives. *SPE Advanced Technology Series*, Vol. 2, No 2, 26-34.

Johns, R. T., Sah, P. and Subramanian, S. K. 2000. Effect of Gas Enrichment Above the MME on Oil Recovery in Enriched-Gas Floods. *SPE Journal*, Vol. 5, No. 3, Sept., 331-338.

Kitanidis, P. K. 1994. The Concept of Dilution Index. *Water Resour. Res*., Vol. 30. No. 7, 2011-2026.

Lake, L. W. 1989. *Enhanced Oil Recovery*. Prentice Hall, NJ, USA

Lake, L. W. and Hirasaki, G. J. 1981. Taylor's Dispersion in Stratified Porous Media. *SPE J*. Aug, 459-468

Lake, L. W. and Jensen, J. L. 1989. A Review of Heterogeneity Measures Used in Reservoir Characterization. *USMS/SPE* 20156

Lantz, R. B. 1971. Quantitative Evaluation of Numerical Diffusion (Truncation Error). *SPE Journal*. Vol. 11, No. 3, 315-320.

Li, D. and Lake, L. W. 1995. Scaling Fluid Flow through Heterogeneous Permeable Media. *SPE Advanced Tech. Series*, Vol. 3, No 1.

Mahadevan, J., Lake, L. W., and Johns, R. T. 2003. Estimation of True Dispersivity in Field Scale Permeable Media. *SPE Journal*, 272-279.

Mathematica ®, *Wolfram Research* Inc., 2008

Matheron, G. and DeMarsily, G. 1980. Is Transport in Porous Media always Diffusive? *Water Resour. Res*. 16, 901-917.

Matlab ®, *Mathworks* 2008b

Mercado, A. (1967). The Spreading Pattern of Injected Water in a Permeability Stratified Aquifer. *Proc. Int. Assoc. Sci. Hydrol*. Symp., Haifa, Publ. No 72, 23-26.

Mercado, A. 1966. Recharge and Mixing Tests at Yavne 20 Well Field. Underground Water Storage Study Tech. Rep. 12, Publ. 611, Tel Aviv.

Myers, R. H. and Montgomery, C. D. 1995. *Response Surface Methodology: Process and Product Optimization Using Designed Experiments*. New York: John Wiley and Sons.

Ogata, A., and Banks, R. B. 1961. A Solution of the Differential Equation of Longitudinal Dispersion in Porous Media. U.S. Geol. Sur., *Water Resource*. Invest.79-27.

Ozisik, M. N. 1980. *Heat Conduction*. John Wiley & Sons, USA.

Parakh, H., and Johns, R. T. 2004. Use of Stripping Ratios to Identify Dispersion Levels and Displacement Mechanisms in Miscible Gas Floods. Paper presented at the SPE Annual Technical Conference and Exhibition, Houston, Texas, 26-29.

Perkins, T. K. and Johnston, O. C. 1963. A Review of Diffusion and Dispersion in Porous Media. *SPE Journal*, Mar., 70-84.

Pickens, J.F. and Grisak, G. E. 1981a. Scale-Dependent Dispersion in Stratified Granular Aquifer. *Water Resour. Res*. 17, 1191-1212.

Pickens, J.F. and Grisak, G. E. 1981b. Modeling of Scale-Dependent Dispersion in Hydrogeologic Systems. *Water Resour. Res*. 17, 1701-1711.

Plackett, R. L. and Burmann, J. P. 1946. *The Design of Optimum Multifactorial Experiments*. Biometrika, University Press, Cambridge, 33, 305.

Pollock, D. W. 1988. Semi-analytical Computation of Path Lines for Finite Difference Models. *Ground Water,* Vol. 26, No.6, 743-750.

Qi, D., and Hesketh, T. 2005. An Analysis of Upscaling Techniques for Reservoir Simulation. *Petroleum Science and Technology*.23:827-842.

Rapoport, L. A. 1955. Scaling Laws for Use in Design and Operation of Water-Oil Flow Models. *Petroleum Trans. AIME*., Vol. 204, 143-150.

Rashid, B., Muggeridge, A. H., Bal, A. and Williams, G. 2012. Quantifying the Impact of Permeability Heterogeneity on Secondary-Recovery Performance. *SPE Journal*. June, 455-468.

Saffman, P. G. 1959. A Theory of Dispersion in Porous Medium. *J. Fluid. Mech*. No. 3, 6, 321-349

Saffman, P. G. 1960. Dispersion Due to Molecular Diffusion and Macroscopic Mixing in Flow through a Network of Capillaries. *J. Fluid. Mech.* No. 2, 7, 194-208.

Saladin, P. and Fiorotto, V. 2000. Dispersion Tensor Evaluation in Heterogeneous Media for Finite Peclet Values. *Water Resour. Resr*. Vol. 36, No. 6, 1449-1455.

Scheidegger, A. E. 1954. Statistical Hydrodynamics in Porous Media. *J. Appl. Phys*. No. 25, 994-1001.

Scheidegger, A. E. 1957. On the Theory of Flow of Miscible Phases in Porous Media. Proc. *IUGG General Assembly*, Toronto 2, 236-242.

Scheidegger, A. E. 1958. Statistical Approach to Miscible Displacements in Porous Media. *Bull. Canada Inst. Min. Met*. 26-30.

Scheidegger, A. E. 1961. General Theory of Dispersion in Porous Media. *J. Geophys. Res*. 66, 3273-3278.

Settari, A. and Aziz, K. 1972. Use of Irregular Grid in Reservoir Simulation. *SPE. Journal*, Apr., 103-113.

Shook, M., Li, D. and Lake, W. L. 1992. Scaling Immiscible Flow through Permeable Media by Inspectional Analysis. *In Situ*, 16(4), 311-349.

Solano, R., Johns, R. T., and Lake, L. W. 2001. Impact of Reservoir Mixing on Recovery in Enriched-Gas Drives above the Minimum Miscibility Enrichment. *SPE Reservoir Evaluation & Engineering*. Vol. 4, No. 5, 358-365.

Stalkup, F. 1998. Predicting the Effect of Continued Gas Enrichment Above the MME on Oil Recovery in Enriched Hydrocarbon Gas Floods. Paper presented at the SPE Annual Technical Conference and Exhibition, Louisiana, New Orleans, 27-30 Sept.

Taylor, G. I. 1953. The Dispersion of Matter in Solvent Flowing Slowly through a Tube. *Proc. R. Soc*. London, Ser. A 219, 186-203.

Wexler, E. J. 1989. Analytical Solution for One-, Two-, and Three-Dimensional Solute Transport in Groundwater Systems with Uniform Flow. U.S Geological Survey, Open-File Report 89-56.

Wood, D. J., Lake, L. W., Johns, R. T., and Nunez, V. 2008. A Screening Model for CO2 Flooding and Storage in Gulf Coast Reservoirs Based on Dimensionless Groups. *SPE Reservoir Evaluation & Engineering*, Vol. 11, No 3, 513-520.

Yang, A. 1990. Stochastic Heterogeneity and Dispersion. PhD dissertation. University of Texas, Austin.